

**Investigating the Process-Structure-Property Relationships of Additively
Manufactured 17-4 Precipitation Hardening Stainless Steel**

by

Pooriya Dastranjy Nezhadfar

A dissertation submitted to the Graduate Faculty of
Auburn University
in partial fulfillment of the
requirements for the Degree of
Doctor of Philosophy

Auburn, Alabama
August 6th, 2022

Keywords: Additive manufacturing, Structure-property, Stainless steel, Microstructure,
Tensile behavior, Fatigue behavior, Shielding gas

Copyright 2022 by Pooriya Dastranjy Nezhadfar

Approved by

Dr. Nima Shamsaei, Chair, Philpott-WestPoint Stevens Distinguished Professor,
Department of Mechanical Engineering

Dr. Jeffrey Suhling, Quina Professor, Department of Mechanical Engineering

Dr. Robert L. Jackson, Albert Smith Jr. Professor, Department of Mechanical Engineering

Dr. Bart Prorok, Interim Program Chair of Materials Engineering Professor, Department of
Materials Engineering

Mr. Paul R. Gradl, Propulsion Department, NASA Marshall Space Flight Center

Dr. Asha-Dee Celestine, Assistant Professor, Aerospace Engineering

Abstract

The present work aims to investigate the process-structure-property relationships for the additively manufactured 17-4 PH stainless steel to improve its mechanical performance. To this end, a multidisciplinary (i.e., micro-/defect-structure correlation with the mechanical properties) investigation is carried out to evaluate the impact of the process (i.e., additive manufacturing techniques, process parameter maneuvering, and post-process surface and thermal treatments) on the micro-/defect-structure, and further mechanical performance of the additively manufactured 17-4 PH stainless steel. The micro-/defect-structural characterization was performed utilizing optical and scanning electron microscopy, X-ray diffraction, electron backscatter diffraction, electron dispersive spectroscopy, and X-ray diffraction computed tomography. The micro-/defect-structure results obtained for different conditions are correlated with the mechanical properties (i.e., tensile, fatigue, fatigue crack growth) and fracture behavior of the material. Several types of heat treatment procedures were applied on the additively manufactured 17-4 PH SS specimens with the as-built and machined surface conditions to find an appropriate heat treatment that results in a good combination of the tensile and fatigue properties. The selection of the most appropriate heat treatment is based on the heat treatment with and without hot isostatic pressing, basically with the presence of defects and elimination of defects, respectively. In addition, the effect of shielding gas type on the micro-/defect-structure and consequently on the mechanical properties is studied. It is shown that using

the N₂ as the shielding gas for the laser powder bed fused 17-4 PH stainless steel refines the micro-/defect-structure and enhances the tensile properties and fatigue up to the very high cycle fatigue regime. Although the N₂ shielding gas results in smaller and fewer defects in laser powder bed fused specimens, the CA-H900 heat treatment results in more scatter in fatigue than in the CA-H1025 heat treatment condition. Therefore, the CA-H1025 heat treatment procedure is recommended for the laser powder bed fused 17-4 PH stainless steel. The 17-4 PH stainless steel's microstructure is found to be dependent on additive manufacturing techniques, laser powder bed fusion, laser powder directed energy deposition, and metal binder jetting. Since the goal is to propose a universal heat treatment scheme, and metal binder jetting specimens are required to be hot isostatic pressed prior to heat treatment, the laser powder bed fused and laser powder directed energy deposited specimens were also hot isostatic pressed. It is seen that in case of defect elimination, the most common heat treatment, i.e., CA-H900, can be an option for the laser powder bed fused and laser powder directed energy deposited 17-4 PH stainless steel; however, metal binder jetted counterpart exhibit a large scatter in fatigue results. The CA-H1150 heat treatment condition is found to be an appropriate scheme for the hot isostatic pressed additively manufactured 17-4 PH stainless steel regardless of the additive manufacturing technique. Nonetheless, laser powder bed fused 17-4 PH stainless steel possesses the best mechanical performance process, which is attributed to the refined microstructure and the absence of δ -ferrite due to using N₂ shielding gas for fabrication.

Acknowledgments

I would like to dedicate this dissertation to my wife, Sanaz, who has supported me, believed in me, and been patient with me over these years. This could have not happened without her inspiration and support.

I would like to thank my advisor Dr. Nima Shamsaei for his advice, guidance, and most importantly his knowledge and expertise, which were pivotal to the successful completion of this dissertation. I would like to thank my committee members, Dr. Jeffrey Suhling, Dr. Robert L. Jackson, Dr. Bart Prorok, and Mr. Paul R. Gradl for their time, valuable feedback, and suggestions, which helped to improve the quality of this dissertation. I would also like to thank Dr. Shuai Shao and Dr. Jutima Simsiriwong for helping me and guiding me through our collaboration studies. Finally, many thanks to my friends and lab mates who made my journey through graduate school memorable and enjoyable.

Table of Contents

| | |
|--|-------|
| Abstract..... | 2 |
| Acknowledgments..... | 4 |
| List of Tables | 12 |
| List of Figures | 15 |
| 1. CHAPTER 1: INTRODUCTION..... | 29 |
| 1.1. Overview and Significance | 29 |
| 1.2. Objectives Overview..... | 38 |
| 1.3. Outline of Dissertation..... | 40 |
| 2. CHAPTER 2: FATIGUE BEHAVIOR OF ADDITIVELY MANUFACTURED PH STAINLESS STEEL: SYNERGISTIC EFFECTS OF SURFACE ROUGHNESS AND HEAT TREATMENT..... | 17-44 |
| 2.1. Abstract | 45 |
| 2.2. Introduction..... | 46 |
| 2.3. Experimental Procedures | 49 |
| 2.3.1. Material and Specimen Fabrication | 49 |
| 2.3.2. Microstructure Characterization | 51 |
| 2.3.3. Mechanical Testing..... | 52 |

| | |
|---|-----|
| 2.4. Experimental Results | 53 |
| 2.4.1. Microstructural Observations..... | 53 |
| 2.4.2. Tensile Behavior | 56 |
| 2.4.3. Fatigue Behavior..... | 57 |
| 2.5. Discussion on Experimental Results..... | 59 |
| 2.5.1. Microstructure and Tensile Behavior..... | 59 |
| 2.5.2. Fatigue Behavior and Fractography | 63 |
| 2.6. Conclusions..... | 69 |
| | |
| 3. CHAPTER 3: FATIGUE CRACK GROWTH BEHAVIOR OF ADDITIVELY MANUFACTURED 17-4 PH STAINLESS STEEL: EFFECTS OF BUILD ORIENTATION AND MICROSTRUCTURE | 97 |
| 3.1. Abstract | 98 |
| 3.2. Introduction..... | 99 |
| 3.3. Experimental Procedures | 102 |
| 3.3.1. Material and Specimen Fabrication | 102 |
| 3.3.2. Microstructural Prediction and Characterization | 104 |
| 3.3.3. Fatigue Crack Growth (FCG) Test and Fractography | 105 |
| 3.4. Results and Discussions..... | 106 |
| 3.4.1. Microstructure..... | 106 |
| 3.4.2. Fatigue Crack Growth (FCG) Behavior..... | 109 |

| | |
|---|-----|
| 3.4.3. Fractography | 114 |
| 3.5. Conclusions..... | 117 |
| 4. CHAPTER 4: IMPROVED HIGH CYCLE FATIGUE PERFORMANCE OF ADDITIVELY MANUFACTURED 17-4 PH STAINLESS STEEL VIA IN-PROCESS REFINING MICRO-/DEFECT-STRUCTURE..... | 135 |
| 4.1. Abstract | 136 |
| 4.2. Introduction..... | 137 |
| 4.3. Experimental Procedures | 143 |
| 4.3.1. Material and Specimen Fabrication | 143 |
| 4.3.2. Microstructure Characterization | 144 |
| 4.3.3. Mechanical Testing..... | 145 |
| 4.4. Experimental Results | 146 |
| 4.4.1. Microstructural Observations..... | 147 |
| 4.4.2. Mechanical Properties..... | 151 |
| 4.5. Discussion on Experimental Results..... | 155 |
| 4.5.1. Tensile Behavior as Affected by Micro-/Defect-Structures | 155 |
| 4.5.2. Enhanced Fatigue Performance via In-Process Refinement of Micro-/Defect- Structure | 158 |
| 4.6. Conclusions..... | 163 |

| | |
|--|-----|
| 5. CHAPTER 5: HIGH AND VERY HIGH CYCLE FATIGUE BEHAVIOR OF ADDITIVELY MANUFACTURED 17-4 PH STAINLESS STEEL: EFFECT OF SHIELDING GAS TYPE | 185 |
| 5.1. Abstract | 186 |
| 5.2. Introduction..... | 187 |
| 5.3. Experimental Procedures | 190 |
| 5.3.1. Material and Fabrication | 190 |
| 5.3.2. Specimen Design | 191 |
| 5.3.3. Micro-/Defect-Structure Characterization | 191 |
| 5.3.4. Fatigue Testing..... | 192 |
| 5.4. Experimental Results | 193 |
| 5.4.1. Microstructure..... | 193 |
| 5.4.2. Defect-Structure | 195 |
| 5.4.3. Fatigue Behavior..... | 196 |
| 5.5. Discussion on the Experimental Results..... | 196 |
| 5.5.1. Effect of Geometry on Fatigue Behavior..... | 196 |
| 5.5.2. Effect of Shielding Gas Type on Fatigue Behavior | 197 |
| 5.5.3. Failure Analysis | 200 |
| 5.6. Conclusions..... | 202 |

| | |
|---|-----|
| 6. CHAPTER 6: VERY HIGH CYCLE FATIGUE BEHAVIOR OF ADDITIVELY MANUFACTURED 17-4 PH STAINLESS STEEL: EFFECT OF HEAT TREATMENT AND SPECIMEN GEOMETRY | 221 |
| 6.1. Abstract | 222 |
| 6.2. Introduction..... | 223 |
| 6.3. Experimental Procedures | 226 |
| 6.3.1. Material, Fabrication, Heat Treatment, and Specimen Design..... | 226 |
| 6.3.2. Microstructure Characterization | 227 |
| 6.3.3. Fatigue Testing..... | 228 |
| 6.4. Results and Discussion | 229 |
| 6.4.1. Effect of Heat Treatment on the Microstructure..... | 229 |
| 6.4.2. Fatigue Behavior..... | 230 |
| 6.4.3. Fractography | 234 |
| 6.5. Conclusions..... | 237 |
| 7. CHAPTER 7: MICROSTRUCTURE AND DEFORMATION BEHAVIOR OF ADDITIVELY MANUFACTURED 17-4 STAINLESS STEEL: INFLUENCE OF MANUFACTURING TECHNIQUES FROM LASER POWDER BED FUSION (L-PBF) TO LASER POWDER DIRECTED ENERGY DEPOSITION (LP-DED) | 253 |
| 7.1. Abstract | 254 |
| 7.2. Introduction..... | 255 |
| 7.3. Experimental Procedure..... | 258 |

| | |
|---|-----|
| 7.4. Results and Discussion | 260 |
| 7.4.1. NHT Microstructure..... | 260 |
| 7.4.2. Heat Treated Microstructure | 262 |
| 7.4.3. Texture Analysis | 263 |
| 7.4.4. Tensile Behavior and Fractography Analysis | 265 |
| 7.5. Conclusions..... | 268 |
| 8. CHAPTER 8: MICROSTRUCTURE AND MECHANICAL BEHAVIOR OF ADDITIVELY MANUFACTURED 17-4 PH STAINLESS STEEL: A COMPARISON ACROSS L-PBF, LP-DED, AND MBJ | 280 |
| 8.1. Abstract | 281 |
| 8.2. Introduction..... | 282 |
| 8.3. Experimental Procedures | 285 |
| 8.3.1. Material and Fabrication Methods | 285 |
| 8.3.2. Post-Thermal Treatment | 286 |
| 8.3.3. Microstructure Characterization | 287 |
| 8.3.4. Mechanical Properties..... | 287 |
| 8.4. Experimental Results | 288 |
| 8.4.1. Melt Pool Analysis: L-PBF vs. LP-DED | 288 |
| 8.4.2. Non-heat treated (NHT) Microstructure | 289 |
| 8.4.3. Heat Treated Microstructure | 290 |

| | |
|---|-----|
| 8.4.4. Tensile Results | 292 |
| 8.4.5. Fatigue Data and Fractography | 293 |
| 8.5. Discussion on the Experimental Results | 294 |
| 8.5.1. Microstructure and Tensile Behavior..... | 295 |
| 8.5.2. Fatigue Behavior..... | 297 |
| 8.6. Conclusions..... | 299 |
| 9. CHAPTER 9: SUMMARY AND POTENTIAL FUTURE WORK | 320 |
| 9.1. Summary and General Discussion | 320 |
| 9.2. Potential Future Studies | 330 |
| 10. CHAPTER 10: REFERENCES | 332 |

List of Tables

| | |
|---|-----|
| Table 2-1. Chemical composition of 17-4 PH SS powder, provided by LPW Technology Inc. | 88 |
| Table 2-2. Suggested L-PBF process parameters for 17-4 PH SS by EOS. | 89 |
| Table 2-3. Heat treatment procedures considered for the as-built and machined specimens in this study. | 90 |
| Table 2-4. Monotonic tensile properties of L-PBF 17-4 PH SS in different heat treatment conditions as well as L-PBF properties reported by EOS for non-heat treated and CA-H900 [70] and the wrought 17-4 PH SS in CA-H900 condition [60]. | 91 |
| Table 2-5. Fully-reversed fatigue test results for heat treated L-PBF 17-4 PH SS specimens in as-built surface condition. | 92 |
| Table 2-6. Fully-reversed fatigue test results for heat treated L-PBF 17-4 PH SS specimens in machined surface condition. | 94 |
| Table 2-7. Fatigue properties of heat treated L-PBF 17-4 PH SS specimens in as-built and machined surface conditions. | 96 |
| Table 3-1. Chemical composition of 17-4 PH stainless steel powder, provided by LPW Inc. | 132 |
| Table 3-2. Recommended process parameters for 17-4 PH stainless steel provided by EOS. | 133 |

| | |
|---|-----|
| Table 3-3. Heat treatment procedures applied to L-PBF and wrought 17-4 PH SS specimens..... | 134 |
| Table 4-1. Chemical composition of 17-4 PH SS powder, provided by LPW Technology Inc. | 178 |
| Table 4-2. The process parameters for L-PBF 17-4 PH SS suggested by EOS..... | 179 |
| Table 4-3. Design of experiment: number of specimens under each build specifications. | 180 |
| Table 4-4. Monotonic tensile properties of L-PBF 17-4 PH SS fabricated under Ar and N ₂ shield gas in both NHT and HT conditions, as well as wrought 17-4 PH SS in CA-H1025 condition [60]. σ_y – yield stress (proof stress at 0.01 of strain), σ_f – true fracture stress (corrected for necking), RA% - area reduction at fracture, and ϵ_f – true fracture strain. | 181 |
| Table 4-5. Paris equation parameters based on best fit in the Paris regime for L-PBF 17-4 PH SS specimens fabricated under N ₂ and Ar shield gases..... | 182 |
| Table 4-6. Fully-reversed fatigue test results of L-PBF 17-4 PH SS fabricated under N ₂ and Ar [15] heat treated following CA-H1025 procedure. | 183 |
| Table 4-7. Basquin equation (Eq. 2) fitting parameters for stress-life behavior of CA-H1025 L-PBF 17-4 PH SS specimens fabricated under N ₂ and Ar shield gases..... | 184 |
| Table 5-1. Fatigue data for the Ar-shielded L-PBF 17-4 PH SS specimens with different geometries. | 219 |
| Table 5-2. Fatigue data for the N ₂ -shielded L-PBF 17-4 PH SS specimens with different geometries. | 220 |
| Table 6-1. Process parameters used for EOS M290 system to fabricate L-PBF 17-4 PH SS specimens..... | 249 |

| | |
|--|-----|
| Table 6-2. Fatigue data for the L-PBF 17-4 PH SS specimens with different specimen geometries in NHT condition..... | 250 |
| Table 6-3. Fatigue data for the L-PBF 17-4 PH SS specimens with different geometries in CA-H900 heat treatment condition..... | 251 |
| Table 6-4. Fatigue data for the L-PBF 17-4 PH SS specimens with different specimen geometries in CA-H1025 heat treatment condition adopted from [175]. | 252 |
| Table 7-1. Chemical composition for 17-4 PH SS powders used for fabrication..... | 279 |
| Table 8-1. Chemical composition for 17-4 PH SS powder used for specimen fabrication via L-PBF, LP-DED, and MBJ AM techniques. The values are in wt. %..... | 314 |
| Table 8-2. Chemical compositions for 17-4 PH SS specimens fabricated via L-PBF, LP-DED, and MBJ AM techniques. The values are in wt. %. | 315 |
| Table 8-3. Process parameters used for fabrication of L-PBF and LP-DED 17-4 PH SS specimens..... | 316 |
| Table 8-4. Tensile properties of the L-PBF, LP-DED, and MBJ 17-4 PH SS undergone CA-H900 and CA-H1150 heat treatment conditions..... | 317 |
| Table 8-5. Fully reversed fatigue test results for heat treated AM 17-4 PH SS specimens at CA-H900 condition..... | 318 |
| Table 8-6. Fully-reversed fatigue test results for heat treated AM 17-4 PH SS specimens at CA-H1150 condition..... | 319 |

List of Figures

| | |
|---|----|
| Figure 1-1. The AM snapshot showing the PSPP relationships. | 31 |
| Figure 1-2. Effect of peak-age heat treatment (CA-H900) on mechanical properties of L-PBF 17-4 PH SS: (a) tensile behavior, (b) fatigue behavior, and (c) a fatigue fracture surface showing a lack of fusion defect. | 32 |
| Figure 1-3. Porosity level comparison for the L-PBF 17-4 PH SS specimens with different size. | 35 |
| Figure 1-4. The microstructure of (a) wrought, and (b) L-PBF 17-4 PH SS specimens. The thermal history and phase change during the L-PBF process are shown in (c). | 36 |
| Figure 1-5. Fatigue comparison of L-PBF and wrought 17-4 PH SS specimens undergone CA-H900 heat treatment procedure. | 37 |
| Figure 2-1 (a) SEM image of argon atomized powder particles of 17-4 PH stainless steel (SS), and (b) a schematic of laser powder bed fusion (L-PBF) process. | 73 |
| Figure 2-2. (a) A CAD image of the as-built vertical specimens, (b) a CAD image of the vertical square bar specimens to be machined, and (c) drawing of specimens, designed based on ASTM E606 standard [65]. | 74 |
| Figure 2-3. Surface roughness profiles for (a) as-built, and (b) machined L-PBF 17-4 PH SS specimens. The different scales of the roughness profiles should be noted. | 75 |
| Figure 2-4. X-ray diffraction (XRD) pattern for non-heat treated (n-HT), and different heat treatment procedures showing the constituent phases. | 76 |

Figure 2-5. Optical micrographs of L-PBF 17-4 PH SS specimens in normal (ND) and transverse (TD) directions with respect to the built direction for: (a)-(b) non heat-treated, (c)-(d) H900, (e)-(f) H1025, (g)-(h) CA-H900, (i)-(j) CA-H1025, and (k)-(l) CA-H1150 procedures. 78

Figure 2-6. Monotonic tensile behavior of L-PBF 17-4 PH SS for non-heat treated as well as different heat treatment procedures utilized in this study, represented by (a) engineering stress-engineering strain curve up to the extensometer removal point, and (b) engineering stress-displacement curve all the way to fracture. 79

Figure 2-7. Stable hysteresis loops of fully-reversed strain-controlled constant amplitude fatigue tests of L-PBF 17-4 PH SS machined specimens in (a) H900, (b) H1025, (c) CA-H900, (d) CA-H1025, and (e) CA-H1150 heat treatments. 80

Figure 2-8. Comparison of L-PBF 17-4 PH SS as-built and machined specimens: stress-life fatigue data for (a) H900, (b) H1025, (c) CA-H900, (d) CA-H1025, and (e) CA-H1150 heat treatments. 81

Figure 2-9. Fracture surface of L-PBF 17-4 PH SS specimens subjected to CA-H1025 heat treatment showing crack(s) initiated from (a) multiple micro-notches in an as-built specimen, and (b) a single spherical pore in a machined specimen..... 82

Figure 2-10. Stress-life fatigue data representing the effect of heat treatment on the fatigue behavior of L-PBF 17-4 PH SS as-built specimens..... 83

Figure 2-11. Fracture surface of an L-PBF 17-4 PH SS as-built specimens subjected to CA-H1150 heat treatment procedure and 0.002 mm/mm strain amplitude showing crack initiation sites, as well as crack growth and final fracture regions. 84

Figure 2-12. Fracture surface of L-PBF 17-4 PH SS specimens at 0.002 mm/mm strain amplitude showing crack growth and final fracture areas as well as the coalescence of cracks from different layers shown in zoomed-in images: (a) CA-H1025 (Sp_50, $2N_f = 113,374$ reversals), and (b) H1025 (Sp_13, $2N_f = 64,446$ reversals) heat treatment..... 85

Figure 2-13. Stress-life fatigue data representing the effect of heat treatment on the fatigue behavior of L-PBF 17-4 PH SS machined specimens and their comparison with the wrought counterpart in H900 condition [83]. 86

Figure 2-14. Fracture surfaces of L-PBF 17-4 PH SS specimens in the machined surface condition subjected to CA-H1150 heat treatment procedure showing the effect of pore size: (a) Sp_17 with 1,488,706 reversals to failure and a pore size of 21 μm , and (b) Sp_19 with 383,866 reversals to failure and a pore size of 28 μm 87

Figure 3-1. (a) Drawing of machined CT specimens based on ASTM E647 [98] and, (b) schematic of two groups of specimens with different notch direction relative to the building direction; set 1 and set 2 have notch direction parallel and perpendicular to the build direction, respectively. 119

Figure 3-2. Ternary phase diagrams generated using Thermo-Calc. software cross sectioned at different temperatures: (a) 482 °C (i.e., H900), (b) 552 °C (i.e. H1025), and (c) 1050°C (i.e. CA). 120

Figure 3-3. X-ray diffraction (XRD) analysis of non-heat treated (n-HT) and heat treated specimens..... 121

Figure 3-4. Optical micrograph of 17-4 PH SS microstructure in different heat treatment conditions; (a) L-PBF H1025, (b) L-PBF CA-H900, and (c) wrought CA-H900..... 122

Figure 3-5. Macro images of cracks in CT specimens subjected to H1025 heat treatment procedure; (a) set 1, and (b) set 2..... 123

Figure 3-6. Microstructure of H1025 L-PBF 17-4 PH SS specimens showing the δ -ferrite strings on the grain boundaries; (a) an optical micrograph, and (b) an SEM micrograph. 124

Figure 3-7. (a) Macro image of a specimen from set 2 subjected to H1025 heat treatment procedure showing locations 1 and 2, (b) microstructure at location 1, and (c) microstructure at location 2. 125

Figure 3-8. EBSD analysis on the microstructure near a secondary crack on a set 2 specimen; (a) shows a typical configuration between the primary and secondary crack, and (b)-(e) show the inverse pole figure maps of locations specified in (a). The inset shows the key to the inverse pole figure maps. 126

Figure 3-9. (a) Microstructure of CA-H900 L-PBF 17-4 PH SS, and (b) δ -ferrite strings in grain boundaries in black..... 127

Figure 3-10. Fatigue crack growth (FCG) rate for L-PBF and wrought CT specimens subjected to CA-H900 heat treatment procedure..... 128

Figure 3-11. Fracture surface of an L-PBF 17-4 PH SS specimen from set 1 subjected to H1025 heat treatment procedure..... 129

Figure 3-12. (a) Schematic of crack growth behavior through columnar grains at location 1 and location 2 of L-PBF 17-4 PH CT specimens from set 2 subjected to H1025 heat treatment procedure, (b) fracture surface image of location 1, (c) contrast enhanced image of location 1, (d) fracture surface image of location 2, and (e) contrast enhanced image of location 2..... 130

Figure 3-13. Fractography of L-PBF-1a from Table 3; (a) presents the stable FCG region, and (b) presents the final fracture region. Fractography of L-PBF-2a from Table 3; (c) presents the stable FCG region, and (d) presents the final fracture region. 131

Figure 4-1. Drawings of (a) round axial fatigue specimens with a uniform gage section, and (b) compact tension (CT) specimens following ASTM E647 standard [98]. 165

Figure 4-2. A schematic of axial fatigue specimen and the cross-sectioned plane parallel to the build direction in the gage section for microstructure characterization, and the EBSD results for NHT L-PBF 17-4 PH SS specimens: (a), (c), (e) IPF NHT-N₂, and (b), (d), (f) IPF NHT-Ar. 166

Figure 4-3. IPF maps of heat treated L-PBF 17-4 PH SS specimens on the cross-sectioned plane parallel to the build direction: (a) HT-N₂, and (b) HT-Ar. 167

Figure 4-4. Post-built melt pool size measurement; the schematic is showing the last printed layer with the laser track direction. (a) Melt pool shape/size in NHT-N₂ specimens, (b) melt pool shape/size in NHT-Ar specimens, and (c) measured melt pool depths and overlap depths. 168

Figure 4-5. Porosity distribution in a cross-sectional plane parallel to the build direction for (a) NHT-N₂ and (b) NHT-Ar specimens. The statistical distribution of the pore size in NHT-N₂ and NHT-Ar specimens in (c) as-built bars, and (d) gage section of the machined specimens. Note that the shaded area in (a) and (b) indicate the portion that was removed by machining for all the tensile and axial fatigue specimens. 169

Figure 4-6. Monotonic tensile behavior of L-PBF 17-4 PH SS specimens fabricated under Ar and N₂ shield gases for both NHT and HT conditions: (a) strain-controlled up to 0.045

strain, and (b) displacement-controlled step after removing the extensometer up to fracture.
..... 170

Figure 4-7. Fatigue crack growth (FCG) rates for L-PBF 17-4 PH SS specimens fabricated under N₂ and Ar shield gases in heat treated condition (CA-H1025). The three different FCG regimes (i.e. near threshold, Paris, and unstable FCG) are magnified and presented in (b), (c), and (d), respectively..... 171

Figure 4-8. Stable hysteresis loops of fully-reversed, strain-controlled constant amplitude fatigue tests of L-PBF 17-4 PH SS specimens: (a) HT-N₂, and (b) HT-Ar [63]. 172

Figure 4-9. (a) Strain-life and (b) stress-life fatigue data for CA-H1025 L-PBF 17-4 PH SS representing the effect of shield gas type (N₂ vs. Ar [63]). Note that hallow marks represent the run-out tests. 173

Figure 4-10. The electron channeling contrast images (ECCI) of L-PBF 17-4 PH SS showing the lath martensite in (a) HT-N₂, and (b) HT-Ar specimens. Note that the yellow dashed arrows are representing the lath martensite thickness. White particles are remnants of the polishing compound, not any secondary phases in the 17-4 PH SS, as confirmed by FIB surface polishing..... 174

Figure 4-11. Fracture surfaces of HT-Ar specimens at 0.0025 mm/mm strain amplitude: (a) specimen “Ar3” with 2,496,340 reversals to failure, (b) specimen “Ar4” with 1,394,730 reversals to failure, and (c) specimen “Ar11” with 690,584 reversals to failure..... 175

Figure 4-12. Fracture surface of an L-PBF 17-4 PH SS specimen fabricated under N₂ shield gas; specimen “N2” with 10,825,018 reversals to failure at 0.0025 mm/mm strain amplitude..... 176

Figure 4-13. Fractography of L-PBF 17-4 PH SS CT specimens fabricated under different shield gas types and heat treated using CA-H1025 procedure: (a) HT-N₂ and (b) HT-Ar. The ‘sawtooth’ features are shown by double-side yellow arrows, and the exposed pores are indicated by yellow arrows. The schematics represent the laths martensite and how the crack is growing in the intergranular and intragranular modes. 177

Figure 5-1. (a) The build layout used for fabricating L-PBF 17-4 PH SS bars under Ar and N₂ shielding gases and (b) schematic illustration of the heat treatment procedure. 205

Figure 5-2. The geometry of fatigue specimens: (a) uniform gage, (b) hourglass and (c) ultrasonic specimens. All the dimensions are in mm..... 206

Figure 5-3. The inverse pole figure (IPF) and electron channeling contrast imaging (ECCI) results showing the microstructure of the heat-treated (CA-H1025) L-PBF 17-4PH SS specimens: (a)&(b) Ar-shielded, and (c)&(d) N₂-shielded. (e) Misorientation angle distribution for the Ar-shielded and N₂-shielded specimens obtained from (a) and (c), respectively. 207

Figure 5-4. EDS analysis of the heat treated (CA-H1025) L-PBF 17-4 PH SS: (a) Ar-Shielded and (a) N₂-shielded specimens..... 208

Figure 5-5. SEM micrographs of the polished powder particles showing the presence of nano-size pores..... 209

Figure 5-6. The visualization and statistical distributions of defects obtained via XCT results for Ar-shielded and N₂-shielded L-PBF 17-4 PH SS specimens with (a) uniform gage, (b) hourglass, and (c) ultrasonic geometries. 210

Figure 5-7. Effect of specimen geometry on fatigue behavior of (a) Ar-shielded and (b) N₂-shielded L-PBF 17-4 PH SS specimens. 211

Figure 5-8. Comparing the effect of shielding gas type on the fatigue performance of L-PBF 17-4 PH SS in different life regimes (i.e., MCF to VHCF regimes) in (a) uniform gage, (b) hourglass, and (c) ultrasonic specimens..... 212

Figure 5-9. Frequency effect on the fatigue behavior of L-PBF 17-4 PH SS: (a) Ar-shielded and (b) N₂-shielded specimens..... 213

Figure 5-10. Fracture surfaces of L-PBF 17-4 PH SS specimens with uniform gage tested at 550 MPa: (a) specimen "Ar12" with 1,007,730 reversals to failure and (b) specimen "N₂12" with 1,757,890 reversals to failure. 214

Figure 5-11. Fracture surfaces of L-PBF 17-4 PH SS specimens with hourglass geometry tested at 600 MPa: (a) specimen "Ar15" with 649,838 reversals to failure and (b) specimen "N₂15" with 348,018 reversals to failure. 215

Figure 5-12. Fracture surfaces of ultrasonic Ar-shielded specimens: (a) specimen "Ar9" tested at 500MPa with 4,308,000 reversals to failure, (b) specimen "Ar4" tested at 475MPa with 95,108,000 reversals to failure, and (c) specimen "Ar1" tested at 450MPa with 420,760,000 reversals to failure..... 216

Figure 5-13. Fracture surfaces of ultrasonic N₂-shielded specimens: (a) specimen "N₂7" tested at 500MPa with 104,574,000 reversals to failure, (b) specimen "N₂5" tested at 475MPa with 180,966,000 reversals to failure, and (c) specimen "N₂1" tested at 450MPa with 1,992,620,000 reversals to failure..... 217

Figure 5-14. Fatigue life data indicating the mode of failure transition from surface defects to internal defects for both Ar-shielded and N₂- shielded ultrasonic specimens in VHCF regime. 218

Figure 6-1. (a) The build layout used for fabricating L-PBF 17-4 PH SS specimens under Ar and N₂ shielding gas, and (b) schematic of the heat treatment procedure. The specimens' geometries are shown in (c) uniform gage, (d) hourglass for conventional fatigue testing, and (e) ultrasonic (hourglass for ultrasonic fatigue testing). 240

Figure 6-2. Microstructure characterization of the L-PBF 17-4 PH SS in (a) NHT, (b) CA-H900, and (c) CA-H1025 heat treatment conditions. 241

Figure 6-3. Effect of geometry on the fatigue behavior of the L-PBF 17-4 PH SS specimens in (a) NHT, (b) CA-H900, and (c) CA-H1025 heat treatment conditions, conducted using conventional fatigue test setup..... 242

Figure 6-4. Effect of heat treatment on the fatigue behavior of L-PBF 17-4 PH SS with (a) uniform gage, (b) hourglass, and (c) ultrasonic type geometry. 243

Figure 6-5. Fracture surfaces of L-PBF 17-4 PH SS specimens with uniform gage tested at 550 MPa: (a) NHT specimen with 315,012 reversals to failure, and (b) CA-H900 specimen with 1,763,988 reversals to failure, and (c) CA-H1025 specimen with 1,757,890 reversals to failure. 244

Figure 6-6. Fracture surfaces of L-PBF 17-4 PH SS specimens with hourglass gauge tested at 550 MPa: (a) NHT heat-treated specimen with 503,150 reversals to failure, and (b) CA-H900 specimen with 2,534,332 reversals to failure, and (c) CA-H1025 specimen with 2,986,876 reversals to failure..... 245

Figure 6-7. Fracture surfaces of L-PBF 17-4 PH SS ultrasonic NHT specimens with uniform gage tested at: (a) 500 MPa with 824,480 reversals to failure, (b) 475 MPa with 1,241,100 reversals to failure, (c) 450 MPa with 2,291,600 reversals to failure. 246

Figure 6-8. Fracture surfaces of L-PBF 17-4 PH SS ultrasonic CA-H900 specimens with uniform gage tested at: (a) 500 MPa with 177,664,000 reversals to failure, and (b) 475 MPa with 283,840,000 reversals to failure, (c) 450 MPa with 915,940,000 reversals to failure. 247

Figure 6-9. Fracture surfaces of L-PBF 17-4 PH SS ultrasonic CA-H900 specimens with uniform gage tested at: (a) 500 MPa with 177,664,000 reversals to failure, and (b) 475 MPa with 283,840,000 reversals to failure, (c) 450 MPa with 915,940,000 reversals to failure. 248

Figure 7-1. The Ni-Cr binary phase diagram samples generated by Thermo-Calc. software using TCFE9 thermodynamic database [99]..... 270

Figure 7-2. The inverse pole figure (IPF) maps along Z direction and ECCI micrographs of (a) L-PBF, and (b) LP-DED 17-4 PH SS specimens in NHT condition. 271

Figure 7-3. The IPF (along Z direction) and phase maps for the heat treated 17-4 PH SS specimens: (a) L-PBF and (c) LP-DED at CA-H900, and (b) L-PBF and (d) LP-DED at CA-H1150. Note that the black boundaries in magnified IPF maps (in the middle) represent the prior austenite grain (PAG) boundaries. 272

Figure 7-4. The ODF maps for the (a) L-PBF and (b) LP-DED 17-4 PH SS specimens, and (c) their quantified texture components for the CA-H900 heat treatment condition. A schematic illustration of the important texture components in bcc for $\varphi_2 = 45^\circ$ is also shown. 273

Figure 7-5. The ODF maps for the (a) L-PBF and (b) LP-DED 17-4 PH SS specimens, and (c) the quantified texture components for the CA-H1150 heat treatment condition. A

schematic illustration of the important texture components in bcc for $\varphi_2 = 45^\circ$ is also shown. 274

Figure 7-6. IPF maps, $\{112\}$ pole figures, and the point-to-point misorientation maps showing the twin-based substructure of the martensite in selected PAG of the L-PBF and LP-DED 17-4 PH SS specimens. CA-H900 condition: (a) L-PBF, (b) LP-DED, and CA-H1150 condition: (c) L-PBF, and (d) LP-DED. 275

Figure 7-7. Tensile behaviors of the L-PBF and LP-DED 17-4 PH SS specimens undergone CA-H900 and CA-H1150 heat treatment conditions: (a) flow stress curves, (b) summarized tensile properties in bar chart, and (c) %elongation vs. ultimate tensile strength. The wrought data has been taken from ASTM A693 [60]. 276

Figure 7-8. Strain analysis of the δ -ferrite phase for the LP-DED 17-4 PH SS specimen undergone CA-H900 heat treatment condition: (a) KAM, (b) Schmid factor maps. Note that loading direction parallel to Z-axis considered for generating the Schmid factor map. 277

Figure 7-9. Tensile fracture surfaces of the L-PBF and LP-DED 17-4 PH SS specimens: (a) CA-H900, and (b) CA-H1150. 278

Figure 8-1. Post-thermal treatment schedules that were applied to the L-PBF, LP-DED, and MBJ 17-4 PH SS specimens: (a) HIP-CA-H900 and (b) HIP-CA-H1150. 302

Figure 8-2. The final geometry of: (a) tensile and (b) fatigue specimens. 303

Figure 8-3. The melt pool analysis of (a) L-PBF and (b) LP-DED 17-4 PH SS specimens. Note that the d_p , d_o , and t_l are the melt pool depth, melt pool overlap depth, and layer thickness, respectively. 304

Figure 8-4. The NHT microstructure of (a) L-PBF, (b) LP-DED, and as-sintered microstructure of the (c) MBJ 17-4 PH SS. The IPF and phase maps obtained from EBSD analysis are shown. 305

Figure 8-5. The IPF and phase maps of the heat treated 17-4 PH SS specimens at CA-H900 condition: (a) L-PBF, (b) LP-DED, and (c) MBJ. 306

Figure 8-6. The IPF and phase maps of the 17-4 PH SS specimens, heat treated at CA-H1150 condition: (a) L-PBF, (b) LP-DED, and (c) MBJ. 307

Figure 8-7. Tensile behavior of the heat treated: (a) L-PBF, (b) LP-DED, and (c) MBJ 17-4 PH SS specimens. 308

Figure 8-8. Fatigue data comparison for the AM 17-4 PH SS at CA-H900 and CA-H1150 heat treatment conditions: (a) L-PBF, (b) LP-DED, and (c) MBJ 17-4 PH SS specimens. 309

Figure 8-9. Fracture surfaces of the L-PBF, LP-DED, and MBJ 17-4 PH SS specimens in CA-H900 and CA-H1150 heat treatment conditions tested at 0.005 mm/mm strain amplitude: (a)&(b) L-PBF, (c)&(d) LP-DED, and (e)&(f) MBJ..... 310

Figure 8-10. Comparison of tensile properties obtained for the L-PBF, LP-DED, and MBJ 17-4 PH SS at (a) CA-H900, and (b) CA-H1150 heat treatment conditions. 311

Figure 8-11. Fatigue life comparison of the L-PBF, LP-DED, and MBJ 17-4 PH SS specimens in (a) CA-H900 and (b) CA-H1150 heat treatment conditions tested at 0.005 mm/mm strain amplitude. 312

Figure 8-12. An example of the MBJ 17-4 PH SS specimen's fracture surface showing the un-sintered region. 313

List of Abbreviations

| | |
|--------|--|
| AMSC | Additive manufacturing standardization collaborative |
| BSD | Backscatter diffraction |
| EBSD | Electron backscatter diffraction |
| ECCI | Electron channeling contrast imaging |
| EDS | Energy dispersive spectroscopy |
| FCG | Fatigue crack growth |
| HCF | High cycle fatigue |
| HIP | Hot isostatic pressing |
| HT | Heat treated |
| IPF | Inverse pole figure |
| L-PBF | Laser powder bed fusion |
| LCF | Low cycle fatigue |
| LoF | Lack of fusion |
| LP-DED | Laser powder directed energy deposition |
| MBJ | Metal binder jetting |
| MCF | Mid-cycle fatigue |
| NHT | Non-heat treated |
| SEM | Scanning electron microscope/microscopy |
| VHCF | Very high cycle fatigue |

Nomenclature

| | |
|------------------------------|---|
| b | Fatigue strength exponent |
| M_s | Start martensite transformation temperature |
| $N_f, 2N_f$ | Cycles to failure, Reversals to failure |
| R_ϵ | Ratio of minimum to maximum strain |
| % RA | Percent reduction in area |
| α' | Martensite |
| γ | Austenite |
| σ'_f | Fatigue strength coefficient |
| σ_a | Stress amplitude |
| σ_m | Mean stress |
| σ_y | Yield strength |
| σ_f | True fracture stress |
| σ_u | Ultimate tensile strength |
| ϵ_f | True fracture strain |
| ϵ_{\max} | Maximum strain |
| ϵ_{\min} | Minimum strain |
| ϵ_a | Total strain amplitude |
| $\frac{\Delta\epsilon_p}{2}$ | Plastic strain amplitude |
| $\frac{\Delta\epsilon_e}{2}$ | Elastic strain amplitude |

CHAPTER 1: INTRODUCTION

This dissertation comprises several research articles that have passed rigorous peer review processes in prestigious journals, and some research articles that are ready to be submitted. The goal of the introduction section is to provide background with the most important and relevant existing literature to highlight the direction of this dissertation.

1.1. Overview and Significance

Additive manufacturing (AM) has transformed the manufacturing process of structural parts in various industries such as aerospace, automotive, medical, defense, and nuclear. The layer-by-layer and track-by-track nature of AM processes allows the manufacture of near-net-shaped parts with complex geometries, reduces the cost and lead times, and facilitates the fabrication of highly customized parts for specific applications (e.g., in the medical field) [1].

The laser-based AM techniques are the most established, which among all the laser powder bed fusion (L-PBF) and laser powder directed energy deposition (LP-DED) techniques are the most commonly used laser-based AM processes. The L-PBF uses a powder bed and feed/build elevators to continuously lower the build platform, raise the feedstock, and bring a new powder layer over the bed. A high-energy laser beam is scanned across the selected area to fuse the newly dispersed powder layer to the part.

On the other hand, LP-DED has flow nozzles adjacent to the laser head to blow powder to the melt pool created by the laser. The laser head adjusts its position for the height of the build. In general, the L-PBF systems are capable of manufacturing much more complex near-net-shaped parts due to their high resolution, while the LP-DED systems are well suited for large-scale parts requiring a post-machining process to acquire the final

desired dimensions. Another booming AM process is metal binder jetting (MBJ), a non-laser-based AM process [2]. In this process, powder layers are bound using a liquid binder, and the fabricated parts are further densified. One of the main advantages of the MBJ AM process compared to the fusion-based methods (e.g., L-PBF, LB-DED) is the minimal residual stress induced to the manufactured parts. However, the MBJ AM process's major drawbacks are higher surface roughness and lower resolution than the L-PBF and LP-DED processes. Most importantly, it is often required to develop appropriate post-process procedures for MBJ materials to enhance their mechanical properties [2,3].

Although AM provides abundant advantages for manufacturing parts, there are drawbacks to these processes, which essentially affect the mechanical performance of additively manufactured (AM) materials, especially their fatigue performance [4]. Such downsides are the presence of process-induced defects such as gas entrapped pore, lack of fusion (LoF), surface roughness, microstructure anisotropy, and residual stresses in the AM parts. These defects act as stress concentrators inducing early fatigue life crack initiation, limiting the potential to produce reliable fatigue-resistant AM parts.

The formation of the abovementioned defects depends on the AM technique, process parameters (i.e., laser power, scan speed, etc.), and design parameters (i.e., time interval, number of parts, size of parts, etc.), all of which influence the thermal history that the part experiences during fabrication. As shown in **Figure 1-1**, the thermal history impacts the structure, and consequently, the property and performance of the parts will be affected. Therefore, establishing process-structure-property-performance (PSPP) relationships, presented in **Figure 1-1**, is essential for various AM materials.

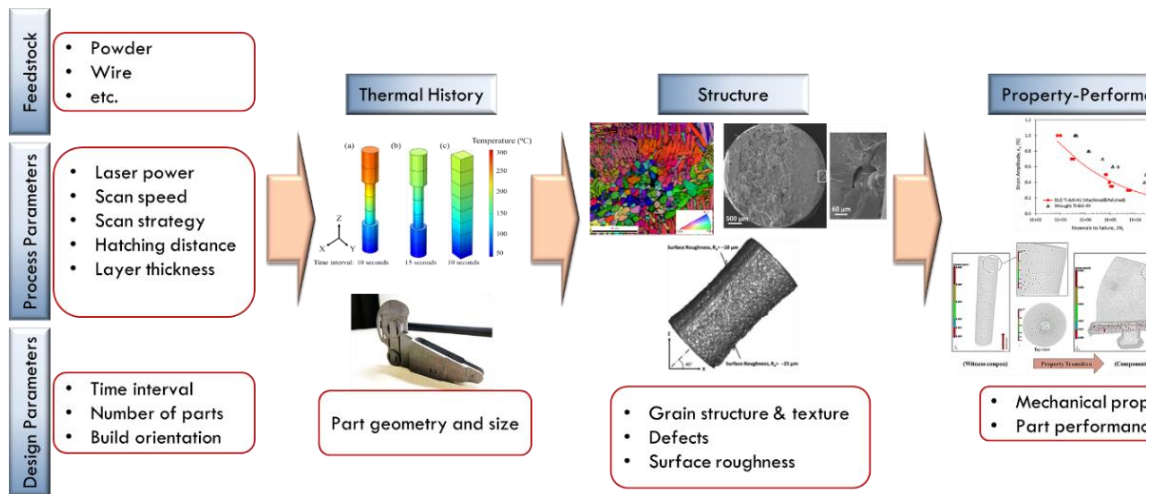


Figure 1-1.The AM snapshot showing the PSPP relationships.

The intricate thermal history (i.e., high cooling/solidification rates, thermal gradient, etc.) that a part experiences in AM process leads to microstructural/surface inhomogeneity, which in most cases, a post-process treatment (e.g., heat treatment, hot isostatic pressing (HIP), surface treatment) is necessary to modify the micro-/defect-structure and surface roughness for enhancing the performance of the material.

However, even performing the most common heat treatment applied on wrought material may not be the best option for the AM counterpart. For instance, it has been shown for the L-PBF 17-4 precipitation hardening (PH) stainless steel (SS) that although the peak-age heat treatment (CA-H900) increases the tensile strength (i.e., yield strength and ultimate tensile strength) as shown in **Figure 1-2(a)**, its fatigue performance is deteriorated in the high cycle fatigue (HCF) regime (see **Figure 1-2(b)**) as compared to the as-built condition (i.e., non-heat treated) [5]. This is attributed to the presence of process-induced defects (e.g., pore, LoF) presented in **Figure 1-2(c)**; the L-PBF 17-4 PH SS, which has

undergone CA-H900 heat treatment (i.e., in its most high strength with low ductility) is more sensitive to the defects under cyclic loading, thus steering to premature failures.

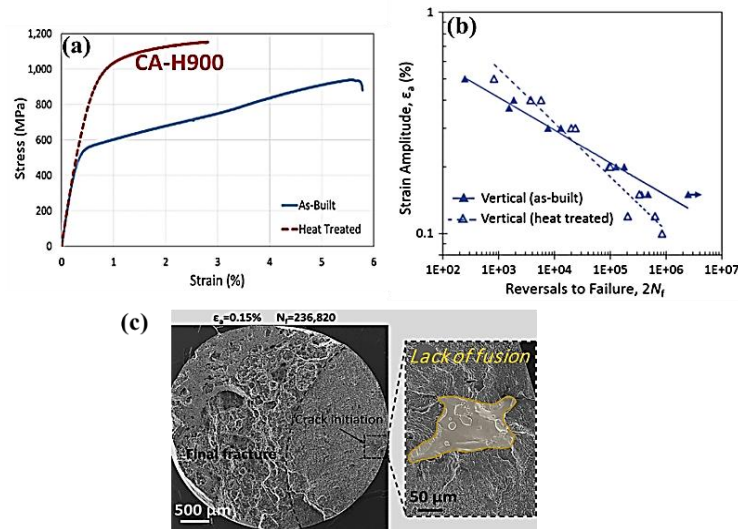


Figure 1-2. Effect of peak-age heat treatment (CA-H900) on mechanical properties of L-PBF 17-4 PH SS: (a) tensile behavior, (b) fatigue behavior, and (c) a fatigue fracture surface showing a lack of fusion defect.

Among the materials adopted for the AM industry, the 17-4 PH SS with high strength, ductility, and corrosion resistance (depending on the applied heat treatment) has drawn much attention from various aerospace and biomedical industries. Considering the presence of process-induced defects, deteriorating the fatigue performance of the AM materials, it is essential to understand the sources of these defects as well as the methods to eliminate/reduce them; on the other hand, if they are inevitable, at least to alleviate their influence on the fatigue performance of the AM materials by conducting appropriate post-process treatments.

As shown in **Figure 1-1**, the sources of these defects may be from feedstock (i.e., powder particles), the AM process characteristic itself, or the process and design parameters. Therefore, optimizing the abovementioned parameters may reduce the defects and enhance the mechanical properties of the AM materials. However, it has been seen that the process-induced defects are still present in the AM materials fabricated using optimized process parameters. This results in considering the post-process treatments (e.g., thermal treatment, surface treatment) to improve the AM materials' performance. Accordingly, the goal of this project is to investigate the effects of various AM techniques (i.e., L-PBF, LPDED, and MBJ), process parameter maneuvering (i.e., change of shield gas), as well as the post-process treatments on the micro-/defect-structure and mechanical properties (i.e., tensile, fatigue, and fatigue crack growth (FCG)) of 17-4 PH SS.

The Fe-17Cr-4Ni-4Cu, often dubbed as 17-4 PH SS, is a martensitic hardenable SS with a desirable combination of strength, ductility, fatigue strength, fracture toughness, and high corrosion resistance, depending on the post-manufacture heat treatment applied. This cost-effective SS often finds use in key engineering, defense, and energy sectors [6]. AM is advantageous over conventional subtractive manufacturing techniques in applications requiring the fabrication of near-net shaped parts with more complex geometries [1]. Therefore, there is a strong incentive in the industry to adopt AM in the fabrication of 17-4 PH SS parts to further benefit from this material's appealing properties.

The repetitious melting-solidification cycles inherent to typical AM processes result in elevated defect content and complex microstructure that are difficult to remediate and predict [7,8]. The defects are stress risers and compromise mechanical performance, especially in fatigue-critical applications [9]. Further, the variability in defects'

morphology, population, distribution, and the surrounding microstructure, exacerbate the uncertainty in the fatigue performance of AM parts [10,11]. While the goal of fabricating high-density components and eliminating the occurrence of defects may be desirable, these imperfections may be inherent to the AM processes and persist even under the most optimum operating conditions. Given this inevitability, further studying the process-structure-property (PSP) relationships is essential to expedite the adoption of AM 17-4 PH SS [4,12].

As in the case of all AM metallic materials, the microstructure and defect characteristics in AM 17-4 PH SS (which govern their mechanical performance) are dictated by solidification dynamics and thermal history. For instance, porosities are formed owing to gas entrapment in the melt pool due to a high cooling/solidification rate [1]. Indeed, owing to heat accumulation (thus larger melt pools and longer solidification time for gas bubbles to escape), porosity levels were shown to decrease in larger L-PBF 17-4 PH SS components [13], as seen in **Figure 1-3**. The LoF defects are formed when there is an insufficient melt pool overlap between layers or interlayer tracks [13,14], which can be affected by the changes in the part geometry, manufacturing process parameters, etc.

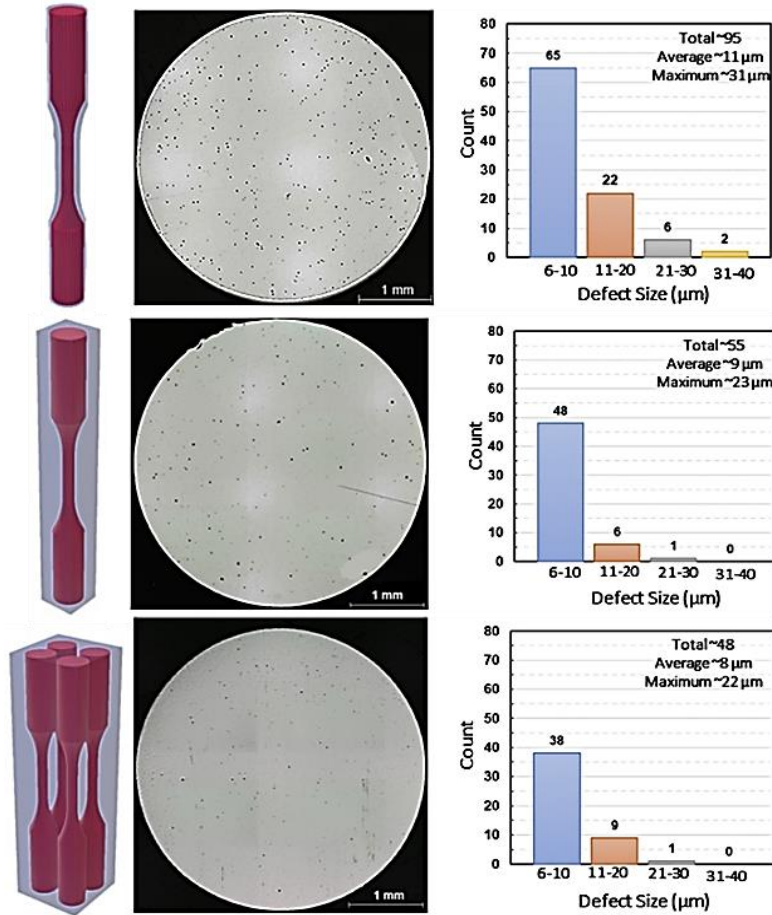


Figure 1-3. Porosity level comparison for the L-PBF 17-4 PH SS specimens with different size.

As for microstructure, although the stable phase at room temperature is body-centered tetragonal (BCT) martensite, the as-fabricated 17-4 PH SS via L-PBF may also include martensite (~60-90%) + austenite (~10-40%) phase composition [15,16]. This is generally due to the compositional heterogeneity (especially the distribution of austenite stabilizer elements such as Ni, Cu, Mn, etc.) induced by rapid solidification. The tetragonality of the BCT lattice is closely related to the carbon content, i.e., $c/a = 1 + 0.046C$, where C is in wt.%. In the case of 17-4 PH SS, as the carbon content is extremely low—0.01%, the lattice is often reported as body centered cubic (BCC) [17].

The as-solidified microstructure typically reported for L-PBF 17-4 PH SS in the literature, consisted of columnar prior- δ grains [18]. In fact, the well-known lath morphology of the martensite phase is not apparent and the microstructure is sometimes reported as ferritic microstructure, as seen in **Figure 1-4**. This has been ascribed to the bypassing austenite formation resulting in the absence of martensite [18].

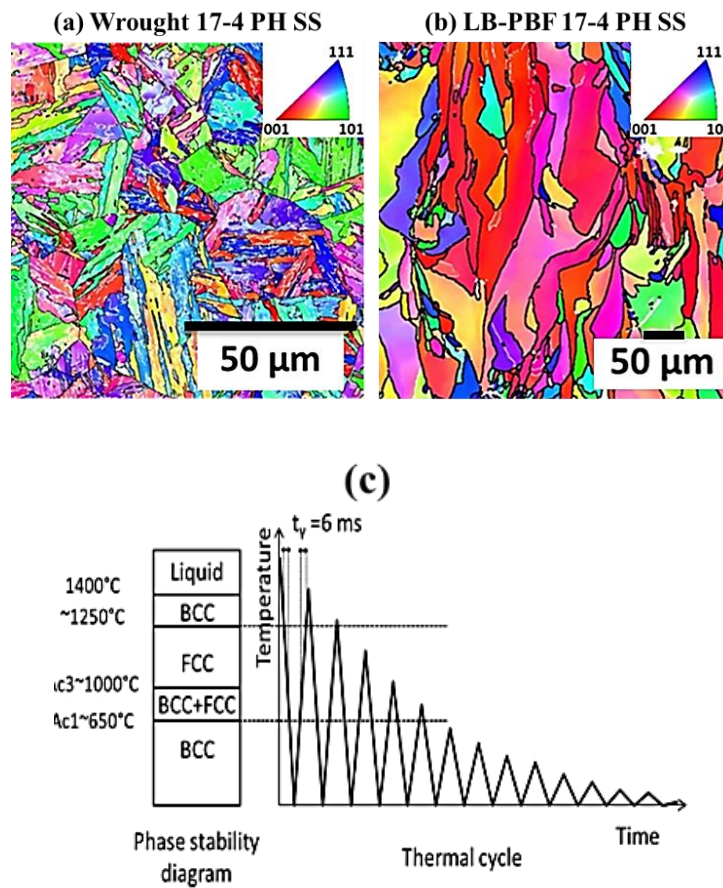


Figure 1-4. The microstructure of (a) wrought, and (b) L-PBF 17-4 PH SS specimens. The thermal history and phase change during the L-PBF process are shown in (c).

Many studies reported that a heat treatment at 1050°C for 30 min could thoroughly homogenize the composition (reaching Condition A) and, if low-temperature aging is

followed, could lead to a relatively uniform, fully martensitic microstructure [15,19]. However, this heat treatment cannot alter the prior- δ morphology, and, upon over-aging, the austenite tends to nucleate at the prior- δ grain boundaries [20]. The parameters which influence on AM 17-4 PH SS's microscopic features, and consequently, mechanical properties have been studied so far include: powder condition (i.e., chemical composition [21,22], recyclability [23,24], atomization media [25,26]), process parameters [13,27,28], geometry and size of the parts [13,29], and post-processing [15,30–32].

The fatigue behavior of L-PBF 17-4 PH SS is compared to that of the wrought counterpart in **Figure 1-5**. It can be seen that L-PBF 17-4 PH SS specimens have significantly lower fatigue performance than the wrought material. This is mainly due to the presence of defects in AM materials, and the effect of heat treatment (i.e., CA-H900) that increased the strength of the L-PBF specimen and reduced its ductility, making it sensitive to the presence of process-induced defects (e.g., pore, LoF).

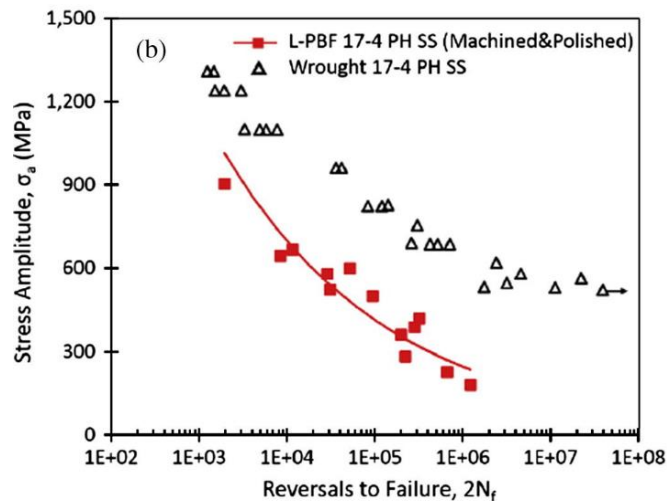


Figure 1-5. Fatigue comparison of L-PBF and wrought 17-4 PH SS specimens undergone CA-H900 heat treatment procedure.

Establishing the PSP relationships for the AM 17-4 PH SS essentially expedites the adoption of this material to the AM industry for being deployed in various applications. It is crucial to investigate the effect of various processes (e.g., L-PBF, LB-DED, and MBJ) on the material's structure (i.e., microstructure, defect structure) due to variation in the thermal history experienced by the part manufactured via each of the processes. Consequently, understanding the micro-/defect-structure of the material can assist with the possibility of optimizing/deciding the proper process parameters and post-process heat treatment procedures to enhance the mechanical properties (i.e., tensile and fatigue) of the AM 17-4 PH SS in the broader testing temperature.

1.2. Objectives Overview

The objectives of this research are to further investigate the PSP relationships of 17-4 PH SS manufactured via L-PBF, LB-DED, and MBJ AM processes to enhance the material's performance. Completing these objectives will establish the effect of process and post-process conditions on the micro-/defect-structural features responsible for crack initiation and the resulting failure under quasi-static and cyclic loadings. Moreover, the data is generated in this study can assist with filling the Gap FMP1 on “materials properties” introduced with a high priority by the AM standardization road map compiled by America Makes & ANSI Additive Manufacturing Standardization Collaborative (AMSC).

1. Investigate the effect of heat treatment on the microstructural features and, consequently, the influence of microstructure on the tensile and uniaxial fatigue performance of L-PBF 17-4 PH SS. After various heat treatments, the effect of

surface roughness conditions, i.e., as-built surface vs. machined surface, on the fatigue performance of L-PBF 17-4 PH SS will be also evaluated.

- **Hypothesis 1a:** the most common heat treatment procedure for the wrought 17-4 PH SS is not appropriate for the AM counterparts to obtain the required property and performance. This is mainly due to the presence of process-induced defects, which makes the material vulnerable to failure upon conducting inappropriate heat treatment procedures.
 - **Hypothesis 1b:** knowing that the surface roughness initiates the fatigue cracks, the microstructure obtained by different heat treatment procedures is influential in retarding the crack initiation and enhancing the fatigue performance.
2. Study the effect of heat treatment and build orientation on the fatigue crack growth (FCG) behavior of L-PBF 17-4 PH SS. The synergistic effect of heat treatment and build orientation is evaluated, and an appropriate heat treatment procedure is proposed to enhance this material's FCG behavior.
- **Hypothesis 2a:** there is a build orientation dependency on fatigue behavior of L-PBF 17-4 PH SS due to the columnar grain structure.
 - **Hypothesis 2b:** direct aging heat treatment does not reduce the fatigue anisotropy, while solution annealing heat treatment diminishes the anisotropy in FCG behavior.
3. Investigate the effect of process manipulation on the micro-/defect-structure and mechanical properties of the L-PBF 17-4 PH SS.

- **Hypothesis 3a:** the thermo-physical properties of the shielding gas type used in the fabrication environment results in a variation in thermal history that the part experiences during fabrication. This influences the level of defects in the AM part.
 - **Hypothesis 3b:** the solubility of the shielding gas in the material results in changes in the microstructure, and consequently, in the material's mechanical properties.
 - **Hypothesis 3c:** in the case of using a shielding gas type that reduces the defect density in the material, the most common heat treatment (i.e., CA-H900 condition) is still applicable.
4. Investigate the process-structure-property relationships of AM 17-4 PH SS; to study the microstructure and mechanical behavior of the 17-4 PH SS manufactured via different AM processes: laser powder bed fusion (L-PBF), laser powder directed energy deposition (LP-DED), and metal binder jetting (MBJ).
- **Hypothesis 4a:** the AM techniques with different procedure characteristics result in different microstructural features due to variations in thermal histories.
 - **Hypothesis 4b:** applying proper heat treatments diminishes the microstructure differences and reduces the mechanical properties variation in the L-PBF, LP-DED, and MBJ 17-4 PH SS materials.

1.3. Outline of Dissertation

This dissertation is organized in the following order: in CHAPTER 2, the synergistic effect of heat treatment and surface roughness on the microstructure, tensile,

and fatigue properties of L-PBF 17-4 PH SS is investigated. Various standard heat treatments proposed for the wrought 17-4 PH SS have been applied to the L-PBF counterparts. The microstructure (i.e., grain structure, phase analysis) and tensile properties are evaluated and compared for different heat treatments. In addition, the fully-reversed strain-controlled fatigue testing is carried out on the L-PBF 17-4 PH SS specimens, which have undergone various heat treatments with the as-built and machined surface conditions. The mechanical properties are correlated with the microstructure and surface roughness condition to propose an appropriate heat treatment procedure for the L-PBF 17-4 PH SS.

In CHAPTER 3, the effect of heat treatment (direct aging vs. solution heat treatment + aging) and build orientation (vertical vs. horizontal) is investigated on the fatigue crack growth (FCG) behavior of the L-PBF 17-4 PH SS in comparison with the wrought counterpart. The effect of heat treatment, including solution heat treatment procedure, on the grain structure and, consequently, on the fatigue crack growth behavior of L-PBF 17-4 PH SS is discussed. In addition, the effect of notch orientation with respect to the build direction on the FCG behavior of the L-PBF 17-4 PH SS is compared for different heat treatment conditions.

In CHAPTER 4, the effect of shielding gas type (Ar vs. N₂) on the micro-/defect-structure, tensile, fatigue, and fatigue crack growth behavior of L-PBF 17-4 PH SS is studied. The microstructure, i.e., grain morphology, size, and crystallographic texture, of the non-heat treated (NHT) Ar-shielded and N₂-shielded specimens are compared. Moreover, the influence of shielding gas type on the melt pool size, geometry, and defect density of the material is shown in 2D microscopy imaging. The specimens are further heat treated at the CA-H1025 condition proposed in CHAPTER 2: FATIGUE BEHAVIOR OF

ADDITIVELY MANUFACTURED 17-4 PH STAINLESS STEEL: SYNERGISTIC EFFECTS OF SURFACE ROUGHNESS AND HEAT TREATMENT. The tensile behavior of the heat treated specimens is compared with the NHT counterparts, and the results are discussed with the obtained microstructural differences due to using various shielding gas types. The fully-reversed strain-controlled fatigue and FCG behavior of the heat treated Ar-shielded, and N₂-shielded specimens are compared and explained based on the micro-/defect-structural differences induced by different shielding gas types.

The very high cycle fatigue (VHCF) behavior of the L-PBF 17-4 PH SS is investigated in CHAPTER 5 and CHAPTER 6, focusing on the effect of shielding gas type, heat treatment, and specimens' geometry type. In CHAPTER 5, L-PBF 17-4 PH SS specimens are fabricated under Ar, and N₂ shielding gas, heat treated at CA-H1025 condition, and further machined to two geometries with uniform gage section and hourglass gage section. Fatigue testing is carried out through 10Hz conventional and 20kHz ultrasonic fatigue testing. The micro-/defect-structure is compared for the Ar-shielded, and N₂-shielded specimens using energy dispersive X-ray spectroscopy elemental mapping, electron backscatter diffraction (EBSD), and X-ray computed tomography (XCT) analysis. The VHCF behavior of Ar-shielded and N₂-shielded fabricated specimens are compared and discussed with respect to their micro-/defect-structure. In CHAPTER 6, the VHCF behavior of N₂-shielded L-PBF 17-4 PH SS in NHT, CA-H900, and CA-H1025 heat treated conditions is discussed in correlation with the variation in their microstructure. Moreover, the geometry type dependency of VHCF behavior in different heat treatment conditions is also evaluated.

In CHAPTER 7, the microstructure and tensile properties of L-PBF and LP-DED 17-4 PH SS are studied and compared. The phase constituent and morphology of the NHT L-PBF and LP-DED 17-4 PH SS are presented and compared. Further, the effect of heat treatment on the crystallographic texture of the AM 17-4 PH SS is discussed and compared for the L-PBF and LP-DED processes. The tensile properties of the L-PBF and LP-DED 17-4 PH SS specimens are compared, and the differences are explained with respect to the variation in their microstructure.

In CHAPTER 8, the influence of various AM techniques on the microstructure and mechanical properties of L-PBF, LP-DED, and MBJ 17-4 PH SS is investigated. The NHT and heat treated microstructure (two different heat treatments) of L-PBF, LP-DED, and MBJ specimens are compared and discussed. The effect of different heat treatments on the tensile and fatigue behavior of L-PBF, LP-DED, and MBJ specimens are evaluated and correlated with the differences in their microstructure. It is shown that using an appropriate similar heat treatment can reduce the variation in the mechanical properties of the AM 17-4 PH SS fabricated via different AM processes.

Finally, in CHAPTER 9, the findings of this study with correspondence to the objectives and hypotheses are summarized. In addition, some future studies are suggested accordingly.

CHAPTER 2: FATIGUE BEHAVIOR OF ADDITIVELY MANUFACTURED 17-4 PH STAINLESS STEEL: SYNERGISTIC EFFECTS OF SURFACE ROUGHNESS AND HEAT TREATMENT

The following chapter has passed rigorous peer-review process and has been published in International Journal of Fatigue (IJF) and Data in Brief (DIB) in 2019.

Nezhadfar, P.D., Shrestha, R., Phan, N., Shamsaei, N., Fatigue behavior of additively manufactured 17-4 PH stainless steel: synergistic effects of surface roughness and heat treatment, International Journal of Fatigue, 2019.

Nezhadfar, P.D., Shrestha, R., Phan, N., Shamsaei, N. Fatigue data for laser beam powder bed fused 17-4 PH stainless steel specimens in different heat treatment and surface roughness conditions, Data in Brief, 2019.

2.1. Abstract

In this study, the synergistic effects of heat treatment and surface roughness on the microstructure and mechanical properties of laser powder bed fusion (L-PBF) 17-4 precipitation hardening (PH) stainless steel (SS) were investigated under monotonic tensile and fatigue loading. Five different heat treatment procedures, with and without primary solution treating cycle, i.e. Condition A (CA), were applied on L-PBF specimens in both as-built and machined surface conditions. Monotonic tensile tests were conducted at a strain rate of 0.001 s^{-1} and, uniaxial fully-reversed ($R = -1$) strain-controlled fatigue tests were carried out at various strain amplitudes ranging from 0.001-0.004 mm/mm. The heat treatment procedures were found to have a significant effect on the microstructure and mechanical properties of L-PBF 17-4 PH SS with the CA thermal cycle improving the fatigue strength considerably. This is due to the more homogenized microstructure obtained after performing the CA thermal cycle. In addition, eliminating the effect of surface roughness by machining and polishing processes enhanced the fatigue strength of the material, somewhat comparable to the one of the wrought counterpart. Fractography analysis revealed surface micro-notches and internal pores as the primary crack initiating factors in the as-built and machined specimens, respectively.

2.2. Introduction

The emergence of fabricating near net shaped parts with complex geometries has made additive manufacturing (AM) a viable option for many industries including aerospace and biomedical. Development in AM technologies has revolutionized industries by offering the capability of manufacturing parts with complicated geometries, functionally graded materials, and even assemblies, which are often unobtainable through traditional manufacturing methodologies [33–35]. Furthermore, some of the benefits associated with AM, include cost-effective low volume production, expedition in delivery time to market, increased component functionality, part customization, and wider design space for optimization [12,36]. Along with various advantages, there are also many challenges associated with the AM techniques [12]. The unique thermal history experienced during the manufacture induces residual stress [4,12], and leads to the formation of defects such as pores (gas entrapped, keyhole) and lack of fusion in the part [1]. The repetitious nature of AM also results in relatively rough surface condition. The aforementioned defects can influence the mechanical behavior of AM parts specifically under cyclic loading resulting in a premature fatigue failure [1,4,37,38].

Despite the presence of defects (i.e. lack of fusion, pores, and surface roughness), the mechanical properties of AM parts under quasi-static tensile loading are reported to be comparable and, in some cases, even superior to the ones of wrought counterparts [1,39,40]. Higher monotonic tensile properties in AM parts were primarily attributed to the ultra-fine microstructure as a consequence of high cooling rate during the AM process [40–42]. Although the influence of defects may be minimal in the case of monotonic loading conditions, these defects can have a detrimental effect when the AM parts are subjected to

cyclic loading. To address the concerns about the structural integrity of AM parts under cyclic loading conditions, many studies have been conducted to investigate the fatigue behavior of various AM metallic materials [10,43–46]. The fatigue behavior of AM parts can be highly sensitive to the surface quality of the fabricated parts. Micro-notches resulting from the partially sintered powder particles attached to the surface of the specimens can act as regions of high stress concentration, and consequently, preferred sites for crack initiation [37,47,48]. In machined AM parts, however, cracks tend to initiate from internal porosity [10]. Based on the recent studies, detrimental effects of such influencing factors can be reduced to some extent by controlling the powder characteristics [23,49–51], optimizing process/design parameters [1,39,52,53] and/or applying post-fabrication processes such as machining and heat treatment [19,54]. Post heat treatment procedures (e.g. stress relieving, solution annealing, and hot isostatic pressing (HIP)) are shown to improve the fatigue performance of the AM parts by eliminating the residual stress, changing the microstructure, and decreasing pores size and shape [44,55–58].

An example of AM materials with the need for post-fabrication heat treatment is 17-4 precipitation hardening (PH) stainless steel (SS), which is a martensitic/austenitic precipitation hardenable grade of stainless steels. Upon applying appropriate heat treatment, this material can possess excellent mechanical properties such as high tensile/impact strength, fracture toughness, and corrosion resistance at service temperature below 300 °C [59]. As a result, 17-4 PH SS is widely used in aerospace, petrochemical, power plants, and marine applications. Moreover, being compatible with AM processes, 17-4 PH SS has recently gained further attraction from above-mentioned industries. However, the mechanical properties of AM 17-4 PH SS are sensitive not only to the

employed process parameters, but also to the utilized post-fabrication heat treatment [60–63].

In general, 17-4 PH SS exhibits superior strength under CA-H900 procedure (i.e. solution heat treatment followed by aging at 482 °C for 1 hour) due to the formation of nanoscale Cu-rich spherical precipitates. As a result, majority of studies applied this heat treatment procedure to the AM 17-4 PH SS to improve its mechanical properties [26,39,64]. However, it has been shown recently that while CA-H900 can significantly improve the yield and ultimate tensile strength of L-PBF 17-4 PH SS, it may have a detrimental effect on the fatigue strength in long life regime [39]. This observation was explained by the more severe effect of lack of fusion defects in absence of plastic deformation in L-PBF 17-4 PH SS specimens hardened by CA-H900 procedure. Mower et al. [42] studied the fatigue performance of vertically built L-PBF 17-4 PH SS, machined, stress relieved, and heat treated at 788 °C for an hour. They reported lower tensile and fatigue strengths compared to the ones for the wrought 17-4 PH SS with the same heat treatment.

LeBrun et al. [64] investigated the effect of some standard heat treatments on the tensile behavior of L-PBF 17-4 PH SS specimens fabricated utilizing water atomized powder. They reported both stable phases (i.e. martensite or austenite) and Cu precipitates (i.e. size, coherency) to be influenced by the employed heat treatment, ultimately affecting the tensile behavior of L-PBF 17-4 PH SS. Cheruvathur et al. [19] investigated the effect of a specific heat treatment, AMS 5355, i.e. homogenization heat treatment at 1150 °C for 2 hours, on the microstructure of L-PBF 17-4 PH SS fabricated parts under nitrogen as the shielding gas, utilizing nitrogen-atomized powder. They observed a decrease in the amount

of austenite from 50% retained in the non-heat treated material to 10% after heat treatment. They also reported elimination of the dendritic microstructure and microsegregation, as well as a higher microhardness than wrought 17-4 PH SS heat treated at 1050 °C for 1 hour.

The effect of heat treatment on the cyclic deformation and fatigue behavior of L-PBF 17-4 PH SS has not yet been thoroughly investigated. Thus, a systematic study seems crucial to elucidate the effect of various heat treatment procedures on the fatigue behavior of this material. Besides, knowing the deterioration of fatigue performance in presence of surface roughness, the synergistic effect of heat treatment and surface condition on the fatigue behavior also needs to be determined. Therefore, this study was designed to investigate the effects of heat treatment on the microstructure and mechanical properties, including monotonic and cyclic behaviors of L-PBF 17-4 PH SS. The observed variations in the tensile and fatigue behavior were justified by the microstructural features specific to each heat treatment. In order to characterize the synergistic effects of surface roughness and heat treatment, fatigue performance of machined specimens was compared to that of the as-built ones for each heat treatment. Finally, fractography analysis was performed on fractured specimens to identify microscopic features responsible for initiating fatigue cracks.

2.3. Experimental Procedures

2.3.1. Material and Specimen Fabrication

Pre-alloyed argon-atomized 17-4 PH SS powder provided by LPW Technology Inc. with chemical composition listed in **Table 2-1**, was used in this study. **Figure 2-1(a)** presents the general morphology of the as-received powder. As seen in the figure, the powder particles were mostly spherical in shape with the average particle size of 25 μm

measured using ImageJ software. The result was consistent with the particle size distribution range of 15-45 μm , reported by the LPW Technology Inc.

All 17-4 PH SS specimens were fabricated by an EOS M290 machine, a laser powder bed fusion (L-PBF) system (**Figure 2-1(b)**), using the process parameter set suggested by EOS, listed in **Table 2-2**. Specimens were fabricated in vertical direction under argon atmosphere with two different geometries; net-shaped round specimens with uniform gage section with as-built surface condition following ASTM E606 standard [65], and square bars as shown in **Figure 2-2(a)** and (b), respectively. To eliminate the effect of surface roughness, square bars were further machined into the round specimens with uniform gage section, also following ASTM E606 standard [65]. The final dimensions of as-built and machined specimens were similar, as shown in **Figure 2-2(c)**.

ASTM A693 [60] recommends various heat treatment procedures for wrought 17-4 PH SS, each resulting in different mechanical properties due to its unique effect on the state of precipitation hardening (i.e. size and coherency of precipitates). To investigate the efficacy of these common heat treatment procedures on the mechanical properties of L-PBF 17-4 PH SS, specimens were heat treated under various conditions listed in **Table 2-3** prior to conducting mechanical testing. All the heat treatments were carried out utilizing a batch furnace in an inert (argon) atmosphere to prevent oxidation and surface decarburization at elevated temperatures.

It is worth mentioning that to obtain accurate area measurement, the gage section of the as-built specimens was slightly polished using 320 grit sandpaper to remove unsintered powder particles attached to their surface. The surface roughness of specimens was then measured using a Keyence digital microscope. The average roughness, R_a , and

maximum peak roughness, R_z , were measured through 1.4 mm evaluation length at the gage section. Measurements were repeated at least three times at different locations in the gage section for each specimen. The average measured surface roughness value for as-built specimens was $3.07 \mu\text{m}$ with a standard deviation of $1.10 \mu\text{m}$, and R_z value of $14.54 \mu\text{m}$ with a standard deviation of $3.14 \mu\text{m}$. In the case of machined specimens, the gage section was further polished using 320-4000 grit sandpapers to remove all the machining marks. The average measured surface roughness value for machined specimens was $0.93 \mu\text{m}$ with a standard deviation of $0.24 \mu\text{m}$, and the R_z value of $4.44 \mu\text{m}$ with a standard deviation of $0.9 \mu\text{m}$. The representative images of surface condition and surface roughness profile for as-built and machined specimens are shown in **Figure 2-3**.

2.3.2. Microstructure Characterization

To accurately trace the microstructure evolution due to various heat treatment procedures, samples were first cut from the gage section of the specimen in parallel and perpendicular direction with respect to the build direction. Standard metallographic procedures were followed for specimen preparation and microstructural analysis based on the ASTM E3-11 [66]. Accordingly, samples were ground using different grit sandpapers, 320 to 2500, to obtain a flat surface, then polished to a mirror-like surface finish using $0.05 \mu\text{m}$ MasterPrep Alumina solution on a ChemoMet pad. After polishing, the samples were etched using Beraha's tint reagent to reveal the microstructure. The microstructural analysis was carried out employing a Keyence VHX-6000 digital optical microscope.

X-ray diffraction (XRD) analysis was also conducted using Bruker AXS-D8 Discover X-ray system with Cu K_α radiation to characterize different constituent phases resulting from different heat treatment procedures utilized in this study. Operating voltage

and current were selected as 45 kV and 40 mA, respectively, and the X-ray diffraction patterns were obtained within a 2θ range of 30° to 90° with a step size of 0.2° .

2.3.3. Mechanical Testing

Both tensile and uniaxial fatigue tests were conducted using an MTS landmark servohydraulic testing machine with 100 kN load cells. An MTS mechanical extensometer was used to measure the strain at the gage section as well as to control the test during the strain control portion of it. Tensile tests were carried out first under strain-controlled mode up to 0.045 mm/mm strain, and then switched to displacement-controlled mode until fracture. The reason for switching from strain control to displacement control during the tensile test was to avoid damage to extensometer because of its limited travel distance. Two tensile tests were performed for each condition to ensure the consistency of the results, and eventually the average values of the results are presenting. It is worth mentioning that the data are compared with the formula of $(\text{difference}\% \pm \text{difference}\% * 0.25)$ to be more conservative, as so many specimens were not tested.

Uniaxial fully-reversed ($R_e = \epsilon_{\min}/\epsilon_{\max} = -1$) strain-controlled fatigue tests were performed based on ASTM E606 [65] standard at various strain amplitudes at room temperature. To maintain a similar average cyclic strain rate throughout all the tests, frequencies were attuned for each test based on the applied strain level. A sinusoidal waveform was applied until failure (complete separation) or up to 10^7 reversals, which was considered as a ‘run-out’ test in this study. To prevent slippage and probable scratches on the specimen’s gage section causes by extensometer’s keen blades, acrylic was applied to the areas where the extensometer was attached. Due to the fact that the elastic deformation was dominant for all the tests conducted in this study and no cyclic stress hardening or

softening was observed, all strain-controlled fatigue tests were stopped after a few thousand cycles and switched to force-controlled tests with applied forces corresponding to their strain-controlled portion. It is worth mentioning that the stress values for the as-built specimens were corrected by using the effective cross-sectional area, as described in [48] for both tensile and fatigue tests. It is worth mentioning that two to three specimens were tested at each strain amplitude for all the heat treatment conditions to investigate the scatter in data.

Fractography analysis was performed on the fracture surfaces using a scanning electron microscope (SEM) to determine factors responsible for the crack initiation and failure mechanisms in L-PBF 17-4 PH SS specimens. Prior to fractography analysis, the fracture surfaces were cut using a precision cutter machine, sonicated in water and alcohol solution, and then washed using acetone to eliminate any moisture and dirt that may be present on the fracture surfaces. A Zeiss EVO50 SEM was utilized for all the fractography analysis in this study.

2.4. Experimental Results

2.4.1. Microstructural Observations

XRD analysis was carried out to characterize the existing phases for each heat treatment procedure utilized and results are presented in **Figure 2-4**. The high intensity peaks comprising γ (austenite) and α' (martensite) with their corresponding crystallographic planes are indicated. It can be observed that for the non-heat treated specimens, martensite (α') was the primary phase; however, low amount of austenite (a low intensity γ (111) peak) was also identified. A trace of austenite peak can also be noticed in H900 condition, indicating that 482 °C temperature is not high enough to change the

constituent phases. On the other hand, by increasing the heat treatment temperature (e.g. H1025 and CA-H1025), the retained austenite was disappeared. Interestingly, a fraction of austenite was identified in the specimen subjected to CA-H1150 procedure, as shown in **Figure 2-4**. Within CA-H1150 specimens, austenite phase may have been formed and stabilized along the lath martensite boundaries due to the diffusion of austenite stabilizer elements (i.e. Cu, Ni, Mn, and N) during the four hours soaking at 662 °C (H1150 portion of the heat treatment procedure), while the temperature for H1025 procedure (i.e. 552 °C) was not sufficient to stabilize austenite [67]. Similar observations were reported for the wrought 17-4 PH SS in H900 and CA-H1150 conditions, which were attributed to the diffusion of austenite stabilizer elements to the grain boundaries along with reversion of martensite into austenite [64,67,68].

To quantitatively calculate the amount of retained austenite, all the diffracted martensite peaks (110), (200), and (211) as well as all austenite peaks (111), (200), and (220) were taken into consideration in Eq. (1) based on the ASTM E975 [44]:

$$V_{\gamma} = \left(\frac{1}{q} \sum_{j=1}^q \frac{I_{\gamma j}}{m_{\gamma j}} \right) / \left[\left(\frac{1}{p} \sum_{i=1}^p \frac{I_{\alpha i}}{m_{\alpha i}} \right) + \left(\frac{1}{q} \sum_{j=1}^q \frac{I_{\gamma j}}{m_{\gamma j}} \right) \right] \quad (1)$$

where V_{γ} , I , R , \square , γ , p , and q are volume fraction of austenite, integrated intensity per angular diffraction peak, proportionality parameter, ferrite/martensite, austenite, number of peaks considered for ferrite/martensite, and number of peaks considered for austenite, respectively. The parameter, m , depends on the interplanar spacing ($h k l$), the Bragg angle, θ , and crystal structure of all the planes, which are provided in the ASTM E975 [69]. Using Eq. (1), the amount of retained austenite was calculated to be approximately 10% for the non-heat treated and H900 and 17% for CA-H1150.

The microstructure characterization was conducted in normal direction (ND), perpendicular to the build direction and, transverse direction (TD), parallel to the build direction, as shown schematically in **Figure 2-5**. **Figure 2-5(a)** and (b) represent non-heat treated microstructure showing columnar grains and lath martensite, indicated by white arrows. During the fabrication process, heat flows toward the previously solidified layers (i.e. parallel to the build direction) due to conduction heat transfer. Accordingly, grains elongate toward the build plate and become columnar. In TD plane (**Figure 2-5(a)**), the melt pools with the width of 100 μm and depth of 40 μm are noticeable, which corresponds to the utilized hatching space and layer thickness, respectively. For the ND plane (**Figure 2-5(b)**), hatching space marks are shown by white dashed lines, which have been rotated approximately by 67° with respect to the ones in the previously deposited layer.

Figure 2-5(c) and (d) present the microstructure after heat treating at 482 $^\circ\text{C}$ for 1 hour (i.e. H900 procedure). Based on the XRD results presented in **Figure 2-4**, the microstructure contains martensite and small fraction of retained austenite ($\sim 10\%$) from the building process. Retained austenite has been shown to form along the narrow lath martensite (1-2 μm) in a previous study [26]. **Figure 2-5(e)** and (f) show the microstructure after heat treating at 552 $^\circ\text{C}$ for four hours (H1025 procedure). The melt pool boundaries, columnar grains, and laser tracks are still observed, while the retained austenite from the building process has fully transformed to the martensite (**Figure 2-4**).

On the contrary, it can be noticed from **Figure 2-5(g) – (l)** that conducting CA prior to the ageing heat treatment procedures changes the microstructure significantly. The microstructure is more homogenized on TD and ND planes, and the melt pool boundaries and the hatching space marks can hardly be seen in CA-H900, CA-H1025, and CA-H1150

specimens. The microstructure is fully martensitic after CA-H900 (**Figure 2-5(g)** and 5(h)) and CA-H1025 (**Figure 2-5(i)** and 5(j)), while a fraction of austenite can be noticed in CA-H1150 indicated by white arrows (**Figure 2-5(l)**), which is in line with the XRD results presented in **Figure 2-4**. Moreover, an increased in grain size can be noticed for CA-H1025 and CA-H1150 with longer soaking time at higher temperature as compared to CA-H900.

2.4.2. Tensile Behavior

Figure 2-6(a) and (b) present the engineering stress-engineering strain and engineering stress-displacement curves for the non-heat treated and heat treated specimens in different conditions. The monotonic tensile properties including, yield strength, σ_y , ultimate tensile strength, σ_u , percentage reduction in area, %RA, true fracture strain or ductility, ε_f , and elastic modulus, E are listed in **Table 2-4**. The tensile results for the CA-H1025 condition was reported in our previous study [59]. The results from the tensile tests of L-PBF 17-4 PH SS were found to be comparable to those of its wrought counterpart reported in ASTM A693 standard [60] and L-PBF specimens reported by EOS [70]. Results from **Figure 2-6** and **Table 2-4** indicate that subjecting specimens to any heat treatment procedure, or at least the ones employed here, make them exhibit higher strength but lower ductility as compared to the non-heat treated ones. For instance, heat treating L-PBF 17-4 PH SS using CA-H900 procedure increased the yield strength and ultimate tensile strength by approximately $29\% \pm 7.25\%$ and $55\% \pm 13.75\%$, respectively, while decreased the ductility by approximately $73\% \pm 18.25$ as compared to the ones obtained from the non-heat treated specimens.

It can be noticed that CA heat treatment prior to other heat treatment procedures, increased the strength. For instance, CA-H900 L-PBF 17-4 PH SS possesses almost

23%±5.75% higher yield and ultimate tensile strength than H900 one, while the ductility is almost similar. Load fluctuations, i.e. serrated flow behavior, were also observed in the case of H900 material within the onset of plastic deformation. In general, the increase in the strength of heat treated 17-4 PH SS specimens compared to the non-heat treated ones is associated with the microstructural evolution and precipitation hardening mechanism activated during heat treatment.

2.4.3. Fatigue Behavior

Figure 2-7 presents the stabilized hysteresis loops of the fully-reversed strain-controlled fatigue tests for machined specimens. As can be seen from the cyclic stress-strain relationship presented by the hysteresis loops in **Figure 2-7**, the L-PBF 17-4 PH SS specimens exhibited very small to no plastic deformation for strain amplitudes considered in this study, irrespective of the heat treatment procedure utilized. However, there was some negligible plastic deformation observed at H900 (**Figure 2-7(a)**) and CA-H1150 (**Figure 2-7(e)**) at higher strain amplitude (i.e. 0.004 mm/mm). This may be attributed to the localized plastic deformation of retained austenite in specimens subjected to these heat treatment procedures. Similar results with minimum plastic deformation were also reported in [39] for L-PBF 17-4 PH SS heat treated under CA-H900 procedure. It is worth mentioning that, similar to the machined specimens, plastic deformation was not considerable for the as-built specimens in this study.

The results of fully-reversed fatigue tests, strain amplitude, ϵ_a , stress amplitude, σ_a , mean stress, σ_m , and reversals to failure, $2N_f$, for the as-built and machined heat treated specimens are summarized in **Table 2-5** and **Table 2-6**, respectively. Some tensile/compressive mean stresses were observed in these tests; however, the values of

mean stresses were calculated to be less than 10% (and in most cases less than 5%) of the corresponding stress amplitude; therefore, they should not have much effects on the fatigue life of L-PBF 17-4 PH SS specimens. Furthermore, the values of plastic strain amplitude calculated by subtracting elastic strain amplitude from the total strain amplitude were found to be very small, which again suggests the absence of plastic deformation in both as-built and machined specimens.

Comparison of machined and as-built stress-life data for each heat treatment procedure is presented in **Figure 2-8**. As can be seen from this figure, by removing the surface roughness through machining, the fatigue strength will be improved significantly as compared to the as-built specimens irrespective of the heat treatment procedure applied. For the machined specimens, the run-out stress for 10^7 reversals was found to be 400 MPa, while the run-out stress for the as-built specimens was only 300 MPa (and in some cases 200 MPa).

Considering the dominating elastic behavior observed in L-PBF 17-4 PH SS specimens regardless of the heat treatment procedure applied, Basquin equation, given below, was employed to generate fatigue properties (fatigue strength coefficient, σ'_f , and fatigue strength component, b, for each heat treatment condition) [9]:

$$\sigma_a = \sigma'_f (2N_f)^b \quad (2)$$

The fatigue parameters, b and σ'_f , for the as-built and machined specimens for each heat treatment condition were determined using the linear least square fit method

employing the Basquin's equation in a log-log scale and reported in **Table 2-7**. It needs to be mentioned that the test data at the run-out level were excluded to obtain the best fit.

2.5. Discussion on Experimental Results

2.5.1. Microstructure and Tensile Behavior

Significant variations observed in the tensile properties of heat treated L-PBF 17-4 PH SS in **Figure 2-6** can be related to the differences in the microstructure (i.e. grain size and constituent phases with different hardening behavior), as well as precipitation hardening mechanism, which vary significantly with each heat treatment condition. Based on the results from the XRD analysis shown in **Figure 2-4**, austenite was retained in the microstructure of the non-heat treated specimens. The austenite phase can be stabilized by diffusion and dissolution of austenite stabilizer elements (i.e. Ni, Cu, Mn, and N) at elevated temperature during the fabrication; thereby, austenite does not transform to the martensite during cooling step and would retain at the room temperature [71]. In addition, in the case of non-heat treated L-PBF 17-4 PH SS specimens, the hydrostatic pressure in the laser melted steel decreases the martensite start temperature, M_s , to lower than room temperature, which ensures the retain of austenite at room temperature [64,72].

The XRD results, presented in **Figure 2-4**, indicated that the H900 heat treatment procedure did not affect the amount of retained austenite in L-PBF 17-4 PH SS. However, increasing the temperature and duration of heat treatment in the case of H1025 eliminated the austenite phase, and resulted in a fully martensitic microstructure. Moreover, as fully martensitic microstructure will be achieved during the CA procedure (**Figure 2-4**), any subsequent heat treatment at temperatures lower than the austenite reversion temperature, i.e. 558 °C, results in a fully martensitic microstructure (i.e. CA-H900 and CA-H1025). On

the other hand, in the case of heat treatments beyond the austenite formation temperature, i.e. CA-H1150, the austenite may retain at room temperature (**Figure 2-4**) due to the dissolution of austenite stabilizer elements in the austenite phase at elevated temperature.

As can be seen in **Figure 2-6** and listed mechanical properties in **Table 2-4**, H1025, CA-H900, and CA-H1025 possess higher strength than non-heat treated, H900, and CA-H1150. This is attributed to the attenuation of precipitation hardening effect in presence of austenite in the microstructure. Since the Cu, the core element for the formation of precipitates, is soluble in austenite, precipitation hardening effect will be reduced in presence of austenite phase in the microstructure [19,64]. Accordingly, due to the absence of austenite in H1025, CA-H900, and CA-H1025, more precipitation occurs, which ultimately hardens the material. As shown in **Figure 2-6**, specimens subjected to H1025 heat treatment procedure possessed $56\% \pm 14\%$ higher ductility as compared to specimens subjected to H900 procedure. In fact, with longer soaking time at higher temperature in H1025 heat treatment procedure, the precipitates become larger and semi-coherent with respect to the matrix, which can result in an increase in ductility [64,68].

Furthermore, specimens undergone CA prior to other heat treatment procedures had an improved strength as compared to the ones heat treated without a prior CA. As can be seen from **Figure 2-6** and **Table 2-4**, CA-H900 specimens exhibited approximately $23\% \pm 5.75\%$ increase in both yield and ultimate tensile strength and $5\% \pm 1.25\%$ decrease in ductility, as compared to the H900 specimens. During CA thermal cycle, the solution treatment at $1050\text{ }^{\circ}\text{C}$ for half an hour, martensite phase in the non-heat treated microstructure transforms to austenite; however, the austenite does not have the opportunity to grow and become stable due to the short period of annealing time [68].

Moreover, 17-4 PH SS has a low stacking fault energy (SFE), 15-20 mJ.m⁻² [16], which further assists the martensitic transformation. Therefore, the reversed fine austenite transforms to the fine martensite in the following cooling step, resulting in a finer and more homogenized microstructure (see **Figure 2-5(g)-(l)**). The martensite matrix after cooling to the room temperature from 1050 °C is supersaturated by Cu element, which consequently steers to the formation of Cu-rich precipitates during the subsequent ageing cycle (i.e. H900, H1025, and H1150) [26].

Cu precipitates will be initially formed in the size of 1 to 5 nm with a coherent interface to the matrix by ageing at low temperature for a short period of time, i.e. CA-H900 procedure [26]. These precipitates hinder the dislocation movement and because of their coherent interface with the matrix, dislocations must cut through these precipitates. This in turn increases the material strength [73], as can be seen in **Figure 2-6** for CA-H900 L-PBF 17-4 PH SS. The size of precipitates start to grow, and they lose their coherency to the matrix as the temperature and period of the ageing time increases, i.e. CA-H1025 and CA-H1150. In such cases, dislocations can loop around and bypass precipitates following Orowan mechanism [73]. As a result of the enhanced dislocation mobility, the strength of the material decreases and the ductility increases. As can be seen from **Table 2-4**, CA-H1025 L-PBF 17-4 PH SS specimens exhibited 12%±3% lower yield strength, 15%±3.75% lower ultimate tensile strength, and approximately 87%±21.75% higher ductility as compared to CA-H900 specimens. In addition, CA-H1150 heat treatment procedure decreased the yield strength for about 21%±5.25% and ultimate tensile strength for 18%±4.5%, while increased the ductility for approximately 60%±15% as compared to CA-H1025 procedure. It is worth mentioning that the decrease in strength and increase in

ductility of CA-H1150 as compared to CA-H1025 may be also attributed to the presence of austenite, which is softer than martensite.

As can be seen in **Figure 2-6**, there is some stress fluctuation noticeable in the tensile behavior of H900 specimens. This behavior has been related in the literature either to twinning in coarse elongated body centered cubic (bcc) grains [74,75] or a phenomenon called dynamic strain ageing (DSA), which is accompanied by a visible serrated flow behavior, so-called Portevin Le Chatelier (PLC) effect [76]. The former is less probable due to the fine microstructure of L-PBF 17-4 PH SS, while the latter mechanism has been reported in various materials such as low carbon steels (both austenitic and ferritic) [77,78], stainless steels [76], and aluminum alloys [79] fabricated by non-AM methods. The major micromechanism associated with the PLC effect is the interaction of moving dislocations and interstitial elements. In fact, interstitial elements pin the dislocations and hinder their movement until the applied stress overcomes the obstacle stresses from the interstitial elements. This unpins the dislocations and results in a drop in stress response. The PLC effect is strongly influenced by the strain rate and temperature. Muller et al. [76] reported the PLC effect in low strain rates (10^{-4} , 10^{-3} s $^{-1}$) for a high-alloy CrMnNi steel, while the PLC effect was suppressed at higher strain rates.

The activation energy of precipitation in wrought 17-4 PH SS is reported to be consistent with the diffusion of Cu in the bcc matrix, i.e. martensite [68]. In addition, the non-heat treated microstructure after fabrication is not homogenized and elements are typically segregated. Considering the fact that H900 procedure cannot homogenize the microstructure due to the low temperature and short duration of annealing, the process of pinning and unpinning of dislocations by interstitial elements may result in the serrated

flow behavior. However, performing CA homogenizes the microstructure by eliminating the segregation of elements and suppresses the serrated flow behavior, as evident by **Figure 2-6**.

2.5.2. Fatigue Behavior and Fractography

Figure 2-8 compares the fatigue behavior of as-built (i.e. only slightly polished) and machined L-PBF 17-4 PH SS specimens subjected to different heat treatment procedures. As seen, removing the surface roughness through machining process significantly improves the fatigue resistance of L-PBF 17-4 PH SS. Therefore, fractography analysis was conducted on both specimen types to better understand the factors responsible for crack initiation and failure in L-PBF 17-4 PH SS specimens.

Figure 2-9(a) and **(b)** present a representative fracture surface of as-built and machined specimens, respectively. As can be seen in **Figure 2-9(a)**, fatigue cracks were observed to initiate from multiple locations indicated by red arrows (even on multiple layers) on the surface due to the presence of micro-notches on the rough surface of as-built specimens. Upon further magnification in **Figure 2-9(a)**, one of these micro-notches was found to be $\sim 110 \mu\text{m}$ wide and $47 \mu\text{m}$ deep, which is indicated by a red dotted line. These short cracks gradually propagated and coalesced (can be seen as white tear ridges in **Figure 2-9(a)**) to form a larger crack, which can grow faster to failure. On the other hand, **Figure 2-9(b)** and the zoomed-in area for a machined specimen show that the crack initiated from a single internal pore (in this case $\sim 19 \mu\text{m}$ in diameter), close to the surface. Similar results were observed for specimens that subjected to other heat treatment procedures; cracks initiated from surface in as-built specimens, and from pores close to the surface or sometimes on the surface in machined specimens.

Cracks starting from defects located on the surface, or close to the surface, can typically grow faster as compared to the ones located away from the surface. Hence, as the defects in as-built specimens (i.e. micro-notches) were always located on the surface, these defects may have more detrimental effects on the fatigue strength as compared to the ones that were away from the surface, more typical in machined specimens. In addition, pores in machined specimens were found to be smaller in size and more spherical with respect to the more irregular-shape, micro-notches on the rough surface of the as-built specimens (compare **Figure 2-9(a)** and (b)). Finally, there were multiple crack initiations in as-built specimens (see **Figure 2-9(a)**), while only one crack initiation site was typically observed in machined specimens. Therefore, due to the combined effects of larger, more irregular defects, greater number of crack initiation sites, and faster crack growth, specimens in as-built surface condition exhibited lower fatigue resistance as compared to the machined ones, as presented in **Figure 2-8**.

Figure 2-10 presents the stress-life fatigue behavior of L-PBF 17-4 PH SS specimens in as-built condition from various heat treatment procedures. As can be seen, heat treatment had some influence on the fatigue strength of L-PBF 17-4 PH SS. Specimens subjected to H900 procedure had the lowest fatigue strength, which could have been resulting from the non-homogeneous microstructure and segregation of constituent elements leading to a faster crack growth. Specimens subjected to other heat treatment procedures exhibited longer fatigue lives in both low and high cycle fatigue regimes as compared to H900 specimens. Better fatigue resistance of those heat treatment procedures may be associated with the finer and more homogenized microstructure as well as the role of precipitation. In the case of H1025 specimens, although the microstructure did not change considerably as

compared to H900 specimens, the higher heat treating temperature (i.e. 552 °C) and longer soaking time (i.e. 4 hours) may have resulted in partial elimination of microsegregation of elements and coarsening of precipitates. These may have increased the ductility of H1025 specimens (**Figure 2-6**), which in turn can improve the fatigue resistance at least in low cycle regime as compared to that of H900 specimens.

Similar to the monotonic tensile behavior, conducting CA prior to the ageing thermal cycles (i.e. CA-H900, CA-H1025, and CA-H1159) enhanced the fatigue resistance of L-PBF 17-4 PH SS specimens, as seen in **Figure 2-10**. Specimens heat treated under CA-H900 and CA-H1025 procedures exhibited better fatigue resistance across all life regimes as compared to those subjected to only H900 and H1025 procedures. In the high cycle fatigue regime, specimens with prior CA thermal cycle were run-out (i.e. reached 10,000,000 reversals) at 300 MPa stress amplitude, while specimens without the CA treatment failed after approximately 1 million reversals at this stress level. The homogeneous and finer microstructure, seen in **Figure 2-5(g)**, (h), (i), and (j), as well as the presence of precipitates may have improved the fatigue behavior of specimens with a prior CA heat treatment.

To better understand the failure mechanism in L-PBF 17-4 PH SS specimens in as-built surface condition, representative specimens from different heat treatment batches were selected for further fractography analysis. Upon close investigation of fracture surfaces, shown in **Figure 2-11**, typical fatigue failure with three distinct features [9]; crack initiation sites (indicated with red arrows), crack growth region (indicated with blue solid arrows up to the blue dashed line), and final fracture region (indicated with black solid arrow), was observed for L-PBF 17-4 PH SS. In most cases for as-built specimens,

fractography analysis revealed that cracks originated from multiple locations on the surface as represented by the red arrows in **Figure 2-11**. These crack initiation sites were often located at different layers, which is also evident from the white ridges indicated by red-dashed circles. These white ridges are formed because of the coalescence of cracks originated from different layers. Similar observation of ridges resulting from the coalescence of cracks initiating from different layers on the fracture surfaces were also reported for L-PBF Ti-6Al-4V specimens with as-built surface condition [48]. Finally, with continued loading, crack growth became more unstable and led to final rupture, represented by the black arrow in **Figure 2-11**. With as-built AM parts having relatively rough surfaces, cracks can generate prematurely from multiple locations/layers (micro-notches on the surface) and merge to form larger cracks, which significantly shorten their fatigue lives as compared to their wrought counterparts.

Fracture surfaces of as-built specimens subjected to CA-H1025 (Sp_50, $2N_f = 113,374$ reversals) and H1025 (Sp_13, $2N_f = 64,446$ reversals) heat treatment procedures, cyclically deformed at 0.002 mm/mm strain amplitudes are presented in **Figure 2-12(a)** and **12(b)**, respectively. For both specimens, their overall fracture surfaces revealed a typical fatigue failure similar to the one shown in **Figure 2-11** with crack initiating from multiple surface micro-notches (indicated by red-dotted arrows) from different layers led into cracks coalescence (indicated by green-dotted arrows). An attempt was made to correlate the differences in fatigue lives with respect to the final fracture area (enclosed by red-dotted line) and distance between the crack initiation and final failure point (distance between points A and B in **Figure 2-12(a)** and **(b)**). The final fracture area was determined to be 2.70 mm² and 3.14 mm² for CA-H1025 and H1025 specimens, respectively.

Additionally, a higher value for the distance between crack initiation point (A) and final fracture region (B) was calculated for CA-H1025 specimen (4.1 mm) compared to H1025 one (3.1 mm).

A minimal difference in final fracture areas can be noticed from **Figure 2-12**, which implies somewhat similar cyclic fracture toughness for CA-H1025 and H1025 L-PBF 17-4 PH SS. The presence of more coarse precipitates in CA-H1025 can increase its fracture toughness [80,81], while its finer microstructure can reduce the fracture toughness [82]. Therefore, the effects of coarser precipitates and finer grain size from CA on the fracture toughness may have cancelled each other, resulting in somewhat similar cyclic fracture toughness for H1025 and CA-H1025. However, as can be seen in **Figure 2-12**, there are more crack initiation sites on the fracture surface of the CA-H1025 specimen (**Figure 2-12(a)**) as compared to the one of H1025 specimen (**Figure 2-12(b)**). The presence of coarse precipitates in the microstructure of CA-H1025 specimen can reduce the crack growth rate [81], as evident by more crack initiation sites on the fracture surface shown in **Figure 2-12(a)**. This indicates that more cracks had sufficient time to initiate during the slower crack growth stage in CA-H1025 specimen. As seen from **Figure 2-12(b)**, less cracks initiated in H1025 specimen which may be an evidence of relatively higher crack growth rate for this condition.

Figure 2-13 compares the fatigue behavior of machined L-PBF 17-4 PH SS in different heat treatments with the one of wrought 17-4 PH SS in H900 condition [83]. It can be noticed from this figure that L-PBF 17-4 PH SS subjected to H900 procedure has $6\% \pm 1.5\%$ lower fatigue strength at about 40,000 reversals, and $28\% \pm 7\%$ lower fatigue strength at about 170,000 reversals as compared to the wrought material in H900 condition.

Similarly, shorter fatigue lives have been reported for other AM materials (in machined surface condition) as compared to their wrought counterparts [10,42], which is often attributed to the presence of pores in AM materials. Based on their size, shape, and location, presence of such defects can significantly affect the fatigue behavior, specifically in the long life regime [10,12].

As an example, fracture surfaces of CA-H1150 machined specimens with considerably different fatigue lives at 0.0025 mm/mm strain amplitude are shown in **Figure 2-14**. As can be seen, in both cases, crack initiated from a spherical pore located close to the surface of the specimen. Upon further analysis, the size of the pores responsible for crack initiation was measured to be 21 μm for Sp_17 ($2N_f = 1,488,706$ reversals) and 28 μm for Sp_19 ($2N_f = 383,866$ reversals), shown in **Figure 2-14(a)** and (b), respectively. Therefore, some scatter found in the high cycle fatigue data of L-PBF 17-4 PH SS machined specimens may be explained by the variations in the pore size responsible for their fatigue failure. It should be noted here that the crack initiating pores in all the machined L-PBF specimens were somewhat spherical and very close to the surface; thus, the variation in the pore size was identified as the main reason for the scatter in fatigue data. Similar observations were made for CA-H1025 L-PBF specimens indicating pore size to be the main factor affecting the fatigue behavior in high cycle regime. For instance, at 0.0025 mm/mm strain amplitude level, Sp_20 specimen had a crack initiated from a pore with the size of 18 μm and the fatigue life was 2,496,340 reversals, while crack initiated from a pore with the size of 25 μm in Sp_21 specimen and the fatigue life was 1,394,730 reversals.

Based on the results and discussions provided in the current study, fatigue properties of L-PBF 17-4 PH SS were found to be affected by the applied heat treatment procedure. Irrespective to the surface conditions, conducting CA procedure before any other ageing treatment was observed to increase the fatigue resistance of L-PBF 17-4 PH SS. Higher fatigue life in CA specimens may be attributed to the more homogenized microstructure obtained, as well as formation and distribution of precipitates that can influence the crack initiation and/or crack growth behavior.

Furthermore, specimens subjected to CA-H900 heat treatment procedure with highest tensile strength, exhibited low fatigue resistance and more scatter in fatigue life data in high cycle fatigue regime as compared to CA-H1025 and CA-H1150 with lower tensile strengths. This can be attributed to the increased sensitivity of high strength materials to defects such as surface micro-notches and internal pores, typical of AM processes [39]. Expectedly, the increased ductility gained from other heat treatment procedures such as H1025, CA-H1025, and CA-H1150 improved fatigue resistance in the low cycle regime.

2.6. Conclusions

The effect of various heat treatment procedures on the microstructure and mechanical properties of AM 17-4 PH stainless steel, fabricated by a laser powder bed fusion (L-PBF) process, was investigated. In addition, the synergistic effect of surface roughness and heat treatment on the fatigue performance of L-PBF 17-4 PH SS was studied. The following conclusions can be drawn based on the experimental results and analysis:

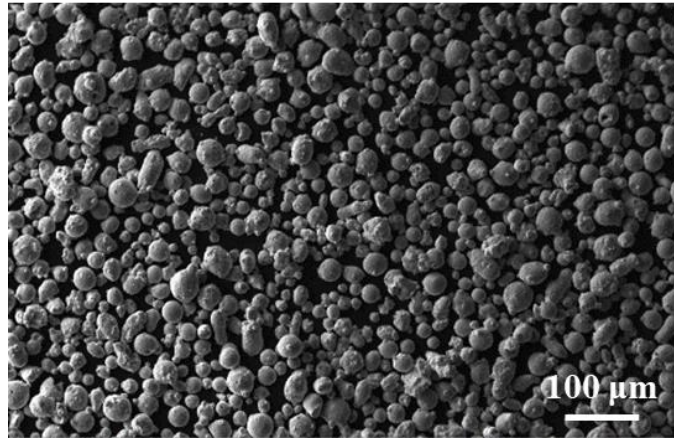
1. Performing Condition A (CA) prior to other heat treatments changed the microstructure significantly. The typical cast-like microstructure was observed in L-PBF 17-4 PH SS when subjected to the ageing heat treatment without CA, while it evolved to a fine martensitic microstructure by performing CA prior to the ageing cycle. Applying CA also increased the tensile strength of the material by eliminating the segregation of elements resulting from the fabrication process as well as by producing a more homogenized microstructure comprising of finer lath martensite.
2. A small amount of austenite was retained at room temperature in the non-heat treated L-PBF 17-4 PH SS. This can be explained by the diffusion of austenite stabilizers to the lath martensite boundaries and mechanical stabilization of austenite by hydrostatic pressure of the melt pool during the fabrication process.
3. The tensile strength of material increased significantly after conducting H900 heat treatment procedure as compared to the non-heat treated specimens. This was due to the formation of nanosize Cu-rich precipitates during this heat treatment. In addition, load instability (serrated flow behavior) was observed in the monotonic tensile behavior of H900 L-PBF 17-4 PH SS, most likely due to the interaction between dislocations and interstitial elements.
4. The tensile strength decreased for the heat treatment procedures with higher temperature and holding time (i.e. H1025, CA-H1025, and CA-H1150). This was attributed to the coarsening of Cu precipitates. In the case of CA-H1150, the presence of austenite, which is a softer phase as compared to martensite, may have also contributed to the observed lower strength and higher ductility.

5. Performing CA prior to other heat treatment procedures (i.e. ageing) also improved the fatigue strength significantly for as-built specimens in both low and high cycle fatigue regimes. For all the heat treated as-built specimens, cracks were observed to initiate from multiple surface micro-notches formed from laser-wise fabrication process and partially sintered powder particles.
6. Applying CA to machined L-PBF specimens also had a beneficial effect on their fatigue strength. As the majority of pores in machined specimens were spherical in shape and located close to the surface, some scatter observed in the high cycle fatigue data may have been resulting from the variation in pore sizes.
7. Higher scatter in fatigue life data was observed for specimens subjected to CA-H900 procedure in both as-built and machined surface conditions. This can be attributed to more sensitivity of the higher strength materials to the presence of defects.
8. Machined heat treated specimens exhibited better fatigue performance as compared to the as-built ones. This higher fatigue resistance for the machined specimens may be associated to a single crack initiation site from an internal, close to the surface spherical pore, as compared to multiple crack initiation sites from irregular-shape, larger micro-notches on the rough surface of as-built specimens.

In summary, further detailed investigations are required to better understand the synergistic effects of strength/ductility and precipitation mechanisms from different heat treatment procedures on the fatigue behavior of L-PBF 17-4 PH SS. In addition, advanced characterization of precipitates with respect to their effect on the crack initiation and propagation is required in future studies. Finally, special attention should be also given to

the presence of defects such as micro-notches and pores when developing a new heat treatment procedure dedicated to L-PBF produced parts. Such research outcomes can ultimately result in developing application/property-specific heat treatment procedures to achieve an improved in-service performance for AM parts.

(a)



(b)

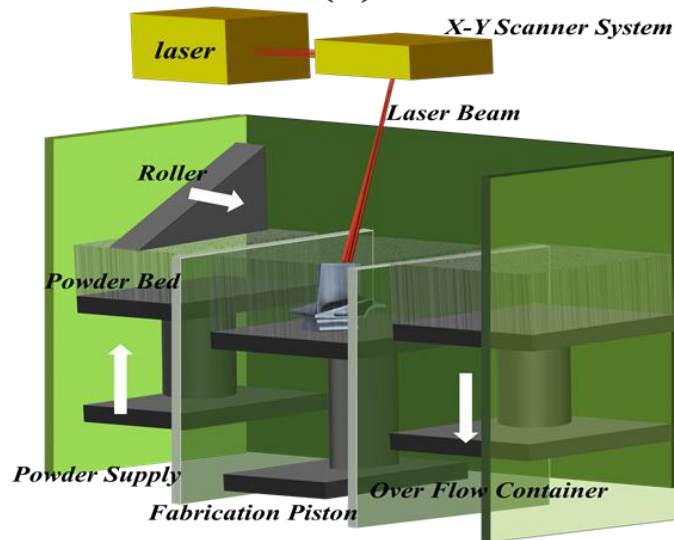


Figure 2-1 (a) SEM image of argon atomized powder particles of 17-4 PH stainless steel (SS), and (b) a schematic of laser powder bed fusion (L-PBF) process.

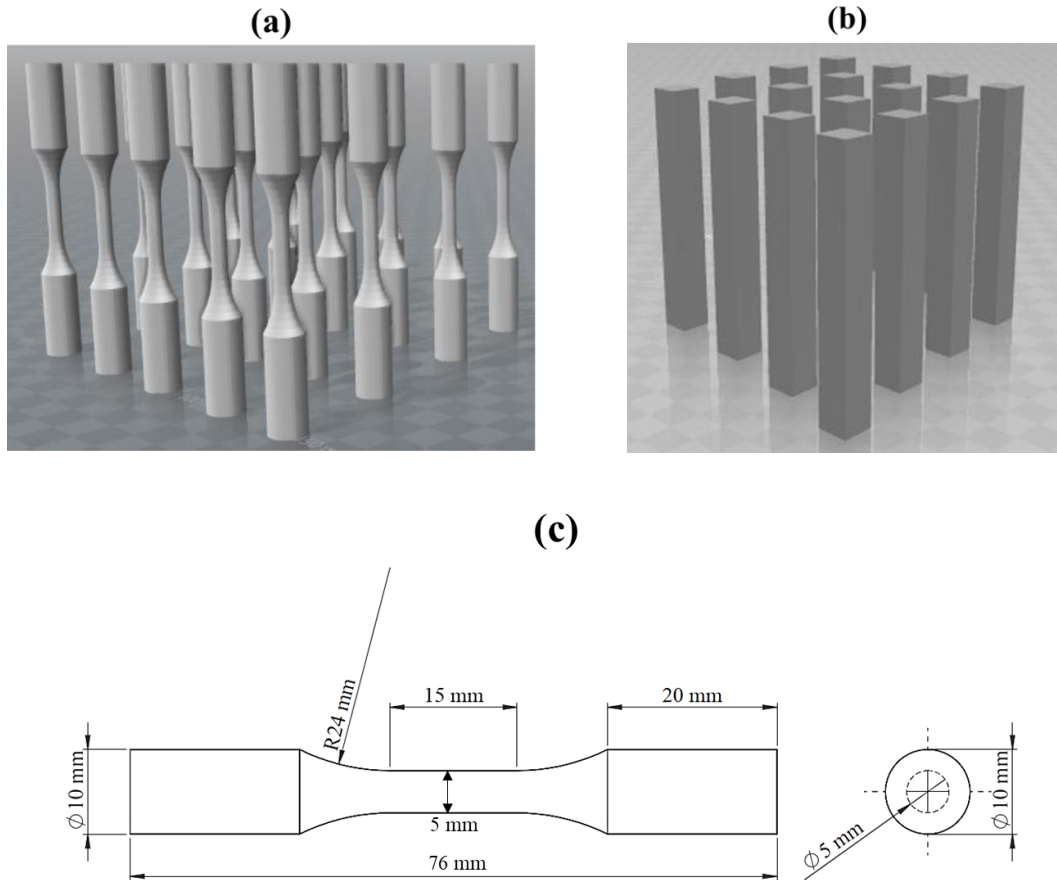
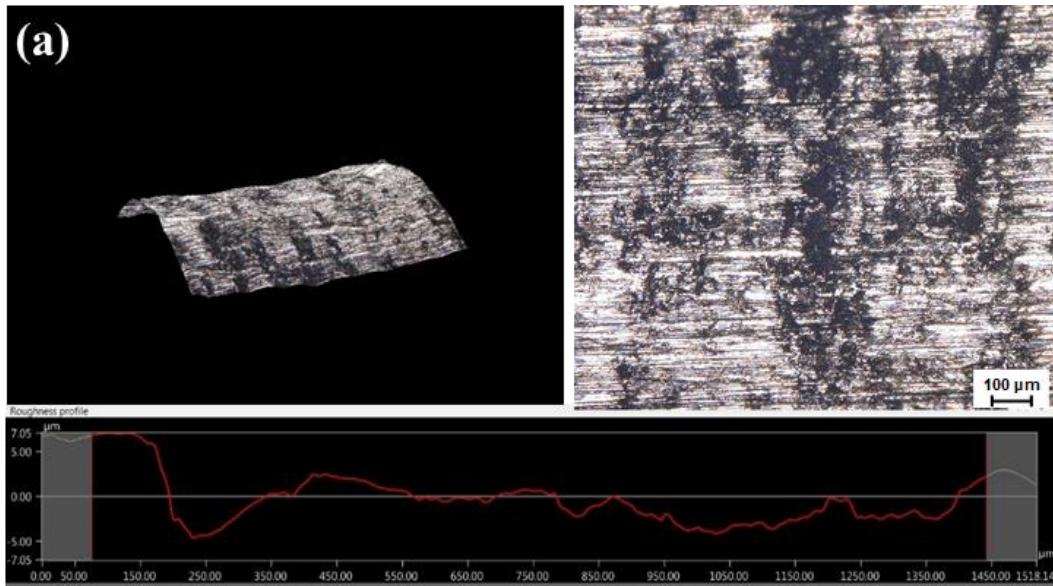
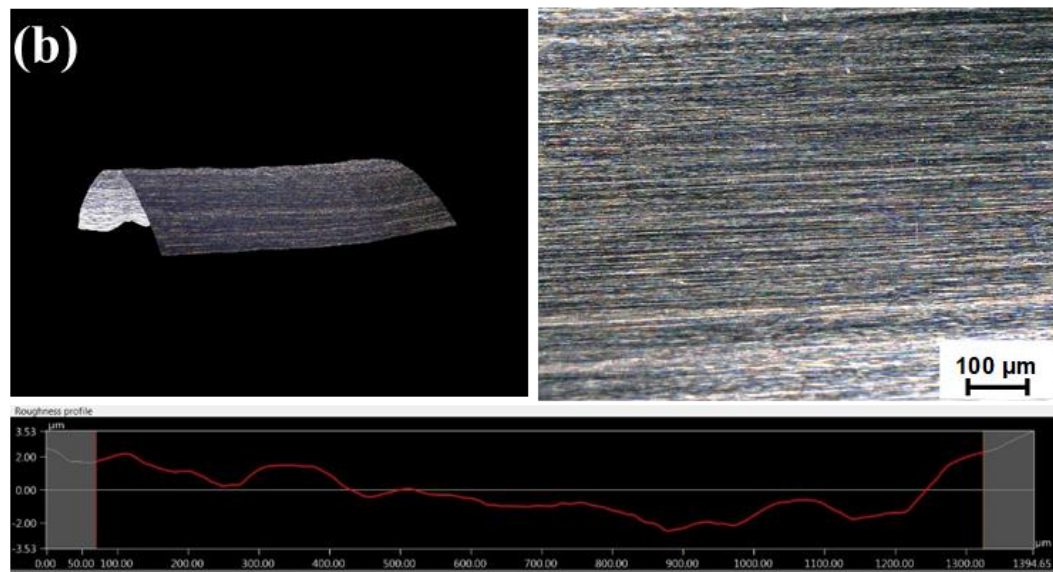


Figure 2-2. (a) A CAD image of the as-built vertical specimens, (b) a CAD image of the vertical square bar specimens to be machined, and (c) drawing of specimens, designed based on ASTM E606 standard [65].



$$R_a = 3.07 \pm 1.10 \mu\text{m}$$

$$R_z = 14.54 \pm 3.14 \mu\text{m}$$



$$R_a = 0.93 \pm 0.24 \mu\text{m}$$

$$R_z = 4.44 \pm 0.9 \mu\text{m}$$

Figure 2-3. Surface roughness profiles for (a) as-built, and (b) machined L-PBF 17-4 PH SS specimens. The different scales of the roughness profiles should be noted.

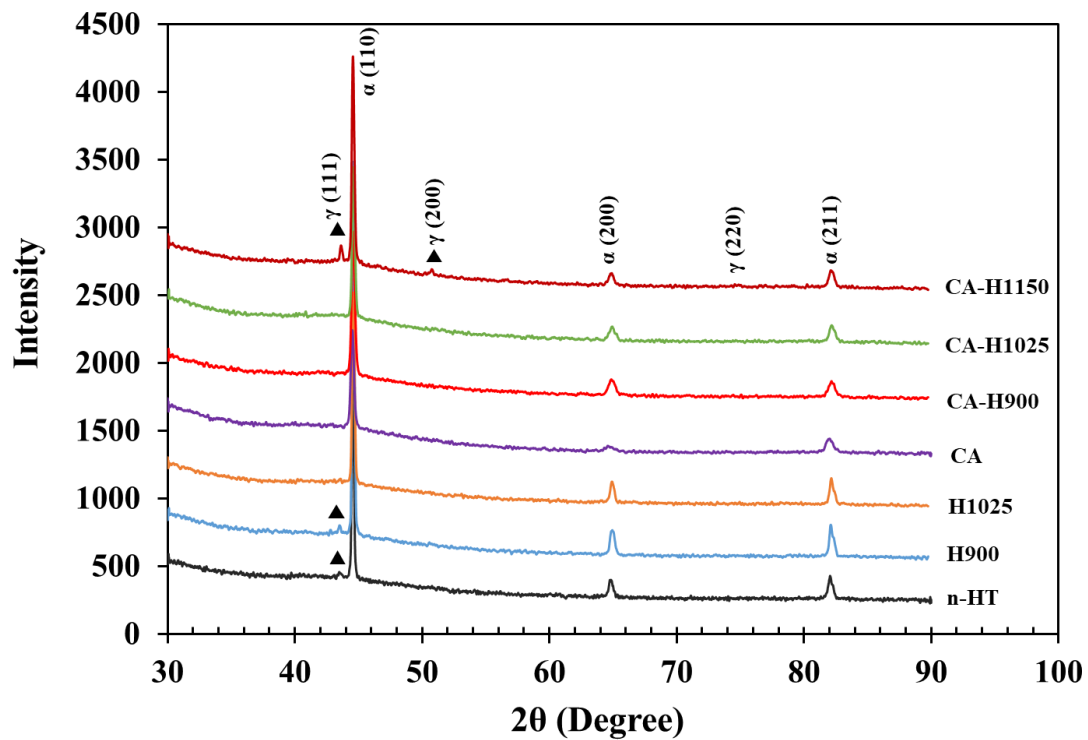
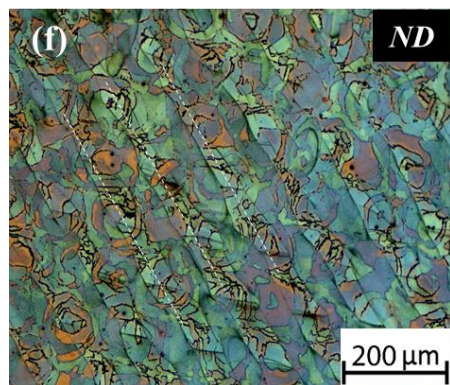
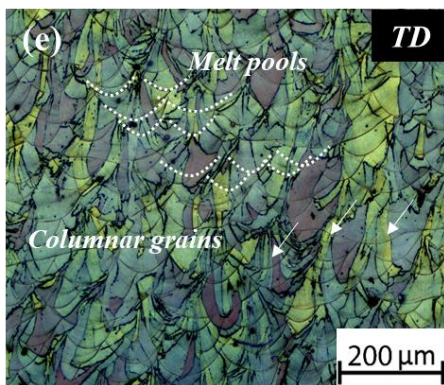
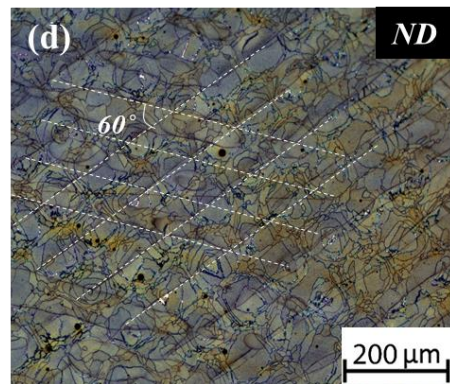
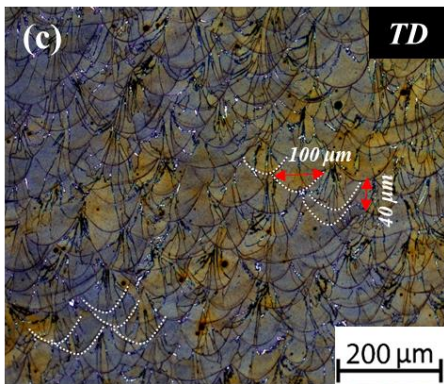
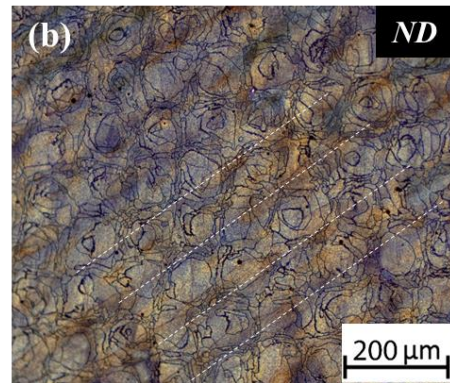
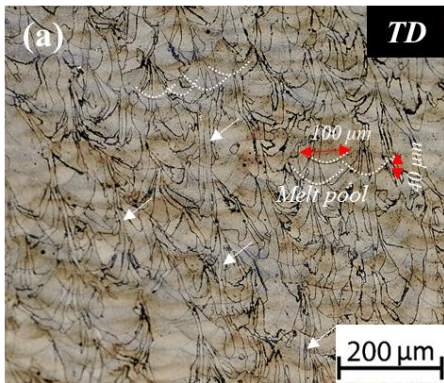
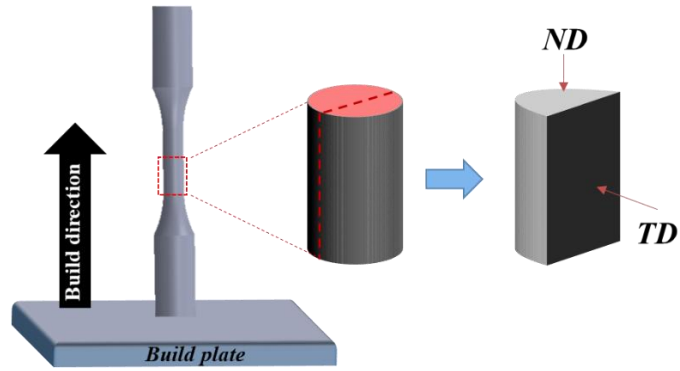


Figure 2-4. X-ray diffraction (XRD) pattern for non-heat treated (n-HT), and different heat treatment procedures showing the constituent phases.



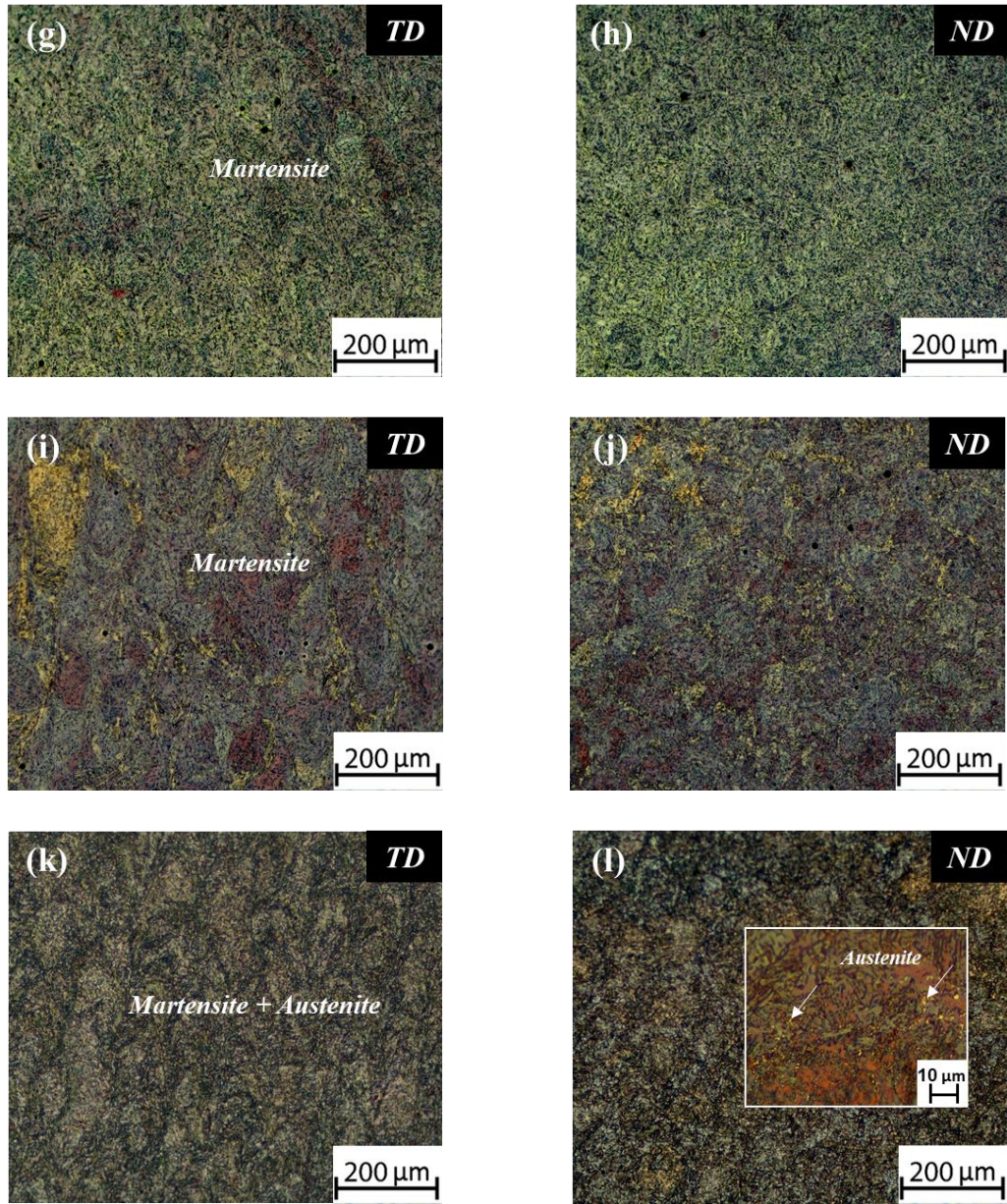


Figure 2-5. Optical micrographs of L-PBF 17-4 PH SS specimens in normal (ND) and transverse (TD) directions with respect to the built direction for: (a)-(b) non heat-treated, (c)-(d) H900, (e)-(f) H1025, (g)-(h) CA-H900, (i)-(j) CA-H1025, and (k)-(l) CA-H1150 procedures.

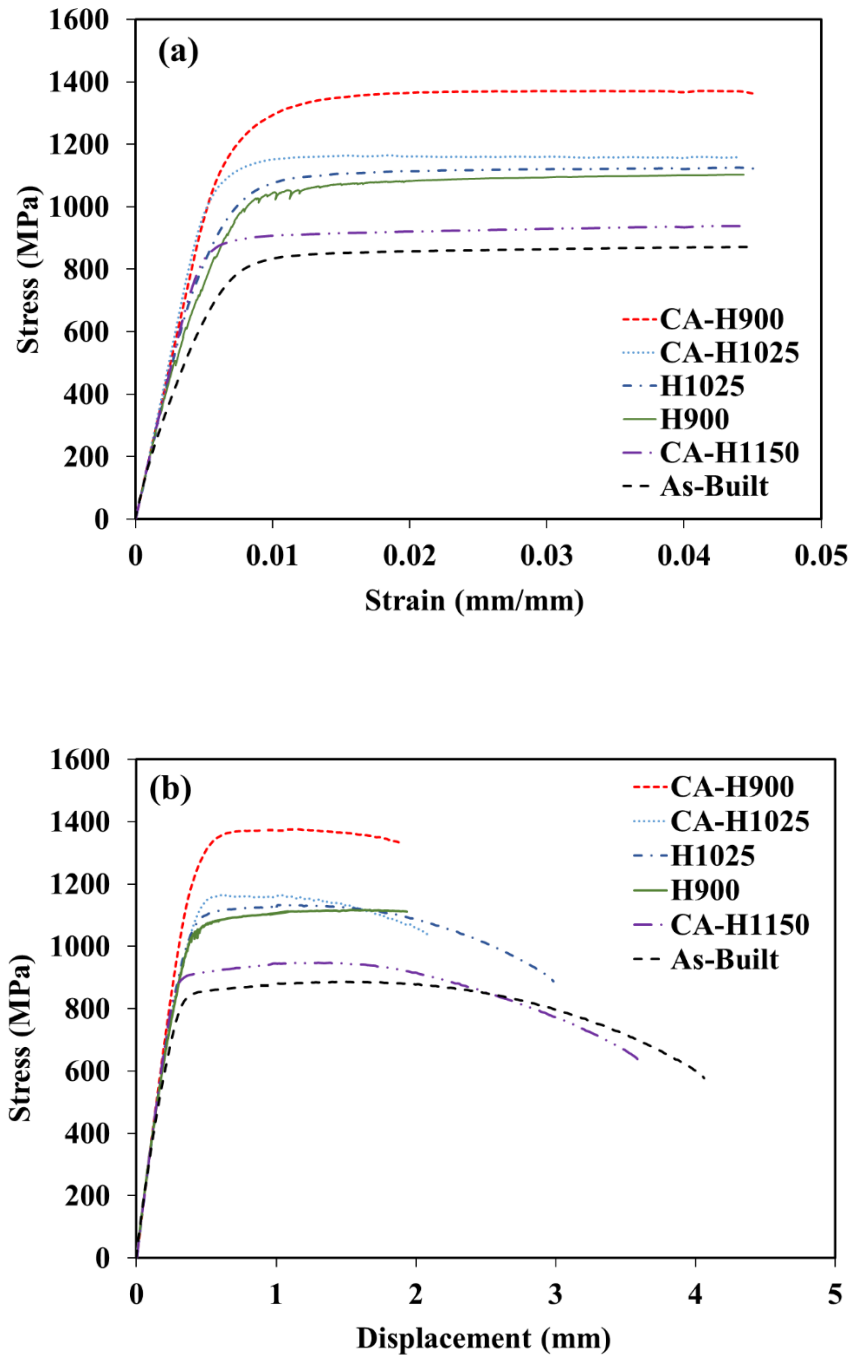


Figure 2-6. Monotonic tensile behavior of L-PBF 17-4 PH SS for non-heat treated as well as different heat treatment procedures utilized in this study, represented by (a) engineering stress-engineering strain curve up to the extensometer removal point, and (b) engineering stress-displacement curve all the way to fracture.

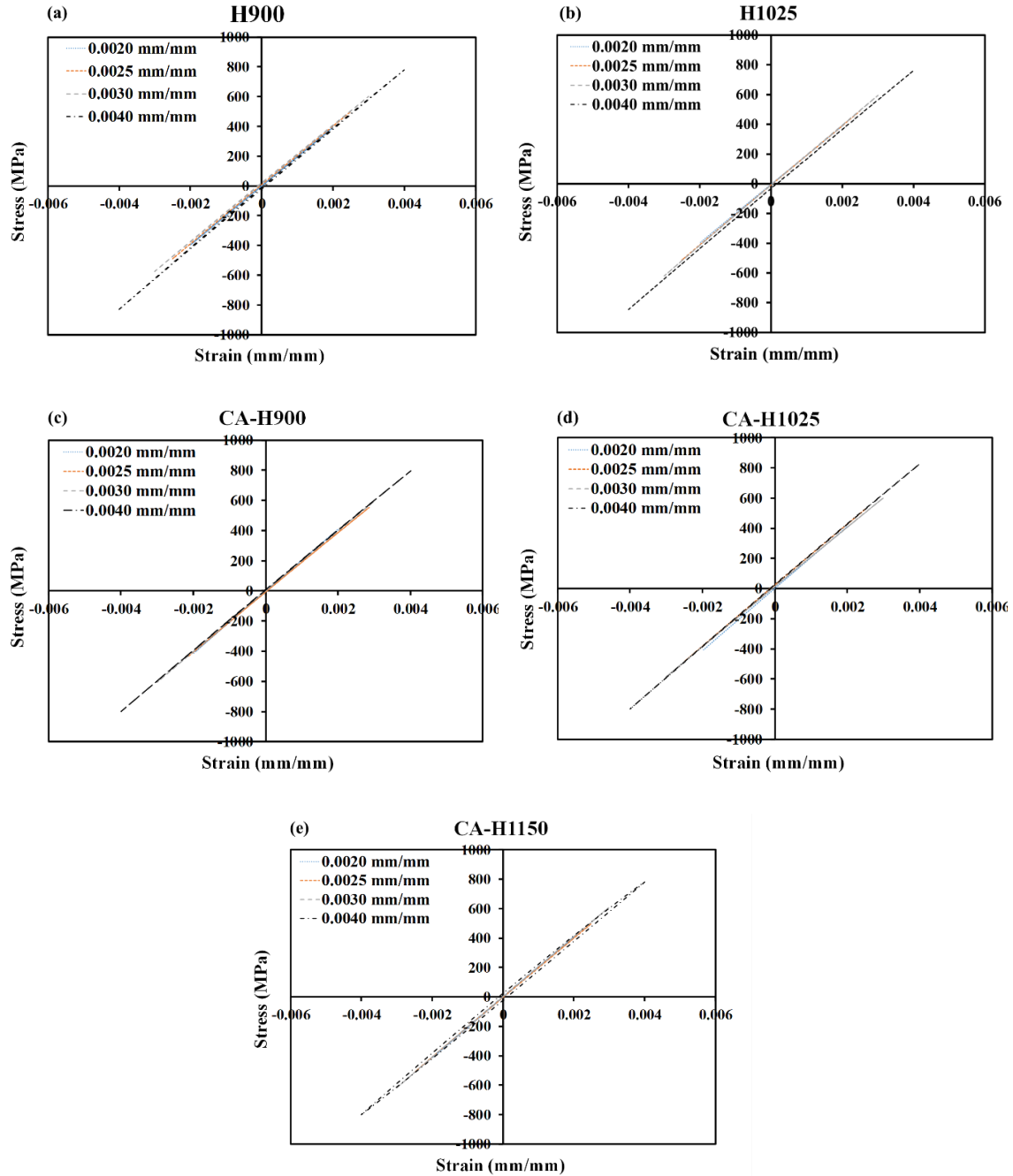


Figure 2-7. Stable hysteresis loops of fully-reversed strain-controlled constant amplitude fatigue tests of L-PBF 17-4 PH SS machined specimens in (a) H900, (b) H1025, (c) CA-H900, (d) CA-H1025, and (e) CA-H1150 heat treatments.

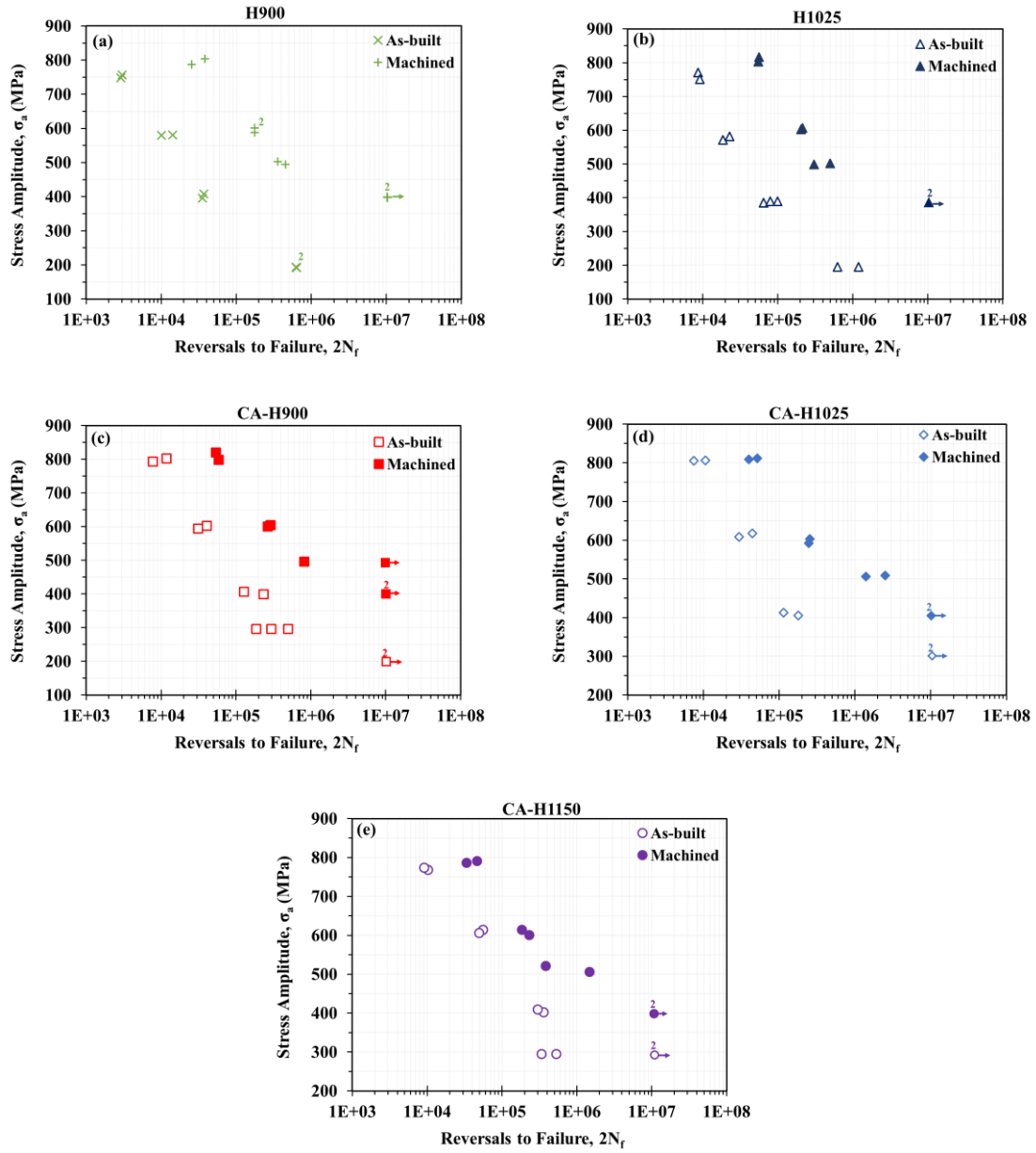


Figure 2-8. Comparison of L-PBF 17-4 PH SS as-built and machined specimens: stress-life fatigue data for (a) H900, (b) H1025, (c) CA-H900, (d) CA-H1025, and (e) CA-H1150 heat treatments.

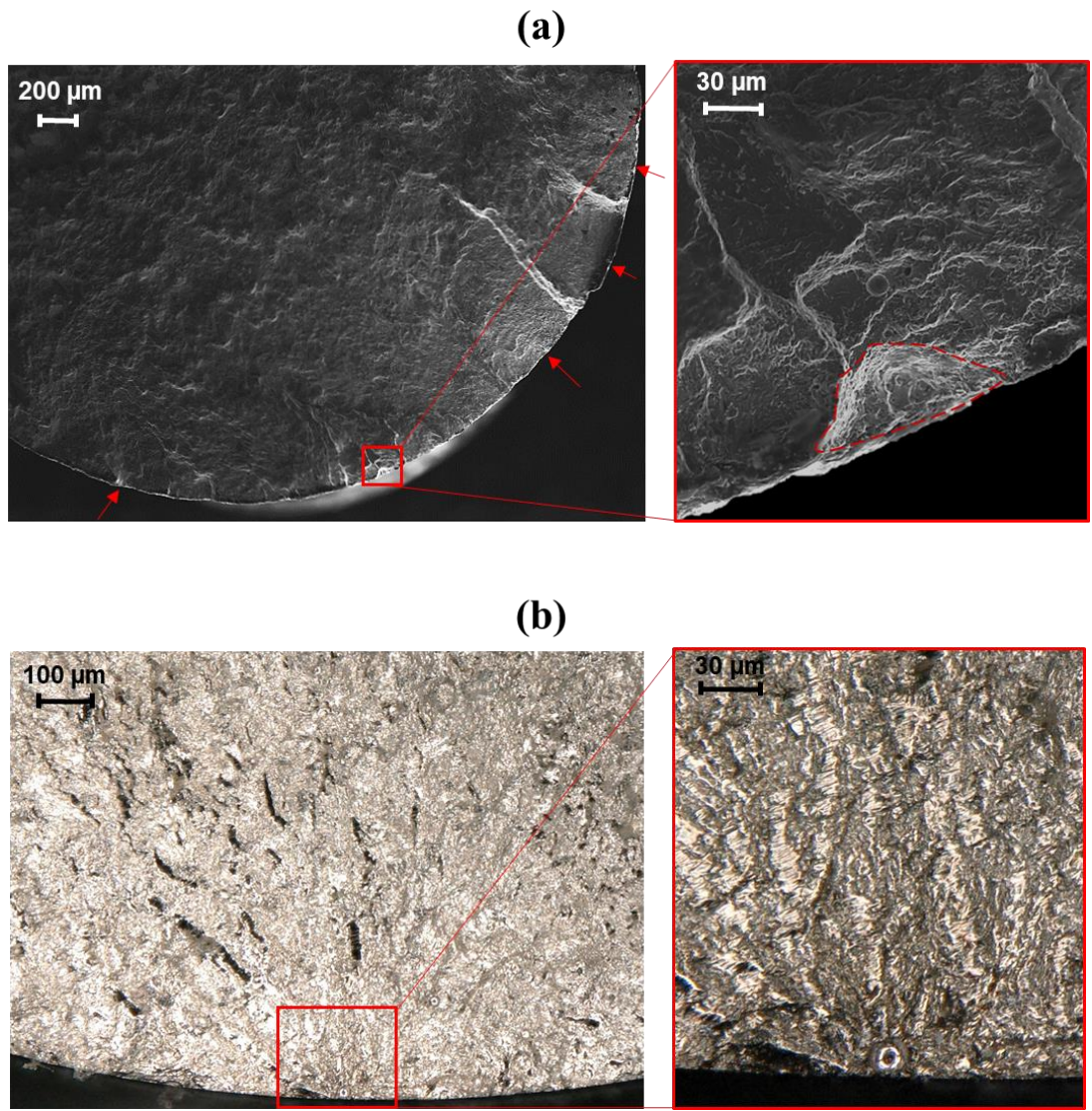


Figure 2-9. Fracture surface of L-PBF 17-4 PH SS specimens subjected to CA-H1025 heat treatment showing crack(s) initiated from (a) multiple micro-notches in an as-built specimen, and (b) a single spherical pore in a machined specimen.

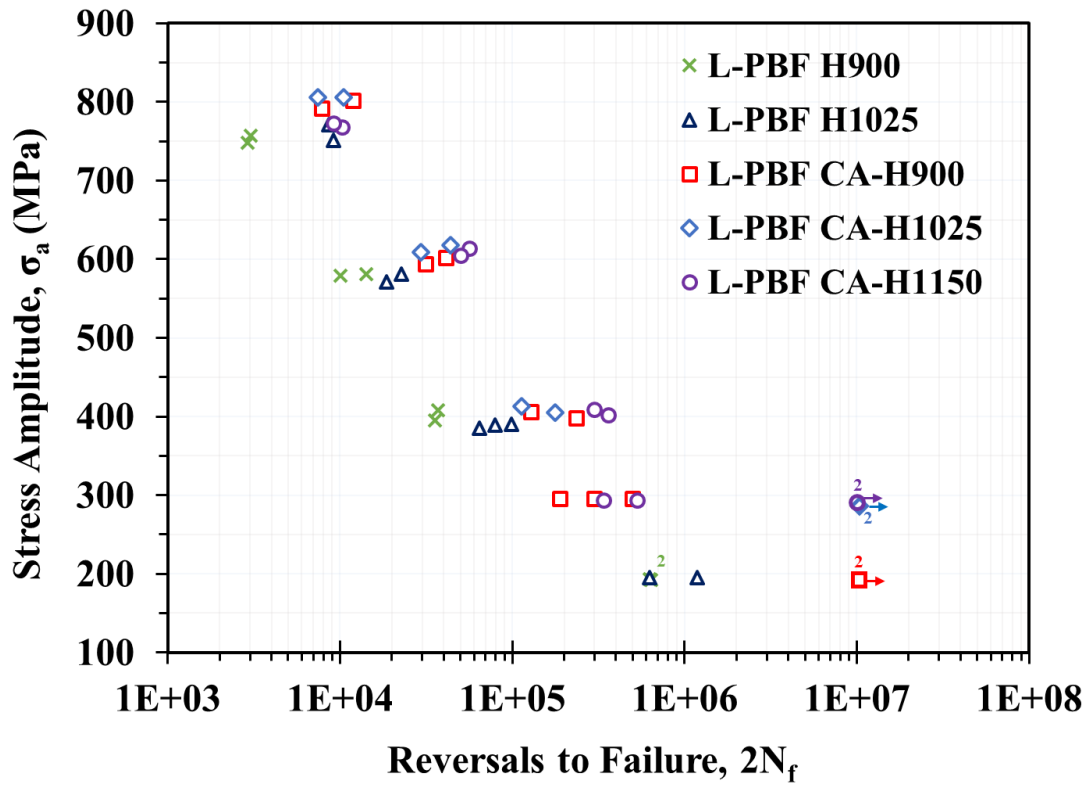


Figure 2-10. Stress-life fatigue data representing the effect of heat treatment on the fatigue behavior of L-PBF 17-4 PH SS as-built specimens.

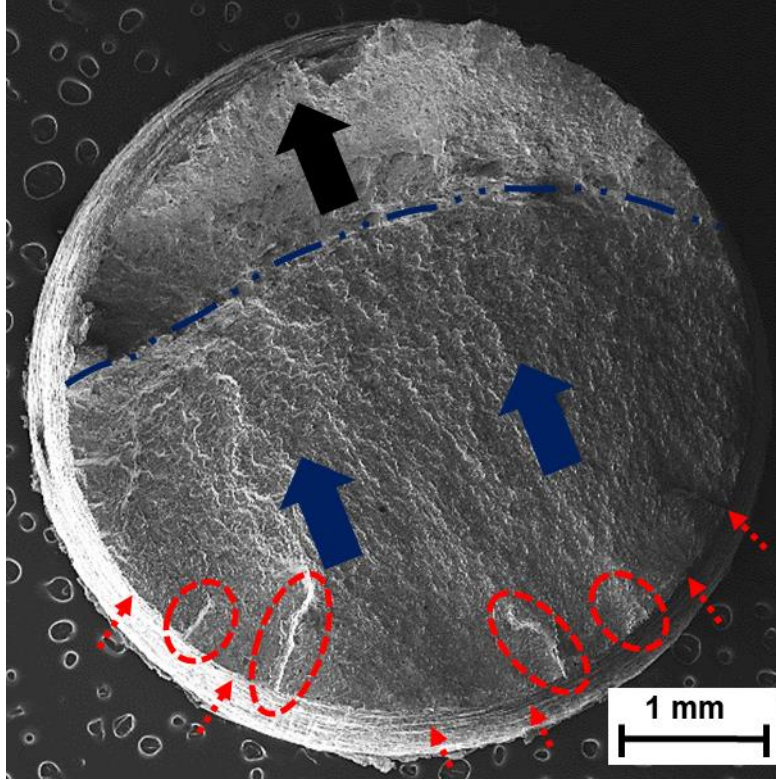


Figure 2-11. Fracture surface of an L-PBF 17-4 PH SS as-built specimens subjected to CA-H1150 heat treatment procedure and 0.002 mm/mm strain amplitude showing crack initiation sites, as well as crack growth and final fracture regions.

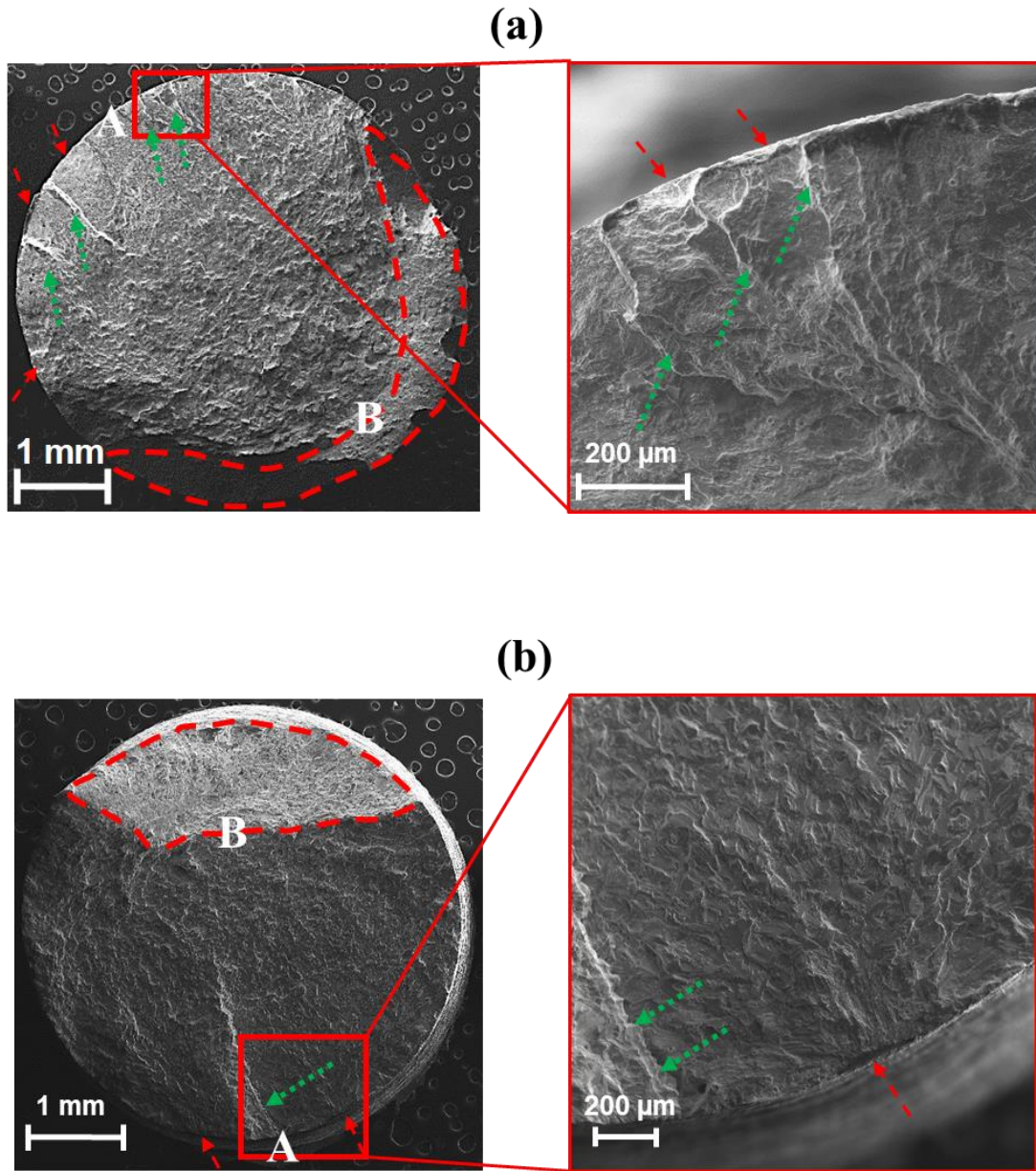


Figure 2-12. Fracture surface of L-PBF 17-4 PH SS specimens at 0.002 mm/mm strain amplitude showing crack growth and final fracture areas as well as the coalescence of cracks from different layers shown in zoomed-in images: (a) CA-H1025 (Sp_50, $2N_f = 113,374$ reversals), and (b) H1025 (Sp_13, $2N_f = 64,446$ reversals) heat treatment.

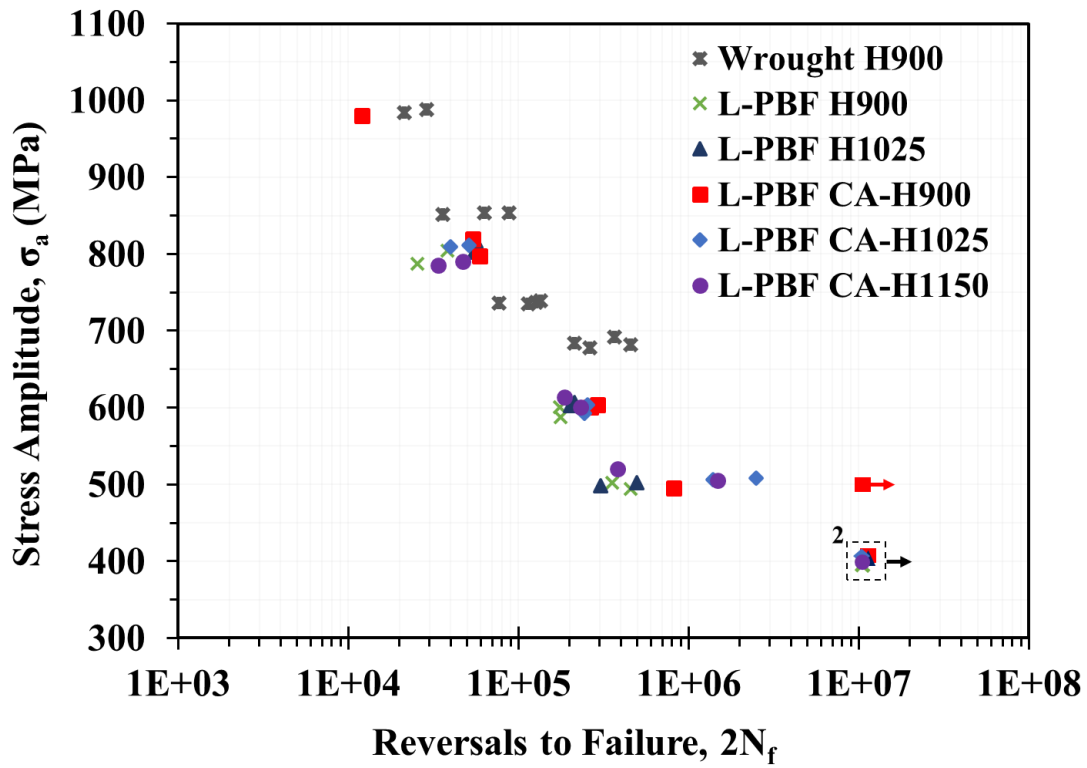


Figure 2-13. Stress-life fatigue data representing the effect of heat treatment on the fatigue behavior of L-PBF 17-4 PH SS machined specimens and their comparison with the wrought counterpart in H900 condition [83].

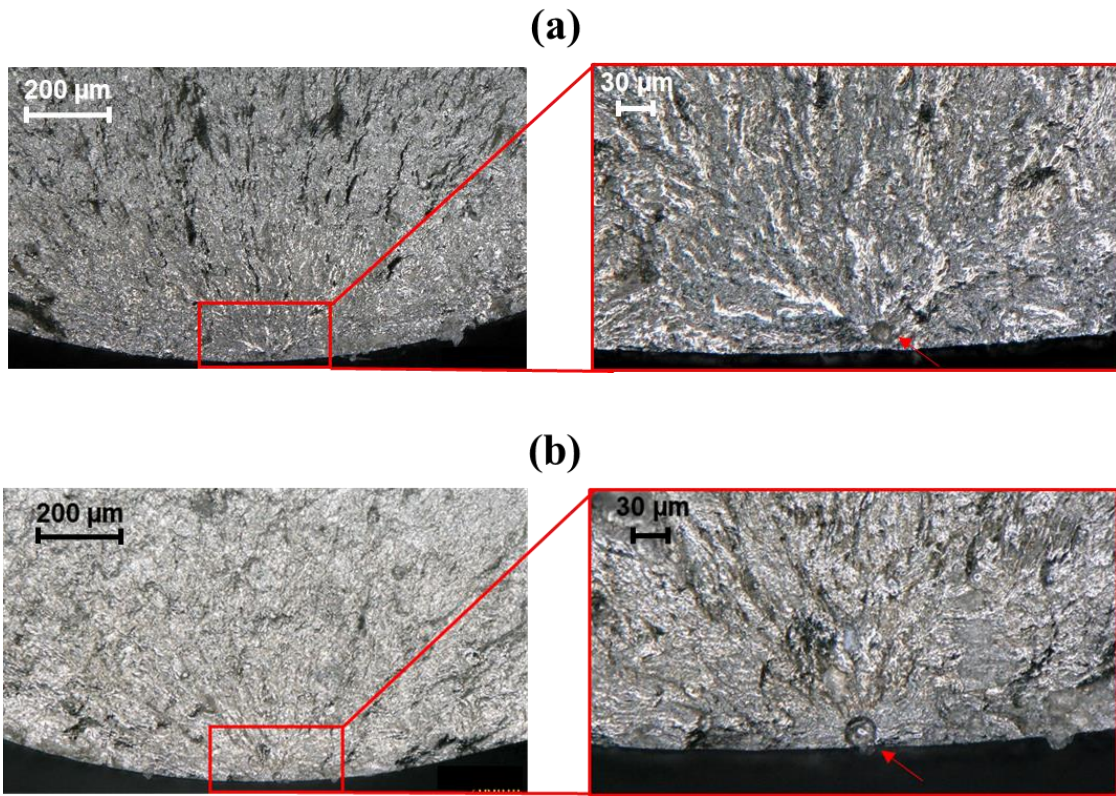


Figure 2-14. Fracture surfaces of L-PBF 17-4 PH SS specimens in the machined surface condition subjected to CA-H1150 heat treatment procedure showing the effect of pore size: (a) Sp_17 with 1,488,706 reversals to failure and a pore size of 21 μm , and (b) Sp_19 with 383,866 reversals to failure and a pore size of 28 μm .

Table 2-1. Chemical composition of 17-4 PH SS powder, provided by LPW Technology Inc.

| | C | Cr | Ni | Cu | Mn | Si | Nb | Mo | N | O | P | S | Fe |
|----------------|----------|-----------|-----------|-----------|-----------|-----------|-----------|-----------|----------|----------|----------|----------|-----------|
| (Wt. %) | 0.01 | 15.6 | 4.03 | 3.89 | 0.24 | 0.29 | 0.33 | <0.01 | 0.01 | 0.05 | 0.004 | 0.003 | Bal. |

Table 2-2. Suggested L-PBF process parameters for 17-4 PH SS by EOS.

| Laser power (W) | Scanning speed (mm/s) | Hatching space (μm) | Layer thickness (μm) |
|----------------------------|----------------------------------|--|---|
| 220 | 755.5 | 100 | 40 |

Table 2-3. Heat treatment procedures considered for the as-built and machined specimens in this study.

| Procedure* | Temperature (°C) | Duration (hour) | Quenching environment |
|-------------------|-------------------------|------------------------|------------------------------|
| H900 | 482 | 1 | Air cooled |
| H1025 | 552 | 4 | Air cooled |
| CA-H900 | 1050 | 0.5 | Air cooled |
| | 482 | 1 | Air cooled |
| CA-H1025 | 1050 | 0.5 | Air cooled |
| | 552 | 4 | Air cooled |
| CA-H1150 | 1050 | 0.5 | Air cooled |
| | 621 | 4 | Air cooled |

*All based on ASTM A693 [60]

Table 2-4. Monotonic tensile properties of L-PBF 17-4 PH SS in different heat treatment conditions as well as L-PBF properties reported by EOS for non-heat treated and CA-H900 [70] and the wrought 17-4 PH SS in CA-H900 condition [60].

| Fabrication method | Heat treatment | E (GPa) | σ_y (MPa) | σ_u (MPa) | RA% | ϵ_f |
|---------------------------|-------------------------------|----------------|------------------------------------|------------------------------------|------------|--------------------------------|
| L-PBF | Non-heat treated | 133 | 830 | 887 | 46 | 0.61 |
| | H900 | 189 | 1050 | 1117 | 16 | 0.17 |
| | H1025 | 188 | 1072 | 1132 | 33 | 0.39 |
| | CA-H900 | 194 | 1300 | 1375 | 15 | 0.16 |
| | CA-H1025 [63] | 200 | 1140 | 1167 | 26 | 0.30 |
| | CA-H1150 | 192 | 895 | 948 | 39 | 0.48 |
| | Non-heat treated (EOS) | N/A | 861 | 924 | N/A | N/A |
| | CA-H900 (EOS) | N/A | 1235 | 1336 | N/A | N/A |
| Wrought | CA-H900 (ASTM) | N/A | 1170 | 1310 | N/A | N/A |

Table 2-5. Fully-reversed fatigue test results for heat treated L-PBF 17-4 PH SS specimens in as-built surface condition.

| | Specimen ID | ϵ_a (mm/mm) | σ_a (MPa) | σ_m (MPa) | 2N_f (Reversals) |
|----------|--------------------|--|------------------------------------|------------------------------------|-----------------------------------|
| H900 | Sp_6 | 0.0010 | 192 | 0 | 636,952 |
| | Sp_5 | 0.0010 | 194 | 0 | 624,146 |
| | Sp_4 | 0.0020 | 408 | 36 | 36,956 |
| | Sp_3 | 0.0020 | 395 | 12 | 35,568 |
| | Sp_2 | 0.0030 | 581 | 9 | 14,164 |
| | Sp_11 | 0.0030 | 579 | -8 | 10,052 |
| | Sp_7 | 0.0030 | 565 | -9 | 4,858 |
| | Sp_8 | 0.0040 | 757 | -26 | 3,026 |
| | Sp_10 | 0.0040 | 749 | -14 | 2,898 |
| | H1025 | Sp_14 | 0.0010 | 195 | 0 |
| Sp_19 | | 0.0010 | 195 | 1 | 645,562 |
| Sp_12 | | 0.0020 | 390 | -10 | 99,010 |
| Sp_13 | | 0.0020 | 386 | -14 | 64,446 |
| Sp_15 | | 0.0020 | 389 | -5 | 79,458 |
| Sp_16 | | 0.0030 | 571 | -36 | 18,612 |
| Sp_17 | | 0.0030 | 581 | -20 | 22,732 |
| Sp_20 | | 0.0040 | 752 | -35 | 9,116 |
| Sp_18 | | 0.0040 | 771 | -29 | 8,630 |
| CA-H900 | Sp_22 | 0.0010 | 198 | 0 | >10,049,222 |
| | Sp_36 | 0.0010 | 199 | 0 | >10,000,000 |
| | Sp_38 | 0.0015 | 296 | 0 | 297,378 |
| | Sp_39 | 0.0015 | 296 | 0 | 188,054 |
| | Sp_45 | 0.0015 | 295 | 0 | 499,102 |
| | Sp_21 | 0.0020 | 386 | -3 | 235,076 |
| | Sp_23 | 0.0020 | 393 | -1 | 128,050 |
| | Sp_25 | 0.0030 | 583 | 26 | 40,988 |
| | Sp_24 | 0.0030 | 575 | 3 | 31,438 |
| | Sp_27 | 0.0040 | 776 | 16 | 11,840 |
| CA-H1025 | Sp_26 | 0.0040 | 767 | 35 | 7,822 |
| | Sp_44 | 0.0015 | 290 | 0 | >10,693,604 |
| | SP_43 | 0.0015 | 293 | 0 | >10,273,224 |
| | SP_49 | 0.0020 | 392 | 2 | 177,810 |
| | SP_50 | 0.0020 | 400 | 7 | 113,374 |
| | Sp_48 | 0.0030 | 598 | 15 | 43,952 |
| | Sp_47 | 0.0030 | 589 | 13 | 29,352 |
| Sp_51 | 0.0040 | 781 | 14 | 10,540 | |

| | | | | | |
|----------|-------|--------|-----|-----|-------------|
| | Sp_52 | 0.0040 | 780 | 33 | 7,426 |
| | Sp_46 | 0.0015 | 304 | 0 | >10,012,162 |
| | Sp_53 | 0.0015 | 302 | 0 | >10,002,396 |
| | Sp_41 | 0.0015 | 299 | 0 | 530,362 |
| | Sp_42 | 0.0015 | 304 | 0 | 339,506 |
| CA-H1150 | Sp_28 | 0.0020 | 402 | -1 | 361,246 |
| | Sp_29 | 0.0020 | 409 | -1 | 300,064 |
| | Sp_30 | 0.0030 | 613 | -54 | 56,068 |
| | Sp_31 | 0.0030 | 605 | -24 | 49,962 |
| | Sp_32 | 0.0040 | 768 | 39 | 10,268 |
| | Sp_33 | 0.0040 | 773 | -40 | 9,176 |

Table 2-6. Fully-reversed fatigue test results for heat treated L-PBF 17-4 PH SS specimens in machined surface condition.

| | Specimen ID | ϵ_a (mm/mm) | σ_a (MPa) | σ_m (MPa) | 2N_f (Reversals) |
|----------|--------------------|--|------------------------------------|------------------------------------|-----------------------------------|
| H900 | Sp_32 | 0.0020 | 393 | 3 | >10,485,384 |
| | Sp_46 | 0.0020 | 395 | -2 | >10,012,062 |
| | Sp_34 | 0.0025 | 495 | 5 | 454,602 |
| | Sp_33 | 0.0025 | 502 | 11 | 355,844 |
| | Sp_27 | 0.0030 | 587 | 13 | 176,086 |
| | Sp_28 | 0.0030 | 601 | 6 | 175,776 |
| | Sp_29 | 0.0040 | 804 | -25 | 38,230 |
| | Sp_30 | 0.0040 | 787 | 23 | 25,472 |
| H1025 | Sp_44 | 0.0020 | 406 | -6 | >10,280,216 |
| | Sp_41 | 0.0020 | 393 | -5 | >10,100,720 |
| | Sp_40 | 0.0025 | 502 | -11 | 496,526 |
| | Sp_39 | 0.0025 | 498 | -15 | 303,788 |
| | Sp_36 | 0.0030 | 607 | -11 | 213,094 |
| | Sp_35 | 0.0030 | 603 | -3 | 203,538 |
| | Sp_38 | 0.0040 | 817 | -28 | 56,462 |
| | Sp_37 | 0.0040 | 803 | -41 | 55,118 |
| CA-H900 | Sp_7 | 0.0020 | 412 | -4 | >10,614,228 |
| | Sp_6 | 0.0020 | 420 | -7 | >10,596,648 |
| | Sp_16 | 0.0025 | 508 | 2 | >10,772,058 |
| | Sp_23 | 0.0025 | 496 | 59 | 820,176 |
| | Sp_4 | 0.0030 | 604 | 9 | 291,556 |
| | Sp_5 | 0.0030 | 600 | -4 | 266,272 |
| | Sp_25 | 0.0030 | 611 | 13 | 255,006 |
| | Sp_2 | 0.0040 | 798 | -1 | 59,286 |
| | Sp_1 | 0.0040 | 820 | -16 | 54,014 |
| | Sp_3 | 0.005 | 980 | 19 | 12,048 |
| CA-H1025 | Sp_22 | 0.0020 | 406 | 13 | >10,603,816 |
| | Sp_31 | 0.0020 | 410 | 0 | >10,109,402 |
| | Sp_20 | 0.0025 | 509 | 24 | 2,496,340 |
| | Sp_21 | 0.0025 | 506 | 23 | 1,394,730 |
| | Sp_15 | 0.0030 | 604 | -2 | 254,274 |
| | Sp_18 | 0.0030 | 593 | 9 | 244,684 |
| | Sp_14 | 0.0040 | 812 | 14 | 51,348 |
| | Sp_13 | 0.0040 | 809 | 24 | 39,764 |

| | | | | | |
|----------|-------|--------|-----|----|-------------|
| | Sp_12 | 0.0020 | 406 | -1 | >10,887,458 |
| | Sp_42 | 0.0020 | 410 | -1 | >10,044,094 |
| CA-H1150 | Sp_17 | 0.0025 | 506 | -7 | 1,488,706 |
| | Sp_19 | 0.0025 | 521 | 12 | 383,866 |
| | Sp_10 | 0.0030 | 601 | 36 | 232,096 |
| | Sp_11 | 0.0030 | 614 | -4 | 185,542 |
| | Sp_9 | 0.0040 | 791 | -9 | 46,852 |
| | Sp_8 | 0.0040 | 786 | 47 | 33,746 |

Table 2-7. Fatigue properties of heat treated L-PBF 17-4 PH SS specimens in as-built and machined surface conditions.

| | σ'_f (MPa) | | b | | R² | |
|-----------------|-------------------|-----------------|-----------------|-----------------|----------------------|-----------------|
| | As-built | Machined | As-built | Machined | As-built | Machined |
| H900 | 6175 | 4989 | -0.259 | -0.177 | 0.99 | 0.97 |
| H1025 | 10519 | 10677 | -0.292 | -0.236 | 0.99 | 0.96 |
| CA-H900 | 9559 | 4511 | -0.269 | -0.160 | 0.93 | 0.93 |
| CA-H1025 | 7018 | 2909 | -0.237 | -0.123 | 0.96 | 0.94 |
| CA-H1150 | 2724 | 3161 | -0.138 | -0.134 | 0.91 | 0.92 |

**CHAPTER 3: FATIGUE CRACK GROWTH BEHAVIOR OF ADDITIVELY
MANUFACTURED 17-4 PH STAINLESS STEEL: EFFECTS OF BUILD
ORIENTATION AND MICROSTRUCTURE**

The following chapter has passed rigorous peer-review process and has been published in International Journal of Fatigue (IJF) in 2019.

Nezhadfar, P.D., Burford, E., Anderson-Wedge, K., Zhang, B., Shao, S., Daniewicz, S. R., Shamsaei, N., Fatigue crack growth behavior of additively manufactured 17-4 PH stainless steel: effects of build orientation and microstructure, International Journal of Fatigue, 2019.

3.1. Abstract

Additive manufacturing (AM) brings more freedom to design and fabricate parts with complex geometries. However, structural integrity of additively manufactured parts must be thoroughly investigated before they can be used in critical, load bearing structural applications. This study investigates the fatigue crack growth (FCG) behavior of 17-4 precipitation hardening (PH) stainless steel (SS) fabricated using laser powder bed fusion (L-PBF) process, and compares it to that of wrought counterpart. The effect of different heat treatment procedures and the notch orientation relative to the build direction were also studied. FCG tests were conducted under force-controlled mode at room temperature with a load ratio of $R = 0.1$ and a frequency of 10 Hz up to fracture. Microstructure characterization and fractography analysis were carried out to elaborate the crack growth mechanism with respect to different heat treatment conditions and crack growth directions. Abnormal FCG behavior was observed for L-PBF 17-4 PH SS subjected to H1025 heat treatment procedure. This was associated with the presence of δ -ferrite and its weak interface with martensite boundaries. However, L-PBF 17-4 PH SS specimens subjected to CA-H900 condition were found to behave similar to the wrought counterparts in the Paris regime.

3.2. Introduction

Additive manufacturing (AM) enables fabricating parts track by track and layer by layer as opposed to the more traditional subtractive manufacturing method [1,4,6]. AM methods can be classified based on the feedstock (i.e. powder, wire) and energy source (i.e. laser, electron beam) [1]. Laser powder bed fusion (L-PBF) is one of the most common AM processes for manufacturing of metallic parts. In this process, parts are fabricated through the repetition of melting and fusing thin layers of powder to the previously fabricated ones by a high power laser source under an inert shielding gas [33]. This technique brings more freedom in design of parts with complex geometries and provides outstanding benefits such as cost-effectiveness, low-volume production, expedition in delivery time to market, and even increasing component functionality [12,84].

Despite the advantages of AM technology, there are some challenges which affect the structural integrity of fabricated parts. Thermal history experienced by parts during the fabrication process often induces residual stresses and formation of defects, such as keyhole pores and lack of fusions [12,36,85,86]. The repetitious nature of additive manufacturing processes also results in parts having relatively rough surfaces. Interestingly, despite the presence of defects, the tensile strength of additively manufactured parts has been reported to be comparable (even sometimes better) to the ones of the wrought counterparts due to the fine microstructure obtained during the AM process as a result of rapid cooling. However, most parts experience cyclic loading in service, and it has been well established that fatigue performance is sensitive to imperfections (i.e. defects) [4]. Therefore, the trustworthiness of additively manufactured parts must be

thoroughly evaluated before additive manufacturing can be utilized to fabricate load bearing, fatigue-critical parts in aerospace, biomedical and automotive applications.

Fatigue behavior of various AM material systems such as titanium and aluminum alloys [48,56,87–89], Nickel-based super alloys [43] and various grades of stainless steels [44,57,90] have been recently studied. In all studies, defects such as porosity, lack of fusions, and surface roughness as well as microstructural heterogeneity and anisotropy were recognized as the most influencing factors affecting the mechanical and fatigue behavior of additively manufactured parts. Recently, the effect of build orientation on defects distribution and fatigue behavior of L-PBF 316L stainless steel was studied by Shrestha et al. [91]. It was shown the build orientation to have more influence in high cycle fatigue regime where there is more sensitivity to defects. In addition, they reported that horizontally fabricated specimens performed better in high cycle fatigue regime compared to the vertical and diagonal specimens, which was related to smaller projected area of defects on the loading plane in horizontal specimens.

Some studies highlighted the effect of microstructure and grain orientation on the fatigue performance and fatigue crack growth (FCG) behavior of additively manufactured parts [10,57,92,93]. Riemer et al. [92] studied the effect of microstructure on FCG behavior of L-PBF 316L stainless steel in as-built as well as stress relief heat treated, and hot isostatic pressing (HIP) conditions. They reported FCG rate to be significantly dependent on the crack growth direction and the grains orientation in as-built and heat treated conditions. It was shown that the stress intensity factor threshold was lower when the crack growth was parallel to the building direction because of the crack propagating along the columnar grains. On the other hand, when the crack growth was perpendicular to the

building direction, FCG rate decreased due to the lower grain boundary spacing. They also showed that HIP changed the as-built columnar grains to equiaxed ones leading to isotropic crack growth properties. In another study, Ran et al. [93] showed improvement in FCG behavior of AerMet100 steel by heat treatment and attributed this to the transition of columnar grains to equiaxed grains.

Among the precipitation hardened stainless steels, 17-4 PH SS is a martensitic/austenitic one that upon appropriate heat treatment can possess excellent mechanical properties such as high tensile/impact strength, fracture toughness and corrosion resistance at service temperature below 300 °C [59]. As a result, 17-4 PH SS is widely used in aerospace, petrochemical, and marine environments for fabricating structural components [94,95]. Moreover, with the increase in interests from these industries, additive manufacturing has given more prominence to 17-4 PH SS recently. The building orientation effect on the fatigue behavior of L-PBF 17-4 PH SS has been investigated in a number studies [39,42]. The results indicated better fatigue resistance for specimens fabricated horizontally as compared to the vertical specimens. This was attributed to the higher stress concentration from lack of fusion defects perpendicular to the loading plane in vertically built specimens as compared to the ones in horizontally built specimens which had smaller projected areas on the loading plane [39].

Nezhadfar et al. [96] recently studied the effect of various heat treatment procedures on the microstructure and fatigue behavior of L-PBF 17-4 PH SS. It was shown that depending on the heat treatment procedure employed, L-PBF 17-4 PH SS exhibited a different combination of ductility and strength; however, applying Condition A (CA), i.e.

a solution treating cycle at 1050 °C for half an hour, prior to the aging stage always had a positive effect on the fatigue behavior.

Due to their popularity in various structural applications, high fatigue resistance is particularly desirable for 17-4 PH SS. Therefore, many recent studies focused on the fatigue crack initiation behavior of L-PBF 17-4 PH SS [42,90,97]. However, there is not much understanding on the fatigue crack growth (FCG) behavior of L-PBF 17-4 PH SS. The FCG behavior and its dependence on microstructure is an important factor in predicting the service life of metallic components bases on a damage tolerance approach. Accordingly, the aim of this study is to investigate the FCG and microstructure-related cracking behavior of L-PBF 17-4 PH SS. Two heat treatment procedures resulting in different microstructural features with one increasing the strength and the other one increasing the ductility are chosen. Consequently, the effect of microstructure on the crack growth behavior is investigated and the FCG behavior of L-PBF 17-4 PH SS is compared to that of its wrought counterpart.

3.3. Experimental Procedures

3.3.1. Material and Specimen Fabrication

In this study, argon atomized 17-4 PH stainless steel powder was used for fabrication of specimens using a laser powder bed fusion (L-PBF) method. The powder batch with the particle size of 15-45 µm were provided by LPW Inc. The certified chemical composition provided by LPW Inc. is listed in **Table 3-1**.

Sixteen walls with the thickness 6.7 mm were built vertically under argon shielding gas using EOS M290 employing the EOS recommended process parameters listed in **Table 3-2**. Fabricated walls were machined using electrical discharge machining (EDM) into

compact tension (CT) specimens. **Figure 3-1** shows the CT specimens designed with a straight through crack with length a , in accordance with ASTM E647 [98] with width, W , of 54.2 mm and thickness, B , of 6 mm. In order to compare the mechanical properties of L-PBF 17-4 PH SS with wrought counterpart, CT specimens with similar dimensions were also machined from wrought 17-4 PH SS plates.

Machining of L-PBF 17-4 PH SS specimens was conducted based on the notch orientation relative to the building direction. Set 1 has the notch parallel to the build direction and set 2 has the notch perpendicular to the build direction as shown in **Figure 3-1(b)**. L-PBF 17-4 PH SS specimens were subjected to CA-H900 and H1025 heat treatment procedures after machining. These common heat treatment procedures for 17-4 PH SS were chosen based on the results presented in previous study [96]. Specimens subjected to CA-H900 exhibit higher strength and lower ductility (i.e. 1300 MPa yield strength, 1375 MPa ultimate strength, and 0.16 true fracture strain) as compared to the specimens subjected to H1025 (1072 MPa yield strength, 1132 MPa ultimate strength, and 0.39 as true fracture strain) [96].

CA-H900 includes two steps, Condition A (CA) followed by H900. Accordingly, specimens were subjected to solution heat treatment at 1050 °C (i.e. 1922 °F) for half an hour followed by air cooling to room temperature (i.e. Condition A (CA)) and second, specimens were held at 482 °C (i.e. 900 °F) for an hour followed by air cooling (H900). For the H1025 condition, specimens were only heat treated at 552 °C (i.e. 1025 °F) for four hours followed by air cooling to room temperature without performing CA step.

To evaluate the effects of notch orientation relative to the building direction and heat treatment, some specimens from each set were subjected to CA-H900 and the rest

were subjected to the H1025 heat treatment condition of which the details are listed in **Table 3-3**. Wrought specimens were all subjected to the CA-H900 procedure.

3.3.2. Microstructural Prediction and Characterization

In order to investigate the microstructure-related crack growth behavior, it is essential to find out the constituent phases due to their different deformation behaviors. To predict the constituent phases for each heat treatment condition, ternary phase diagrams were generated using Thermo-Calc. software. For this purpose, TCFE9 [99] thermodynamic database for various types of Fe-based alloys and steels such as stainless steels, was employed. For simulating the ternary phase diagrams, Ni_{eq} (Nickel equivalent) and Cr_{eq} (Chromium equivalent) were calculated based on the Schaeffler equations [100], Eqs. (1) and (2). Based on these equations, Ni_{eq} considers the effect of austenite stabilizer elements and Cr_{eq} considers the effect of ferrite stabilizer elements.

$$Ni_{eq} = \%Ni + 0.5(\%Mn) + 0.3(\%Cu) + 25(\%N) + 30(\%C) \quad (1)$$

$$Cr_{eq} = \%Cr + 2(\%Si) + 1.5(\%Mo) + 1.75(\%Nb) \quad (2)$$

Accordingly, Ni_{eq} and Cr_{eq} were calculated to be 5.8 and 16.8 wt%, respectively, based on the chemical composition of powder utilized. The ternary phase diagrams cross sectioned at 1050 °C and 482 °C, i.e. CA-H900 shown in **Figure 3-2(a)** and (c), and 552 °C, i.e. H1025 shown in **Figure 3-2(b)**. The present alloy (i.e. 17-4 PH SS chemical composition) is indicated with a red dot in each temperature cross-section in accordance to the calculated Ni_{eq} and Cr_{eq} values. It can be seen that at 552 °C, i.e. H1025 heat treatment procedure, alloy is in body centered cubic (BCC) region. On the other hand, in the case of CA-H900 heat treatment procedure, CA step makes the alloy austenitic (i.e. face centered cubic (FCC)), and at 482 °C, i.e. H900 heat treatment procedure, alloy is in BCC region.

Specimens were cross-sectioned for further microstructure characterization in normal direction (ND), i.e. plane perpendicular to the building direction, and transverse direction (TD), i.e. plane parallel to the building direction. Standard metallographic procedures based on the ASTM E3-11 [66] were followed for samples preparation and microstructural observations. Accordingly, the samples were subjected to progressive grinding using sand papers ranging from 320 to 2500 grit and eventually were polished utilizing ChemoMet accompanied by 0.05-micron MasterPrep Alumina to get close to a mirror finished surface. The microstructure features were revealed using Beraha's tint etchant and observed using a Zeiss optical microscope.

X-ray diffraction (XRD) analysis was also conducted to characterize the variation in existing phases as a result of different heat treatment procedures employed. Bruker AXS-D8 Discover X-ray system with Cu K_a radiation with 45 kV and 40 mA as operating voltage and current, respectively, was used. The XRD patterns were obtained within a 2θ range of 30° to 90° with a step size of 0.2°.

3.3.3. Fatigue Crack Growth (FCG) Test and Fractography

FCG tests were performed on a servo-hydraulic testing machine. The low-stress fatigue tests (i.e. high cycle fatigue regime) were conducted on CT specimens under load-control at room temperature with a sinusoidal loading waveform with a load ratio $R = 0.1$ and frequency $f = 10$ Hz until failure. During pre-cracking, a crack mouth opening displacement (CMOD) gage was used to measure crack length and monitor each specimen until the pre-crack length reached to 11-14 mm to achieve a corresponding initial \sqrt{K} value of approximately $10 \text{ MPa}\sqrt{\text{m}}$, as directed by ASTM 647 [98]. Pre-cracking was performed at the same loading used for the fatigue crack growth rate testing. Load amplitudes ranged

from 4275 N to 1575 N. FCG rate, da/dN , and stress intensity factor ranges, ΔK , were determined using the recorded CMOD values, load range, and the measured cycle count in accordance with ASTM E647. To address variability, FCG tests were carried out on four CT specimens from each category, as described in **Table 3-3**.

Fractography analysis was performed on the fracture surfaces to better understand the crack growth mechanism influenced by different heat treatment and notch orientation relative to the building direction (see **Table 3-3**). The fracture surfaces were sonicated and cleaned, then dried using acetone. Fractography was carried out using Zeiss EVO50 scanning electron microscope (SEM) and a FEI Quanta3D FEG dual-beam scanning electron microscope/focused ion beam (SEM/FIB) instrument. The SEM/FIB instrument includes an electron backscatter diffraction (EBSD) attachment.

EBSD analysis was also conducted on specimens' front/back surfaces near the fracture surface to reveal detailed information of relationships between the fatigue crack propagation and the grain boundaries. Prior to examination, the specimens were mechanically polished with SiC polishing papers of various grit sizes, followed by a fine polishing process with 6, 3, and 1 μm diamond suspension. Eventually, specimens were vibratory polished with 50 nm silica suspension on a GIGA 0900 Vibratory Polisher for 12 hrs. EBSD operating voltage, current and step size were 30 kV, 23 nA and 0.3 μm , respectively.

3.4. Results and Discussions

3.4.1. Microstructure

Figure 3-2 shows the ternary phase diagrams cross-sectioned at 482 °C, 552 °C and 1050 °C. The present alloy is shown with red dot in each phase diagram. **Figure 3-2(a)**

shows that at 482 °C (i.e., H900) the alloy is in BCC (base centered cubic) region (i.e. martensite). By increasing the temperature to 552 °C (i.e., H1025), the alloy still stays in BCC region (**Figure 3-2(b)**). However, during the CA heat treatment (**Figure 3-2(c)**), the alloy is expected to stabilize in FCC (face centered cubic), i.e., austenite, region. To evaluate the thermodynamic predictions, XRD analysis was performed. **Figure 3-3** presents the XRD analysis of the as-built (non-heat treated) and heat treated specimens showing the existing phases in each condition. It can be seen that the as-built specimen consisted of martensite, α' , and a fraction of austenite, γ . However, the austenite phase disappeared after heat treatment. Accordingly, samples treated by H1025, CA, and CA-H900 only consist of martensite, α' . For the CA condition, as shown in **Figure 3-2(c)**, austenite reverts from martensite at 1050 °C; however, it transforms back to martensite during the cooling step. The martensite transformation onset temperature for 17-4 PH SS, M_s , is relatively stable across a relatively wide range of cooling rates and is approximately 150 °C [16,101]. At this temperature, the austenite starts to transform to martensite during cooling [16].

Figure 3-4(a) and **(b)** show the microstructure of L-PBF 17-4 PH SS samples undergone CA-H900 and H1025 heat treatment procedures, and **Figure 3-4(c)** shows the microstructure of wrought 17-4 PH SS undergone CA-H900 heat treatment procedure. As can be seen on the TD plane of L-PBF 17-4 PH SS at H1025 condition in **Figure 3-4(a)**, the columnar grains are elongated parallel to the building direction. In fact, during the repeated melting and solidification process during a build, grains grow epitaxially along the heat dissipation path toward the substrate. These grains are comprised of α' -martensite as characterized by the XRD in **Figure 3-3**. Moreover, the melt pools have the

characteristic width of $\sim 100 \mu\text{m}$ (similar to the hatching distance reported in **Table 3-2**), as shown by the arc-line marks in TD plane and the straight-line marks in the ND plane of **Figure 3-4(a)**. It is worth noting that the molten tracks overlap with the adjacent ones on the same and the previous deposited layer, which is necessary for the good fusion of layers during the building process.

In contrast, as can be seen in **Figure 3-4(b)** for the L-PBF 17-4 PH SS, the as-built microstructural features such as elongated grains and melt pools disappeared after CA-H900 heat treatment. The CA-H900 led to a fully martensitic and a more homogeneous microstructure as compared to the H1025 treatment. By performing CA (1050 °C for half an hour), the initial martensite resulted from the fabrication process first transforms to austenite as shown in **Figure 3-2(c)**. Due to the higher solubility of the Cu and Ni elements in austenite at the elevated temperature (1050 °C), the austenite becomes supersaturated when the specimens are gradually cooled down. Accordingly, supersaturated austenite transforms to supersaturated martensite after cooling to the room temperature. The subsequent heat treatment (i.e. H900) results in the formation of fine coherent Cu-rich precipitates within the martensite matrix. The obtained fine martensite microstructure, along with the presence of the precipitates after performing CA-H900 heat treatment, increases the strength and reduces the ductility in 17-4 PH SS.

It is worth mentioning that H1025 heat treatment is not capable of homogenizing the microstructure and results in coarsened (sparsely distributed) precipitates that lead into the higher ductility as compared to the CA-H900 treatment [19,64]. The detailed monotonic deformation behavior of these heat treatment conditions can be found elsewhere [28]. Moreover, the microstructure of wrought 17-4 PH SS subjected to CA-H900 heat

treatment procedure in **Figure 3-4(c)** shows coarser grains than the ones from L-PBF 17-4 PH SS at CA-H900 condition. The microstructure of AM materials are often finer than that of wrought counterparts due to the high cooling rate during the AM processes [1,39].

3.4.2. Fatigue Crack Growth (FCG) Behavior

3.4.2.1. H1025 L-PBF 17-4 PH SS CT specimens

Figure 3-5 shows the crack propagation behavior, affected by the relative angle of notch orientation with respect to build direction, in specimens subjected to H1025 heat treatment procedure. **Figure 3-5(a)** illustrates a specimen from set 1, whose build direction is parallel to the notch orientation. Interestingly, cracks formed at the notch immediately after heat treatment with no need for an external force. This phenomenon occurred for all the specimens of set 1 (with notch orientation parallel to build direction) subjected to H1025 heat treatment procedure. Therefore, no FCG testing was performed on these specimens, which were considered as failed specimens.

Similar cracking induced by heat treatment is reported for wrought 17-4 PH SS in the literature [95,102]. Tian et al. [102] reported the crack formation in piston rods made of wrought 17-4 PH SS after heat treating at 620 °C for six hours. They have ascribed the crack formation after heat treatment to two main reasons. First, the segregation of Cu and Ni elements, as austenite stabilizers, to lath martensite boundaries and the grain boundaries, forms the austenite with low strength. Second, the presence of brittle δ -ferrite in the martensite matrix whose interface with martensite offers a preferred path for crack propagation. It has been reported that 17-4 PH SS solidifies as a primary ferrite from the liquid phase and will transform to austenite during cooling, by solid-state diffusion following solidification, between the liquidus and solidus temperatures [67]. Subsequently,

as the temperature reduces to the M_s temperature (150 °C), austenite transforms to the martensite, while some δ -ferrite may be retained in the microstructure on the primary austenite grain boundaries. The δ -ferrite is a brittle phase and has weak boundaries with the martensite, creating a low energy path for cracks to propagate [95].

In the present work, as no peaks of austenite appeared in XRD of H1025 specimens (see **Figure 3-3**), the first explanation, related to Cu and Ni segregation, may not apply. Considering the second explanation in the present work, XRD analysis cannot distinguish the δ -ferrite from martensite since both are body centered cubic (bcc) with near-identical lattice constants [103]. Thus, α' peaks in XRD results, presented in **Figure 3-3**, may comprise the δ -ferrite phase as well. **Figure 3-6(a)** and **(b)** show the optical and SEM image of H1025 microstructure, respectively. It can be seen that string-like δ -ferrite are present on the grain boundaries. Consequently, the presence of string-like δ -ferrite may have resulted in crack formation during heat treatment. In addition to the presence of δ -ferrite, thermal stresses during cooling as well as notch being parallel to the columnar grains must be taken into account as the influential factors causing crack formation, adjacent and parallel to the notch, after/during) heat treatment.

More interestingly, for specimens from set 2 (with notch orientation perpendicular to build direction), as shown in **Figure 3-5(b)**, the crack started to deviate from mode I, and propagated parallel to the loading direction during the FCG tests, i.e. becoming a mode II crack in violation of crack straightness requirements in ASTM E647 [98]. It is worth mentioning that there would be no crack tip plastic zone size disparity to overcome, as the same loading was used both during pre-cracking and crack growth testing. It should be noted that columnar grains are also parallel to the build direction in H1025 L-PBF 17-4 PH

SS CT specimens. Similarly, Rack and Kalish [80] reported the deviation of crack from mode I to mode II for wrought 17-4 PH SS specimens heat treated at 593 °C due to the presence of string-like δ -ferrite on the grain boundaries. They have attributed this behavior to the weak interface between δ -ferrite and martensite grain boundaries. Moreover, they stated that the amount and distribution of δ -ferrite affect the crack propagation behavior . In addition, Srinath et al. [95] showed the crack propagation along the interfaces between δ -ferrite strings and lath martensite in wrought 17-4 PH SS which is attributed to the weak tensile strength of such interfaces. Therefore, the presence of δ -ferrite strings along the elongated grain boundaries (see **Figure 3-6**) may be the primary reason for the observed deviation in crack propagation for specimens subjected to H1025 heat treatment procedure.

Srinath et al. [95] also showed the formation of adiabatic shear bands close to the δ -ferrite and failure area. Formation of similar shear bands near the fracture surfaces was also observed in the present work. **Figure 3-7** shows the microstructure along the crack growth path of a H1025 L-PBF 17-4 PH SS CT specimen from set 2. The microstructural features of location 1 and 2 in **Figure 3-7(a)** are shown in **Figure 3-7(b)** and (c), respectively. Shear bands observed adjacent to the crack growth path are indicated by arrows these figures. It is mentioned in [95] that these deformation bands occur in localized deformed regions and are attributed to the δ -ferrite which accelerates the crack growth rate due to the weak interface of δ -ferrite and martensite as well as low plasticity and brittleness behavior of δ -ferrite.

In addition, secondary cracks were observed in some H1025 L-PBF 17-4 PH SS specimens from set 2. **Figure 3-8(a)** presents the schematic illustration of typical primary-secondary crack configuration. To reveal detailed relationships between the fatigue crack

propagation and the grain boundaries as well as α' - δ phase boundaries, EBSD analysis was performed on the microstructure near the secondary cracks. In fact, due to the fact that it is difficult to characterize the crack growth behavior when the specimens is fractured, investigations on the secondary cracks behavior were necessary. Inverse pole figure maps are provided in **Figure 3-8(b)-(e)**. Small, string-like “grains”, as marked by black ellipses, are visible in these maps, which resemble the morphology of the δ phase observed in **Figure 3-6**. The examined secondary crack appeared in the transition between the Mode I (horizontal portion) and Mode II regimes of the primary crack (bold solid line in **Figure 3-8(a)**).

At its early stage, the secondary crack is mostly transgranular, although the grain boundaries have clearly influenced the path of the crack, as evident by the evident turns of cracks along the grain boundaries at the locations marked by black arrows in **Figure 3-8(b)**. The red arrow also indicates the location of a possible δ -phase, which suggests that the crack may have been propagating along the α' - δ phase boundaries. As its later stages, the secondary crack appears to have propagated through grains but more along grain boundaries (shown in **Figure 3-8(c)-(e)**). For instance, in **Figure 3-8(c)**, the crack between the two black arrows tied by a dashed line, is along a grain boundary, while other portions seem to be transgranular. Similar crack propagation behavior is seen in **Figure 3-8(d)** (marked by a black arrow) and **Figure 3-8(e)** (marked by arrows tied by dashed lines).

3.4.2.2. CA-H900 17-4 PH SS CT specimens

Figure 3-9(a) displays the microstructure of CA-H900 in higher magnification. As seen, the microstructure is finer as compared to the one for H1025 L-PBF 17-4 PH SS. This is due to the primary solution heat treatment step (i.e. CA) in which fine austenite

grains revert from martensite and then transform to fine martensite in the subsequent cooling step. Moreover, **Figure 3-9(b)** shows the δ -ferrite strings indicated with red arrows on the grain boundaries. It can be observed that δ -ferrite strings are also fine and uniformly distributed through the microstructure. Since the alloy is in the austenite region at 1050 °C (**Figure 3-2(c)**), prior δ -ferrite strings may have fully transformed to austenite during CA. New δ -ferrite then nucleated and formed on the grain boundaries during the cooling step.

Figure 3-10 compares the FCG rate of the L-PBF 17-4 PH SS CT specimens (set 1 and set 2) with the one of the wrought counterpart, all heat treated utilizing CA-H900 procedure. As seen from this figure, the wrought material exhibited superior crack growth resistance in the near threshold regime. Interestingly, FCG rates of L-PBF 17-4 PH SS and wrought materials in the Paris regime are similar. There is also an insignificant variation in FCG rate of L-PBF set 1 and set 2 specimens in this regime, which is attributed to the homogenous fine microstructure obtained through CA-H900 heat treatment procedure, as shown in **Figure 3-4(b)**. In addition, the employed heat treatment procedure should have removed any residual stresses induced from the L-PBF process.

Increased levels of variability were observed for data collected at both lower and higher ΔK levels between L-PBF 17-4 PH SS CT specimens and wrought counterparts. This is commonly observed [104] when microstructural features begin to exert more influence. It can be seen from **Figure 3-4(b)** that microstructure of L-PBF 17-4 PH SS is finer than that of wrought counterpart in **Figure 3-4(c)**. As the spacing of grain boundaries are shorter in the case of finer grains as compared to that of coarser grains, microstructurally short crack may propagate faster [92]. Additionally, the wrought material exhibited more resistance in the instability region as compared to the L-PBF one, which

may imply a higher cyclic fracture toughness for the wrought 17-4 PH SS. The finer microstructure of L-PBF 17-4 PH SS may have reduced its fracture toughness compared to the wrought material containing coarser grains [105]. The presence of pores in the L-PBF material could also have a detrimental effect on the fracture toughness [86].

3.4.3. Fractography

To further understand the crack growth behavior in L-PBF 17-4 PH SS, the fracture surfaces of some CT specimens from each heat treatment condition were analyzed. **Figure 3-11** and **Figure 3-12** show the fracture surfaces of L-PBF 17-4 PH SS CT specimens subjected to H1025 heat treatment procedure from set 1 and set 2, respectively. In general, the fracture surfaces of the H1025 heat treated CT specimens are a mixture of transgranular and intergranular fracture. The fractography for a CT specimen from set 1, where crack is parallel to the build direction (see **Figure 3-5(a)**), is shown in **Figure 3-11**. Clear evidence of brittle fracture characterized by large area fractions of cleaved facets decorated by river marks are noticeable in this figure (indicated by red arrows). The fracture surface contains substantial fraction of area with tortuous features, as marked by the white arrows. This indicates the involvement of grain boundary fracture associated with the δ -phase on the grain boundaries [95]. A typical region of the fracture surface of this specimen, revealing details of the cleavage and grain boundary/ δ -phase fracture (indicated by white arrows in **Figure 3-11**), has been magnified and provided on the right-hand side.

Similar fracture characteristics in **Figure 3-12** can be observed for specimens from set 2, where the crack deviated from the loading plane and propagated out of mode I (see **Figure 3-5(b)**). Interestingly, the area fraction of the tortuous features varies as a function of crack orientation. The unique fracture behavior in L-PBF CT specimens from set 2 may

be ascribed to the alignment of the columnar grains coexisting with string-like δ phases, with respect to the initial direction of FCG (i.e. notch orientation).

Shown in **Figure 3-12(b)** is the fracture surface at location 1, which was comprised mostly of cleavage facets with very little tortuous features. In the initial stage (as illustrated by the insets in **Figure 3-12(a)**), the crack mainly proceeded in a transgranular fashion; consequently, very small fraction of the fracture surface involves grain boundary/ δ -phase fracture. This FCG mode, i.e. transgranular dominated, may be associated with relatively high resistance. As discussed before, the grain boundaries as well as the α' - δ phase boundaries may possess reduced tensile strengths. Therefore, the crack gradually re-orientes to be parallel to the long axis of the columnar grains to propagate with less energy. The fracture surface in this stage (at location 2) reveals substantially higher fraction of grain boundaries/ δ -phase induced fracture, as shown in **Figure 3-12(d)**.

To better observe fracture mechanisms, the fracture surface contrasts for both locations have been enhanced and provided in **Figure 3-12(c)** for location 1, and **12(e)** for location 2. The enhanced images accentuate the tortuous, grain boundary/ δ -phase like features with light gray, while suppressing other regions with dark gray. The comparison made here for H1025 L-PBF 17-4 PH SS between location 1 (**Figure 3-12(c)**) and location 2 (**Figure 3-12(d)**) is qualitatively in agreement with the observations made by EBSD analyses on the secondary crack, presented in **Figure 3-8**. As is evident in this comparison, this FCG mode involves a substantially higher contribution of intergranular or δ -induced fracture and may be associated with them being brittle and having relatively low fracture resistance (i.e. reduced tensile strength). Therefore, the unique crack deviation behavior

observed in H1025 L-PBF 17-4 PH SS CT specimens may be a result of cracks seeking paths with least resistance.

Fracture surfaces of selected CA-H900 L-PBF 17-4 PH SS CT specimens (L-PBF-1a from set 1 and L-PBF-2a from set 2 in **Table 3-3**) have also been examined and shown in **Figure 3-13**. The fracture surfaces of these specimens display two distinct regions, i.e. a smoother region, which is evident for stable fatigue crack propagation, and a rougher region, which is formed by the final fracture. Fractography was performed on both regions of each specimen set (i.e. sets 1 and 2). The fatigue propagation path of the specimen L-PBF-2a revealed substantially more pores than specimen L-PBF-1a. Pores are shown by arrows in **Figure 3-13** (a) and (c). This may be due to the fact that for L-PBF-2a, the notch orientation is parallel to the orientation of the consecutively deposited layers (see **Figure 3-1(b)**), and that the pores predominantly form near the interlayer fusion regions. The higher population of pores on the fracture surface of specimen L-PBF-2a did not significantly affect the FCG behavior as compared to the L-PBF-1a specimens in **Figure 3-13**.

In addition, comparing **Figure 3-11**, **Figure 3-12** (H1025) and **Figure 3-13** (CA-H900), the fracture surface of the CA-H900 specimen seems to be slightly rougher (note the difference in scale bars in **Figure 3-11**, **Figure 3-12** (H1025) and **Figure 3-13** (CA-H900)). This may be attributed to FCG through the uniformly distributed δ -ferrite strings on the grain boundaries, shown in **Figure 3-9**. Nonetheless, the overall features of the fractures surfaces, both the initial FCG region (**Figure 3-13**(a) and (c) and the final fracture region (**Figure 3-13**(b) and (d)) appear to be quite similar, which explains similarity in the FCG behavior observed between CA-H900 specimen sets 1 and 2 in **Figure 3-10**. In

addition, although the final fracture regions of the CA-H900 specimens appearing slightly smoother than those of H1025 specimens, they do share the similar morphology as H1025 specimens, i.e. a combination of transgranular (flat facets with river marks) and intergranular (torturous regions) features.

3.5. Conclusions

Microstructure-related FCG behavior of L-PBF 17-4 PH SS was investigated in the present study. Two different heat treatments were applied, and the crack growth mechanism was characterized in correlation with the notch orientation. The following conclusions can be drawn based on the observations and analysis:

1. L-PBF 17-4 PH SS heat treated at 552 °C for four hours, i.e. H1025 condition, resulted to premature crack formation for specimens with the notch parallel to the build direction (set 1) during heat treatment. This is attributed to the segregation of elements to the grain boundaries, which are parallel to the notch orientation, as well as the presence of δ -ferrite on grain boundaries.
2. For H1025 specimens with the notch perpendicular to the build direction (set 2), crack initially propagated in mode I and turned to mode II, i.e. parallel to the build direction, as it continued to grow. This behavior indicates the crack's tendency to propagate along the columnar grain boundaries due to the weak interface of δ -ferrite and martensite.
3. The wrought 17-4 PH SS in CA-H900 exhibited a better fatigue crack growth resistance in the near threshold regime as compared to the L-PBF counterpart. However, L-PBF and wrought 17-4 PH SS CT specimens in CA-H900 had a similar fatigue crack growth behavior in Paris regime irrespective of the notch orientation.

4. A notch orientation independency for fatigue crack growth behavior was seen in L-PBF CT specimens heat treated under CA-H900 procedure. In addition, the fracture surfaces were rougher than those of heat treated under H1025 procedure. This is attributed to the fatigue crack propagation through finer and more uniformly distributed δ -ferrite on the grain boundaries of CA-H900 L-PBF 17-4 PH SS material.
5. EBSD and fractography analysis revealed the crack to seek the path of least resistance provided by δ -ferrite/martensite interfaces in grain boundaries of H1025 CT specimens. Accordingly, the mostly transgranular crack growth behavior altered to a mixed mode of transgranular + intergranular crack propagation as the crack deviated to mode II following the columnar grains elongated perpendicularly with respect to notch orientation.

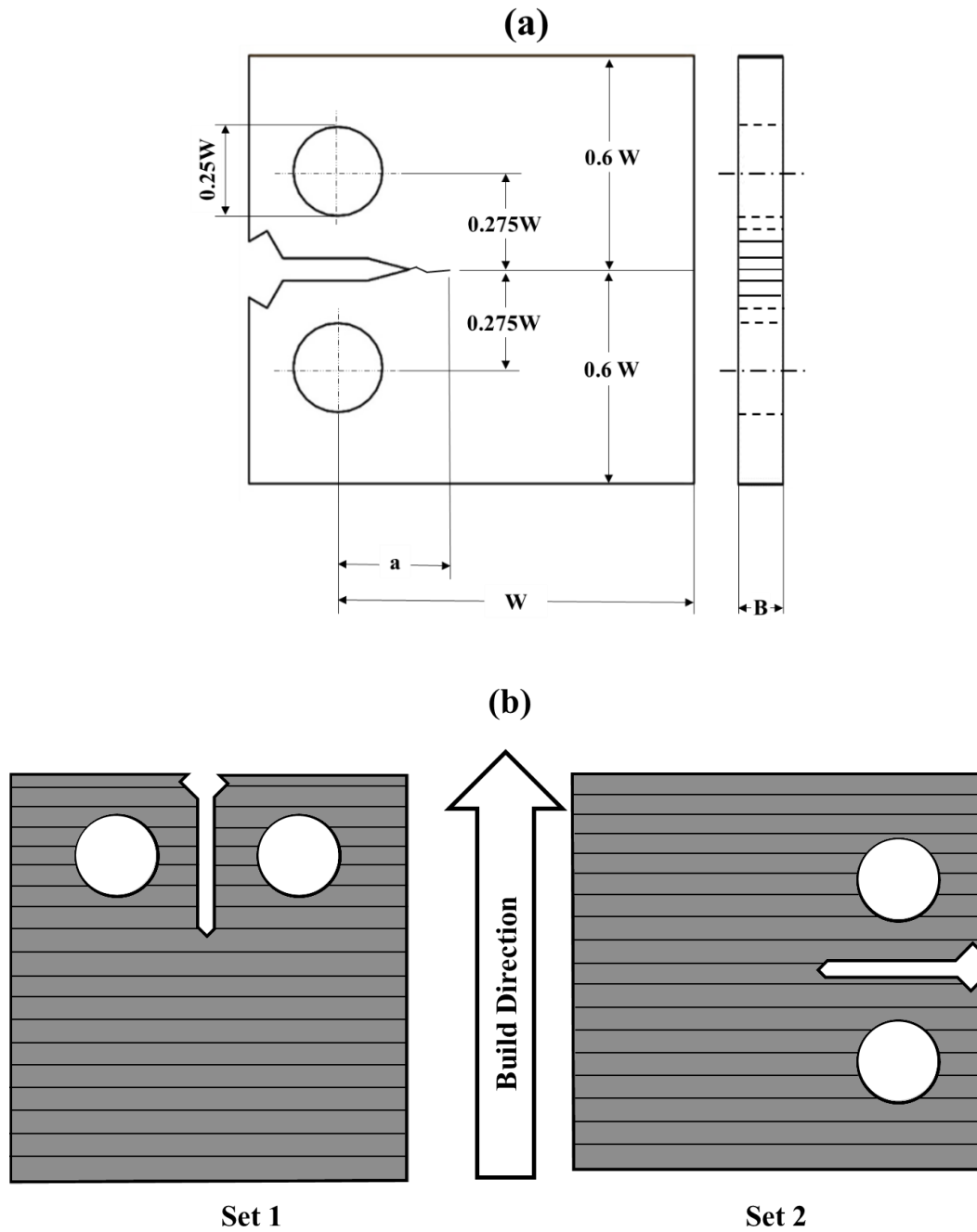


Figure 3-1. (a) Drawing of machined CT specimens based on ASTM E647 [98] and, (b) schematic of two groups of specimens with different notch direction relative to the building direction; set 1 and set 2 have notch direction parallel and perpendicular to the build direction, respectively.

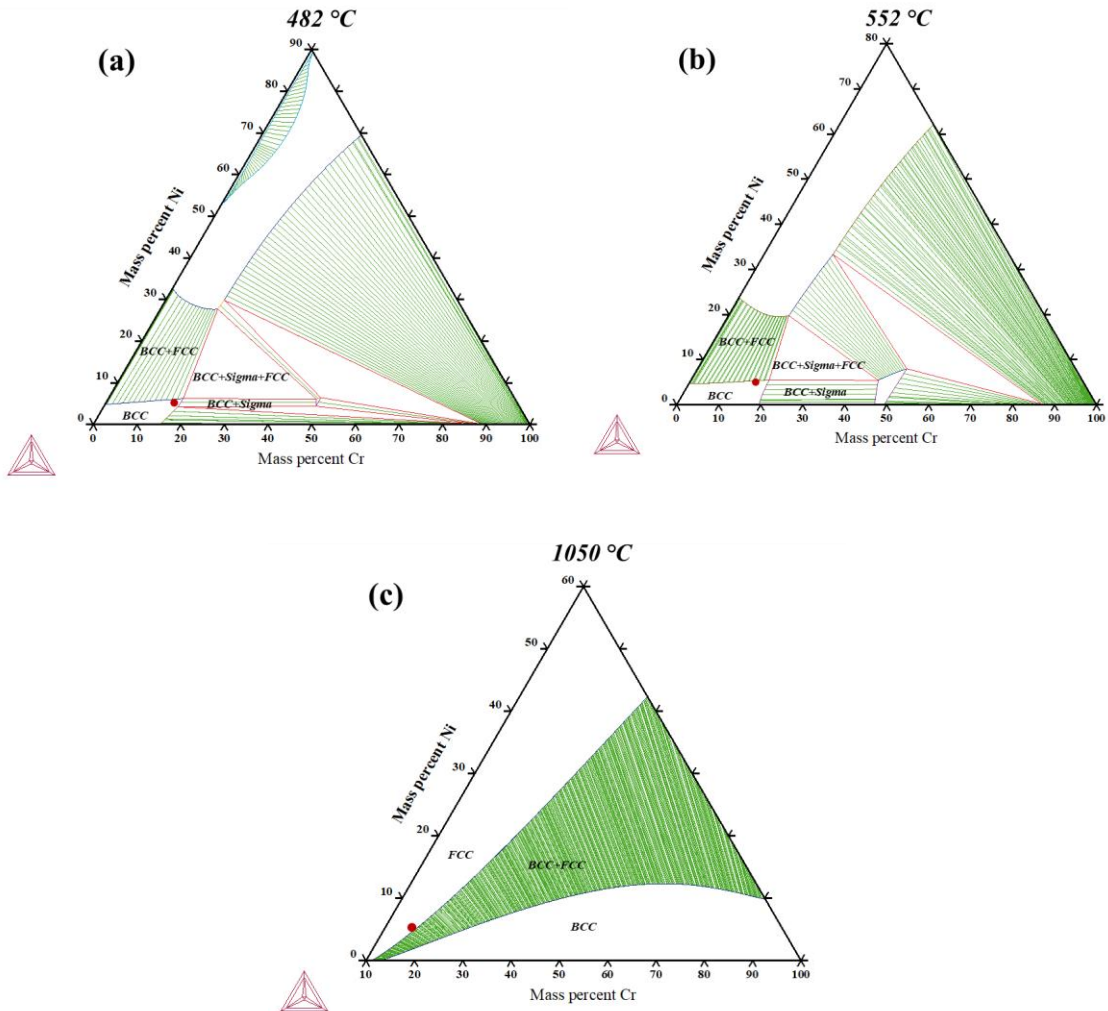


Figure 3-2. Ternary phase diagrams generated using Thermo-Calc. software cross sectioned at different temperatures: (a) 482 °C (i.e., H900), (b) 552 °C (i.e. H1025), and (c) 1050°C (i.e. CA).

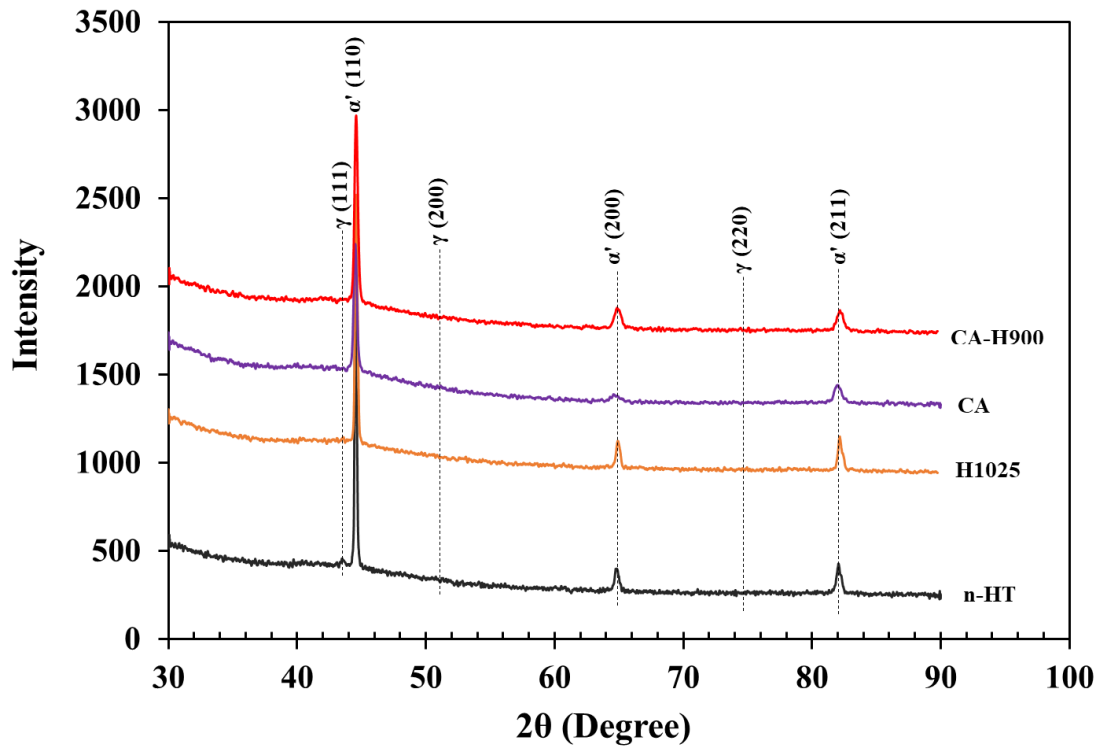


Figure 3-3. X-ray diffraction (XRD) analysis of non-heat treated (n-HT) and heat treated specimens.

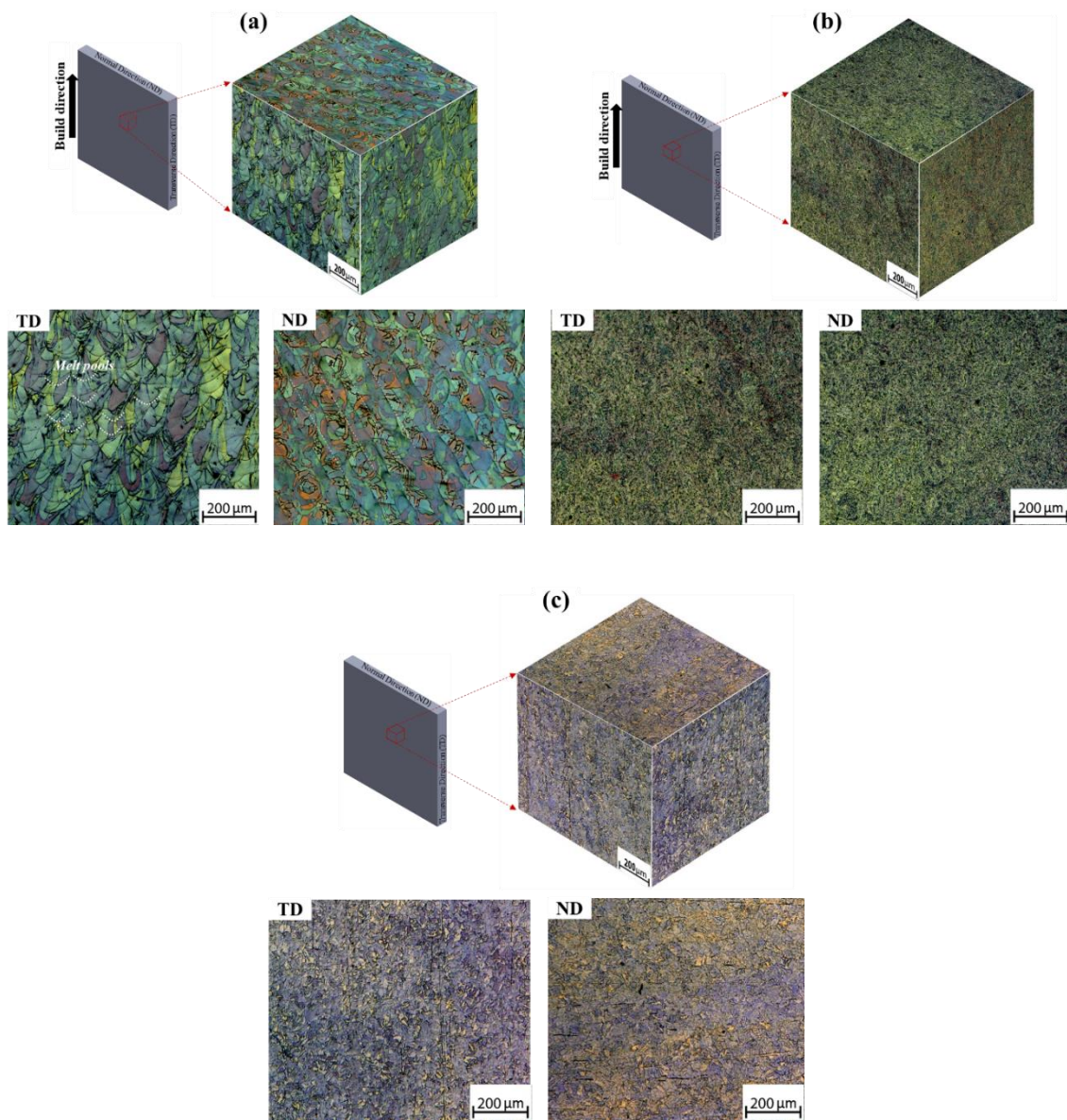


Figure 3-4. Optical micrograph of 17-4 PH SS microstructure in different heat treatment conditions; (a) L-PBF H1025, (b) L-PBF CA-H900, and (c) wrought CA-H900.

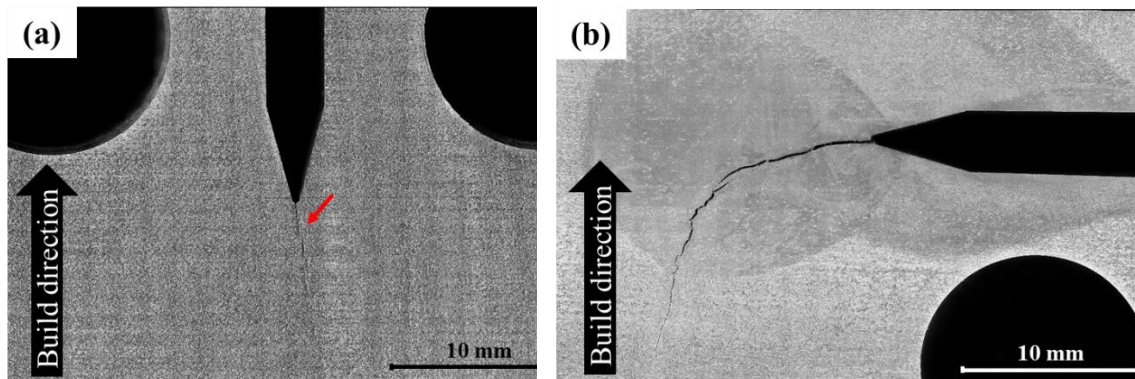


Figure 3-5. Macro images of cracks in CT specimens subjected to H1025 heat treatment procedure; (a) set 1, and (b) set 2.

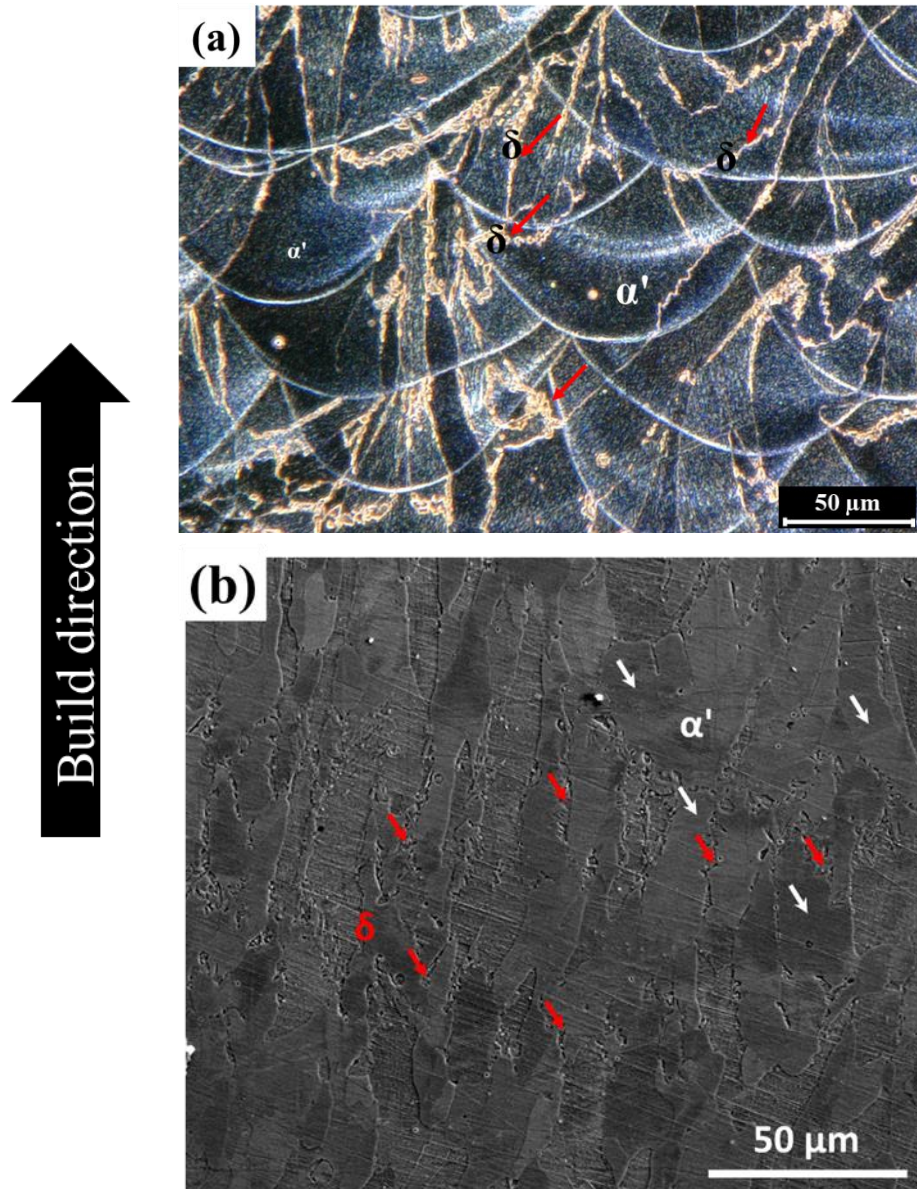


Figure 3-6. Microstructure of H1025 L-PBF 17-4 PH SS specimens showing the δ -ferrite strings on the grain boundaries; (a) an optical micrograph, and (b) an SEM micrograph.

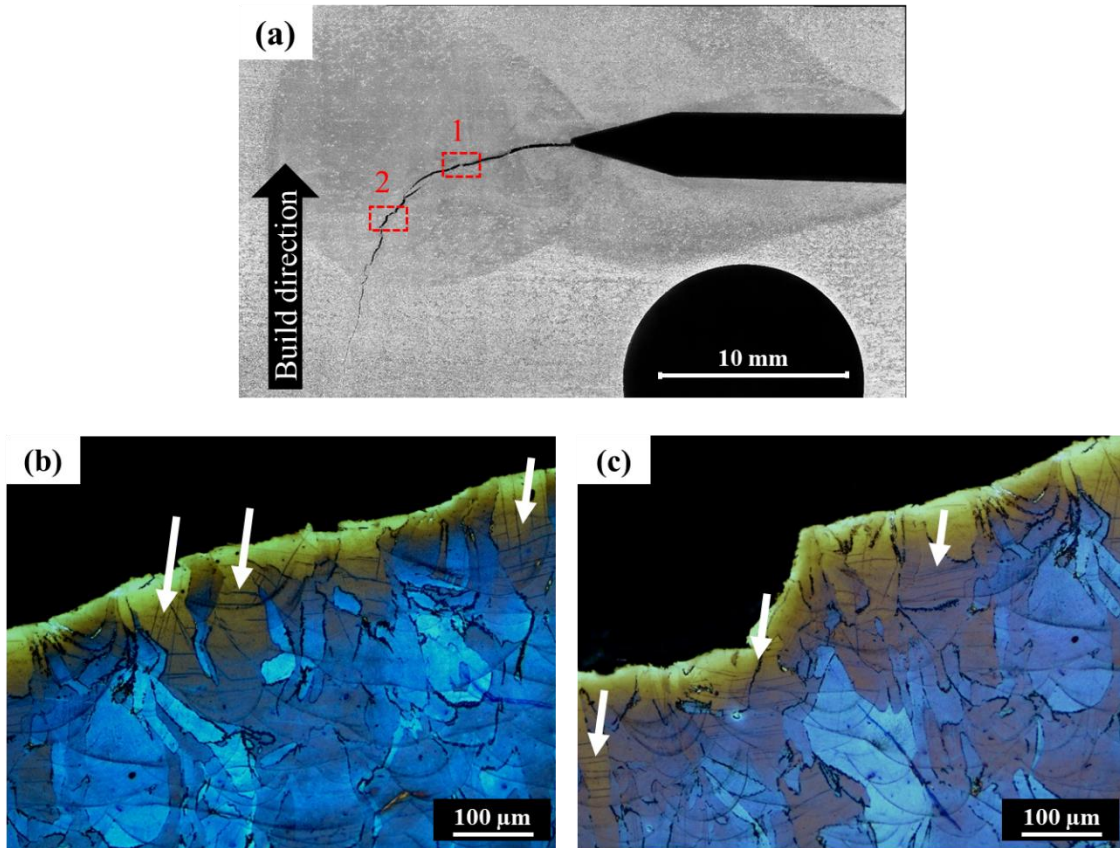


Figure 3-7. (a) Macro image of a specimen from set 2 subjected to H1025 heat treatment procedure showing locations 1 and 2, (b) microstructure at location 1, and (c) microstructure at location 2.

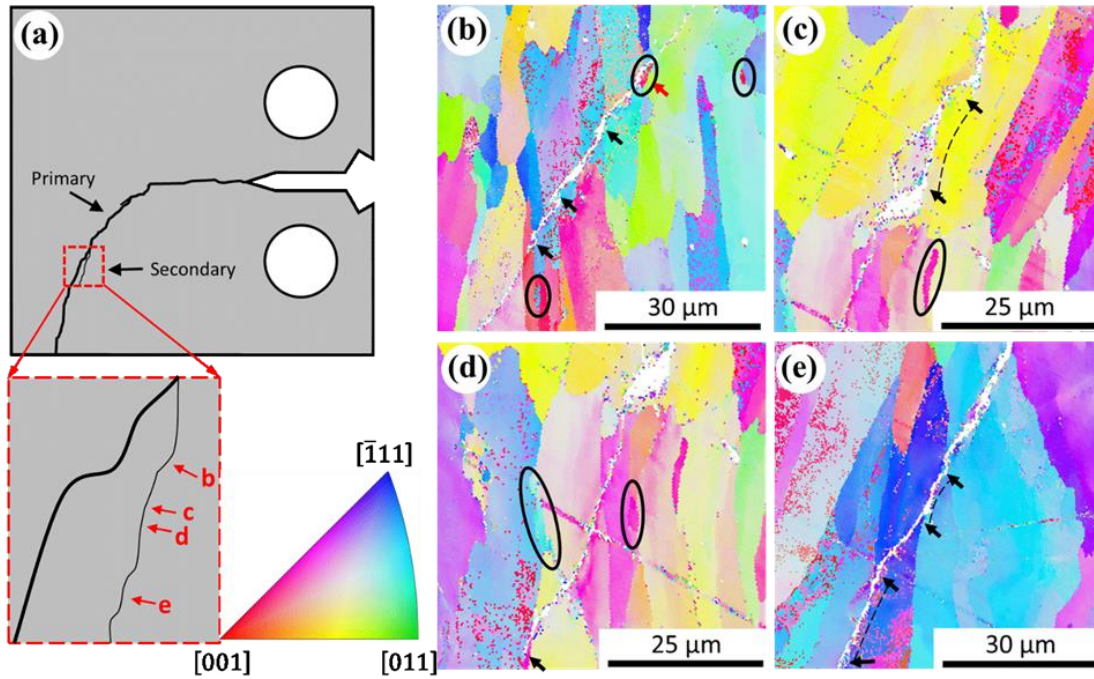


Figure 3-8. EBSD analysis on the microstructure near a secondary crack on a set 2 specimen; (a) shows a typical configuration between the primary and secondary crack, and (b)-(e) show the inverse pole figure maps of locations specified in (a). The inset shows the key to the inverse pole figure maps.

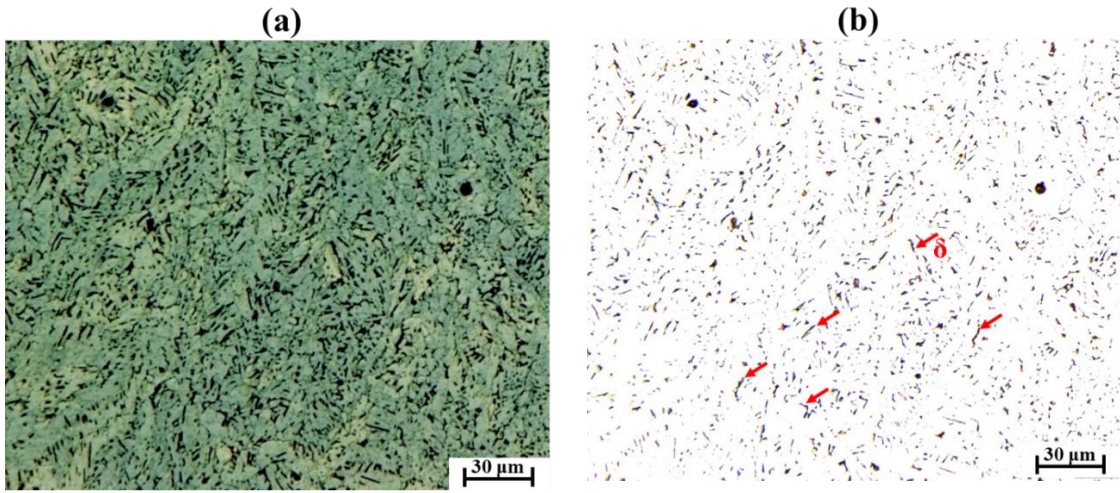


Figure 3-9. (a) Microstructure of CA-H900 L-PBF 17-4 PH SS, and (b) δ -ferrite strings in grain boundaries in black.

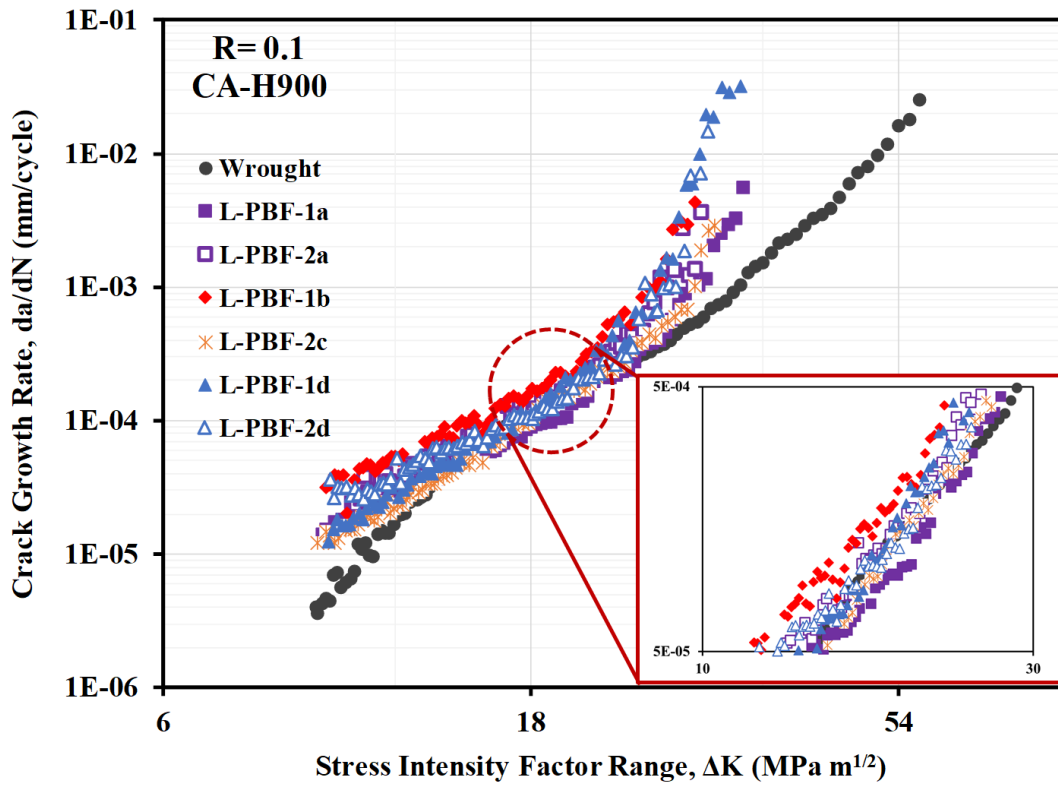


Figure 3-10. Fatigue crack growth (FCG) rate for L-PBF and wrought CT specimens subjected to CA-H900 heat treatment procedure.

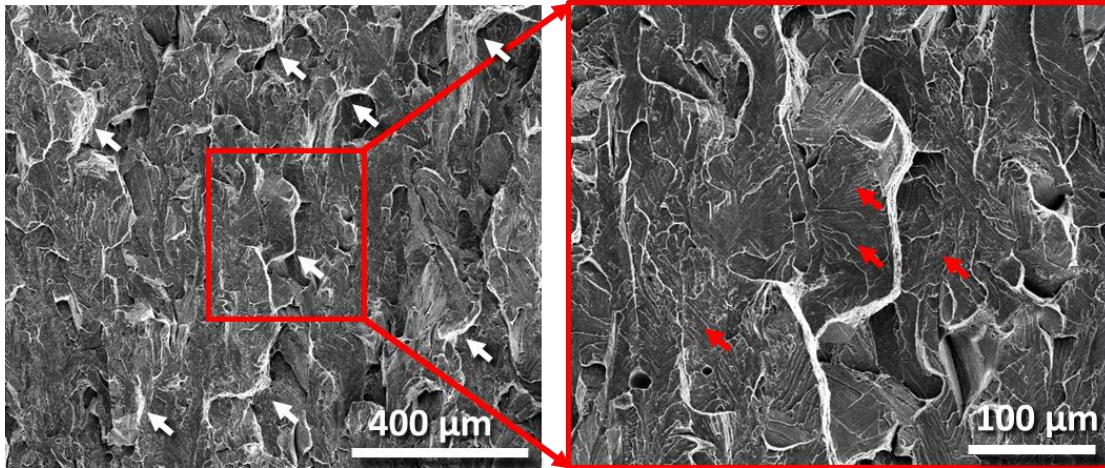


Figure 3-11. Fracture surface of an L-PBF 17-4 PH SS specimen from set 1 subjected to H1025 heat treatment procedure.

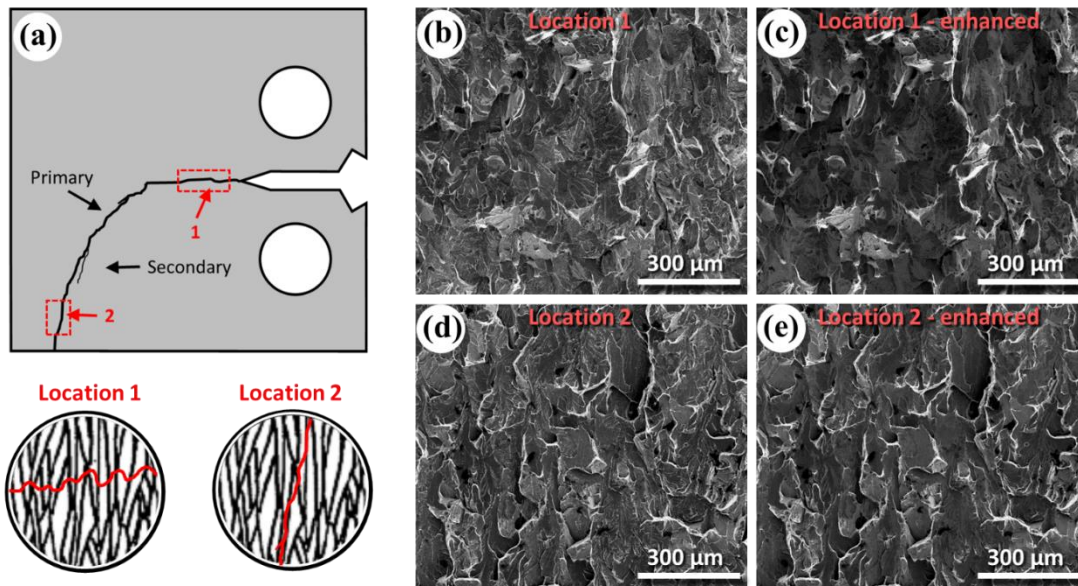


Figure 3-12. (a) Schematic of crack growth behavior through columnar grains at location 1 and location 2 of L-PBF 17-4 PH CT specimens from set 2 subjected to H1025 heat treatment procedure, (b) fracture surface image of location 1, (c) contrast enhanced image of location 1, (d) fracture surface image of location 2, and (e) contrast enhanced image of location 2.

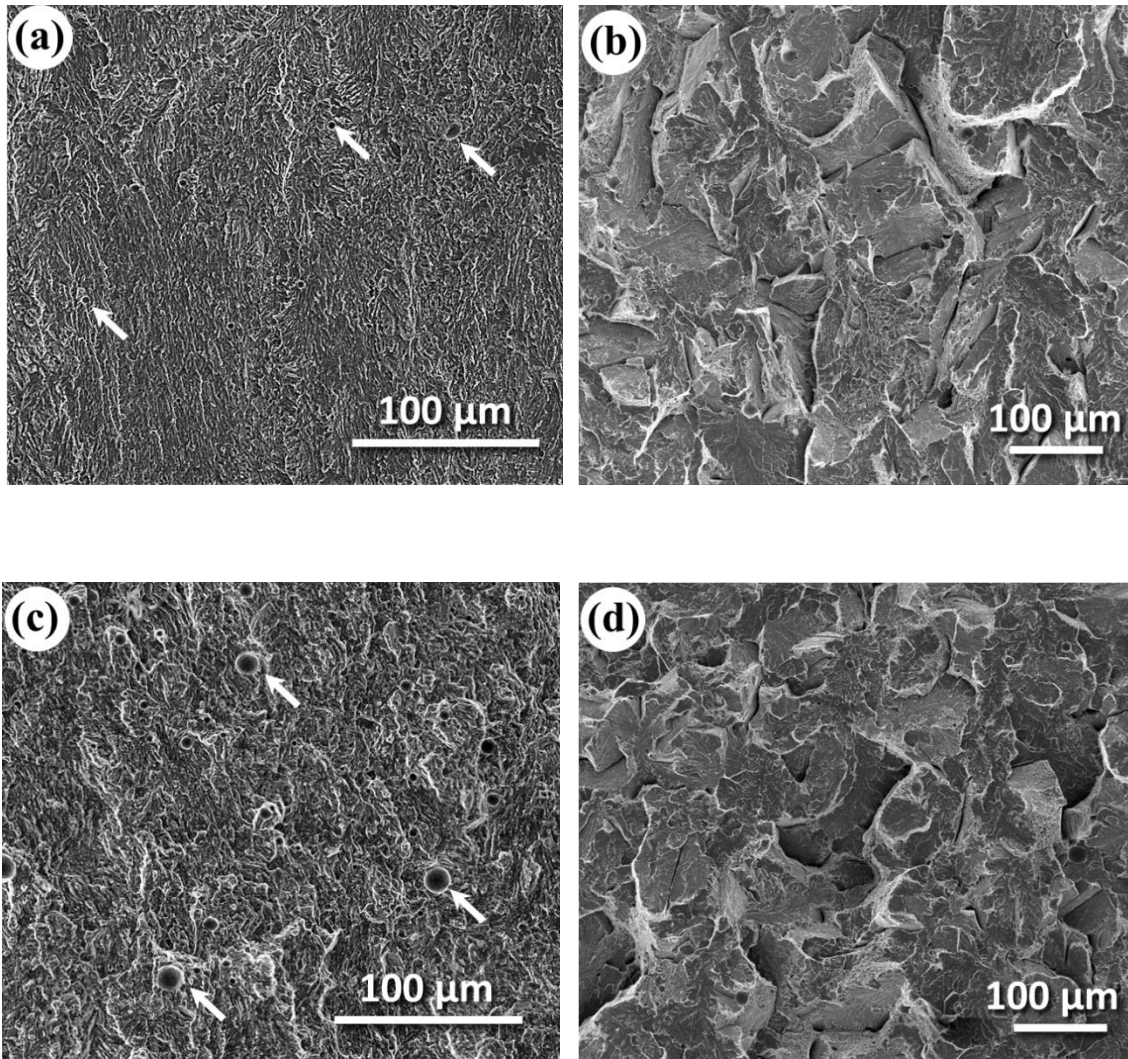


Figure 3-13. Fractography of L-PBF-1a from Table 3; (a) presents the stable FCG region, and (b) presents the final fracture region. Fractography of L-PBF-2a from Table 3; (c) presents the stable FCG region, and (d) presents the final fracture region.

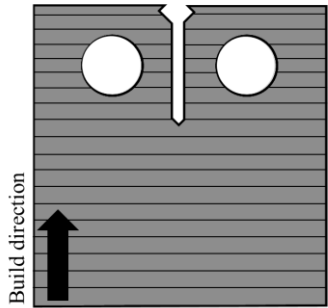
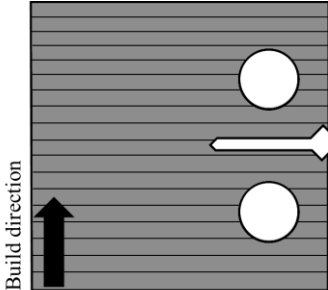
Table 3-1. Chemical composition of 17-4 PH stainless steel powder, provided by LPW Inc.

| | C | Cr | Ni | Cu | Mn | Si | Nb | Mo | N | O | P | S | Fe |
|----------------|----------|-----------|-----------|-----------|-----------|-----------|-----------|-----------|----------|----------|----------|----------|-----------|
| (Wt. %) | 0.01 | 15.6 | 4.03 | 3.89 | 0.24 | 0.29 | 0.33 | <0.01 | 0.01 | 0.05 | 0.004 | 0.003 | Bal |

Table 3-2. Recommended process parameters for 17-4 PH stainless steel provided by EOS.

| Laser power (W) | Scanning speed (mm/s) | Hatching distance (μm) | Stripe width (mm) | Layer thickness (μm) |
|----------------------------|----------------------------------|---|------------------------------|---|
| 220 | 755.5 | 100 | 100 | 40 |

Table 3-3. Heat treatment procedures applied to L-PBF and wrought 17-4 PH SS specimens.

| Specimen ID | Heat treatment | Notch orientation relative to the build direction |
|--|----------------|--|
| L-PBF-1a L-PBF -1b L-PBF -1c L-PBF -1d | CA-H900 | <p style="text-align: center;">Set 1</p>  |
| L-PBF -1e L-PBF -1f L-PBF -1g | | |
| L-PBF -2a L-PBF -2b L-PBF -2c L-PBF -2d | CA-H900 | <p style="text-align: center;">Set 2</p>  |
| L-PBF -2e L-PBF -2f L-PBF -2g | | |
| Wrought | CA-H900 | N/A |

**CHAPTER 4: IMPROVED HIGH CYCLE FATIGUE PERFORMANCE OF
ADDITIVELY MANUFACTURED 17-4 PH STAINLESS STEEL VIA IN-
PROCESS REFINING MICRO-/DEFECT-STRUCTURE**

The following chapter has passed rigorous peer-review process and has been published in Additive Manufacturing in 2020.

Nezhadfar, P. D., Kathryn Anderson-Wedge, S. R. Daniewicz, Nam Phan, Shuai Shao, and Nima Shamsaei. "Improved high cycle fatigue performance of additively manufactured 17-4 PH stainless steel via in-process refining micro-/defect-structure." Additive Manufacturing 36 (2020): 101604.

4.1. Abstract

The usage of an appropriate shield gas for laser beam powder bed fusion (L-PBF) of the popular 17-4 precipitation hardened (PH) stainless steel (SS) has long been debated in the additive manufacturing (AM) community. While the inertness of Ar is often desirable as the shield gas from unwanted chemical reactions, its low solubility combined with the violent nature of the melt pool inevitably results in the formation of defects that are detrimental to the fatigue performance of the alloy. On the other hand, although N₂ is reactive with some alloys (e.g., titanium), it may have remarkable favorable effects on the mechanical properties and fatigue performance of 17-4 PH SS. In this article, the advantageous effects of N₂ as an in-process micro-/defect-structure refiner of L-PBF 17-4 PH SS, and in turn, an enhancer of its mechanical/fatigue properties are demonstrated. It is shown that, compared to Ar, the use of N₂ shield gas induces more retained austenite, refines grains, makes the melt pools deeper, produces fewer and smaller pores, and as a result, slightly improves tensile properties, moderately improves crack growth resistance, and considerably improves axial fatigue properties in the high cycle regime.

4.2. Introduction

The Fe-17Cr-4Ni-4Cu precipitation-hardening (PH) stainless steel (SS), often dubbed as 17-4 PH SS, is a martensitic hardenable SS with a desirable combination of strength, ductility, fatigue strength, fracture toughness, and high corrosion resistance, depending on the post-manufacture heat treatment applied. This cost-effective SS often finds use in key engineering, defense, and energy sectors [6]. Additive manufacturing (AM) is advantageous over conventional subtractive manufacturing techniques in applications requiring the fabrication of near-net shaped parts with more complex geometries [1]. Therefore, there is a strong incentive in the industry to adopt AM in the fabrication of 17-4 PH SS parts to further benefit from this material's appealing properties.

The repetitious melting-solidification cycles inherent to typical AM processes result in elevated defect content and complex microstructure that are difficult to remediate and hard to predict [7,8]. The defects serve as stress risers and compromise mechanical performance, especially in fatigue critical applications [9]. Such defects include volumetric ones, e.g. gas entrapped pores and lack-of-fusion (LoF) defects, and surface roughness, with the latter being very detrimental to the fatigue performance of additively manufactured (AM) parts in their as-built surface condition [15]. Further, the variability in defects' morphology, population, and distribution as well as the surrounding microstructure, exacerbate the uncertainty in the fatigue performance of AM parts [10,11]. While the goal to fabricate high-density components eliminating the occurrence of defects may be desirable, these imperfections may be inherent to the AM processes and persist even under the most optimum operating conditions. Given this inevitability, establishing the process-structure-property-performance relationships is therefore essential to expedite

the adoption of AM (such as laser beam powder bed fusion (L-PBF) method) 17-4 PH SS [4,12].

As in the case for all AM metallic materials, the microstructure and defect characteristics in AM 17-4 PH SS (which govern their mechanical performance) are dictated by the solidification dynamics and thermal history. For instance, porosities are formed due to the gas entrapment in the melt pool as a result of a high cooling/solidification rate [1]. Indeed, owing to heat accumulation (thus larger melt pools and longer solidification time for gas bubbles to escape), porosity levels were shown to decrease in larger L-PBF 17-4 PH SS components [13]. The LoF defects are formed when there is an insufficient melt pool overlap either between layers, or between intralayer tracks [13,14], which can be affected by the changes in the part geometry, manufacturing process parameters, etc.

As for microstructure, although the stable phase at room temperature is body centered tetragonal (BCT) martensite, the as-fabricated 17-4 PH SS via L-PBF may include a martensite (~60-90%) + austenite (~10-40%) phase composition [15,16]. This is generally due to the compositional heterogeneity (especially the distribution of austenite stabilizer elements such as Ni, Cu, Mn, etc.) induced by rapid solidification. The tetragonality of the BCT lattice is closely related to the carbon content, i.e. $c/a = 1 + 0.046C$, where C is in wt.%. In the case of 17-4 PH SS, as the carbon content is extremely low—0.01%, the lattice is often reported as body centered cubic (BCC) [17].

In the microstructure typically reported in the literature for L-PBF 17-4 PH SS, the morphology of the as-solidified, columnar prior- δ grains are visible [18]. In fact, the well-known lath morphology of the martensite phase is not obvious and the microstructure is

sometimes reported as ferritic microstructure (by-passing the formation of austenite, and therefore, absence of martensite) [18]. Many studies reported that a heat treatment at 1050°C for 30 min can fully homogenize the composition (reaching Condition A) and, if low-temperature aging is followed, can lead to a relatively uniform, fully martensitic microstructure [15,19]. However, this heat treatment cannot alter the prior- δ morphology, and, upon over-aging, the austenite tends to nucleate at the prior- δ grain boundaries [20]. The parameters whose influence on AM materials' microscopic features, and consequent mechanical properties have been studied so far include powder condition (i.e. chemical composition [22], recyclability [23,24] atomization media [25]), process parameters [27], geometry and size of the parts [13,29], and post processing [15].

Shield gas is another process parameter that can significantly impact the solidification and thermal history of AM SSs and was found influential in altering the microstructure as well as porosity levels of materials [63,106–108]. The appropriate shield gas for L-PBF 17-4 PH SS is perhaps among the most debated topics in the AM community [64,71,107]; however, mostly focusing on the static mechanical properties such as hardness and tensile strength. The most popular shield gas types for the L-PBF 17-4 PH SS appear to be Ar and N₂ [26]. However, systematic investigations regarding the process-structure relationships seem to exist predominantly in research related to laser welding, which has an affinity to laser AM [109–111]. Relevant knowledge (K) in the area can be summarized below:

K1) Compared to Ar, N₂ has good solubility in molten high-Cr SS (3.4×10^{-5} wt. %), and the large (mm sized) N₂ bubbles, formed during laser welding, can be dissolved

quickly (within 30 μ s) into the melt pool [112]. Utilization of N_2 , therefore, reduces the tendency for porosity formation [112,113].

K2) Dissolved N in the steel, which tends to exist as interstitial atoms in the octahedral site of a face center cubic (FCC) parent lattice [114], is a potent austenite stabilizer [16]. Indeed, N_2 has been reported to accelerate the ferrite to austenite phase transformation during solidification resulting in less δ -ferrite retained in the microstructure [109,115]. In addition, N-doped alloys can overcome the strength-ductility trade-off due to the capability of N element to produce hierarchical, heterogeneous fine-grain microstructure [116].

K3) In response to fiber laser excitation (wavelength $\sim 1 \mu$ m, a popular wavelength among metal AM machines), stainless steels typically produce similar weakly ionized metal plumes under the shielding of either Ar or N_2 gases [117,118]. When the shield gas flow is inadequate, the laser is significantly attenuated by the plume [106]. On one hand, the laser attenuation reduces the direct energy input to the melt pool, which can alleviate the formation of keyholes. On the other hand, the laser attenuation in the plume heats the shield gas, which can serve to heat the materials/powder around the melt pool, and as a result, lead to larger melt pools and reduced gas entrapped pores.

K4) N_2 has higher thermal conductivity ($\sim 40\%$ higher) and molar heat capacity (50% higher) as compared to Ar [26,119]. Assuming the same flow rate for N_2 and Ar gases, on one hand, this results in a more efficient convection heat transfer between the melt pool and N_2 shield gas and a higher cooling rate [26]. On the other hand, such properties of N_2 favor the heat transfer from the metal plume to the shield gas

(see K3), which then releases the absorbed energy to the surrounding surface [118,120]. N₂ shield gas can, therefore, lead to a higher laser energy absorption, and as a result, formation of larger melt pools, better overlap of the melt pools in subsequent layers as well as the adjacent tracks within a layer. This should reduce the formation tendency for LoF defects.

K5) During L-PBF, N₂ gas reacts with Cr in the molten metal and forms Cr₂N nano-precipitates, which has been well known to serve as a strong inhibitor of grain growth [121–123]. These nano precipitates may also serve as heterogeneous nucleation sites for solid phase during solidification [116]. Therefore, the microstructure of L-PBF 17-4 PH SS specimens fabricated under N₂ atmosphere is anticipated to be finer compared to the ones under Ar.

Given the facts listed above, N₂ shield gas may be an appealing candidate for L-PBF 17-4 PH SS to realize in-process refinement of microstructure and defects, leading not only to better static mechanical properties, but also enhanced fatigue performance. Fatigue damage of materials commonly occurs in three main stages: I. crack initiation, II. crack propagation, and III. final fracture. Fatigue behavior of materials, depending on the applied stress levels, can be roughly divided into two regimes, i.e. low cycle fatigue (LCF) regime ($N_f < 10^4$ cycles), and high cycle fatigue (HCF) regime ($N_f > 10^5$ cycles).

In the LCF regime, fatigue life is dominated by crack propagation (Stage II) which is strongly influenced by the amount of crack-tip plastic deformation [9,124]. The anticipated improvements in ductility (due to higher retained austenite content and less internal defects) afforded by the utilization of N₂ shield gas as opposed to Ar, may improve the crack growth resistance of the L-PBF 17-4 PH SS. Increase in strength without sacrifice

in ductility, in other words, increase in tensile toughness, is known to improve the fracture toughness of materials that undergo ductile failure [124]. In the HCF regime, the fatigue life is governed by the initiation of fatigue cracks, which is strongly influenced by the presence of defects (including gas entrapped pores and LoF defects) for machined 17-4 PH SS [13]. As N_2 tends to reduce the defect levels, the N_2 shielded L-PBF 17-4 PH SS, is expected to outperform their Ar shielded counterparts in HCF regime.

The present study attempts to achieve the in-process refinement of microstructure and defects in L-PBF 17-4 PH SS via the use of N_2 shield gas as an alternative to Ar, and, through which, demonstrate an enhanced fatigue performance. The authors also aim to shed light on the effect of shield gas types, N_2 versus Ar, on the microstructure, porosity state, melt pool geometry, and their consequent results on the fatigue performance of L-PBF 17-4 PH SS. For the first time to the authors' knowledge, the effect of shield gas type on the fatigue crack initiation and growth behavior of L-PBF 17-4 PH SS is revealed. This article is organized as follows: in Section 2, the experimental design of this study is delineated in detail. In Section 3, the experimental results, including microstructural (Section 3.1) and mechanical (Section 3.2) properties, are presented along with their immediate observations. The findings of this study are further discussed in section 4, where the observed variations in fatigue behaviors due to the utilization of N_2 shield gas, as opposed to Ar, are attributed to microstructural and defect characteristics. Finally, conclusions are drawn in Section 5.

4.3. Experimental Procedures

4.3.1. Material and Specimen Fabrication

The chemical composition of 17-4 PH SS powder used in this study is listed in **Table 4-1**. The pre-alloyed and argon-atomized powder was provided by LPW Technology Inc. with the powder particle size within the range of 15-45 μm .

An EOS M290 machine (an L-PBF system) with 400 Watt Yb (Ytterbium) fiber laser and with a wavelength of 1060 nm was utilized to fabricate all 17-4 PH SS specimens. The employed main process parameters for fabricating 17-4 PH SS under Ar shield gas suggested by EOS are listed in **Table 4-2**. To understand the effect of shield gas type, the same process parameters were used to fabricate parts under N_2 shield gas. It is worth noting that the gases' flow rate was the same for both shield gases, and the scan strategy utilized was a conventional parallel scan with a 67° interlayer rotation.

The design of experiment is detailed in **Table 4-3**. Two sets of $11.5 \times 11.5 \times 77$ mm square bars were fabricated in the vertical direction and machined to the round axial fatigue specimens with a uniform gage section, shown in **Figure 4-1(a)**. All the machined specimens were further hand polished to remove the machining marks and make the surface mirror-finished. The surface roughness of the gage section was measured after polishing to be $R_a = 0.93 \pm 0.24$ μm using Keyence VHX6000, a digital optical microscope. It must be mentioned that the tensile tests were performed using the same geometry. Two sets of walls with the dimension of $65 \times 6.5 \times 65$ mm were fabricated vertically and further machined by electrical discharge machining (EDM) into compact tension (CT) specimens in **Figure 4-1(b)**, following ASTM E647 standard [98]. For each type of specimens (i.e. axial fatigue

and CT), one set was fabricated under Ar shield gas (dubbed “Ar specimens”), and one set of specimens was fabricated under N₂ shield gas (dubbed “N₂ specimens”).

All the axial fatigue and CT specimens were subjected to CA-H1025 heat treatment (HT) procedure (solution heat treating at 1050 °C for 0.5 h followed by air cooling (Condition A, or CA), then aging at 552 °C for four hours followed by air cooling (H1025 [15]) utilizing a box furnace in an Ar atmosphere to prevent oxidation and surface decarburization. Some non-heat treated specimens were reserved for microstructural analysis and tensile tests to examine the as-fabricated properties. The gage section of all the fatigue specimens was further polished using P320-P4000 grit sandpapers to remove all the machining marks. To track each set of specimens throughout the article, figures, and tables, HT-Ar and HT-N₂ are the designations used for the heat treated, and NHT-Ar and NHT-N₂ are used for the non-heat treated specimens fabricated in Ar and N₂ atmospheres, respectively. Besides, the red color in figures is assigned to N₂ specimens and blue color represents Ar specimens.

4.3.2. Microstructure Characterization

To characterize the microstructure, samples were first cut from the gage section of the specimens parallel to the build direction. Specimen preparation and microstructural analysis were carried out based on the ASTM E3-11 standard [66]. For optical microscopy, the microstructure was revealed using Beraha’s tint reagent. Microstructural characterization and any measurement (i.e. pore size, melt pool size, grain size) were carried out employing Keyence VHX6000, a digital optical microscope, and a Zeiss Crossbeam 550 focused ion beam scanning electron microscope (FIB-SEM). The

microstructure also was studied using electron backscattered diffraction (EBSD) and electron channeling contrast imaging (ECCI).

4.3.3. Mechanical Testing

Tensile and uniaxial fully-reversed strain-controlled fatigue tests were conducted using an MTS landmark servohydraulic testing machine with 100 kN load cells. In order to measure the strain at the gage section, an MTS mechanical extensometer was utilized. Regarding the tensile tests, to avoid any damage to the extensometer which has a limited travel distance, tests were performed in two consecutive steps, i.e. a strain-controlled and displacement-controlled steps. Tensile tests were started first under strain-controlled mode up to a 0.045 mm/mm strain, paused to remove the extensometer, and then switched to displacement-controlled mode until fracture. For certainty of the results, two tensile tests were conducted for each condition, and the results were fairly consistent. It is worth noting that there were limited specimens available for the tensile testing, therefore, the average of the results is reported for comparison, not for being used in the design purposes.

Room-temperature, uniaxial fully-reversed ($R_{\square} = \square_{min}/\square_{max} = -1$) strain-controlled fatigue tests were performed based on ASTM E606 standard [65] at constant amplitude strain amplitudes within the range of 0.002-0.004 mm/mm. To maintain a similar average cyclic strain rate throughout all the tests, frequencies were attuned for each test based on the applied strain amplitude. A sinusoidal waveform was applied until failure (complete separation) or up to 10^7 reversals, which was considered ‘run-out’ in this study. It is worth noting that all strain-controlled fatigue tests were stopped after a few thousand cycles and switched to the force-controlled mode since no pronounced macroscopic plastic strain was observed during the fatigue tests performed in this study.

The low-stress fatigue crack growth (FCG) tests were carried out on CT specimens under load-control at room temperature with a sinusoidal loading waveform with a load ratio of $R = 0.1$ and frequency of $f = 10$ Hz until fracture. It is worth noting that there will not be a crack tip plastic zone size disparity to overcome since the pre-cracking loading was the same as the one applied for FCG rate testing. Load amplitudes ranged from 4275 N to 1575 N (the first test was started with higher load amplitude to initiate the crack, however, as the confidence was obtained that the crack would initiate, the load amplitude level was reduced for further tests). It is worth mentioning that the load ratio, R , remained constant ($R = 0.1$) for all the tests, therefore, change in the load amplitude should not have any influence on the FCG rate. FCG rate, da/dN , and stress intensity factor ranges, ΔK , were determined using the recorded crack mouth opening displacement (CMOD) values, load range, and the measured cycle count. Pre-cracking was conducted up to a length of 11-14 mm to achieve a corresponding initial ΔK value of approximately $10 \text{ MPa}\sqrt{\text{m}}$. To ensure the consistency of the results, FCG tests were repeated 3 times for each processing condition.

To study the factors responsible for fatigue crack initiation and failure mechanisms in L-PBF 17-4 PH SS specimens, fractography analysis was performed using SEM. Before fractography analysis, the fracture surfaces were cut using a precision cutter, sonicated in water and alcohol solution, and then washed using acetone to eliminate any moisture and dirt that may be present on the fracture surfaces.

4.4. Experimental Results

In this section, the experimental observations on the in-process induced microstructure and defects refinement in L-PBF 17-4 PH SS, and the related favorable

variations in mechanical properties, due to the use of N₂ as shield gas, are presented. Specifically, the effect of shield gas change from Ar to N₂ on the phase constituent (i.e. martensite, austenite, etc.), grain sizes, melt pool geometry (i.e. depth, and overlap depth), and porosity size and number are inspected. The resulting mechanical properties (i.e. tensile, FCG, and fatigue) of L-PBF 17-4 PH SS specimens are also presented. In this section, only the experimental results, and corresponding to which, the immediate observations and brief discussion are made. The relationships between the shield gas type and micro-/defect-structure, as well as the relationships between the micro-/defect-structure and mechanical properties, are formally established in Section 4.

4.4.1. Microstructural Observations

4.4.1.1. Grain Size, Morphology, and Phases

Figure 4-2 shows a schematic of an axial fatigue specimen and the sample for microstructure characterization cut from the gage section, which was cross-sectioned parallel to the build direction. The EBSD inverse pole figure (IPF) maps in the direction normal to the cross-sections (i.e., along the Z direction) for the non-heat treated specimens are presented in **Figure 4-2**. The apparent grain shapes on the cross-sections of both NHT-N₂ (**Figure 4-2(a)**) and NHT-Ar (**Figure 4-2(b)**) specimens are “U” shaped, dictated by the solidification history unique to track-by-track and layer-by-layer fabrication strategy in AM. In fact, the grains are grown epitaxially along the heat dissipation path, center of the melt pool, toward the build plate during fabrication [115].

It can be seen in IPF maps for both NHT-N₂ and NHT-Ar specimens that the grains appear to be randomly oriented (i.e., there is not any preferred grain orientation) and must be noted that they do not resemble the typical morphology of the lath martensite, albeit

martensite being the stable phase in the room temperature. According to Alnajjar et al. [18], these grains are δ ferrites, which could be the result of fast cooling. They reported that fast cooling through the γ -stable temperature range by-passes the γ phase and δ ferrite retains at room temperature. As expected, a small fraction (1 %) of retained austenite was detected by EBSD in the cross-sectioned plane of NHT-N₂ specimens (N is a strong austenite stabilizer as was mentioned in K2 in the introduction), while there was no retained austenite detected in NHT-Ar specimens. According to the Fe-Cr-N phase diagrams [125], the Cr concentration of 15.6 wt. % (**Table 4-1**), an increase of 50 ppm N in the material can stabilize the austenite in the microstructure. Therefore, using the N₂ shielding gas increases the possibility of the dissolution of N in the material, which in conjunction with the effect of other elements such as Cu, Ni, and Mn, stabilizes the austenite, and results in the austenite retainment to the room temperature (K1 and K2 mentioned in the introduction).

In addition, it appears that the grains are finer in NHT-N₂ specimen as compared to those of NHT-Ar one. A closer look into the microstructure, there are islands of equiaxed ultra-fine grains in the NHT-N₂ specimen (**Figure 4-2(c)** and (e)), while the grains are coarse and elongated in the NHT-Ar condition (**Figure 4-2(d)** and (f)). The equiaxed ultra-fine grains are mostly found around the spherical gas entrapped pores in NHT-N₂ specimens. As summarized in the introduction in K1 and K5, N₂ can be rapidly dissolved into the melt pool [119,126], the atomic N then forms nitrides (mostly Cr₂N), which either prevents grain growth or acts as heterogeneous nucleation sites during solidification [116,121]. The average grain size for NHT-N₂ and NHT-Ar were found based on EBSD results to be $5.4 \pm 1 \mu\text{m}$ and $15.5 \pm 2.3 \mu\text{m}$, respectively.

Figure 4-3(a) and **(b)** show the mosaic of consecutive EBSD IPF maps of the vertical cross-sections (same orientation as the ones exposed in **Figure 4-2**) of the HT-N₂ and HT-Ar specimens, respectively. The microstructure of the heat treated specimens is clearly lath martensitic. It appears from the IPF maps that the martensitic laths in the HT-N₂ specimens are finer than those in the HT-Ar ones. The exact lath thickness is quantified in Section 4.1 using high-resolution ECCI. There is also a finite fraction of austenite retained in HT-N₂ condition (1%) in the inspected cross-sectioned plane after heat treatment, while the HT-Ar specimens have fully martensitic microstructure.

4.4.1.2. Melt pools

In order to investigate the effect of shield gas type on the melt pool dimensions, specimens were cross-sectioned perpendicular to the known laser scan direction and parallel to the build direction, on the most top layer, as is schematically presented in **Figure 4-4**. The very top layer does not get re-melted, and therefore, the melt pool can be fully revealed. The cross-sections were polished and etched to reveal the melt pool boundaries for both NHT-N₂ and NHT-Ar specimens (**Figure 4-4(a)** and **(b)**). Recently, NASA has proposed a methodology [14] for melt pool analysis based on the ratios between the melt pool depth (d_p) and the layer thickness (t_L), as well as between the overlap depth (d_0) to t_L , i.e. d_p/t_L and d_0/t_L , respectively. In fact, the above-mentioned ratios show how deep the melt pools are, and whether the overlap of the melt pools is sufficient to avoid the formation of LoF defects. Accordingly, the melt pool depths and overlap depths were measured for N₂ and Ar specimens and the results are presented in **Figure 4-4(a)**, **(b)**, and **(c)**.

As seen, both the average melt pool depth and overlap depth are higher for the specimens fabricated under N₂ as compared to the ones fabricated under Ar shield gas, indicating larger melt pools. The d_p/t_L and d_0/t_L ratios are 3.5 and 2.3 for NHT-N₂ specimens, while they are 3.1 and 1.9 for NHT-Ar ones. Higher values of d_p/t_L and d_0/t_L ratios for N₂ specimens are less favorable, respectively, for the formation of gas entrapped pores and LoF defects, as compared to Ar specimens. The slightly deeper melt pools evident in the NHT-N₂ specimens can be explained by the better laser energy absorption associated with the use of N₂ shield gas (as summarized in Points K3 and K4 in the introduction), resulting in lower overall cooling/solidification rates, which permits more time for the pores to scape.

4.4.1.3. Defects

Figure 4-5 shows the typical porosity distribution of specimens fabricated under both shield gases in the cross-sectional plane parallel to the build direction (see **Figure 4-2**) in the gage section. The red dashed lines in **Figure 4-5(a)** and (b) indicate the depth to which the surface machining is performed for all tensile and axial fatigue specimens. It is evident that the pores in the N₂ specimens (**Figure 4-5(a)**) are not only smaller in population, but also smaller in size compared to those in the Ar specimens (**Figure 4-5(b)**). This is supported by the statistical analysis presented in **Figure 4-5(c)** for the square bars and **Figure 4-5(d)** for the gage section after machining, which have been performed on 5 polished sections (including the ones shown in **Figure 4-5(a)** and (b)). It is worth noting that the specimens used for defect analysis were selected from the same location on the build plate of N₂ and Ar prints.

The fewer and finer pores in the N₂ specimens can be associated with the larger melt pools as well as the better solubility of N₂ than Ar in the metal (Points K1, K3, and K4 as summarized in the introduction). The better solubility may result in shrinkage of the pores as N can dissolve in the material [126–128]; therefore, pores become smaller in size. In addition, considering the lower cooling/solidification rates in N₂ specimens as compared to those of Ar specimens, the gas pores in the melt pool have more opportunity to escape [13,129], resulting in less gas entrapped pores in N₂ specimens (see **Figure 4-4(c)**). The larger melt pools observed in the N₂ specimens are believed to be the result of the better laser energy absorption when N₂ is used as shield gas (Points K3 and K4), which overcomes any additional convection cooling effects imposed by N₂.

4.4.2. Mechanical Properties

4.4.2.1. Tensile Results

Figure 4-6 shows the monotonic tensile behavior of L-PBF 17-4 PH SS fabricated under N₂ and Ar shield gases in both non-heat treated and heat treated conditions. In addition, the details of tensile properties obtained for each condition are listed in **Table 4-4** and compared to those of the wrought counterpart undergone the same heat treatment (i.e. CA-H1025). **Figure 4-6(a)** shows the engineering stress-strain curve in the strain-controlled portion of the tensile test up to 0.045 mm/mm strain, and **Figure 4-6(b)** represents the engineering stress-displacement curve of the displacement-controlled portion of the test, all the way up to fracture. It must be mentioned that the Bridgman correction factor was employed to account for the stress triaxiality imposed by necking to obtain the true fracture stress [9].

As reported in **Table 4-4**, regardless of the shield gas type, the heat treated L-PBF 17-4 PH SS specimens exhibit substantially higher yield strength (σ_y) than their wrought counterparts in the same heat treatment condition [60]. This is attributed to the finer microstructure produced by the AM process as compared to the conventional manufacturing method [15]. As is evident in **Figure 4-6** (see solid curves) and **Table 4-4**, the non-heat treated L-PBF 17-4 PH SS specimens fabricated in N_2 (NHT- N_2) has higher σ_y , σ_f , and ϵ_f than the Ar ones (NHT-Ar). This increase in tensile strength (σ_y , and σ_f) can be ascribed to the grain refinement (see **Figure 4-2**). The improvement in ductility may be associated with the less porosity formed in N_2 specimens (see **Figure 4-5(d)**) [130]. Besides, the presence of retained austenite in the microstructure may enhance the ductility of the material; first, austenite is softer than the martensite and can accommodate more plastic deformation [131]. Second, stacking faults can be formed in austenite during deformation and lead to martensite transformation induced plasticity increasing the ductility of the material [132].

After heat treatment, the HT- N_2 specimens possess slightly higher σ_y and ϵ_f , but lower σ_f than the HT-Ar ones. The increase in σ_y seen for HT- N_2 specimens is attributed to the finer microstructure, however, this might have decreased the potential for strain hardening and consequently resulted in lower σ_f than HT-Ar specimens. Moreover, the presence of austenite can affect the strength of heat treated 17-4 PH SS in two ways. First, austenite itself is softer and more ductile compared to the martensite. Second, Cu as an austenitic stabilizer dissolves easily in austenite phase, which reduces the Cu fraction in martensite, and consequently, lessens the precipitation hardening effect of Cu [19,107]. Therefore, it is not expected that N_2 -shielded material to have significantly higher tensile

strength than the Ar-shielded counterparts, as evident in the tensile data generated in this study. The slight increase in ductility for HT-N₂ specimens may be due to the less porosity formed as well as the presence of retained austenite in HT-N₂ specimens [107].

4.4.2.2. Fatigue crack growth (FCG) results

The FCG behavior of L-PBF 17-4 PH SS specimens fabricated under Ar and N₂ shield gases and undergone CA-H1025 heat treatment procedure (i.e. the HT-Ar and HT-N₂ specimens) are compared in **Figure 4-7**. As seen in, the HT-N₂ specimens exhibit lower fatigue crack growth rate (FCGR) near the threshold regime (i.e. Regime I) shown in **Figure 4-7(b)** as compared to that of HT-Ar ones. The finer microstructure and the consequential increased resistance to slip in HT-N₂ may have contributed to the slower growth of the microstructurally small cracks, which is governed by slip. The higher porosity level (larger and more pores) and the associated stress concentrations in Ar specimens may also have increased their FCGR and resulted in lower ΔK_{th} values as compared to the N₂ specimens. In the Paris regime (i.e. Regime II), HT-N₂ specimens possess a slightly higher slope as compared to the HT-Ar counterparts; the FCG rates of HT-N₂ and HT-Ar specimens become nearly identical toward the end of Regime II (**Figure 4-7(c)**). By fitting the data in the Paris regime to the Paris equation:

$$\frac{da}{dN} = A(\Delta K)^n \quad (1)$$

where A and n are the y-intercept and slope of the line, respectively), the fitting parameters shown in **Table 4-5** are obtained for each condition. In Regime III, the HT-N₂ specimens exhibit higher cyclic fracture toughness as compared to the HT-Ar ones, which

may be attributed to the substantially lower population of volumetric defects in HT-N₂ specimens, as shown in **Figure 4-5**.

4.4.2.3. Axial fatigue results

Figure 4-8 presents the stabilized hysteresis loops of fully-reversed strain-controlled fatigue tests for HT-N₂ (**Figure 4-8(a)**) and HT-Ar (**Figure 4-8(b)**) L-PBF 17-4 PH SS specimens. As seen, irrespective of the shield gas type, L-PBF 17-4 PH SS showed very little to no macroscopic plastic deformation under the applied strain amplitudes in this study. This has been also reported for L-PBF 17-4 PH SS undergone other heat treatment conditions [15].

Table 4-6 summarizes the results of axial fatigue tests, including strain amplitude, ϵ_a , stress amplitude, σ_a , mean stress, σ_m , and reversals to failure, $2N_f$, for HT-N₂ and HT-Ar conditions. It is noted that the tensile/compressive mean stresses were calculated to be around, and in most cases, less than 5% of the respective stress amplitude; hence, they should not have affected the fatigue behavior. **Figure 4-9(a)** and **(b)** compare, respectively, the strain-life and stress-life fatigue behavior of L-PBF 17-4 PH SS specimens fabricated under N₂ and Ar shield gases and heat treated following the CA-H1025 schedule. It is evident that the HT-N₂ specimens in general exhibit a better fatigue performance at both LCF and HCF regimes and almost at all strain levels. As shown in **Figure 4-9**, two out of three HT-N₂ specimens were run-out at 0.0025 mm/mm strain amplitude, while only one out of four HT-Ar specimens reached the run-out defined in this study. The only failure of the HT-N₂ specimen at 0.0025 mm/mm strain amplitude occurred at a substantially higher

life than the HT-Ar failed specimens (by at least a factor of four). As elastic behavior dominated the fatigue performance (**Figure 4-8**), the Basquin equation, given below [9], was used to obtain the stress-life fatigue properties (i.e. fatigue strength coefficient, σ'_f , and fatigue strength exponent, b, for each condition):

$$\sigma_a = \sigma'_f (2N_f)^b \quad (2)$$

Accordingly, the linear least square fit method using the Basquin's equation in a semi log-log scale was used to obtain the fatigue parameters, σ'_f and b, for HT-N₂ and HT-Ar specimens (see **Figure 4-9(b)**). It is worth noting that the run-out data were excluded to obtain the best fitting results. The results are listed in **Table 4-7**, noting that the data at the run-out level were excluded to obtain the best fit.

4.5. Discussion on Experimental Results

In this section, the enhancement in mechanical properties (including the tensile, axial fatigue, and FCG behavior) of the L-PBF 17-4 PH SS due to the use of N₂ shield gas instead of Ar is comprehensively discussed and correlated with the refined microstructure and defects, including grain size, melt pool geometry, and porosity size and distribution.

4.5.1. Tensile Behavior as Affected by Micro-/Defect-Structures

As expected, and in agreement with the literature, performing heat treatment increases the strength of the L-PBF 17-4 PH SS. This can be attributed to the formation of nano-size Cu-rich precipitates (the size of only several nm) [26,133] and the formation of fine lath martensitic structure which reduces the mean free path of dislocations, limiting the ductility of the materials [26,134]. Indeed, as the strength increases, the ductility of the

specimens significantly decreases, i.e., from a fracture strain of ~0.65 to ~0.35 (see **Table 4-4**).

The utilization of N₂ shield gas does impose favorable effects on the tensile properties of L-PBF 17-4 PH SS, although the effects on the true fracture stress are overwhelmed by the effect of the heat treatment. Specifically, due to the use of N₂ shield gas, both the yield strength, σ_y , and ductility, ϵ_f , of the heat treated and non-heat treated specimens noticeably improved, as is evident in **Figure 4-6** and **Table 4-4**. The NHT-N₂ and HT-N₂ specimens respectively possess 0.05 and 0.09 higher strain at fracture than NHT-Ar and HT-Ar ones (**Table 4-4**). This is consistent with the higher cyclic fracture toughness for the HT-N₂ specimens than HT-Ar ones observed during the FCG tests in **Figure 4-7**.

The slightly increased ductility in HT-N₂ specimens as compared to the HT-Ar ones can be attributed to more retained austenite stabilized by the dissolved N atoms (summarized in Point K2 in the introduction) and less and smaller volumetric defects formed in N₂ specimens as compared to the Ar counterparts. Indeed, literature has reported as high as 7% percent of retained austenite in non-heat treated L-PBF 17-4 PH SS fabricated in N₂ (this also depends on the powder atomization media, N₂ versus Ar). This work measured around 1% retained austenite via EBSD scan of a cross-sectioned plane (for Ar-atomized powder) consistently in non-heat treated and heat treated N₂ specimens. The higher ductility, in addition to the higher fraction of retained austenite, can be also ascribed to the smaller size and population of pores in the N₂ specimens. It has been reported for the L-PBF 316L that the ductility improved considerably by reducing the volumetric defects [130].

The slightly increased yield strength for both NHT-N₂ and HT-N₂ conditions as compared to their Ar counterparts can be generally attributed to the refined microstructure. For NHT specimens, the strength is expected to be governed by the Hall-Petch relation, where the strength is inversely related to grain size. While the reduction in grain size occurred in some regions for NHT-N₂ specimens, this does not lead to a substantial change in the yield strength, only ~ 15 MPa higher yield strength than the NHT-Ar specimens. For HT specimens, the improvement in yield strength as a result of using N₂ shield gas is slightly more notable (~ 28 MPa). This originates from a reduction in the martensitic lath thickness in the HT-N₂ specimens compared to the HT-Ar ones. Indeed, the ECCI micrographs presented in **Figure 4-10**, comparing the thickness of lath martensite (yellow dashed arrows) for HT-N₂ and HT-Ar specimens, support this argument. As seen in **Figure 4-10(a)**, the HT-N₂ specimens have smaller martensite thickness (average of ~560 nm) as compared to that of HT-Ar ones in **Figure 4-10(b)** (average of ~1400 nm). The fine grains formed after fabrication in the NHT-N₂ specimen (see **Figure 4-2(c)**) transform to fine austenite grains during the CA heat treatment step (i.e. fine $\delta \rightarrow$ fine γ), which consequently influence the final laths martensite size upon quenching. Note that white particles are remnants of the polishing compound, not any secondary phases in the 17-4 PH SS, as confirmed by FIB surface polishing.

To elaborate, martensitic phases nucleated from the prior γ grains obeys the Kurdjumov-Sachs (K-S) orientation relation, i.e. $\{111\}_{\gamma} // \{110\}_{\alpha'}$ and $\langle 110 \rangle_{\gamma} // \langle 111 \rangle_{\alpha'}$. The habit plane of the γ - α' interface is always a $\{111\}$ or a near- $\{111\}$ plane. Since there are four sets of $\{111\}$ planes in the FCC γ phase, the choice of these habit plane is always randomized [131]. After the $\gamma \rightarrow \alpha'$ transformation, the prior γ grain is divided into

“packets” of laths that share the same habit planes, and each packet is further subdivided into blocks (the group of laths with the same orientation). The size of the packets, blocks, and consequently, the laths are related to the prior γ grain size. The finer the prior γ grains are; the finer the packets, blocks, and laths are for the HT specimens [135,136]. As for NHT ones, the lath martensitic structure is unclear, as was reported by others [18], and quantification on the lath thickness is not meaningful.

It is, however, interesting to note that the true fracture stress of the HT-N₂ specimens is substantially lower than that of the HT-Ar specimens. This, again, maybe attributed to the substantially smaller martensite lath thicknesses (as low as ~200 nm) observed for the HT-N₂ specimens. At such small lath interface spacings, the mutual reactions and multiplications of dislocations are minimized, leading to low strain hardening capacity, and therefore, lower true fracture stress of the HT-N₂ specimens. In addition, it has been reported that the presence of retained austenite can attenuate the precipitation hardening effect.

4.5.2. Enhanced Fatigue Performance via In-Process Refinement of Micro-/Defect-Structure

In general, defects such as surface roughness, LoF, pores, etc., compromise the fatigue performance of materials. In the case of machined specimens (i.e. absence of surface roughness), volumetric defects (i.e. pores, LoF defects, etc.) typically dominate the fatigue behavior [12,13]. The LoF defects in AM materials normally form when the ratio of overlap depth/layer thickness (d_0/t_L) is close to (or lower than 1), where the fusion of subsequent layers cannot occur successfully [13,14]. Referring to **Figure 4-4**, the d_0/t_L ratio for both HT-N₂ and HT-Ar specimens is higher than 1, therefore, technically the possibility

for formation of LoF defects is low in both conditions. However, the porosity size and distribution are different for HT-N₂ and HT-Ar specimens (see **Figure 4-5**); the HT-N₂ specimens have fewer and smaller pores as compared to those of HT-Ar specimens. Accordingly, HT-N₂ specimens are expected to have higher fatigue resistance than HT-Ar ones, specifically in the HCF regime.

Figure 4-9 shows that HT-N₂ specimens have slightly higher fatigue lives at 0.004 mm/mm strain amplitude. In this case, although the smaller pores in HT-N₂ specimens (see **Figure 4-5**) may have delayed the crack initiation, a considerable portion of the fatigue life in the LCF regime is dominated by crack growth, in which regard the HT-N₂ only performed slightly better than HT-Ar specimens (lower FCG rates for HT-N₂ near threshold as well as in the Paris regime shown in **Figure 4-7**). As such, there is only minimal improvement in fatigue resistance of these specimens observed.

In the HCF regime, as the majority of life is dominated by the initiation of fatigue cracks, the improvement in fatigue behavior of HT-N₂ specimens is mainly associated with its smaller and fewer pores as compared to those of the HT-Ar counterparts (**Figure 4-5**). It has been shown for various AM material systems (e.g. Ti-6Al-4V [137], AlSi10Mg [138], etc.) that the stress concentrations associated with pores are effective crack initiators and the internal pore size correlates well with the high cycle fatigue strength of the materials [139–142], i.e. fatigue life is shorter in the cases where the pores are larger.

In addition to volumetric defects, the surrounding microstructure may also influence the fatigue performance of AM materials. Indeed, the initiation and growth of microstructural small cracks are governed by slip and require a sufficient amount of plastic deformation which can be suppressed by refined microstructure. In wrought materials, the

initiation and growth of microscopic cracks are generally delayed by refined grains, and the fatigue limits have been found to be inversely related to grain size [9]. With the presence of porosity induced stress concentration, similar arguments apply. For instance, enhancement in high cycle fatigue performance attributed to the fine grains around the defects has been reported for hot isostatic pressed (HIPed) L-PBF Ti-6Al-4V [143]. Similarly, in the case of L-PBF 17-4 PH SS, the finer microstructure observed in HT-N₂ specimens (**Figure 4-2(c)** and (e)) as compared to the HT-Ar specimens (**Figure 4-2(d)** and (f)) can also provide additional fatigue resistance in the HCF regime.

Figure 4-11 shows the fracture surfaces of specimens fabricated in Ar shield gas at 0.0025 mm/mm strain amplitude with different fatigue lives. Cracks are seen to initiate from pores close to the machined surface for all the specimens. More importantly, fatigue lives depend on the pore size, i.e. generally the smaller the pore; the longer the fatigue life [113]. For instance, for specimen “Ar3” with 2,496,340 reversals to failure (**Figure 4-11(a)**), crack initiated from a pore close to the surface with the size of 18 μm , while the fatigue resistance decreased as the size of the pore increased to 31 μm (**Figure 4-11(b)**) for specimen “Ar4” with 1,394,730 reversals to failure. It is worth noting that the edge is seen on the fracture surface close to the pore in **Figure 4-11(a)** occurred due to the compression during the fully-reversed fatigue loading.

Figure 4-11(c) shows the fracture surface of “Ar11” with 690,584 reversals to failure. The crack initiated from two pores, one with the diameters of 37 μm and exposed to the surface, and the second with a diameter of 14 μm and very close to the surface. The reason for the shorter fatigue life obtained for this specimen as compared to previous cases (see **Figure 4-11(a)** and (b)) is that the cracks were initiated from multiple pores on the

surface of the specimen, in addition to one of these pores being relatively large compared to the crack initiating pores in other specimens. It has been reported that the mutual interaction of pores and pore-surface interaction induced stress concentrations may accelerate the initiation of cracks [137,142,144,145].

Figure 4-12 presents the fracture surface of L-PBF 17-4 PH SS specimen fabricated under N₂ shield gas (“N₂” specimen), which failed shortly after 10⁷ cycles. It is of interest to investigate the crack initiation mechanism in this particular specimen, as two other tests in this strain amplitude level did not fail within the tested period. For the “N₂” specimen, the major crack was seen to have initiated from a pore close to the surface, with a diameter of 10 μm. The longer life observed in HT-N₂ specimens at 0.0025 mm/mm strain amplitude is attributed to the smaller pore as compared to the ones in Ar specimens seen in **Figure 4-11**.

The smaller population of pores in N₂ specimens as compared to the Ar counterparts also reduces the chance for a pore to be exposed on (or very close to) the machined surface. To ensure the longer fatigue lives obtained for N₂ specimens as compared to the Ar ones are indeed the result of smaller pores, all fracture surfaces at various strain amplitudes were examined. It was observed that the crack initiating pores for N₂ specimens are all smaller than 20 μm, while the ones for Ar specimens range from 20 to 35 μm. It is postulated that the smaller pores in the N₂ specimens and the finer surrounding microstructure collectively resulted in a considerably better fatigue performance.

As seen in **Figure 4-7**, the Ar specimens have inferior FCG resistance near threshold (Regime I), while exhibiting more or less identical FCG resistance toward the end of the Paris regime (Regime II) as compared to N₂ ones. The higher FCG resistance of

N₂ specimens near the threshold region is due to the grain refinement observed in **Figure 4-2(c)** and **Figure 4-10(a)**. It is well established that the growth of microstructurally small cracks is governed by slip and are along high Schmid-factor slip planes. Refined microstructure, therefore, retards the growth of these short cracks since it is typically associated with higher slip strengths [146,147]. Therefore, higher ΔK_{th} is expected for N₂ specimens as compared to that of Ar ones. To compare the stable crack growth mechanism of N₂ specimens with that of Ar ones, fractography analysis is carried out showing the role of grain refinement as well as the precipitation states in both conditions.

The fractography investigations of CT specimens at the Paris regime (i.e. Regime II) and Regime III are shown in **Figure 4-13(a)** and (b) for HT-N₂ and HT-Ar specimens, respectively. It can be seen in fractography images for the Paris regime that crack growth appears to be a mixture of intergranular and intragranular modes (see the schematics embedded) and a ‘sawtooth’ feature is displaced (shown by double-side yellow arrows). The “grains” being referred here are the martensitic laths. Close inspection reveals that the size of the teeth correlates well with the thickness of the martensite laths in the two types of specimens. The sawtooth features are formed by crack growth and they are coarser for HT-Ar specimens (**Figure 4-13(b)**) than HT-N₂ counterparts (**Figure 4-13(a)**). This is ascribed to the difference in the microstructure of Ar and N₂ specimens. As shown in **Figure 4-10(b)**, HT-Ar specimens have coarser laths martensite (~1,400 nm) as compared to HT-N₂ specimens (~560 nm), and it can be seen from **Figure 4-13** that the sawtooth's sizes are identical to the lath martensite thicknesses in both conditions. The average sawtooths' size measured in **Figure 4-13** for HT-Ar and HT-N₂ are 1500 nm and 600 nm,

respectively. It is therefore inferred that the fatigue cracks grew along the lath martensite boundaries even in the long crack growth regime.

In Regime III, HT-N₂ specimens exhibit higher cyclic fracture toughness by tolerating higher ΔK values than the HT-Ar specimens, as seen in **Figure 4-7**. Correspondingly, the fracture surfaces in this regime revealed far less and smaller pores for the HT-N₂ specimens (**Figure 4-13(a)**) than for HT-Ar specimens (**Figure 4-13(b)**). It is therefore apparent that the presence of a high fraction of defects (i.e. gas entrapped pores) in HT-Ar specimens decreases the material tolerance in the presence of a crack, resulting in an earlier fracture.

4.6. Conclusions

This study demonstrated an enhanced fatigue performance for L-PBF 17-4 PH SS via in-process refinement of microstructure and defects using N₂ shield gas as an alternative to Ar. The effects of the shield gas on the microstructure, defects, fatigue crack initiation and growth behavior of L-PBF 17-4 PH SS were investigated and presented. Based on the results obtained in this study, the following conclusions can be drawn:

1. The use of N₂ as the shield gas led to finer microstructure containing more retained austenite as compared to specimens fabricated under Ar shield gas. This is attributed to the high solubility of N₂ in 17-4 PH SS and its austenite-stabilizing ability.
2. Islands of fine equiaxed grains observed close to the entrapped gas pores in the microstructure of N₂ specimens proved the fact that N₂ had diffused to the melt pool and prohibited grain growth.
3. The pores formed in N₂-shielded specimens were smaller both in size and in population. This is because the N₂ gas pores may 1) be absorbed by the melt pool and

dissolve in material shrinking the pore, or 2) escape the melt pool by either having more time during the slower solidification or by re-melting during printing the subsequent layer noting that melt pools of N₂ specimens were found to be deeper.

4. The N₂-shielded specimens possessed higher yield strength and ductility as compared to the Ar-shielded ones (for both non-heat treated and heat treated conditions). The higher ductility may be attributed to the lower internal defects as well as the presence of retained austenite, and the higher yield strength is ascribed to the fine equiaxed grains of N₂ specimens.
5. The finer lath martensite in HT-N₂ specimens decreased the potential for strain hardening of the material, and resulted in lower true fracture stress as compared to the HT-Ar counterparts.
6. Axial fatigue performance of L-PBF 17-4 PH SS was increased moderately in low cycle fatigue, and considerably in high cycle fatigue regime when N₂ was used as the shield gas. The improvement in fatigue resistance of L-PBF 17-4 PH SS fabricated under N₂ shield gas was attributed to the refined micro-/defect-structure.
7. Using N₂ as shield gas resulted in a moderately lower FCG rate for L-PBF 17-4 PH SS in a wide range of ΔK levels (including the near-threshold regime and the Paris regime) as compared to the condition where Ar was used as the shield gas. This can be attributed to the grain refinement (i.e. islands of fine equiaxed grains) effects. Ar specimens have lower cyclic fracture toughness, which is due to the larger and more pores in the specimens.

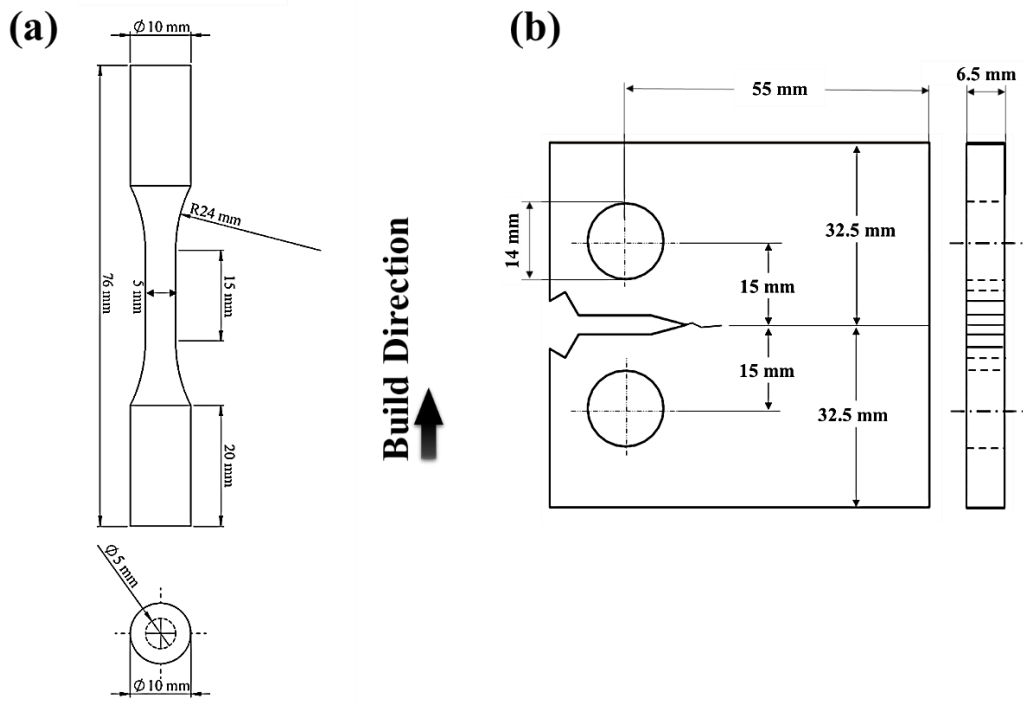


Figure 4-1. Drawings of (a) round axial fatigue specimens with a uniform gage section, and (b) compact tension (CT) specimens following ASTM E647 standard [98].

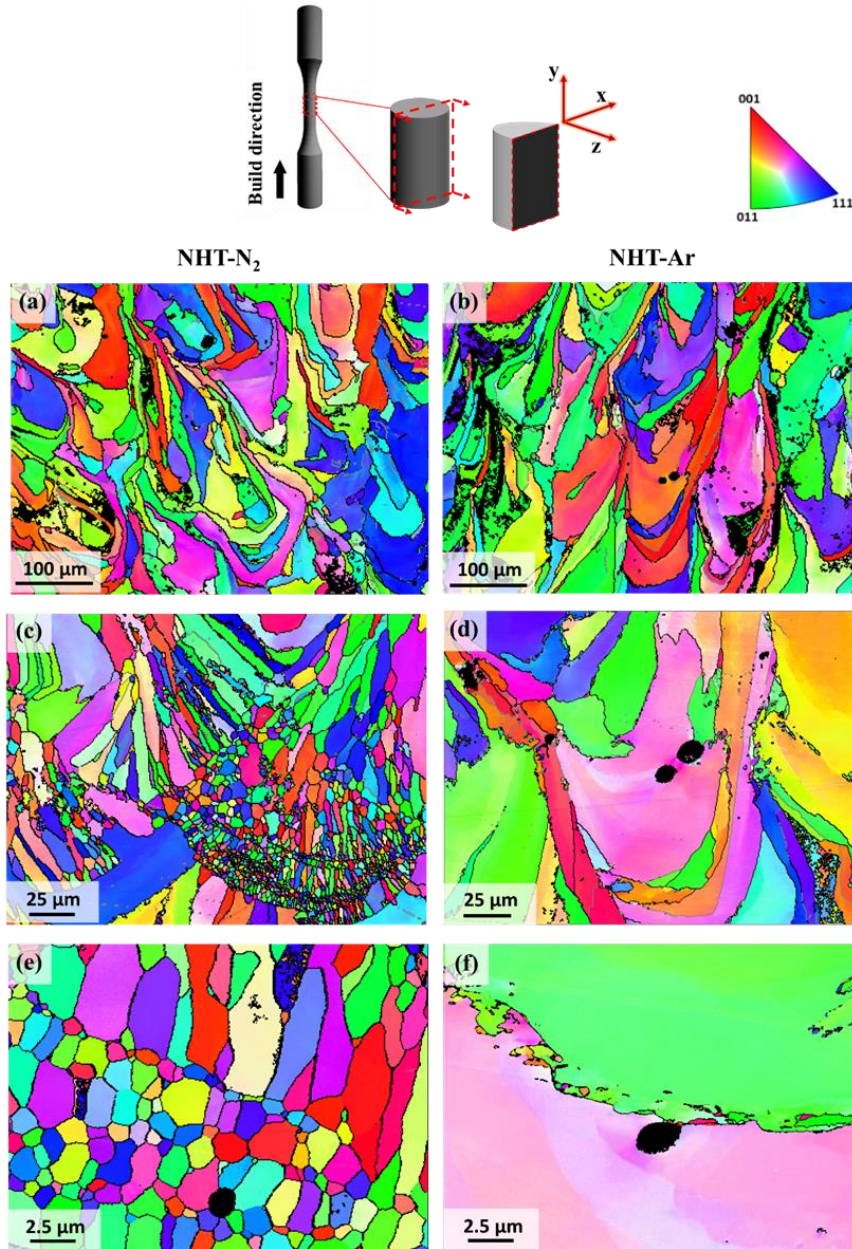


Figure 4-2. A schematic of axial fatigue specimen and the cross-sectioned plane parallel to the build direction in the gage section for microstructure characterization, and the EBSD results for NHT L-PBF 17-4 PH SS specimens: (a), (c), (e) IPF NHT-N₂, and (b), (d), (f) IPF NHT-Ar.

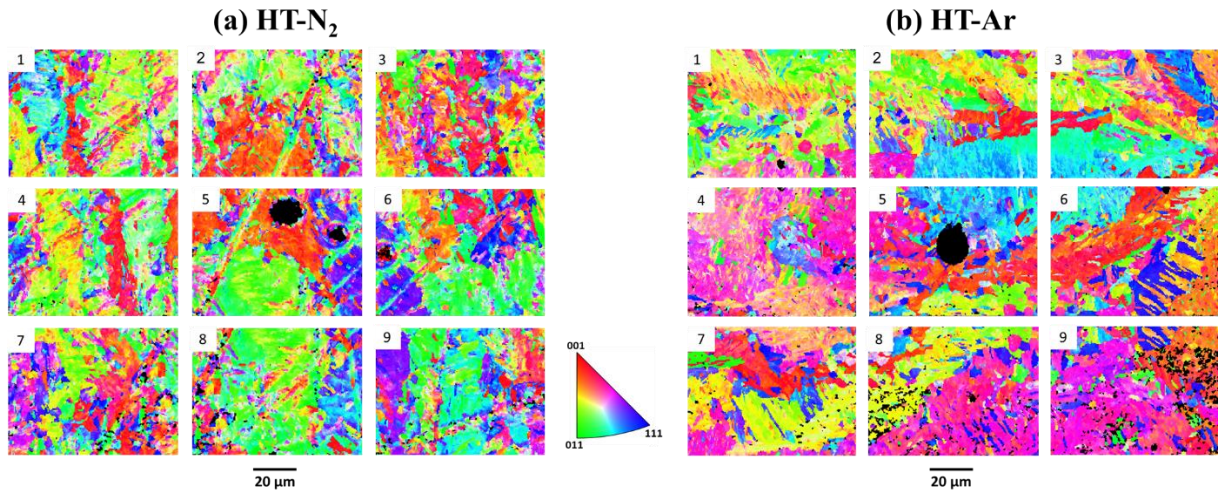


Figure 4-3. IPF maps of heat treated L-PBF 17-4 PH SS specimens on the cross-sectioned plane parallel to the build direction: (a) HT-N₂, and (b) HT-Ar.

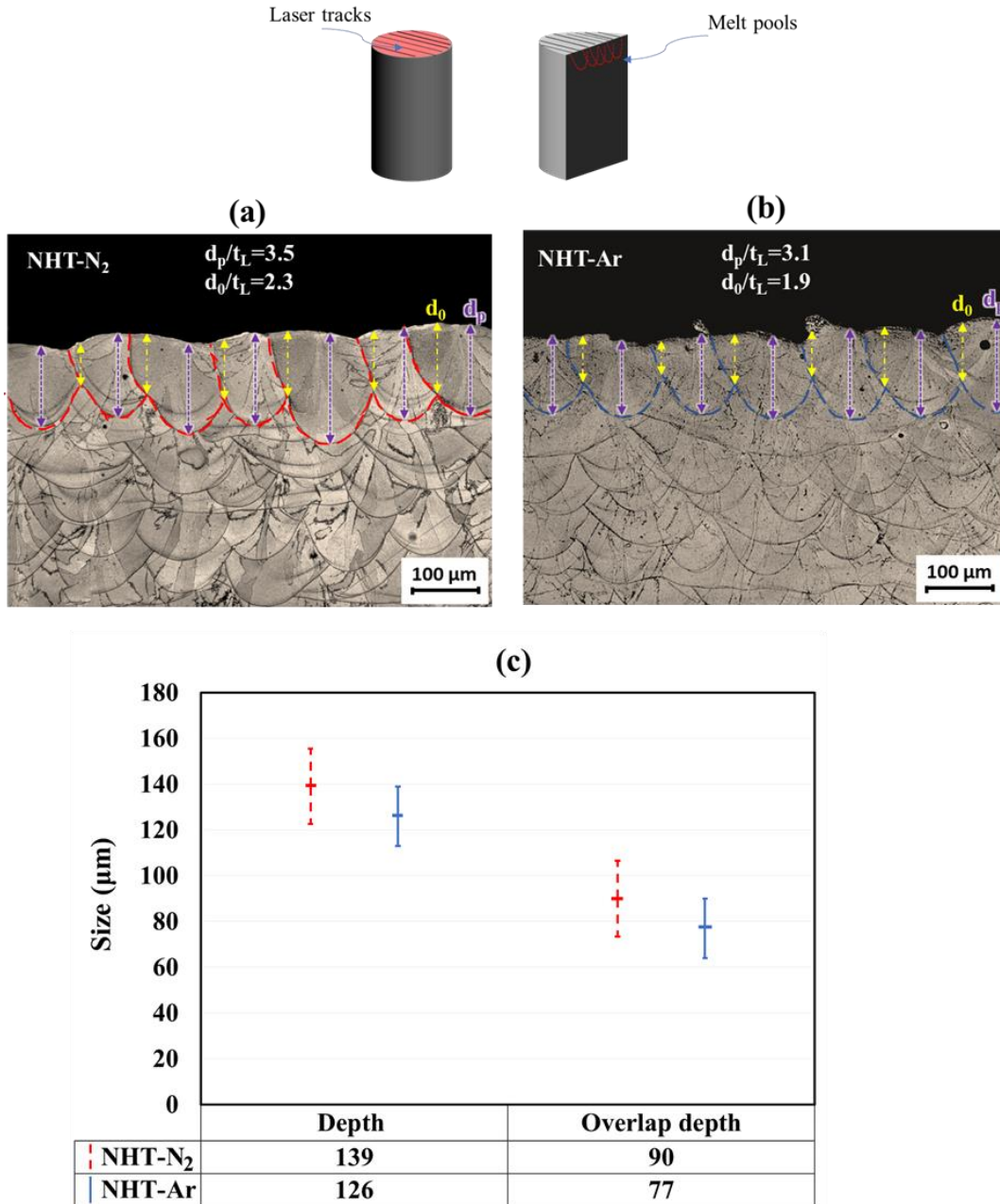


Figure 4-4. Post-built melt pool size measurement; the schematic is showing the last printed layer with the laser track direction. (a) Melt pool shape/size in NHT-N₂ specimens, (b) melt pool shape/size in NHT-Ar specimens, and (c) measured melt pool depths and overlap depths.

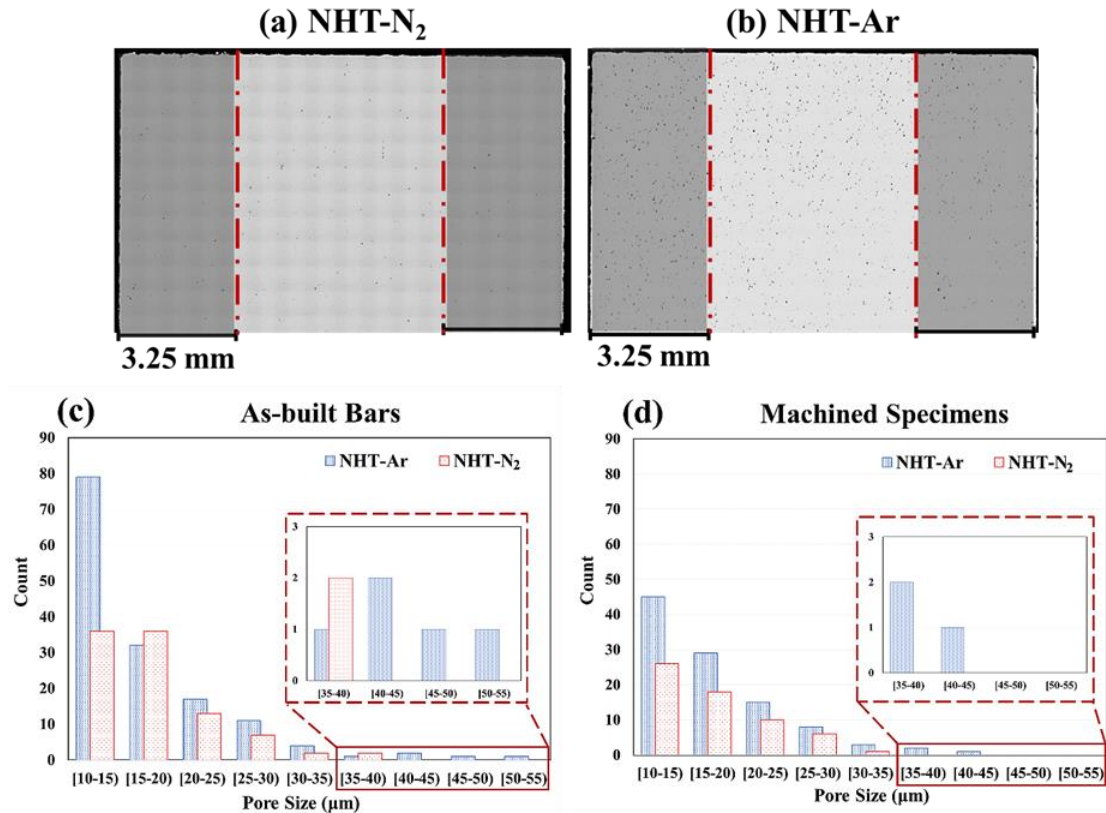


Figure 4-5. Porosity distribution in a cross-sectional plane parallel to the build direction for (a) NHT-N₂ and (b) NHT-Ar specimens. The statistical distribution of the pore size in NHT-N₂ and NHT-Ar specimens in (c) as-built bars, and (d) gage section of the machined specimens. Note that the shaded area in (a) and (b) indicate the portion that was removed by machining for all the tensile and axial fatigue specimens.

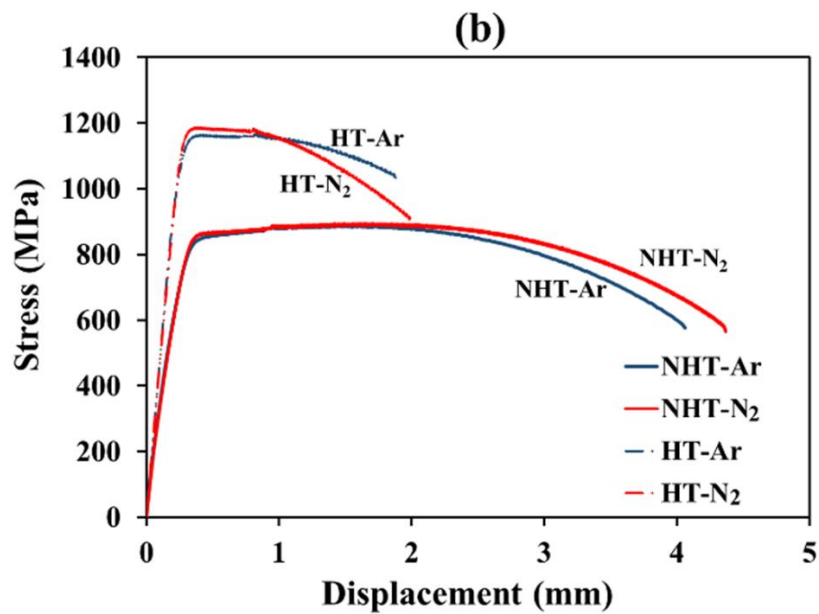
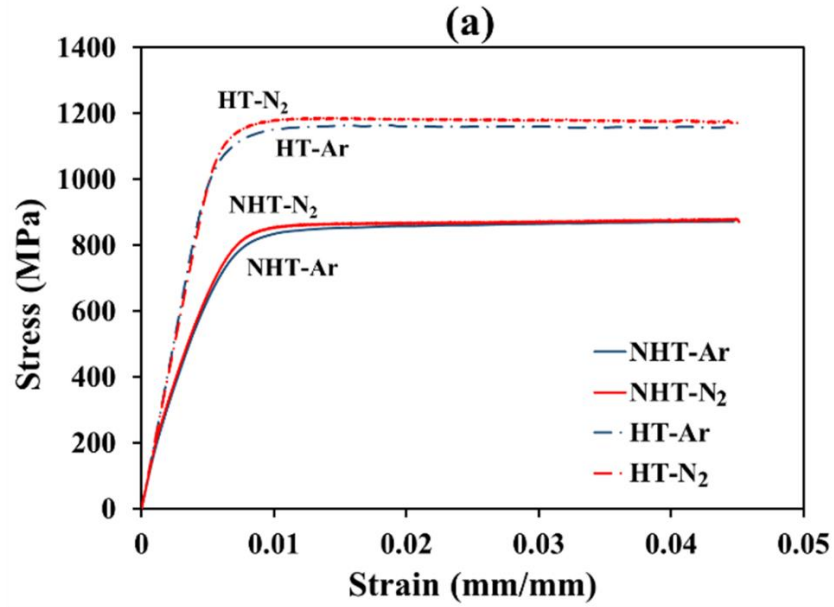


Figure 4-6. Monotonic tensile behavior of L-PBF 17-4 PH SS specimens fabricated under Ar and N₂ shield gases for both NHT and HT conditions: (a) strain-controlled up to 0.045 strain, and (b) displacement-controlled step after removing the extensometer up to fracture.

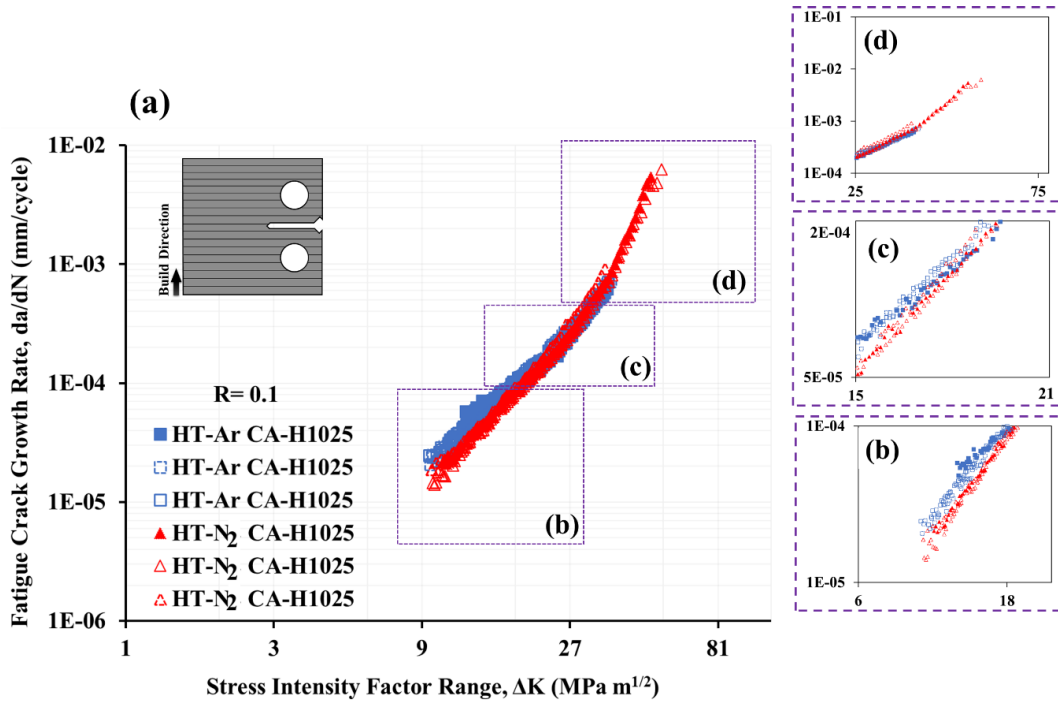


Figure 4-7. Fatigue crack growth (FCG) rates for L-PBF 17-4 PH SS specimens fabricated under N₂ and Ar shield gases in heat treated condition (CA-H1025). The three different FCG regimes (i.e. near threshold, Paris, and unstable FCG) are magnified and presented in (b), (c), and (d), respectively.

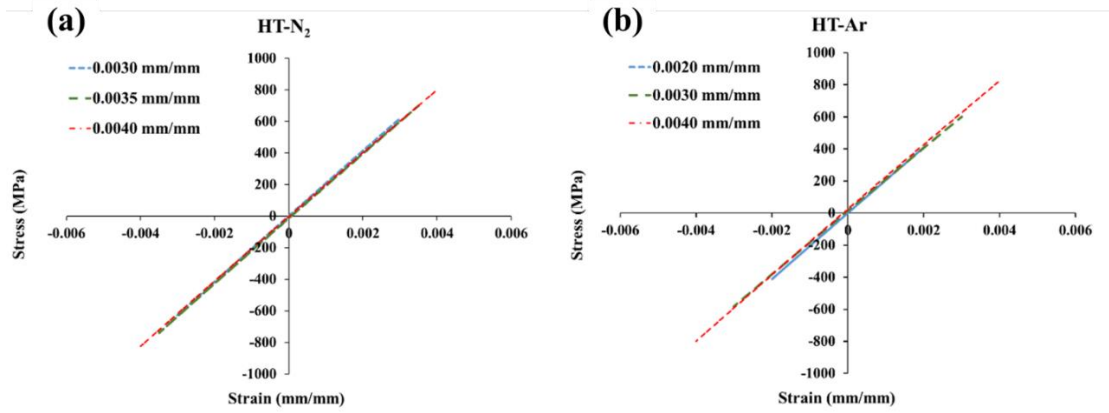


Figure 4-8. Stable hysteresis loops of fully-reversed, strain-controlled constant amplitude fatigue tests of L-PBF 17-4 PH SS specimens: (a) HT-N₂, and (b) HT-Ar [63].

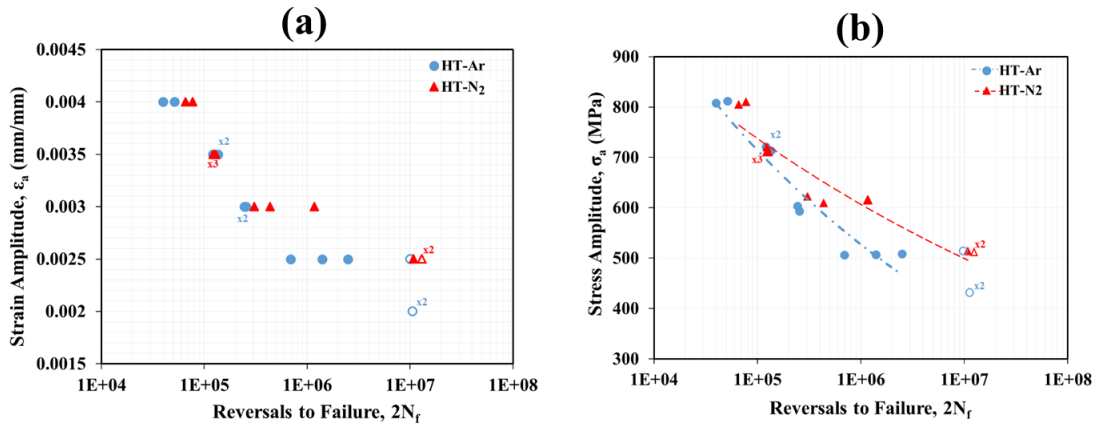


Figure 4-9. (a) Strain-life and (b) stress-life fatigue data for CA-H1025 L-PBF 17-4 PH SS representing the effect of shield gas type (N₂ vs. Ar [63]). Note that hollow marks represent the run-out tests.

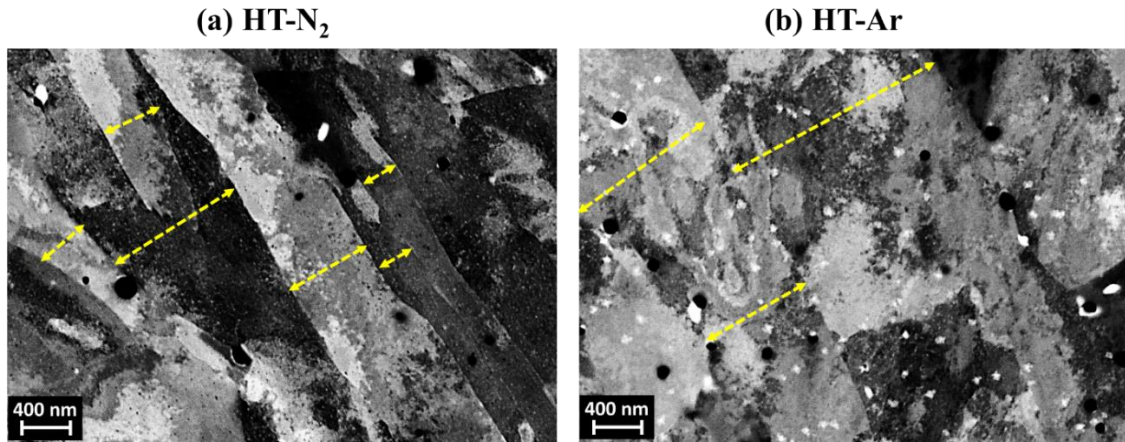


Figure 4-10. The electron channeling contrast images (ECCI) of L-PBF 17-4 PH SS showing the lath martensite in (a) HT-N₂, and (b) HT-Ar specimens. Note that the yellow dashed arrows are representing the lath martensite thickness. White particles are remnants of the polishing compound, not any secondary phases in the 17-4 PH SS, as confirmed by FIB surface polishing.

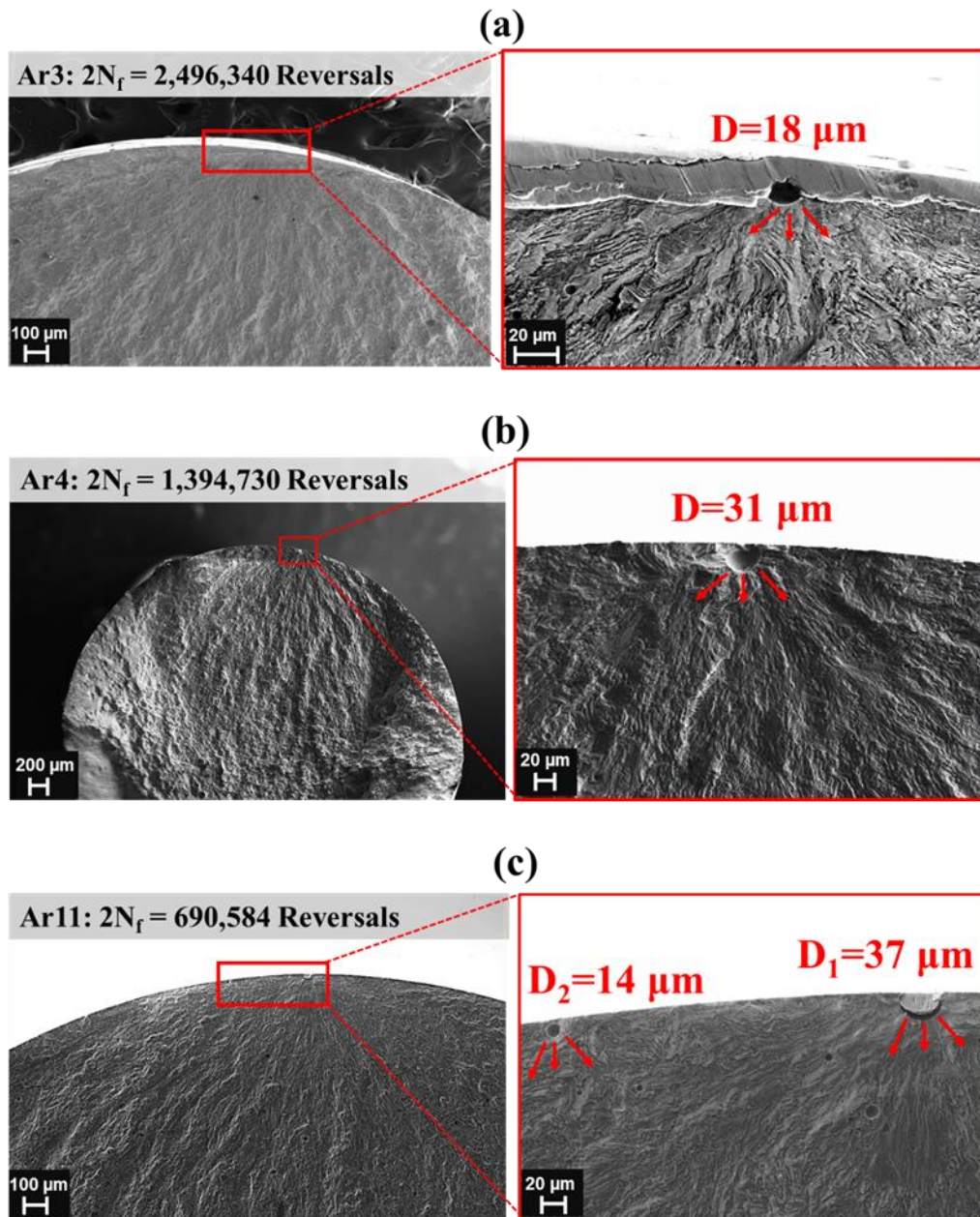


Figure 4-11. Fracture surfaces of HT-Ar specimens at 0.0025 mm/mm strain amplitude: (a) specimen “Ar3” with 2,496,340 reversals to failure, (b) specimen “Ar4” with 1,394,730 reversals to failure, and (c) specimen “Ar11” with 690,584 reversals to failure.

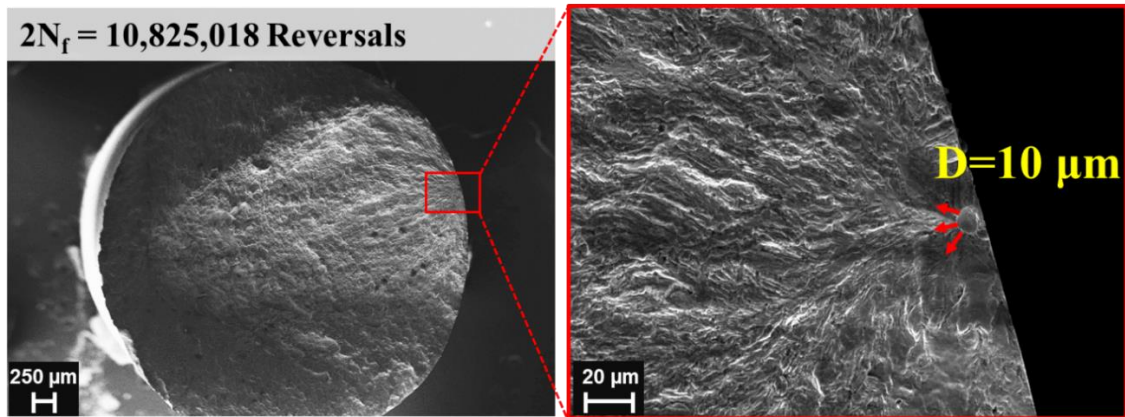


Figure 4-12. Fracture surface of an L-PBF 17-4 PH SS specimen fabricated under N₂ shield gas; specimen “N2” with 10,825,018 reversals to failure at 0.0025 mm/mm strain amplitude.

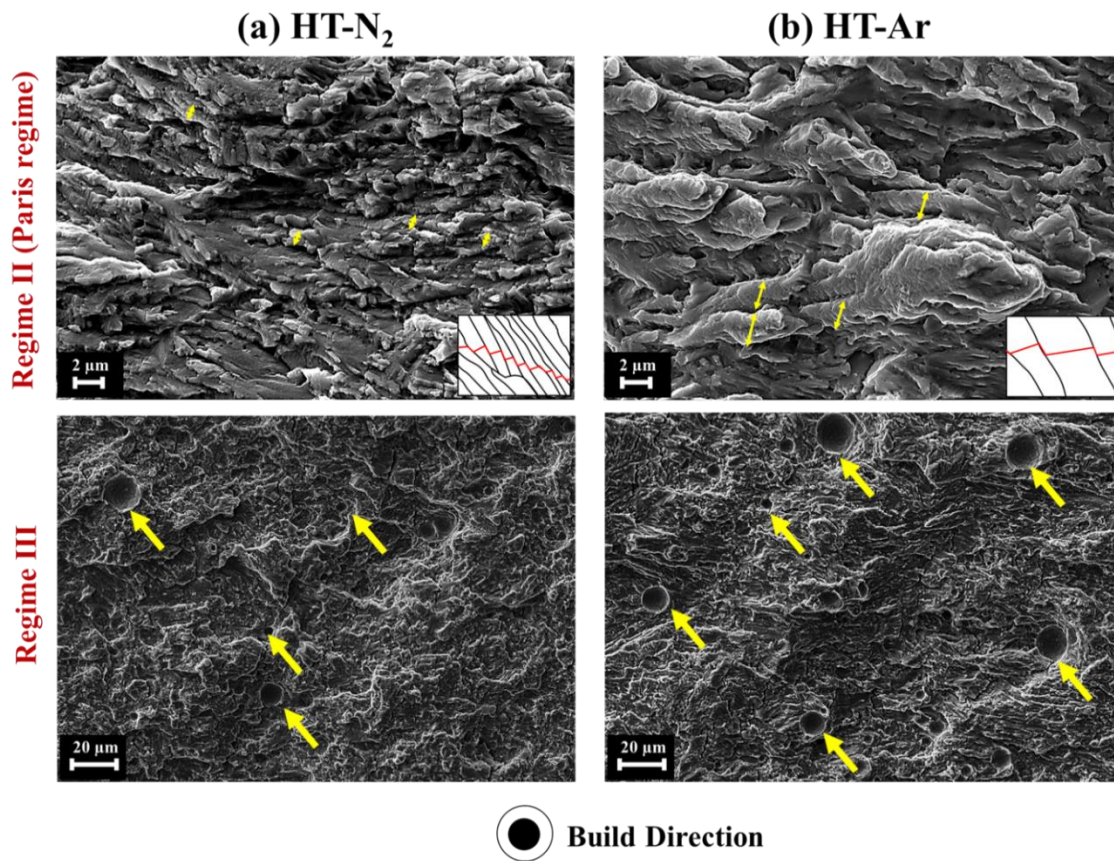


Figure 4-13. Fractography of L-PBF 17-4 PH SS CT specimens fabricated under different shield gas types and heat treated using CA-H1025 procedure: (a) HT-N₂ and (b) HT-Ar. The ‘sawtooth’ features are shown by double-side yellow arrows, and the exposed pores are indicated by yellow arrows. The schematics represent the laths martensite and how the crack is growing in the intergranular and intragranular modes.

Table 4-1. Chemical composition of 17-4 PH SS powder, provided by LPW Technology Inc.

| | C | Cr | Ni | Cu | Mn | Si | Nb | Mo | N | O | P | S | Fe |
|----------------|----------|-----------|-----------|-----------|-----------|-----------|-----------|-----------|----------|----------|----------|----------|-----------|
| (Wt. %) | 0.01 | 15.6 | 4.03 | 3.89 | 0.24 | 0.29 | 0.33 | <0.01 | 0.01 | 0.05 | 0.004 | 0.003 | Bal. |

Table 4-2. The process parameters for L-PBF 17-4 PH SS suggested by EOS.

| Laser power (W) | Scanning speed (mm/s) | Hatch distance (μm) | Layer thickness (μm) |
|----------------------------------|--|--|---|
| 220 | 755.5 | 100 | 40 |

Table 4-3. Design of experiment: number of specimens under each build specifications.

| Specimen type | Ar shield gas | N₂ shield gas | Build dimensions |
|-----------------------|----------------------|---------------------------------|-------------------------|
| Axial fatigue/tensile | 18 | 18 | 11.5×11.5×77 mm |
| Compact tension (CT) | 4 | 4 | 65×6.5×65 mm |

Table 4-4. Monotonic tensile properties of L-PBF 17-4 PH SS fabricated under Ar and N₂ shield gas in both NHT and HT conditions, as well as wrought 17-4 PH SS in CA-H1025 condition [60]. σ_y – yield stress (proof stress at 0.01 of strain), σ_f – true fracture stress (corrected for necking), RA% - area reduction at fracture, and ϵ_f – true fracture strain.

| Fabrication method | Heat treatment | σ_y (MPa) | σ_f (MPa) | RA% | ϵ_f (mm/mm) |
|---------------------------|--------------------------|------------------------------------|------------------------------------|------------|--|
| L-PBF | NHT-N₂ | 855 | 900 | 49 | 0.66 |
| | NHT-Ar | 840 | 887 | 46 | 0.61 |
| | HT-N₂ | 1178 | 1192 | 33 | 0.39 |
| | HT-Ar | 1150 | 1238 | 26 | 0.30 |
| Wrought | CA-H1025 [60] | 1000 | N/A | N/A | N/A |

Table 4-5. Paris equation parameters based on best fit in the Paris regime for L-PBF 17-4 PH SS specimens fabricated under N₂ and Ar shield gases.

| | A (MPa.m^{1/2}) | n |
|-------------------------|--------------------------------|----------|
| HT-N₂ | 3.6×10 ⁻⁸ | 2.7 |
| HT-Ar | 3.9×10 ⁻⁷ | 2.1 |

Table 4-6. Fully-reversed fatigue test results of L-PBF 17-4 PH SS fabricated under N₂ and Ar [15] heat treated following CA-H1025 procedure.

| | Specimen ID | ϵ_a (mm/mm) | σ_a (MPa) | σ_m (MPa) | 2N _f (Reversals) |
|-------------------|-------------|----------------------|------------------|---------------------|-----------------------------|
| HT-N ₂ | N1 | 0.0025 | 495 | 0 | >11,000,000 |
| | N11 | 0.0025 | 496 | 0 | >11,000,000 |
| | N2 | 0.0025 | 513 | -1 | 10,825,018 |
| | N4 | 0.0030 | 615 | 15 | 1,173,562 |
| | N5 | 0.0030 | 609 | -10 | 434,606 |
| | N3 | 0.0030 | 622 | 5 | 305,686 |
| | N7 | 0.0035 | 710 | 20 | 128,870 |
| | N6 | 0.0035 | 720 | 19 | 123,384 |
| | N8 | 0.0035 | 710 | -2 | 122,300 |
| | N10 | 0.0040 | 803 | -6 | 77,218 |
| | N9 | 0.0040 | 805 | -12 | 65,948 |
| HT-Ar | Ar1 | 0.0020 | 406 | 13 | >11,000,000 |
| | Ar2 | 0.0020 | 410 | 0 | >11,000,000 |
| | Ar12 | 0.0025 | 505 | 2 | >11,000,000 |
| | Ar3 | 0.0025 | 509 | 24 | 2,496,340 |
| | Ar4 | 0.0025 | 506 | 23 | 1,394,730 |
| | Ar11 | 0.0025 | 506 | 25 | 690,584 |
| | Ar5 | 0.0030 | 604 | -2 | 254,274 |
| | Ar6 | 0.0030 | 593 | 9 | 244,684 |
| | Ar7 | 0.0035 | 713 | -12 | 135,110 |
| | Ar8 | 0.0035 | 721 | -9 | 121,066 |
| | Ar9 | 0.0040 | 812 | 14 | 51,348 |
| | Ar10 | 0.0040 | 809 | 24 | 39,764 |

Table 4-7. Basquin equation (Eq. 2) fitting parameters for stress-life behavior of CA-H1025 L-PBF 17-4 PH SS specimens fabricated under N₂ and Ar shield gases.

| | σ'_f (MPa) | b | R² |
|-------------------------|-------------------|----------|----------------------|
| HT-N₂ | 1956 | -0.085 | 0.88 |
| HT-Ar | 3269 | -0.132 | 0.91 |

**CHAPTER 5: HIGH AND VERY HIGH CYCLE FATIGUE BEHAVIOR OF
ADDITIVELY MANUFACTURED 17-4 PH STAINLESS STEEL: EFFECT OF
SHIELDING GAS TYPE**

The following chapter is ready to be submitted to International Journal of Fatigue (IJF) in 2022.

Nezhadfar, P.D., Welsh, J., Simsiriwong, J., Shao, S., Shamsaei, N., High and very high cycle fatigue behavior of additively manufactured 17-4 PH stainless steel: effect of shielding gas type, International Journal of Fatigue.

5.1. Abstract

This study investigates the effect of shielding gas type, on the high cycle fatigue (HCF) and very high cycle fatigue (VHCF) behaviors of laser powder bed fused (L-PBF) 17-4 precipitation hardening (PH) stainless steel (SS). Specimens with hourglass and uniform gage section geometries were fabricated under Ar and N₂ shielding gases. Fatigue testing was performed on the uniform and hourglass specimens utilizing a conventional (10 Hz) and hourglass specimens using ultrasonic (20 kHz) test setups, respectively. The micro-/defect-structure of the Ar-shielded and N₂-shielded specimens are compared and correlated with their fatigue properties. Results show that the microstructure of Ar-shielded specimens contains δ -ferrite, which is absent in the N₂ shielded ones. In addition, there are fewer and smaller defects in N₂-shielded specimens compared to the Ar-shielded ones. These characteristics permitted the N₂-shielded L-PBF 17-4 PH SS specimens superior fatigue lives than the Ar-shielded ones, especially in the HCF and VHCF regimes. In addition, the hourglass specimens, regardless of the shielding gas type, slightly outperform the fatigue behavior of the specimens with uniform gage section. This is due to the lower risk-volume of the hourglass specimens (32 mm³) than the uniform gage ones (122 mm³).

5.2. Introduction

The role of additive manufacturing (AM) in the fabrication of near-net-shaped parts and part prototyping has grown significantly in various engineering industries such as aerospace, automotive, biomedical, etc. Although the demand for more customized components with complex geometries is being met with the increased use of AM, qualifying and certifying the additively manufactured (AM) parts for critical load-bearing applications still is a challenge [85]. The main reason is the fatigue performance of AM materials often being inferior to their wrought counterpart and are associated with significant uncertainty [148]. Therefore, research efforts are much needed to identify potential influencing factors of mechanical properties and characterize their effects, which are essential for accelerating the qualification of the AM materials. In line with this need, America Makes & ANSI additive manufacturing standardization collaborative (AMSC), has identified the Gap FMP1 on "materials properties" to generate the baseline tensile and fatigue properties of various materials [149].

In response to the Gap FMP1, a large number of studies are currently evaluating the influence of various factors on mechanical properties of AM materials (e.g., Ti-6Al-4V, Ni-based superalloys, aluminum, stainless steels, etc.), such as effects of powder recycling [24,150], process optimization [151,152], surface treatment [153,154], post thermal treatment [31,155], build orientation [11,139,156], to name a few. It has been shown that process induced defects (i.e., surface roughness, and volumetric defects, such as gas entrapped pores, keyholes, and lack of fusion (LoF)) and their variations in response to the influencing factors are the main limiting factor of AM materials mechanical properties—especially fatigue—and the uncertainty therein. They are also the main reason

to prohibit the widespread use of AM components in critical load-bearing applications [4]. AM defects typically do not significantly penalize tensile properties. In fact, the tensile properties of AM materials are often comparable, if not superior, to those of the wrought counterparts. On the other hand, fatigue properties in the high cycle ($N_f > 10^5$) and very high cycle ($N_f > 10^7$) fatigue regimes, in which the component service lives of many advanced applications (e.g., ships/high-speed trains' components, aircraft turbine components, etc.) fall [157], are strongly influenced by defects. —are often time intensive to acquire by means of conventional approaches (such as servohydraulic load frames). Accelerated fatigue tests, such as the ones via ultrasonic fatigue tests (at frequencies > 20 kHz), capable of reaching 10^9 cycles within days are therefore appealing.

There are, however, challenges in correlating the data from ultrasonic fatigue tests and the fatigue performance of AM parts due to the effects of cyclic frequency (cyclic strain rate) and hourglass shape of specimens. Under ultrasonic frequencies, materials can experience at least 3 orders of magnitude higher cyclic strain rate as compared to when they are under servohydraulic fatigue tests. Slip-induced fatigue damage accumulation in coarse grained materials (such as pure Cu, Fe, or austenitic alloys) is governed by occurrence of interruptive events, such as cross-slip, which alter the paths of screw dislocation segments moving to-and-fro and generates residual edge dislocations as a result [38,158]. Under a given stress amplitude, the rate of cross-slip is only temperature- and material- dependent, the significantly smaller time window constrained by the much higher strain rates can severely limit the total counts of the cross-slip events, suppressing damage. FCC alloys such as Inconel 718 typically have wide dislocation cores, are difficult to cross-slip, and are not sensitive to test frequency [159]. On the contrary, BCC alloys are

significantly more rate sensitive due to their significantly constricted dislocation cores [160].

In addition, the uncertainty in the statistical distribution of defects' location and size in AM materials require a relatively large specimen gauge volume to effectively evaluate their fatigue response. The hourglass geometry used for ultrasonic fatigue testing has a low risk-volume experiencing the maximum stress during testing; therefore, there is a lower probability for more detrimental defects to exist in this volume which can also make such tests over estimate fatigue life, especially in the HCF and VHCF regimes [161].

One of the most prominent materials for the AM processes is 17-4 precipitation hardening (PH) stainless steel (SS) due to its advantageous properties, such as good corrosion resistance, high toughness, and desired strength and ductility based on the applied heat treatment. Recently, Nezhadfar et al. [162] showed that the high cycle fatigue (HCF) performance of the L-PBF 17-4 PH SS is superior in case it is fabricated under N₂ shielding gas compared to the Ar, using similar process parameters (i.e., laser power, scan speed, etc.) [162]. This was mainly attributed to the retarded fatigue crack initiation by refined micro-/defect structure due to the use of N₂ shielding gas. This enhancement effect was expected to be even stronger in the VHCF regime given the even more importance of fatigue crack initiation under lower loading amplitudes. Nevertheless, although there are many investigations on the LCF and HCF fatigue behavior of the L-PBF 17-4 PH SS in the literature, the studies on the VHCF performance of the L-PBF 17-4 PH SS are scarce. This is likely due to the limitations in test frequencies of conventional load frames as well as the lack of understanding on the frequency (cyclic strain rate) dependency of 17-4 PH SS's fatigue response. Indeed, the mechanism of frequency effect on fatigue damage

accumulation in coarse grained materials (which requires long free slip distances) may not apply to 17-4 PH SS whose microstructure mainly comprises martensitic laths of a few hundred nanometers or thinner.

Accordingly, this study aims to evaluate the fatigue behavior of L-PBF 17-4 PH SS fabricated under Ar and N₂ shielding gas, with focus on the VHCF regime. In addition, the effects of specimen geometry and test frequency (cyclic strain rate) on fatigue performance are studied. This article is organized in the following order: in Section 2, the material, fabrication, specimen geometry, and testing methods are presented in detail. The experimental results, including the micro-/defect-structure analysis and fatigue data, are presented in Section 3. In Section 4, the fatigue behavior of the L-PBF 17-4 PH SS in different fatigue life regimes is discussed and correlated to their micro-/defect-structure, shielding gas type, and specimen geometry. Finally, Section 5 summarizes this study's findings and draws conclusions.

5.3. Experimental Procedures

5.3.1. Material and Fabrication

Argon atomized 17-4 PH SS powder with the chemical composition reported in [5] was used to fabricate the specimens. It has been reported that employing moderately reused powder increases powder flowability on the powder bed, which mitigates the specimen location dependency on fatigue behavior of L-PBF 17-4 PH SS [6]. An EOS M290 system was used to fabricate cylindrical bars with a height of 75 mm and diameter of 12 mm. The cylindrical specimens were printed vertically (**Figure 5-1(a)**); one set of specimens was manufactured using Ar shielding gas, and one set under N₂ shielding gas, having similar process parameters reported by Nezhadfar et al. [7]. Both set of specimens were heat-

treated to the CA-H1025 condition (i.e., Condition A (CA): 1050 °C/0.5 hour/air-cooled + H1025: 552 °C/4 hours/air-cooled) as schematically shown in **Figure 5-1(b)**. The CA-H1025 , had been shown to result in a good combination of high tensile strength and ductility, as well as moderate fatigue resistance.

5.3.2. Specimen Design

The heat treated bars were further machined into fatigue specimens of three geometries with the same 3mm-gage diameter, i.e., uniform and hourglass gages for conventional tests, and ultrasonic test specimens (see **Figure 5-2**). Note that the ultrasonic specimens' gage is also hourglass-shaped; however, they are referred to as 'ultrasonic' specimens throughout the manuscript for better distinction.

5.3.3. Micro-/Defect-Structure Characterization

For defect-structure characterization, one specimen from each group of uniform gage, hourglass, and ultrasonic ones were scanned using a Zeiss X-ray computer tomography (XCT) instrument. The scans were conducted on 6.5 mm-long sections in the middle of the specimen gages with a voxel size of 6.5 μm. A Zeiss Crossbeam 550 scanning electron microscope (SEM) equipped with Oxford electron backscatter diffraction (EBSD) and energy dispersive spectroscopy (EDS) detectors was employed for microstructure characterization. Microstructural samples were cut from the gage section of heat-treated specimens and cross-sectioned parallel to the build direction of the L-PBF specimens, i.e., transverse direction (TD) plane. The microstructure samples were mounted, ground, and polished to a mirror-finished surface condition prior to conducting the EBSD analysis and electron channeling contrast imaging (ECCI).

5.3.4. Fatigue Testing

The ultrasonic specimens were subjected to uniaxial fully-reversed cyclic loading using a Shimadzu USF-2000A system at a nominal resonance frequency of 20 kHz. The specimen failure was indicated when the shift in resonance frequency was beyond ± 500 Hz. The specific geometry shown in **Figure 5-2(c)** was designed to achieve the maximum applied stress at the center of the specimen and the maximum displacement at the free end. To negate heating effects that may occur while testing at the very high frequency, compressed cooled air at 35 psi, through an air dryer to eliminate any moisture in the air and possible synergistic fatigue (i.e., corrosion and fatigue) damage, was aimed at the center of the specimens' gage section and. An intermittent pulse/pause oscillation was used to decrease the amount of internal heat generation within the specimens where the pulse and pause times were 110 ms and 800 ms, respectively. Three fatigue tests were performed for each stress amplitude level to evaluate the repeatability of the results. Specimens with number of reversals to failure (i.e., $2N_f \geq 10^9$) were considered as run-out. Fracture surfaces were cleansed in a methanol bath using a sonicator before conducting fractography. A Tescan VEGA3 scanning electron microscope was used for the fractography of the ultrasonic specimens.

A Table-top MTS load frame was used for the conventional uniaxial fully-reversed force-controlled fatigue testing on the uniform gage and hourglass specimens. The test frequency was kept constant at 10 Hz, and three fatigue tests were performed at each stress amplitude level. The specimens with number of reversals to failure (i.e., $2N_f \geq 10^7$) without fracture were considered run-out for the conventional fatigue testing. Before fractography, the fractured specimens were cleansed in an isopropanol bath using a sonicator. A Zeiss

Crossbeam 550 SEM was utilized for fractography for the uniform gage and hourglass specimens.

5.4. Experimental Results

5.4.1. Microstructure

The microstructure of L-PBF 17-4 PH SS specimens (both Ar-shielded and N₂-shielded) after CA-H1025 heat treatment characterized by EBSD and ECCI are shown in **Figure 5-3**. The EBSD results show the prior austenite grain (PAG) boundaries (one of the PAGs was highlighted in each condition on the micrographs) and the martensitic microstructure for both the Ar-shielded and N₂-shielded specimens in **Figure 5-3(a)** and **Figure 5-3(c)**, respectively. The Ar-shielded specimen have coarse columnar PAG, whereas the PAGs are more equiaxed-like in the N₂-shielded ones. It can be seen that the N₂-shielded specimen (**Figure 5-3(c)**) has finer PAGs as compared to the Ar-shielded one (**Figure 5-3(a)**). The grain-refining effect of N₂ shielding gas in non-heat treatment (NHT) condition has been reported before for the L-PBF 17-4 PH SS [5]. The finer grain structure of the N₂-shielded specimens in NHT condition then gives rise to finer PAGs after CA heat treatment.

The finer PAGs result in finer lath martensite upon cooling; as seen in **Figure 5-3(d)**, the N₂-shielded specimen has finer (~600 nm) lath martensite than the Ar-shielded specimen (~1200 nm) shown in **Figure 5-3(b)**. Similar results have been reported in the previous study [5]. Accordingly, the martensitic blocks in the PAGs can have a higher fraction of lath martensite for the N₂-shielded specimen. It has been shown that the martensite in L-PBF 17-4 PH SS are twin-based, holding the 60° misorientation angle with the matrix [163]. This can be seen in **Figure 5-3(e)**, which compares the fraction of

misorientation angles for the N₂-shielded specimens with that of Ar-shielded ones. A higher fraction of 60° misorientation angle for the N₂-shielded specimens shows the higher fraction of lath martensite boundaries compared to that of the Ar-shielded ones.

In addition to the variation in the grain structure of the Ar-shielded and N₂-shielded specimens, there are differences in the chemical analysis/elemental distribution of the specimens fabricated under different shielding gas types (i.e., Ar and N₂). The SEM image, elemental maps, X-ray energy spectra, and composition of the Ar- and N₂-shielded specimens are shown in **Figure 5-4(a)** and (b), respectively. The difference between Ar- and N₂-shielded specimens in chemistry is only visible in the redistribution of the elements, while the quantitative values are essentially identical.

On the contrary to the N₂-shielded specimens, there is a segregation of Cr element in Ar-specimen, showing the presence of δ -ferrite in the microstructure. Interestingly, there is a depletion of Ni and Cu in the δ -ferrite, as these elements are not ferrite stabilizers. As seen for the N₂-shielded specimen in **Figure 5-4(b)**, there are nano-size Cu-, Nb-, Mo-, and Si- rich precipitates in the microstructure, whereas **Figure 5-4(a)** presents the presence of coarser Cu-, Nb-, Mo-, and Si- rich precipitates in the microstructure of the Ar-shielded specimen. In addition, some of the very fine black specs, as seen in the SEM images in **Figure 5-4(a)** and (b), are in fact the nano-size pores that may have been inherited from the powder particles. To validate, the microstructure of the powder particles is polished and examined in high magnification in **Figure 5-5**, which revealed nano-size pores in the powder particles. Nevertheless, these nano-size pores may not play a significant role in diminishing the structural integrity of the material. Further investigations may need to be carried out to confirm.

5.4.2. Defect-Structure

XCT analysis was conducted on randomly selected Ar-shielded and N₂-shielded specimens with different geometries to compare their defect content. The visualization and statistical results are presented in **Figure 5-6**. The scans were performed on a 6.5-mm length in the middle of the specimen gages. The 'risk volume', defined as the volume within the specimen that experiences >95% of the maximum stress, of each geometry is indicated by black dashed lines and arrows. The risk-volume for the uniform gage specimen is the entire gage volume; note that only 6-mm of the gage is shown in **Figure 5-6(a)**. For the hourglass (**Figure 5-6(b)**) and ultrasonic (**Figure 5-6(c)**) specimens, the risk-volume is obtained using the finite element analysis (FEA) to be 32 mm³. For the uniform gage section, the risk-volume is found by FEA to be 122 mm³. The number of the defects in each corresponding risk-volume found by FEA was normalized by the total count of defects in the total scanned volume for statistical analysis. It is worth noting that the defects with the size of <10 μm were excluded to avoid false defect detection from noise.

As seen, regardless of the geometry, the Ar-shielded specimens contain larger and more defects than the N₂-shielded counterparts. It has been reported that using N₂ shielding gas to fabricate L-PBF 17-4 PH SS can reduce the size and population of defects compared to those in Ar-shielded specimens [162]. Furthermore, due to the small risk-volume of the hourglass and ultrasonic specimens (32 mm³) compared to the uniform gage (169 mm³, for the scanned volume here), fewer and smaller defects may be captured. Hence, these specimens are expected to have better fatigue performance than the uniform gage specimens.

5.4.3. Fatigue Behavior

The fatigue data including the \sqrt{area} of crack initiating defects of L-PBF 17-4 PH SS for different specimen geometries (i.e., uniform gage, hourglass, and ultrasonic) are listed in **Table 5-1** and **Table 5-2** for the Ar-shielded and N₂-shielded specimens, respectively. According to the defined run-out life criteria (i.e., $>10^7$ reversals) for conventional fatigue tests at 10 Hz, the Ar-shielded uniform gage section and hourglass specimens reached run-out at 500 MPa (see **Table 5-1**), while N₂-shielded counterparts reached run-out at 550 MPa. In contrast, failure was detected for all ultrasonic specimens, including those tested under much lower stress amplitudes. This calls for caution when applying conventionally defined fatigue limits to designs for extended service life.

5.5. Discussion on the Experimental Results

5.5.1. Effect of Geometry on Fatigue Behavior

Comparing different specimen geometries (i.e., uniform gage vs. hourglass) under conventional fatigue testing in **Figure 5-7**, it can be seen that hourglass specimens exhibit slightly superior fatigue performance as compared to the uniform gage specimens fabricated under Ar shielding gas. However, the difference in fatigue life of N₂-shielded hourglass and uniform gage specimens is minimal. In general, hourglass specimen has been reported to have superior fatigue performance compared to the uniform gage specimens [159]. This is attributed to the lower risk-volume in hourglass specimens; therefore, there is a lower probability of the presence of defects within this volume initiating the cracks. As seen in **Figure 5-6(a)**, higher frequency (cyclic strain rate) of defects is present in the uniform gage section specimens as compared to those of hourglass specimens in **Figure 5-6(b)** and (c). This is attributed to the larger risk-volume of uniform gage specimens than

the hourglass ones. Therefore, the probability of seeing larger defects in the uniform gage specimens is significantly higher, leading to reduced fatigue lives—especially at lower stress amplitudes.

5.5.2. Effect of Shielding Gas Type on Fatigue Behavior

Fatigue behavior of the Ar-shielded and N₂-shielded specimens is compared in different geometries (i.e., uniform gage, hourglass, and ultrasonic) and fatigue regimes (LCF to VHCF) in **Figure 5-8**. Note that the hollow markers and arrows indicate run-out tests, i.e., the specimens reaching 10⁷ reversals using the conventional fatigue testing (**Figure 5-8(a)** and (b)) and 10⁹ reversals using the ultrasonic fatigue testing (**Figure 5-8(c)**) without failure. It can be seen in **Figure 5-8(a)** that N₂-shielded specimens with uniform gage sections exhibit slightly superior fatigue lives in the mid cycle fatigue (MCF), and considerably higher fatigue lives in HCF regimes as compared to the Ar-shielded ones. For the hourglass specimens shown in **Figure 5-8(b)**, fatigue lives of Ar-shielded and N₂-shielded specimens are generally comparable. However, as seen in **Figure 5-8(c)**, N₂-shielded, ultrasonic specimens outperform the Ar-shielded counterparts in VHCF regimes.

The finer microstructure (i.e., in terms of lath thickness and the spacing between precipitates) in N₂-shielded specimens seen in **Figure 5-3** and **Figure 5-4** increases the strength of the material and consequently assists with the higher fatigue resistance of N₂-shielded specimens relative to the Ar-shielded counterparts. In addition, it has been shown that N₂-shielded specimens possess higher ductility than the Ar-shielded counterparts, which is due to a higher fraction of retained austenite and the absence of detrimental δ-ferrite in the microstructure [128,164]. The slightly higher fatigue lives of N₂-shielded

specimens in the MCF regime may be ascribed to its higher cyclic fracture toughness (i.e., higher strength and ductility) than the Ar-shielded ones.

In the HCF and VHCF regimes, the fewer and smaller size of volumetric defects in N₂-shielded specimens (see **Figure 5-6**) improves the fatigue life compared to the Ar-shielded ones. In addition, the higher fraction of lath martensite boundaries seen in **Figure 5-3(e)** may also contribute to the fatigue enhancement. It has been reported for the martensitic steels that slip systems are not all activated under high frequencies [165]. The dislocations aligned with the corresponding inactive slip systems reside within the lath martensite, decelerating the crack initiation and propagation along with the lath martensite [166]. The lath martensite boundaries themselves also serve as crack growth barriers and higher fraction them in N₂-shielded specimens inhibits early crack propagation.

The difference in fatigue performance of the Ar-shielded and N₂-shielded specimens are more apparent among uniform gage specimens compared to the hourglass ones. For the uniform gage specimens, the stress is distributed to a higher volume of material, whereas lower volume of material is experiencing the higher stress in hourglass specimens. More defects observed in larger risk volume in uniform gages are more representative of the true defects statistics as the result of Ar and N₂ shielded materials. Accordingly, hourglass specimens may not represent the fatigue resistance of the material as much as the uniform gage counterparts do.

Fatigue behavior of L-PBF 17-4 PH SS are compared for the Ar-shielded and N₂-shielded L-PBF 17-4 PH SS specimens, considering the frequency (cyclic strain rate) effect, in **Figure 5-9(a)** and (b), respectively. It can be seen that there is no apparent frequency (cyclic strain rate) effect at the high stress amplitude (700 MPa); the hourglass

Ar-shielded and N₂-shielded specimens tested via the conventional fatigue testing (10 Hz) and ultrasonic fatigue testing (20 kHz), exhibit similar fatigue lives. However, for the Ar-shielded specimens, ultrasonic specimens (20 kHz) exhibit inferior fatigue life to the hourglass specimens (10 Hz) at/below 600 MPa, while there is not much deviation in fatigue lives of the ultrasonic and hourglass N₂-shielded specimens tested at/below 600 MPa.

Interestingly, as shown in **Figure 5-6**, the defect size for the Ar-shielded ultrasonic specimens is comparable and, in most cases, even smaller than those of the hourglass conventional fatigue specimens, which is expected to result in longer fatigue lives for the ultrasonic specimens than the hourglass ones. However, the frequency effect might have deteriorated the fatigue performance of the Ar-shielded ultrasonic specimens as compared to the hourglass counterparts. As seen in **Figure 5-4(a)**, there is Cr segregation and δ -ferrite formation in the microstructure of the Ar-shielded specimens, while using N₂ as the shielding gas prohibited the δ -ferrite formation and stabilized austenite to be retained in the microstructure. Krupp et al. [167] showed that Cr segregation in martensitic steels leads to more fatigue damage under high frequencies (20kHz). The damage under high frequencies manifests itself in protrusion bands with high density, forming shallow fatigue cracks.

It is worth noting that, due to the run-out criterion of the conventional testing method being at 10⁷ reversals; only ultrasonic specimens were tested at 450 and 475 MPa. It is however assumed that the difference in fatigue lives between the two testing methods for the Ar-shielded specimens would have persisted at the lower stress levels at 450 and 475 MPa if the specimens were allowed to run to failure. However, based on the trend seen at

stress levels above 500 MPa (**Figure 5-9(b)**), it is less likely for the N₂-shielded specimens to show a frequency effect in lower stress amplitudes.

5.5.3. Failure Analysis

The fracture surfaces of Ar-shielded and N₂-shielded specimens with different geometries are examined and compared to assess the influence of the shielding gas type and geometry on the fatigue failure mechanism of the L-PBF 17-4 PH SS. Fracture surfaces of selected Ar-shielded and N₂-shielded L-PBF 17-4 PH SS specimens with uniform gage tested at 550 MPa are compared in **Figure 5-10**. It can be seen that for both Ar-shielded and N₂-shielded specimens, the crack started from surface pores. Crack initiation from surface pores in uniform gage section specimens is well established for most non-HIPed AM materials with machined surface conditions [137,168]. It has also been shown that the size and location of the pores may dictate the fatigue life in an identical build orientation [156]. As seen, the N₂-shielded specimen (**Figure 5-10(b)**) with a smaller pore size outperforms the Ar-shielded counterpart (**Figure 5-10(a)**).

The fracture surfaces of the Ar-shielded and N₂-shielded L-PBF 17-4 PH SS specimens with hourglass geometry tested at 600 MPa are presented in **Figure 5-11**. Similar to the uniform gage specimens, and regardless of the shielding gas type, pores are the crack initiators. However, for the hourglass specimens, since a smaller volume of material experiences the maximum stress concentration in hourglass geometry compared to the uniform gage, fatigue life depends on the defect population probable of appearing within the risk volume. Since the density of smaller defects (20 μm or smaller) is significantly higher than large ones as shown in **Figure 5-6** and the presence of such defects even within the small risk volumes is very probable, comparable fatigue lives for the Ar-

shielded and N₂-shielded specimens with hourglass geometry (see **Figure 5-8**) were seen irrespective of the fact that N₂-shielded specimens contain fewer and smaller defects overall (**Figure 5-6**).

To understand the transition of fatigue failure mechanism for the L-PBF 17-4 PH SS at different stress levels, selected fracture surfaces of ultrasonic specimens were analyzed in VHCF regimes. Fracture surfaces of the ultrasonic Ar-shielded and N₂-shielded specimens are shown in **Figure 5-12** and **Figure 5-13**, respectively. The failure mode-fatigue data is summarized on the S-N diagram in **Figure 5-14**.

Similar to both uniform gage and hourglass specimens using conventional fatigue testing, failure in ultrasonic specimens is induced by gas entrapped pores. The fracture surfaces depicted in **Figure 5-12(a)-(c)** are ultrasonic Ar-shielded specimens tested at three different stress levels of 500 MPa, 475 MPa, and 450 MPa, respectively. There is a noticeable crack initiation transition from defects close to the surface being the primary mode of failure at high-to-mid stress levels to internal defects at lower stress levels in VHCF regime. The material at specimen surface typically experiences less constraints from the surrounding due to surface relief effect. On one hand, the surface relief permit larger plastic deformation under relatively high loading amplitudes and favors crack initiation at surface. On the other hand, under very low loading amplitudes the less material constraint at surface generates less intergranular deformation incompatibility which favor crack initiation in the internal regions [159]. The transition stress level may be related to the strength of the material, i.e., the higher the strength, the higher the transition stress.

The fracture surfaces of the ultrasonic N₂-shielded specimens are shown in **Figure 5-13(a)-(c)** at stress levels corresponding with **Figure 5-12**. A similar failure mode transition is observed from surface defects at high-to-mid stress levels to internal defects at lower stress levels. However, the shift from crack initiation at-surface to internal defects occur at 450 MPa for the ultrasonic Ar-shielded specimens, while it occurs at 500 MPa for the ultrasonic N₂-shielded specimens. This appear to correlate with the difference in strength of the Ar and N₂ shielded specimens (~50 MPa in ultimate tensile strength) [162] and the fact that N₂-shielded specimens outperform the Ar-shielded ones in VHCF regime (see **Figure 5-8**). This transition in failure mechanism (from surface pore to the internal pore crack initiation in VHCF regime) of the N₂-shielded specimens to a higher stress level (500 MPa) than that of the Ar-shielded ones (450 MPa) may be another manifestation of the higher fatigue resistance of N₂-shielded L-PBF 17-4 PH SS specimens than the Ar-shielded counterparts.

5.6. Conclusions

High cycle fatigue (HCF) and very high cycle fatigue (VHCF) behavior of L-PBF 17-4 PH SS was investigated in this study. The micro-/defect-structure of Ar-shielded and N₂-shielded specimens were examined at a similar heat treatment condition (CA-H1025) and were correlated to their fatigue performance. In addition, the fatigue behavior of the Ar-shielded and N₂-shielded specimens was evaluated for different geometries (i.e., hourglass vs. uniform gage section) and frequencies (i.e., 20 kHz vs. 10 Hz). The following conclusions can be drawn from the experimental results obtained in this study:

1. N₂-shielded L-PBF 17-4 PH SS specimens containing finer PAG resulted in finer lath martensite than the Ar-shielded ones. In addition, N₂ shielding gas prohibited the formation of δ -ferrite in the microstructure relative to the Ar shielding gas.

2. Comparable LCF and HCF fatigue results were obtained for the hourglass Ar-shielded and N₂-shielded specimens, while N₂-shielded uniform gage specimens outperformed Ar-shielded counterparts. This was attributed to the smaller risk-volume of the hourglass specimens compared to the specimens with uniform gage section.
3. Although there was no frequency (cyclic strain rate) effect on fatigue lives observed for the N₂-shielded counterparts, Ar-shielded specimens were found to be impacted by high frequency (cyclic strain rate); Ar-shielded specimens exhibited shorter fatigue lives under ultrasonic fatigue testing. This was due to Cr segregation and the presence of δ -ferrite in Ar-shielded specimens being more susceptible to fatigue damage under high cyclic strain rates.
4. N₂-shielded L-PBF 17-4 PH SS outperformed the Ar-shielded ones in the HCF and VHCF regimes regardless of the geometry. This was attributed to the fewer and smaller defects in the N₂-shielded specimens. In addition, δ -ferrite in the Ar-shielded specimens assisted the crack initiation and deteriorated the VHCF life of the Ar-shielded specimens.
5. In the LCF and HCF regimes, near-surface pores initiated the cracks regardless of the shielding gas type (i.e., Ar and N₂) and geometry (i.e., uniform gage and hourglass). However, crack initiation transitioned from surface to internal pores in the VHCF regime. This transition occurred at 500 MPa for the N₂-shielded specimens and 450 MPa for the Ar-shielded ones.

Structural integrity of additively manufactured (AM) products is improving with the gradual mature of the technologies making their application in modern fatigue critical

components a reality. However, design with fatigue data from conventional testing methods (such as via servohydraulic frames) is associated with apparent risks due to their life limitation typically below 10^7 cycles. Although ultrasonic fatigue testing can easily reach 10^9 cycles and therefore can be a promising alternative, the results from this study advise caution, and to carefully evaluate the effects of cyclic strain rate and specimen geometry for AM components—even for the ones fabricated with the same powder but with different process parameters (such as shield gas).

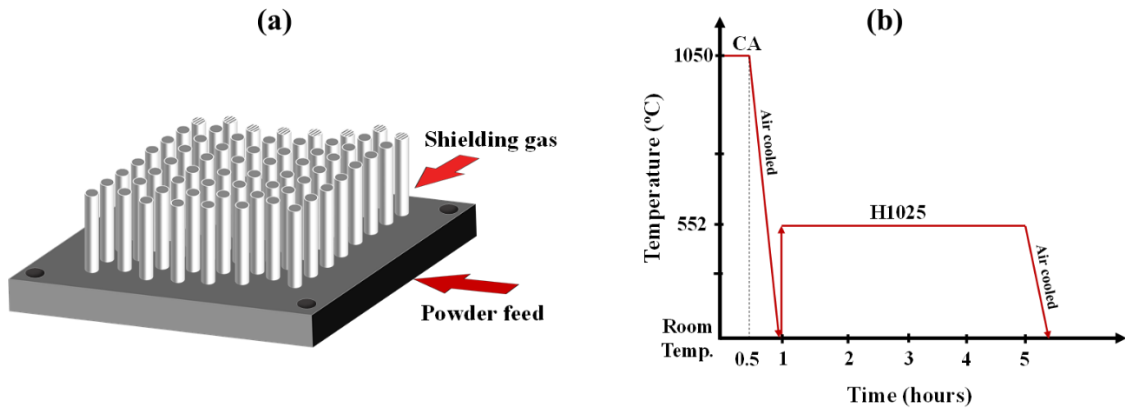


Figure 5-1. (a) The build layout used for fabricating L-PBF 17-4 PH SS bars under Ar and N₂ shielding gases and (b) schematic illustration of the heat treatment procedure.

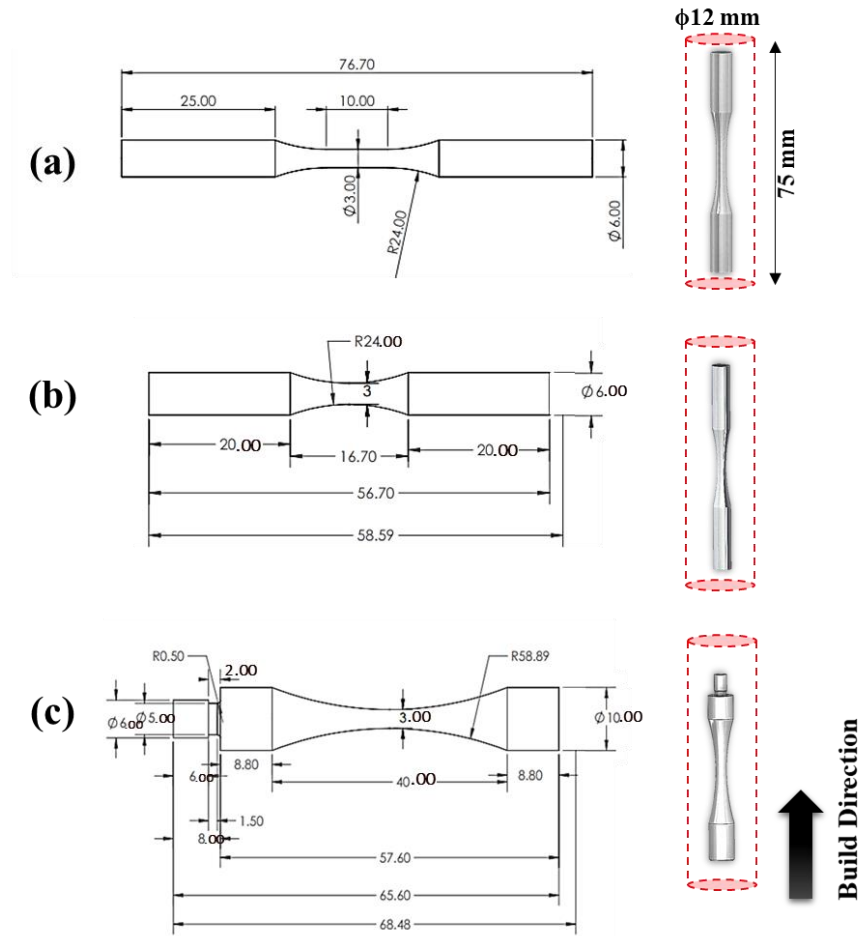


Figure 5-2. The geometry of fatigue specimens: (a) uniform gage, (b) hourglass and (c) ultrasonic specimens. All the dimensions are in mm.

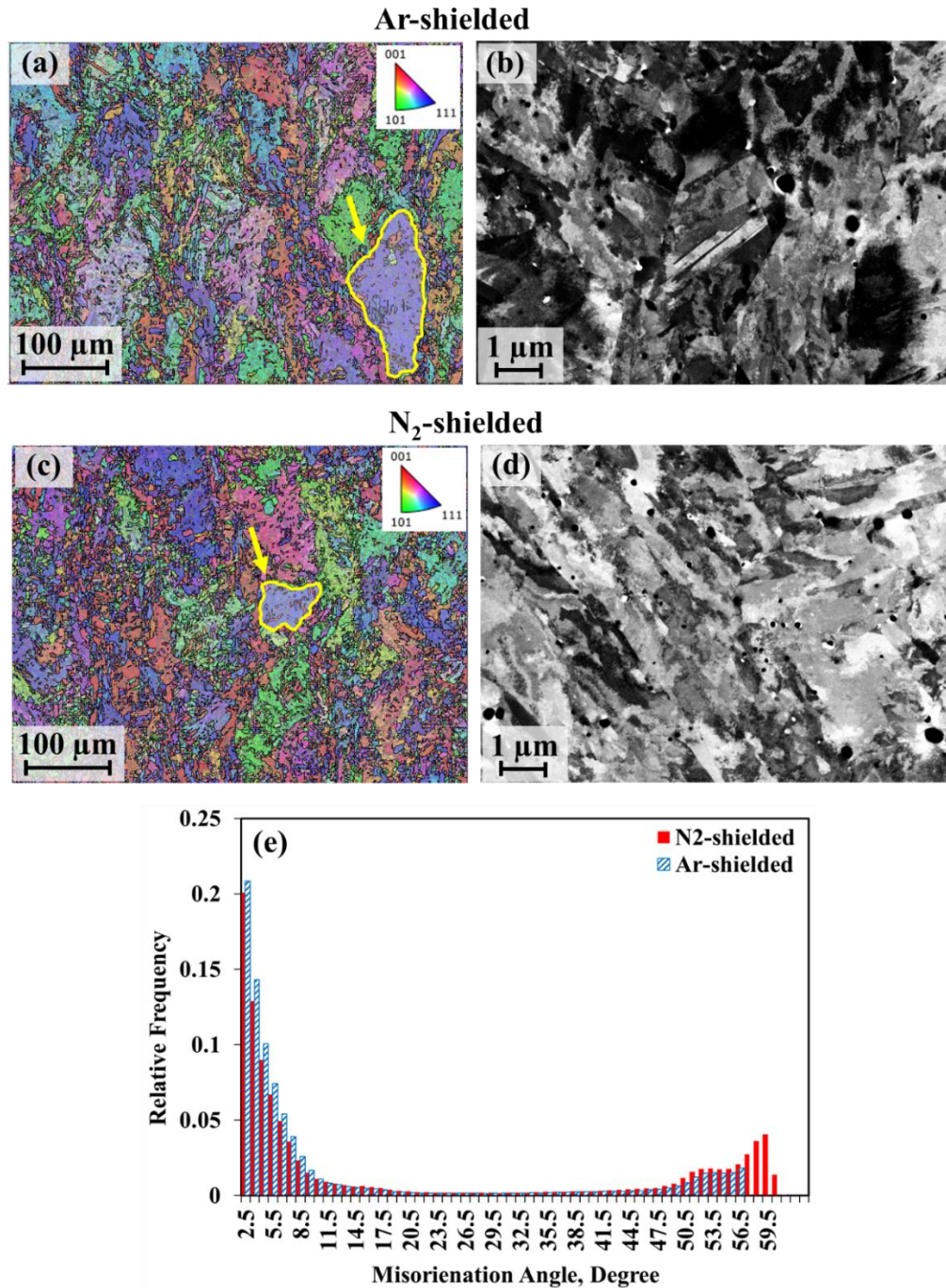


Figure 5-3. The inverse pole figure (IPF) and electron channeling contrast imaging (ECCI) results showing the microstructure of the heat-treated (CA-H1025) L-PBF 17-4PH SS specimens: (a)&(b) Ar-shielded, and (c)&(d) N₂-shielded. (e) Misorientation angle distribution for the Ar-shielded and N₂-shielded specimens obtained from (a) and (c), respectively.

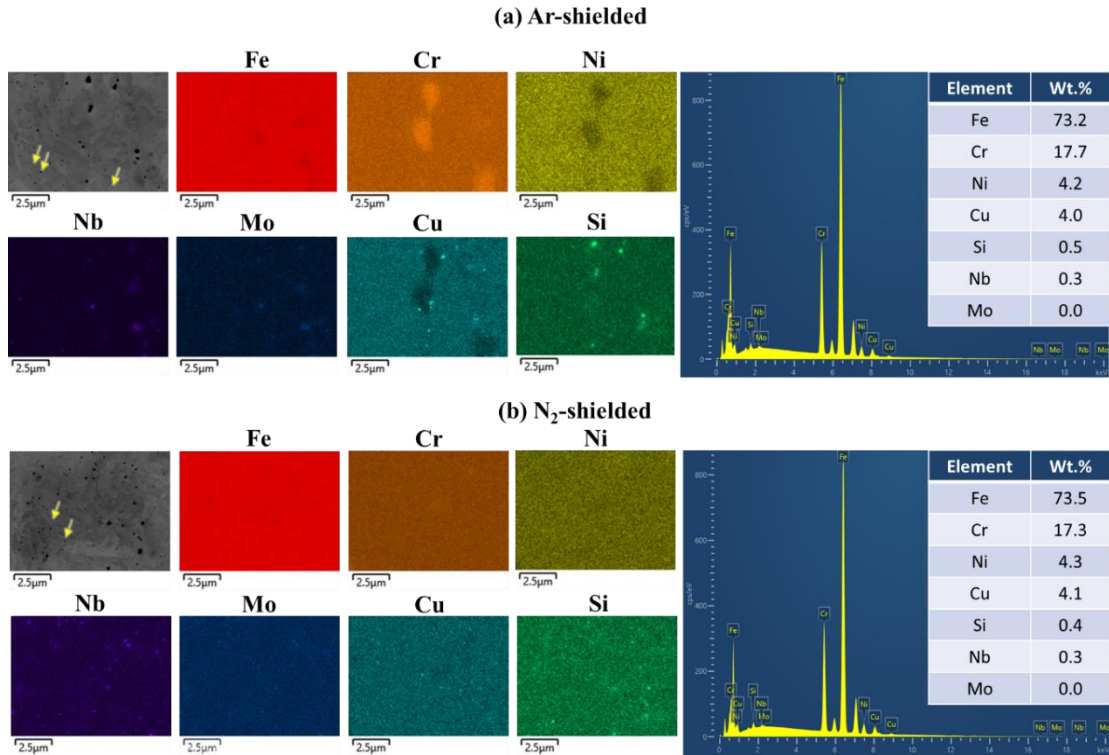


Figure 5-4. EDS analysis of the heat treated (CA-H1025) L-PBF 17-4 PH SS: (a) Ar-Shielded and (a) N₂-shielded specimens.

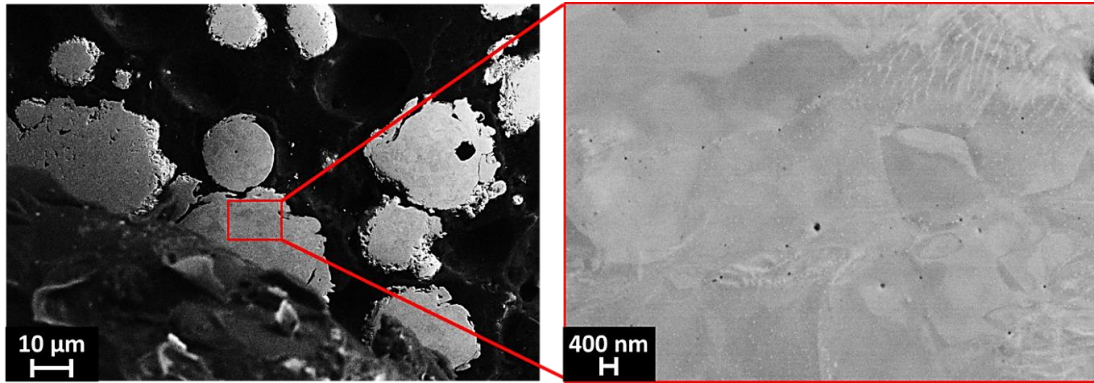


Figure 5-5. SEM micrographs of the polished powder particles showing the presence of nano-size pores.

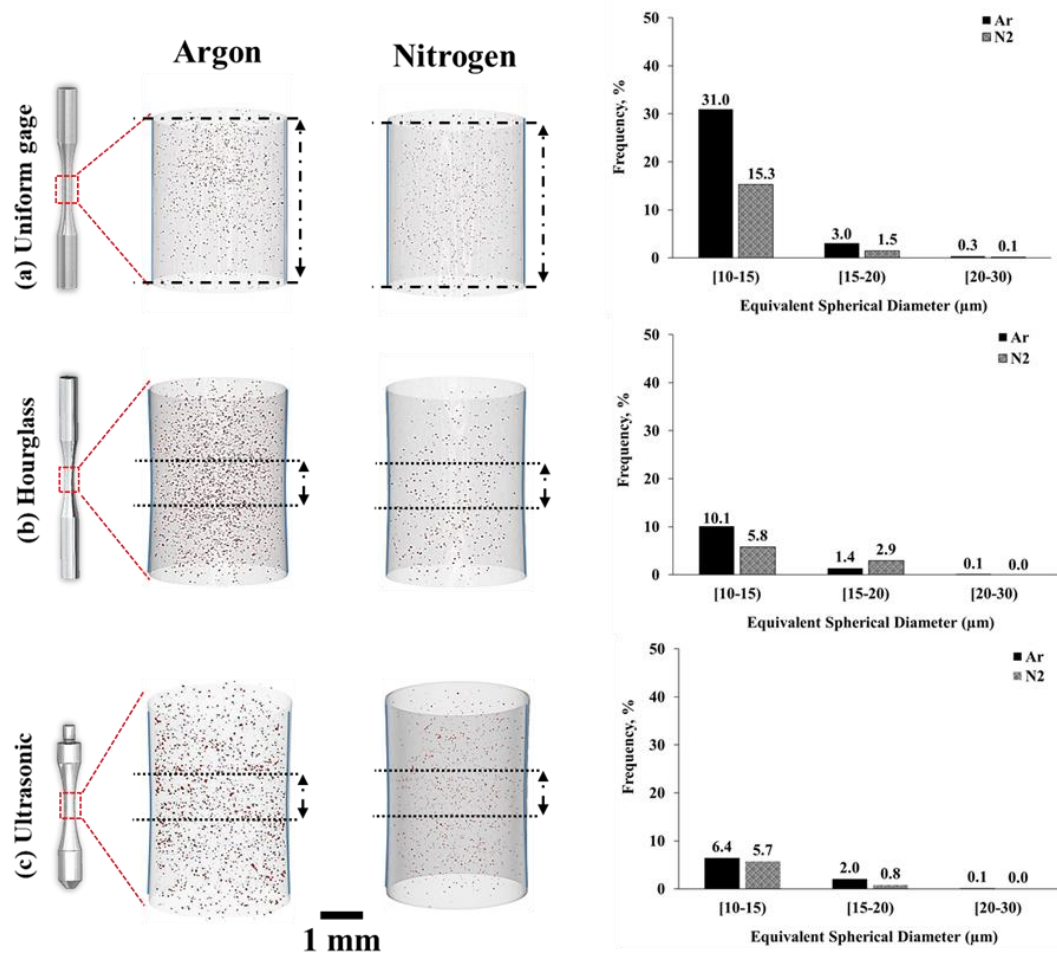


Figure 5-6. The visualization and statistical distributions of defects obtained via XCT results for Ar-shielded and N₂-shielded L-PBF 17-4 PH SS specimens with (a) uniform gage, (b) hourglass, and (c) ultrasonic geometries.

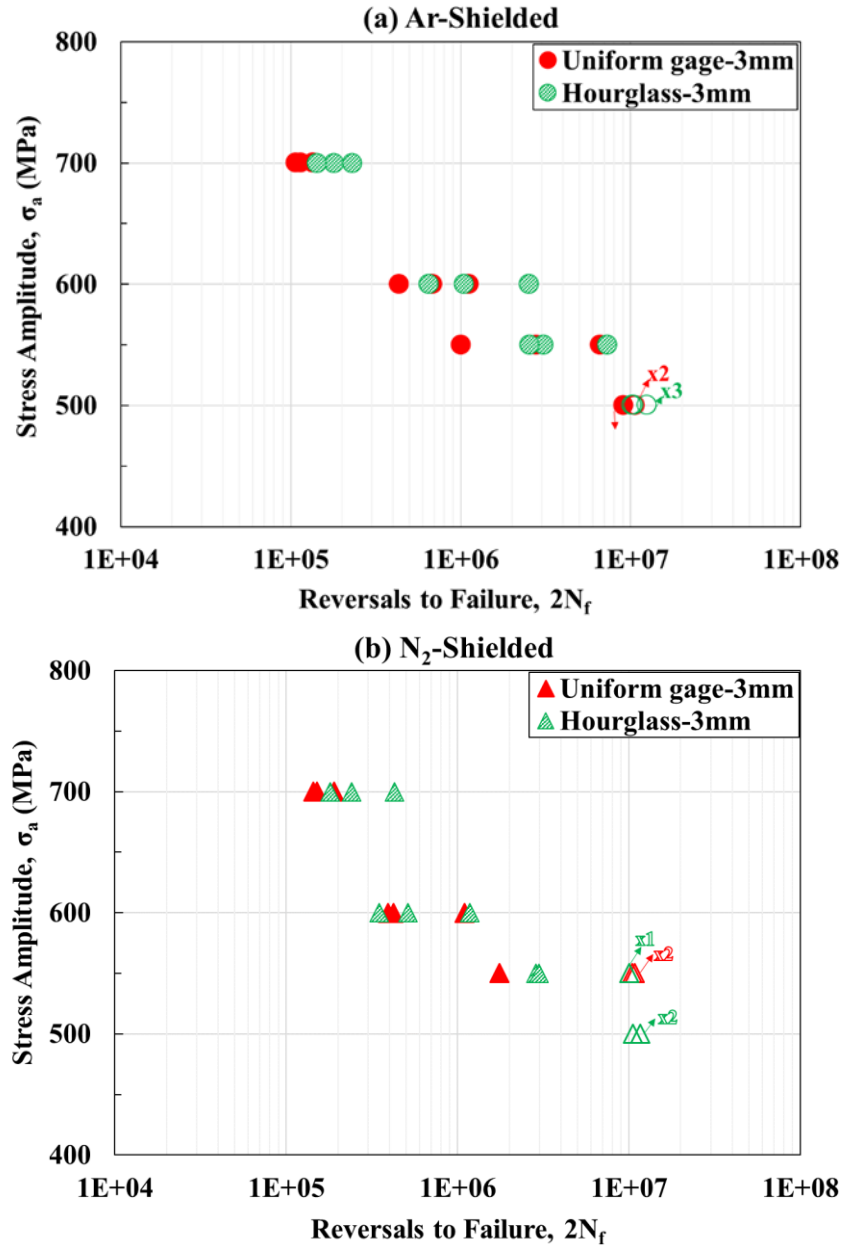


Figure 5-7. Effect of specimen geometry on fatigue behavior of (a) Ar-shielded and (b) N₂-shielded L-PBF 17-4 PH SS specimens.

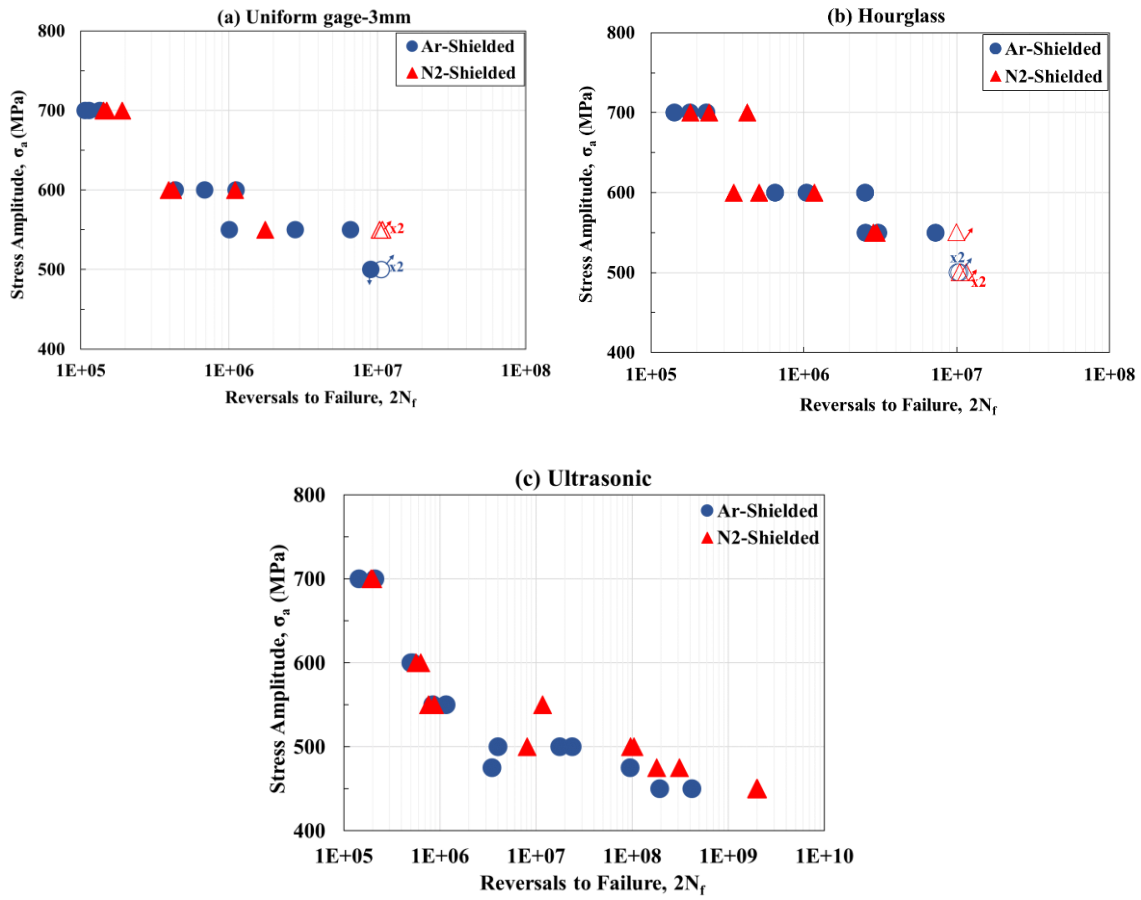


Figure 5-8. Comparing the effect of shielding gas type on the fatigue performance of L-PBF 17-4 PH SS in different life regimes (i.e., MCF to VHCF regimes) in (a) uniform gage, (b) hourglass, and (c) ultrasonic specimens.

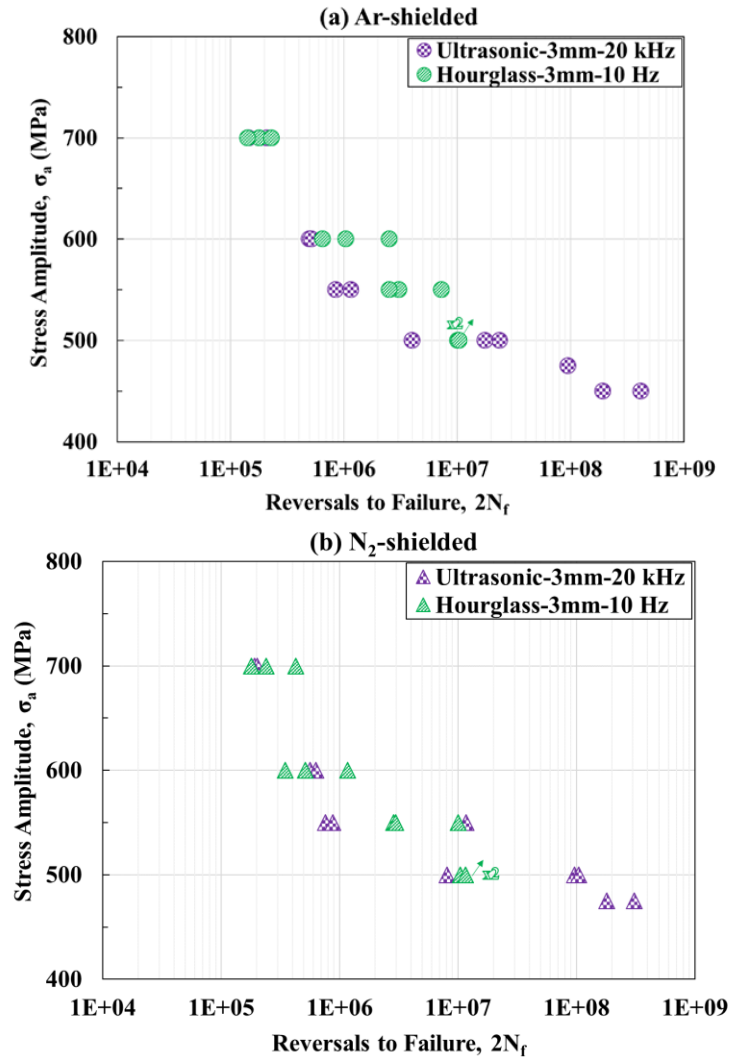


Figure 5-9. Frequency effect on the fatigue behavior of L-PBF 17-4 PH SS: (a) Ar-shielded and (b) N₂-shielded specimens.

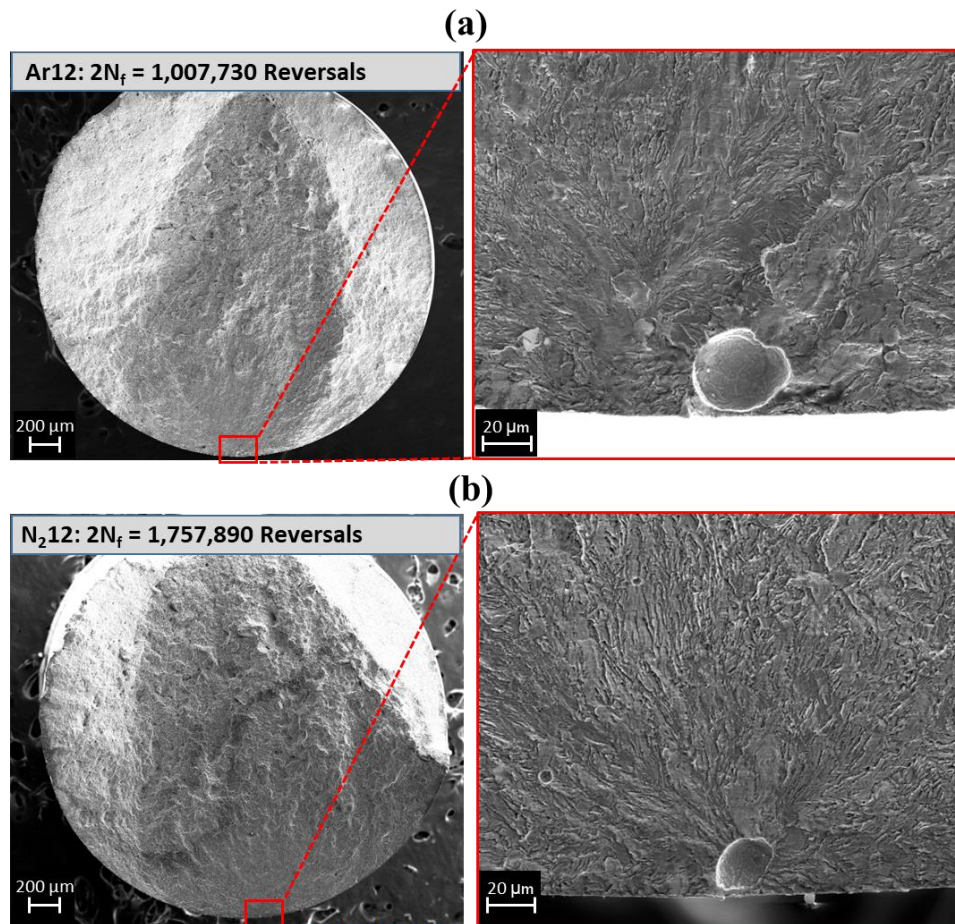


Figure 5-10. Fracture surfaces of L-PBF 17-4 PH SS specimens with uniform gage tested at 550 MPa: (a) specimen "Ar12" with 1,007,730 reversals to failure and (b) specimen "N₂12" with 1,757,890 reversals to failure.

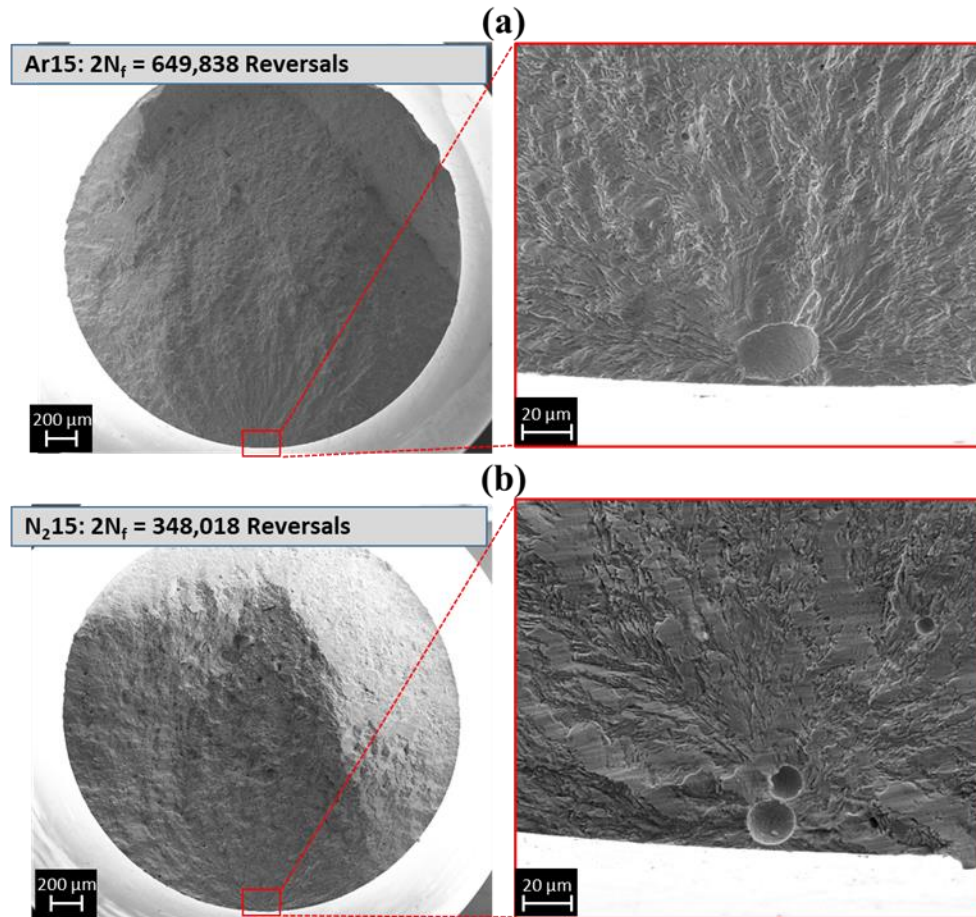


Figure 5-11. Fracture surfaces of L-PBF 17-4 PH SS specimens with hourglass geometry tested at 600 MPa: (a) specimen "Ar15" with 649,838 reversals to failure and (b) specimen "N₂15" with 348,018 reversals to failure.

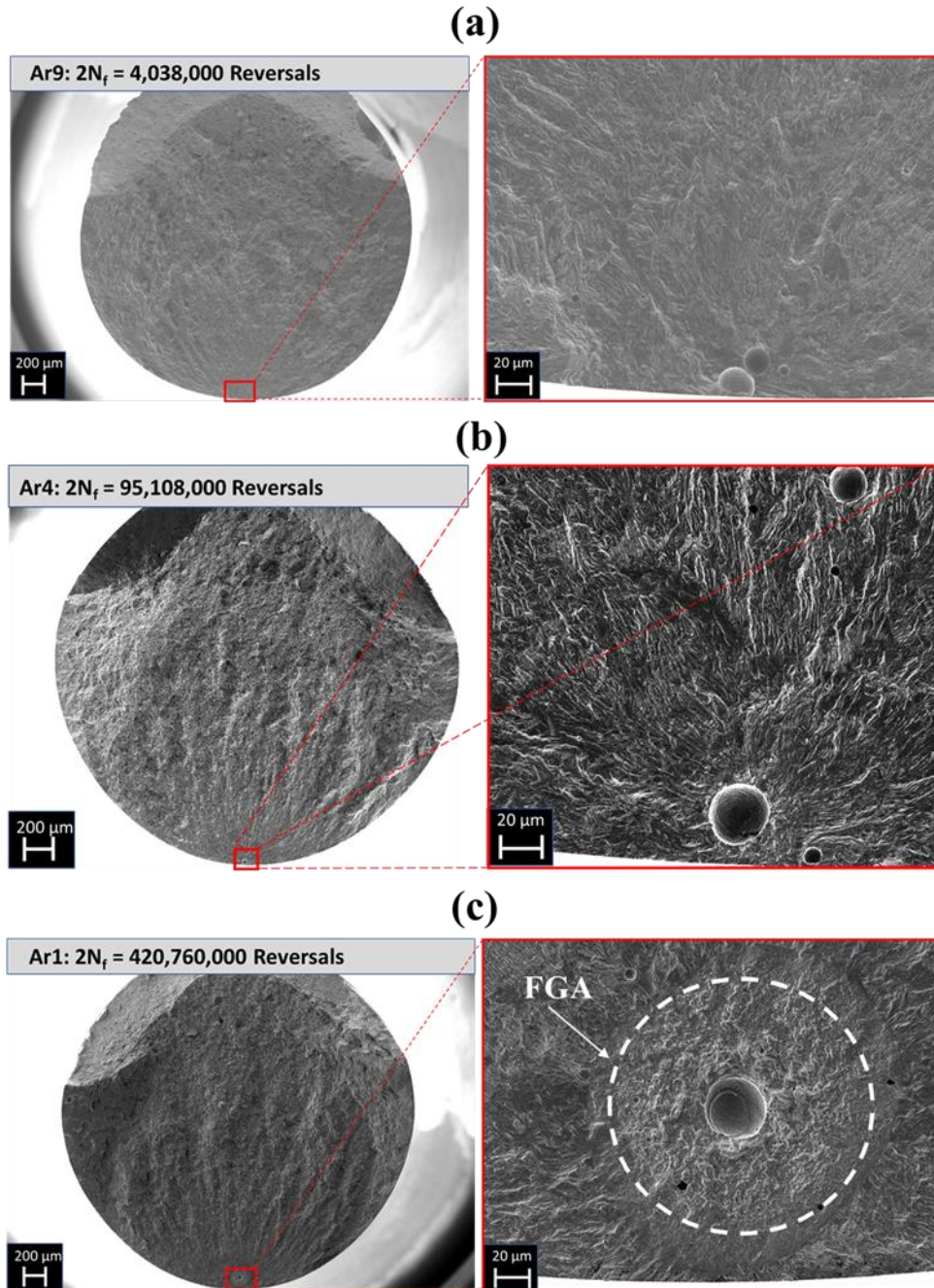


Figure 5-12. Fracture surfaces of ultrasonic Ar-shielded specimens: (a) specimen “Ar9” tested at 500Mpa with 4,308,000 reversals to failure, (b) specimen “Ar4” tested at 475Mpa with 95,108,000 reversals to failure, and (c) specimen “Ar1” tested at 450Mpa with 420,760,000 reversals to failure.

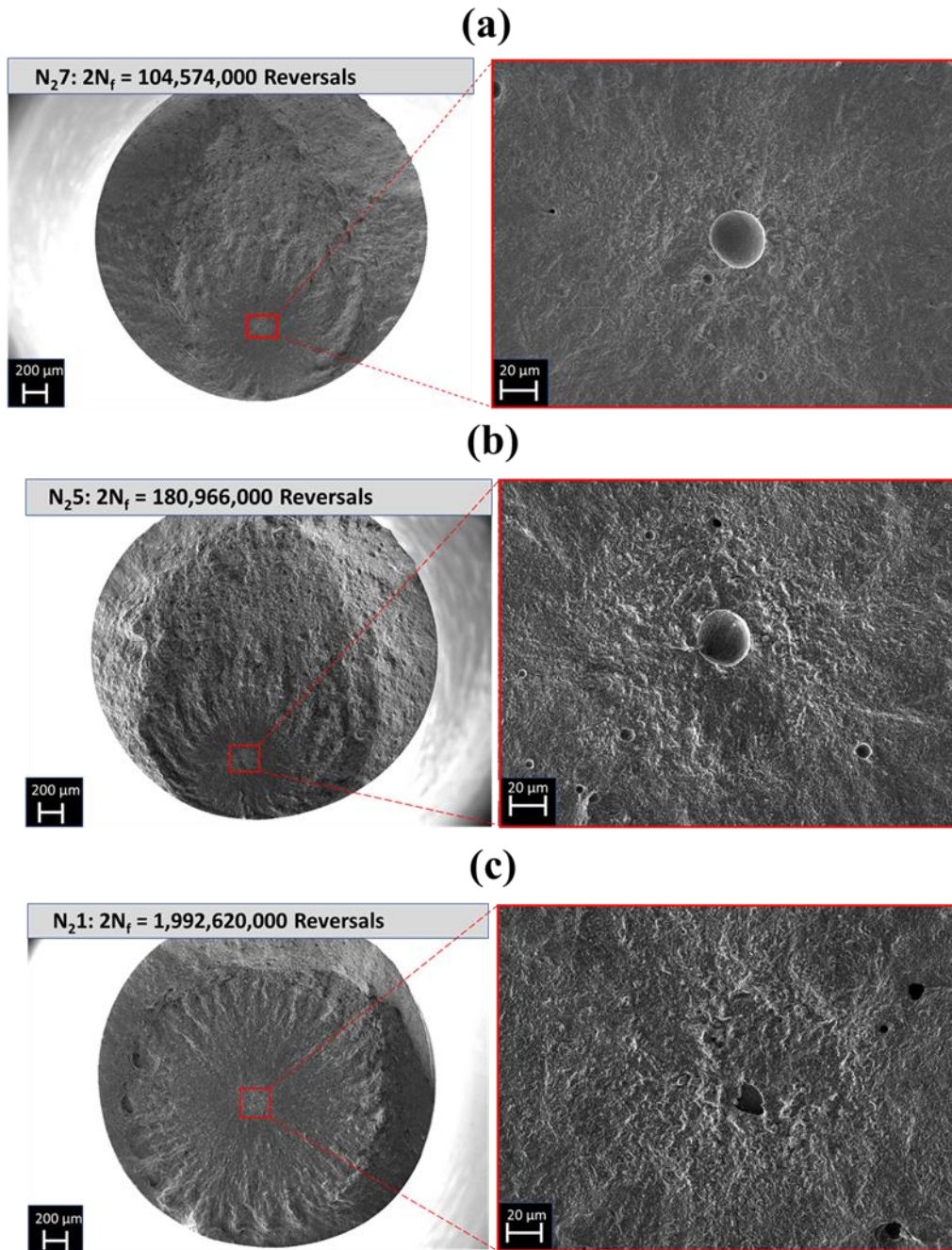


Figure 5-13. Fracture surfaces of ultrasonic N_2 -shielded specimens: (a) specimen "N₂7" tested at 500MPa with 104,574,000 reversals to failure, (b) specimen "N₂5" tested at 475MPa with 180,966,000 reversals to failure, and (c) specimen "N₂1" tested at 450MPa with 1,992,620,000 reversals to failure.

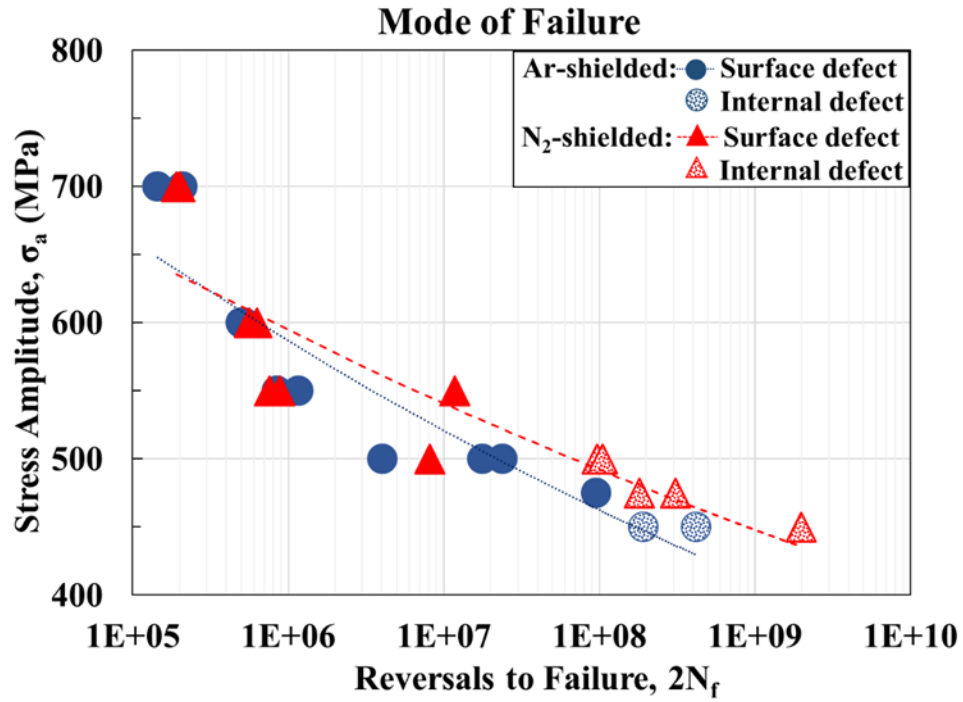


Figure 5-14. Fatigue life data indicating the mode of failure transition from surface defects to internal defects for both Ar-shielded and N₂- shielded ultrasonic specimens in VHCF regime.

Table 5-1. Fatigue data for the Ar-shielded L-PBF 17-4 PH SS specimens with different geometries.

| ID | Stress Amplitude, σ_a (MPa) | Uniform gage- 3mm | | Hourglass- 3mm | | Ultrasonic- 3mm | |
|-----------|------------------------------------|------------------------------|---------------------------------|------------------------------|---------------------------------|------------------------------|---------------------------------|
| | | Reversals to Failure, $2N_f$ | \sqrt{area} (μm) | Reversals to Failure, $2N_f$ | \sqrt{area} (μm) | Reversals to Failure, $2N_f$ | \sqrt{area} (μm) |
| 1 | 450 | No test | N/A | No test | N/A | 420,760,000 | 33* |
| 2 | | | | | | 193,490,000 | 24* |
| 4 | | | | | | 95,108,000 | 27 |
| 7 | 500 | > 10,636,324 | N/A | >10,456,162 | N/A | 23,688,000 | 15 |
| 8 | | 9,051,222 | 18 | > 10,177,524 | N/A | 17,682,000 | 16 |
| 9 | | >10,000,000 | N/A | >12,488,716 | N/A | 4,038,000 | 17 |
| 10 | 550 | 6,621,478 | 16 | 7,267,822 | 14 | 1,155,820 | 16 |
| 11 | | 2,802,364 | 23 | 3,075,774 | 18 | 846,700 | 22 |
| 12 | | 1,007,730 | 31 | 2,537,966 | 18 | No test | N/A |
| 13 | 600 | 1,122,396 | 20 | 2,522,354 | 18 | 519,400 | 15 |
| 14 | | 687,072 | 19 | 1,043,884 | 25 | 496,940 | 14 |
| 15 | | 435,664 | 23 | 649,838 | 24 | No test | N/A |
| 16 | 700 | 135,472 | 15 | 230,654 | 13 | 209,680 | 18 |
| 17 | | 114,514 | 27 | 179,714 | 21 | 144,604 | 18 |
| 18 | | 107986 | 23 | 142,772 | 19 | No test | N/A |

*Internal defects far from the specimen's surface.

Table 5-2. Fatigue data for the N₂-shielded L-PBF 17-4 PH SS specimens with different geometries.

| ID | Stress Amplitude, σ_a (MPa) | Uniform gage- 3mm | | Hourglass- 3mm | | Ultrasonic- 3mm | |
|----|------------------------------------|------------------------------|---------------------------------|------------------------------|---------------------------------|------------------------------|---------------------------------|
| | | Reversals to Failure, $2N_f$ | \sqrt{area} (μm) | Reversals to Failure, $2N_f$ | \sqrt{area} (μm) | Reversals to Failure, $2N_f$ | \sqrt{area} (μm) |
| 1 | 450 | No test | N/A | No test | N/A | 1,992,620,000 | 15* |
| 4 | 475 | | | | | 308,700,000 | 20* |
| 5 | | | | | | 180,966,000 | 29* |
| 7 | 500 | | | >10,496,378 | N/A | 104,574,000 | 29* |
| 8 | | | | > 11,592,826 | N/A | 96,284,000 | 32* |
| 9 | | | | No test | N/A | 8,106,200 | 17 |
| 10 | 550 | >10,811,080 | N/A | >10,000,000 | N/A | 11,711,200 | 15 |
| 11 | | >10,407,386 | N/A | 2,986,876 | 25 | 759,240 | 25 |
| 12 | | 1,757,890 | 22 | 2,851,652 | 18 | No test | N/A |
| 13 | | 1,097,884 | 24 | 1,172,000 | 22 | 632,040 | 21 |
| 14 | | 600 | 421,230 | 32 | 511,472 | 19 | 562,220 |
| 15 | 392,808 | | 35 | 348,018 | 24 | No test | N/A |
| 16 | 700 | 190,514 | 27 | 426,756 | 22 | 200,640 | 32 |
| 17 | | 150,542 | 23 | 240,604 | 19 | 191,814 | 18 |
| 18 | | 143,290 | 22 | 180,958 | 12 | No test | N/A |

*Internal defects far from the specimen's surface.

**CHAPTER 6: VERY HIGH CYCLE FATIGUE BEHAVIOR OF ADDITIVELY
MANUFACTURED 17-4 PH STAINLESS STEEL: EFFECT OF HEAT
TREATMENT AND SPECIMEN GEOMETRY**

The following chapter is ready to be submitted to International Journal of Fatigue (IJF) in 2022.

Nezhadfar, P.D., Nandi, I., Welsh, J., Simsiriwong, J., Shamsaei, N., Very high cycle fatigue behavior of additively manufactured 17-4 PH stainless steel: effect of heat treatment and geometry, International Journal of Fatigue.

6.1. Abstract

This study investigates the effect of heat treatment and specimen geometry on the high cycle fatigue (HCF) and very high cycle fatigue (VHCF) performance of laser powder bed fused (L-PBF) 17-4 precipitation hardened (PH) stainless steel (SS) fabricated under N₂-shielding gas. The cylindrical bars were machined into two types of specimen geometry (uniform gage and hourglass) and subjected to three different heat treatment conditions: non-heat treated (NHT), CA-H900, and CA-H1025. Uniaxial fully-reversed fatigue tests were conducted on the uniform gage and hourglass L-PBF 17-4 PH SS specimens to capture the effect of heat treatment and geometry on the fatigue behavior up to the HCF regime. Ultrasonic fatigue tests were carried out on the hourglass specimens to obtain the influence of heat treatment on the VHCF behavior of the material. The experimental results show that the specimen geometry in this study minimally affects the fatigue resistance of L-PBF 17-4 PH SS, whereas heat treatment can significantly enhance the fatigue performance of the material. The HCF and VHCF performance of L-PBF 17-4 PH SS is improved when the specimens are subjected to CA-H900 or CA-H1025 heat treatments compared to the specimens in NHT condition. This is attributed to the transformation of the microstructure from columnar body-centered cube (BCC) grains in NHT condition to the fine lath martensite after heat treatment. The CA-H1025 heat-treated specimens exhibit slightly longer fatigue lives than the CA-H900 ones in the VHCF regime. The higher strength and less ductility of specimens in the CA-H900 condition relative to the CA-H1025 result in more defect sensitivity and lower fatigue crack propagation resistance for the CA-H900 heat-treated L-PBF 17-4 PH SS. In addition, gas-entrapped pores are found to be responsible for crack initiation in all specimens in this study. Fatigue cracks initiate from either surface or sub-surface pores for all specimens up to the HCF regime. For the heat-treated specimens, fatigue cracks initiate from either sub-surface or internal pores in the VHCF regime. However, there is no relation between the location of pores to the surface and the heat treatment condition is observed.

6.2. Introduction

Post-manufacturing thermal processes (e.g., hot isostatic pressing (HIP), stress-relieving, solutionizing, and aging) have been known as the critical step in part production to improve their mechanical properties [35,169]. For additive manufacturing (AM) processes, post-process heat treatment is commonly applied to metallic AM parts to modify their microstructure by, for example, homogenizing the microstructure, inducing precipitates, and/or altering the morphology and crystallographic texture of grains to achieve the desired part property and performance [155,170]. In addition, depending on the material type, heat treatment can be employed to reduce the residual stresses of parts inherited from high solidification and cooling rates in AM processes [11]. Combined with high-pressure thermal treatments such as HIP, internal gas-entrapped pores in AM parts can also be eliminated, resulting in improved fatigue resistance [31,143].

For 17-4 precipitation hardened (PH) stainless steel (SS), it has been shown that, due to the high cooling and solidification rates of the AM processes, the solidification order for the 17-4 PH SS is changed from $L \rightarrow L+\delta \rightarrow \delta+\gamma \rightarrow \delta+\alpha'$ to $L \rightarrow L+\delta \rightarrow \delta$ [18,162]. The as-built microstructure (i.e., non-heat treated (NHT)) of laser powder bed fusion (L-PBF) 17-4 PH SS is reported to be columnar body-centered cubic (BCC) ferrite grains. Therefore, L-PBF 17-4 PH SS typically requires post-process heat treatment to change its ferritic microstructure to a martensitic microstructure [62]. In addition, compared to L-PBF 17-4 PH SS specimens in NHT condition, it has been observed that solution heat treatment followed by aging can re-distribute δ -ferrite and induce nano Cu-enriched precipitates, which contribute to an increased tensile strength [82]. Despite the improvement in tensile strength due to heat treatment, the high cycle fatigue (HCF) resistance of L-BPF 17-4 PH

SS can be deteriorated. For instance, after applying CA-H900, which is the most common heat treatment for 17-4 PH SS, the material can be more sensitive to the presence of volumetric defects (i.e., pores, lack of fusion (LoF)) and the fatigue performance is alleviated [5,96]. Therefore, the effects of post-process heat treatment on the microstructure features and mechanical properties of AM 17-4 PH SS should be carefully investigated to achieve the required mechanical behavior for a given application [30,155].

Although direct aging (i.e., aging after the fabrication without solutionizing) can increase the tensile strength of L-PBF 17-4 PH SS to some extent, its fatigue crack growth (FCG) behavior is deteriorated due to the presence of string-like δ -ferrite on the grain boundaries as reported by Nezhadfar et al. [82]. The cracks formed on the interface of the δ -ferrite with the matrix, deviated the crack growth path from mode I to mode II, along the columnar grains and resulted in abnormality in FCG behavior of L-PBF 17-4 PH SS. To eliminate the columnar grains and re-distribute the δ -ferrite in the microstructure, an additional solutionizing step, known as Condition A (CA), is required before aging. CA was performed at 1050°C for half an hour, followed by air cooling to room temperature. It was shown that performing CA prior to aging resulted in a similar FCG behavior with the wrought counterpart in the Paris regime [82,162]

Zhao et al. [171] studied the effects of solution heat treatment temperature and aging duration on the microstructure and tensile properties of the L-PBF 17-4 PH SS. The specimens were solution heat-treated at 940°C, 990°C, 1040°C, and 1140°C for 2 hours, followed by aging at 480°C for 4 hours. It was found that increasing the solution heat treatment temperature to 1140°C could not eliminate the δ -ferrite; however, it slightly increased the retained austenite in the microstructure. The solution heat treatment at

1040°C resulted in higher tensile strength and wear properties than other solution heat treatment temperatures.

In a different study by Li et al. [30], the effect of solution heat treatment duration on the microstructure and tensile properties of L-PBF 17-4 PH SS was investigated. The solution heat treatment was performed at 1150°C for 0.5-8 hours, followed by aging at 482°C for 1 hour. It was reported that 1 hour of solutionizing at this specific temperature resulted in a good combination of strength and ductility. The yield and ultimate tensile strength were found to be comparable to those reported by KC et al. [172], where L-PBF 17-4 PH SS specimens were subjected to solution heat treatment at 1050°C for 0.5 hour, and aging at 482°C for 1 hour. However, the ductility of the material reported in Li et al. [30] is reduced in case of long-term homogenization, ascribed to the coarser lath martensite and precipitates.

In a comprehensive and extensive research on the effect of various standard heat treatment conditions on fatigue behavior of L-PBF 17-4 PH SS, it was shown that CA-H1025 heat treatment, 0.5 hour at 1050°C followed by aging for 4 hours at 552°C, results in superior fatigue behavior with less scatter in fatigue lives in the HCF regime compared to the CA-H900 condition [173]. This was attributed to the less sensitivity of the CA-H1025 heat treatment to the volumetric defects and surface roughness (in the as-built surface specimens) than the CA-H900 heat treatment condition in the HCF regime, due to the lower strength and higher ductility than CA-H900 heat treatment condition. The effect of heat treatment on the sensitivity of AM materials to the defects in the HCF or very high cycle fatigue (VHCF) regime is even more challenging if the geometry effects are considered. Pegues et al. [174] reported fatigue sensitivity to the gage volume; a lower

gage volume resulted in better fatigue performance. They reported that the cracks in the lower gage volume specimens initiated from the internal defects as the surface defects were removed by deep machining; therefore, longer fatigue lives were obtained for the lower gage volume specimens. However, applying a heat treatment that increases the material's sensitivity to volumetric defects may not result in a better fatigue performance even with a lower gage volume.

Therefore, in response to the challenge of appropriate heat treatment and the effect of specimen geometry on the fatigue behavior of the L-PBF 17-4 PH SS, the goal of this study is to evaluate the fatigue behavior dependency of L-PBF 17-4 PH SS on different geometries at various heat treatment conditions, particularly in HCF and VHCF regimes.

6.3. Experimental Procedures

6.3.1. Material, Fabrication, Heat Treatment, and Specimen Design

In this study, Argon atomized 17-4 PH SS powder with the chemical composition 0.01C-15.80Cr-4.60Ni-3.67Cu-0.51Mn-0.32Si-0.32Nb-0.21Mo-0.02N-0.04O-0.0035P-0.014S-0.027(Nb+Ta)-Bal.Fe (% wt.) was used for specimen fabrication. An EOS M290, an L-PBF system, was employed using the recommended process parameters as listed in **Table 6-1**. All specimens were fabricated under a nitrogen environment.

The cylindrical specimens with a height of 75 mm and diameter of 12 mm were fabricated vertically, as shown schematically in **Figure 6-1(a)**. The specimens were heat-treated and separated into different groups according to their heat treatment condition. These are non-heat treated (NHT) and CA-H900 (i.e., CA: 1050 °C/0.5 hour/air-cooled + H900: 482 °C/1 hours/air-cooled). The third group of specimens was heat-treated using CA-H1025 (i.e., CA: 1050 °C/0.5 hour/air-cooled + H1025: 552 °C/4 hours/air-cooled), which were

performed in the authors' previous study [175]. The heat treatment schedules for the CA-H900 and CA-H1025 are shown schematically in **Figure 6-1(b)**.

Each set of specimens was further machined to three different geometries, including specimens with uniform gage sections for conventional fatigue testing (**Figure 6-1(c)**), hourglass specimens for conventional fatigue testing (**Figure 6-1(d)**), and hourglass specimens for ultrasonic fatigue testing (**Figure 6-1(e)**). The conventional fatigue specimens were designed following ASTM E466, while the ultrasonic specimen was designed to achieve a natural frequency of 20 kHz. To distinguish between the different types of specimens in this study, the hourglass specimens for ultrasonic fatigue testing will be called 'ultrasonic specimens,' and the hourglass specimens for conventional fatigue testing will be called 'hourglass specimens' throughout the manuscript. All specimens were manually polished prior to testing.

6.3.2. Microstructure Characterization

A Zeiss Crossbeam 550 SEM/FIB scanning electron microscope (SEM) instrument equipped with an Oxford electron backscatter diffraction (EBSD) detector was used for microstructure characterization. Microstructure samples were cut in the transverse direction or TD, (i.e., parallel to the build direction for the L-PBF specimens), ground, and polished with 320-2500 grit SiC sandpapers, followed by final polishing using ChemoMet with 0.05 μm colloidal silica suspension. A final vibratory polishing step was carried out using a 0.02 μm colloidal silica suspension for 12 hours. Specimens were further cleansed thoroughly prior to performing EBSD analysis.

6.3.3. Fatigue Testing

For conventional fatigue testing, uniform gage section and hourglass specimens were subjected to uniaxial fully-reversed force-controlled cyclic loading using a table-top MTS test frame with 25 kN load cell. The conventional fatigue tests were carried out at a frequency of 10 Hz. For ultrasonic fatigue test, specimens were subjected to fully-reversed cyclic loading at constant stress amplitude. The tests were conducted using a Shimadzu USF-2000A piezoelectric system operated at a constant frequency of 20 kHz. Intermittent oscillation (110 msec on/800 sec off) and compressed cooled air were utilized to minimize the adiabatic heating in the specimen during ultrasonic fatigue tests. The failure of the ultrasonic specimen is specified by the changing of test frequency (by ± 500 Hz) due to the presence of a fatigue crack that alters the natural frequency of the specimen. All tests were conducted at room temperature and relative humidity

For both conventional and ultrasonic fatigue test methods, three tests were performed at each stress amplitude level to evaluate the repeatability of the results. Specimens with reversals ($2N_f \geq 10^7$ and $2N_f \geq 10^9$) were regarded as run-out for conventional and ultrasonic fatigue tests, respectively. Fracture surfaces were cleansed in a methanol bath using an ultrasonic instrument before examining the fractography of the specimens. A Zeiss Crossbeam 550 SEM was utilized for fractography analysis of the uniform gage and hourglass specimens, while a Tescan VEGA3 SEM was used for the fractography analysis of the ultrasonic specimens.

6.4. Results and Discussion

6.4.1. Effect of Heat Treatment on the Microstructure

Microstructure analysis of L-PBF 17-4 PH SS in NHT, CA-H900, and CA-H1025 conditions is shown in **Figure 6-2**. The phase map (PM) and the inverse pole figure (IPF) are presented for the plane parallel to the build direction (i.e., YZ-plane) in two different magnifications; column I is an overview, and column II is the higher magnification of the indicated rectangular in column I. Moreover, the IPF triangle, which displays the crystallographic texture of the grains, is shown for each heat treatment condition in parallel to the build direction, which is the loading direction.

As seen in **Figure 6-2(a)**, the L-PBF 17-4 PH SS in NHT condition has columnar and typical 'U' shape grains parallel to the build direction. Although Alnajjar et al. [18] reported austenite by-passing due to the high cooling rate in the L-PBF process, using nitrogen as shielding gas promotes the formation of austenite during the solidification. As seen in **Figure 6-2(a)**, column II, austenite is retained in the microstructure close to some martensitic regions. It has been reported that nitrogen shielding gas reduces the solidification rate and stabilizes the austenite. The austenite formed during the solidification will further transform to martensite, as the martensitic start temperature (i.e., M_s) is above room temperature for the L-PBF 17-4 PH SS [15,16]. However, there may be inhomogeneity in the segregation of austenite stabilizer elements, which increases the stability of austenite to be remained at room temperature. The formation of austenite during solidification would also alter the grains' crystallographic orientation, reducing the strong preferred $\langle 001 \rangle$ orientation, which has been reported for most L-PBF materials [168,176]. As seen **Figure 6-2(a)**, the grains in NHT 17-4 PH SS specimens oriented toward both

$\langle 001 \rangle$ and $\langle 111 \rangle$ crystallographic orientations. The $\langle 111 \rangle$ -oriented grains can be attributed to the formation of austenite during solidification.

After applying heat treatment on L-PBF 17-4 PH SS specimens, the columnar BCC grains, retained austenite, and martensite, will transform to a fully austenitic phase after the CA step and further transforms to martensitic microstructure after cooling to room temperature. As seen, the CA-H900 heat treatment condition has a martensitic microstructure with a very fine block and lath martensite, as shown in column II in **Figure 6-2(b)**. In addition, the crystallographic orientation of the grains rotates more toward the $\langle 111 \rangle$ orientation, and the texture intensity is alleviated due to the high cooling rate during fabrication. By increasing the aging temperature and duration of the CA-H1025 heat treatment condition (see **Figure 6-2(c)**), the martensite blocks and lath are coarsened compared to the CA-H900 one. In addition, the texture intensity is reduced further due to the austenite reversion from martensite; a small fraction of retained austenite can be seen in **Figure 6-2(c)** after applying CA-H1025 heat treatment.

6.4.2. Fatigue Behavior

The fatigue data for the NHT, CA-H900, and CA-H1025 heat-treated L-PBF 17-4 PH SS specimens with different geometries (i.e., uniform gage section and hourglass) and different fatigue testing methods (i.e., conventional vs. ultrasonic) is listed in **Table 6-2**, **Table 6-3**, and **Table 6-4**. In addition, the type, location, and \sqrt{area} of initiation defects in each specimen were also determined and tabulated. It should be noted that internal pores listed in these tables are defined as gas-entrapped pores located at 40 μ m or more away from the specimen's surface. The fatigue behavior of specimens with uniform gage section and hourglass L-PBF 17-4 PH SS specimens are compared in **Figure 6-3** to evaluate the

geometry dependency for different heat treatment conditions. The comparison is performed for up to the HCF regime for the specimens tested using a conventional fatigue test setup. The fatigue data for the CA-H1025 heat-treated L-PBF 17-4 PH SS specimens were adopted from the study by Nezhadfar et al. [175].

In the low cycle fatigue regime (LCF), i.e., at 600-700 MPa, similar fatigue behavior is observed for both specimen types (i.e., uniform gage and hourglass) for all the heat treatment conditions. In addition, it can be observed from **Table 6-2** and **Table 6-3** that, fatigue cracks in both uniform and hourglass specimens (conventional and ultrasonic testing) for a given stress amplitude and a given heat treatment condition (e.g., NHT or CA-H900) initiate from the surface pore, subsurface pore, or internal pore. However, there is no trend between pore size and specimen geometry with the fatigue lives. Similar observation (i.e., the relationship between the specimen geometry and the defect size) is observed for the LCF behavior of CA-H1025 heat-treated specimens in the study by Nezhadfar et al. [175] (see **Table 6-4**).

The differences between the fatigue lives of the hourglass and uniform gage specimens may be more prominent at the lower stress amplitude levels, where the crack initiation plays a more critical role than the crack propagation. In the mid-cycle fatigue (MCF) to the HCF regime, i.e., 550 MPa to 450 MPa, the hourglass specimens in NHT condition slightly outperform the fatigue performance of the uniform gage counterparts (see **Figure 6-3(a)**). This is due to the fact that the hourglass specimens have a smaller gage volume, which consequently leads to a smaller risk-volume (i.e., the volume within the specimen that experiences >95% of the maximum stress) than the uniform gage specimens. The risk-volume for the hourglass specimens and uniform gage ones are 32 mm³ and 122

mm³, respectively [175]. Therefore, there is a lower probability of the critical defects residing in the hourglass specimens' risk-volume compared to the specimens with uniform gage section. As a result, better fatigue resistance at lower stress levels is expected for hourglass specimens.

On the other hand, almost similar MCF and HCF fatigue results were obtained for the uniform gage and hourglass specimens in the CA-H900 and CA-H1025 conditions (see **Figure 6-3**(b) and (c), respectively). However, the scatter in fatigue results is increased for the heat-treated specimens compared to the NHT ones. Although it is expected for the hourglass specimens to have longer fatigue lives compared to the uniform gage ones, the higher strength and lower ductility of the heat-treated specimens make them more sensitive to the presence of defects compared to the NHT condition. The distance from the defect inducing failure to the nearest edge of the fracture surface is also tabulated in **Table 6-2** and **Table 6-3**. It is seen that no trend in defect location with the specimen geometry in any given heat treatment condition can be observed.

The effect of heat treatment on the fatigue behavior of L-PBF 17-4 PH SS with each particular geometry and type of fatigue testing (i.e., conventional and ultrasonic) is compared in **Figure 6-4**. Regardless of the geometry type, heat treating the L-PBF 17-4 PH SS enhances the fatigue behavior slightly in the LCF regime and significantly in the HCF and VHCF regimes compared to the NHT condition. Considering the fact that all the specimens were machined from cylindrical bars fabricated in one build plate, the size and distribution of defects will less likely be varied for different heat treatment conditions. This is seen by the similar \sqrt{area} of defects listed in **Table 6-2** and **Table 6-3**. Therefore, the

improvement in fatigue performance of the material after heat treatment is ascribed to the changes in the microstructure, not the effect of defect sizes.

As seen in **Figure 6-2**, the NHT L-PBF 17-4 PH SS grain structure is changed from columnar grains to fine lath martensite after CA-H900 or CA-H1025 heat treatment. Microstructure refinement has been reported to enhance the fatigue behavior of L-PBF 17-4 PH SS [162]. This improvement is more noticeable in the HCF and VHCF regimes as the most portion of fatigue life is spent in the crack initiation stage. It is well known that fine microstructure delays the crack initiation compared to a coarse grain structure [141]. Accordingly, the CA-H900 and CA-H1025 heat treatment conditions with a finer microstructure, as seen in **Figure 6-2**, lead to an enhanced fatigue behavior compared to the NHT L-PBF 17-4 PH SS with coarse columnar grain structure.

In **Figure 6-4(a)** and **(b)** for uniform gage and hourglass specimens tested using conventional fatigue testing, CA-H1025 heat treatment condition results in slightly better fatigue resistance of L-PBF 17-4 PH SS in the HCF regime compared to the CA-H900 condition. This is due to the lower strength and higher ductility of the CA-H1025 heat treatment condition, making the material more resilient to crack initiation and propagation compared to the specimens with CA-H900 heat treatment. In **Figure 6-4(c)**, the ultrasonic fatigue results show a comparable fatigue performance for the CA-H900 and CA-H1025 heat-treated specimens. However, it can be seen that CA-H900 results in more scatter in fatigue lives compared to the CA-H1025 heat treatment condition (see **Figure 6-4**).

As discussed earlier, the CA-H900 heat treatment condition has been reported to have higher tensile strength and lower ductility than the CA-H1025 condition [173]. This is attributed to the size of precipitates in the CA-H900 heat treatment condition, known as

the peak-age condition for the L-PBF 17-4 PH SS. However, increasing the aging duration coarsens the size of the precipitates and improves the ductility of the material. This can help with less scatter in fatigue life of the CA-H1025 heat treatment specimens compared to the CA-H900 ones. Although reducing the level of defects by modifying the process parameters, herein using nitrogen shielding gas, may help with fatigue life enhancement, CA-H900 heat treatment condition may not still be the best option for the L-PBF 17-4 PH SS due to the scatter in fatigue lives.

6.4.3. Fractography

Fractography analyses were performed on the selected failed specimens to reveal insights into the crack initiation and fatigue failure mechanism of the L-PBF 17-4 PH SS specimens with different heat treatments and geometries. It must be mentioned that the fractography analysis has been carried out on all the failed specimens, and the corresponding defect type, size, and location are listed in **Table 6-2** and **Table 6-3** for the NHT and CA-H900 heat-treated specimens, respectively. The defects size for the CA-H1025 heat-treated specimens are also listed in **Table 6-4**, which has been adopted from the study by Nezhadfar et. al [175]. It is found that surface and subsurface gas entrapped pores are the crack initiator for all specimens tested at conventional fatigue testing setup. In contrast, subsurface and internal pores are identified as the crack initiator for ultrasonic specimens.

As previously discussed, most of the fatigue life in the HCF and VHCF regimes is spent on the crack initiation, while in the LCF regime, crack(s) initiates early, and most of the fatigue life is related to the crack propagation prior to failure. Therefore, volumetric defects' size and location and the surrounding microstructure, can influence both the crack

initiation and propagation under cyclic loading. Although specimens (uniform gage, hourglass, and ultrasonic) are from the same build job, and there should not be differences in the level of defects, geometry may influence the fatigue results as the risk-volume between the hourglass and uniform gage specimens is different. In addition, heat treatment influences the microstructure and toughness of the material, which impacts crack initiation and growth.

The fracture surfaces of selected uniform gage and hourglass specimens in NHT, CA-H900, and CA-H1025 heat treatment conditions are compared in **Figure 6-5** and **Figure 6-6**. It can be seen that, regardless of the geometry (i.e., uniform gage and hourglass) and heat treatment conditions (NHT, CA-H900, and CA-H1025), cracks initiated from pores on the surface of the specimens. However, due to the microstructural differences seen in **Figure 6-2**, the crack propagation path on the fracture surfaces varies depending on the heat treatment conditions. In addition, longer fatigue life is observed for the heat-treated specimens compared to the NHT condition, which may be attributed to their fine martensitic microstructure compared to the coarse microstructure in the NHT condition.

As seen in **Figure 6-5**, the fracture surfaces for selected NHT, CA-H900, and CA-H1025 heat-treated specimens with uniform gage sections are compared. The surface pores with $\sqrt{\text{area}} = 20 \mu\text{m}$, $\sqrt{\text{area}} = 28 \mu\text{m}$, and $\sqrt{\text{area}} = 22 \mu\text{m}$ initiate the cracks in NHT, CA-H900, and CA-H1025 specimens tested at 550 MPa, respectively. Although the NHT specimen has smaller defect, the heat-treated specimens exhibit a longer fatigue life than the NHT specimen. It can be seen that there are coarse facets on the crack propagation region of the NHT specimen, while there are more fine ridges seen on the crack propagation area for the CA-H900 and CA-H1025 heat-treated specimens. The facets in the NHT

condition are ascribed to its coarse columnar BCC microstructure, whereas the ridges and tortuous fracture surface of the CA-H900 and CA-H1025 heat-treated specimens are related to the fine lath martensite in their microstructure (see **Figure 6-2**).

A similar fracture mechanism to uniform gage specimens is observed for the hourglass specimens in NHT, CA-H900, and CA-H1025 heat-treated specimens (see **Figure 6-6**). The coarse facets are observed in the crack propagation region of the NHT specimen, while fine ridges and tortuous fracture surfaces are found for the CA-H900 and CA-H1025 ones. This represents the independency of the L-PBF 17-4 PH SS to the geometry in different heat treatment conditions. By comparing the fatigue lives of the CA-H900 and CA-H1025 heat-treated specimens in **Figure 6-6(b)** and (c), it can be seen that the CA-H1025 heat-treated specimen with $\sqrt{\text{area}} = 26 \mu\text{m}$ exhibits a longer fatigue life than the CA-H900 one with $\sqrt{\text{area}} = 24 \mu\text{m}$. The longer fatigue life for the CA-H1025 heat-treated specimen is ascribed to the high cyclic fracture toughness of L-PBF 17-4 PH SS in this heat treatment condition [162].

To obtain the fracture mechanism of L-PBF 17-4 PH SS in the HCF to VHCF regime, fracture surfaces of selected NHT, CA-H900, and CA-H1025 heat-treated ultrasonic specimens tested at 500 MPa, 475 MPa, and 450 MPa are presented in **Figure 6-7**, **Figure 6-8**, and **Figure 6-9**, respectively. As seen in **Figure 6-7** and **Table 6-2**, all NHT specimens failed below the VHCF regime, and surface pores as well as subsurface pores (located $< 6 \mu\text{m}$ from the surface) are identified as crack-initiating defects in all the NHT specimens. On the other hand, the crack initiation mechanism from surface pores transfer to the internal pores for the CA-H900 and CA-H1025 heat-treated specimens as the stress level decreases to 450 MPa (see **Figure 6-8**). At the same stress level, for

example, in 450 MPa, a surface pore is the crack initiator for the NHT condition, while an internal pore initiates the crack at the CA-H900 or CA-H1025 conditions. As the geometry of the specimens is the same, the heat treatment affects this transition by changing the microstructure from coarse ferrite grains to a fine martensitic microstructure.

The transition in crack initiation from the surface to the internal defects in the VHCF regime is due to the less material constraint at the surface under low loading amplitudes, which reduces the surface cyclic plasticity [159]. This increases the internal localized cyclic plasticity, especially around the inclusions or the defects [177]. As a result, a fine granular area (FGA) is formed by occurrence of recrystallization [178]. Another representative feature for the internal crack initiation is a fish-eye feature, a round area around the FGA with different topography [179]. There is no evidence of the fish-eye or FGA on the fracture surface of the NHT specimens in the low stress levels shown in **Figure 6-7**. This shows that the cyclic plastic deformation on the surface of the NHT specimens is high enough to initiate the cracks from the defects near the surface. However, the fish-eye and FGA features on the fracture surface of the CA-H900 and CA-H1025 heat-treated specimens shown in **Figure 6-8** and **Figure 6-9**, represent the low surface cyclic plasticity for the heat-treated specimens. Therefore, micro-cracks are formed around the internal defects and grow through the FGA, resulting in a fracture in the VHCF regime. The low surface cyclic plasticity in heat-treated specimens may be due to the high strength of material after heat treatment.

6.5. Conclusions

The effect of heat treatment and specimen geometry on the fatigue behavior of laser powder bed fused (L-PBF) 17-4 PH SS up to the very high cycle fatigue (VHCF) regime

were investigated in this study. The L-PBF 17-4 PH SS microstructure was examined in NHT, CA-H900, and CA-H1025 heat treatment conditions. Fatigue behavior of the material in each heat treatment condition was evaluated with different specimen geometries, including uniform gage, hourglass, and ultrasonic. Finally, failure mechanisms for each specimen and heat treatment condition were compared. The following conclusions can be drawn from this study:

1. The L-PBF 17-4 PH SS microstructure in NHT condition is comprised of coarse ferrite grains, lath martensite transferred from austenite during solidification, and retained austenite. The CA-H900 and CA-H1025 heat treatments transformed the microstructure to a martensitic microstructure; however, a small fraction of austenite was reversed from the martensite due to the longer aging duration for the CA-H1025 heat treatment condition.
2. Although it is expected that the hourglass specimens with lower risk-volume to outperform the uniform gage ones, there seem to be minimal influences of specimen geometry on the LCF behavior of L-PBF 17-4PH SS in all heat treatment conditions. This was attributed to the crack propagation being more dominant over crack initiation in the LCF regime.
3. For specimens in NHT condition, hourglass specimens slightly outperformed uniform gage specimens in the high-cycle fatigue (HCF) regime. This is due to the smaller risk-volume in hourglass specimens and consequently fewer defects residing in the risk-volume to initiate the cracks. However, for the heat treatment conditions (i.e., CA-H900 and CA-H1025), hourglass and uniform gage specimens possessed similar fatigue resistance in the low cycle fatigue (LCF) and mid-cycle

- fatigue (MCF) regimes due to their higher sensitivity to defects compared to the specimens in NHT condition.
4. The fatigue resistance of L-PBF 17-4PH SS specimens, regardless of the geometry type, was improved after heat treatment due to their finer microstructure (i.e., fine lath martensite and reversed austenite). The finer microstructure in the heat-treated specimens resulted in a better crack initiation resistance compared to the coarse ferritic microstructure of specimens in NHT condition.
 5. The CA-H1025 and the CA-H900 heat-treated specimens exhibit similar fatigue performance in the LCF regime. However, more scatter in fatigue results in the MCF to the VHCF regimes was observed for the CA-H900 heat-treated specimens. This was attributed to the higher strength and lower ductility of the CA-H900 heat-treated specimens, resulting in higher material sensitivity to the defects compared to the CA-H1025 ones.
 6. Fractography analysis of the specimens indicated that the gas-entrapped pore is the crack initiator in all specimens, regardless of the heat treatment and geometry type. For the ultrasonic NHT specimens, fatigue failures were below the VHCF regime, and cracks were initiated from either surface pores or subsurface pores (located $< 6 \mu\text{m}$ from the surface). A transition from the surface crack initiation to internal crack initiation (i.e., fish-eye failure) due to the low surface cyclic plasticity in the VHCF regime was observed for heat-treated specimens at stress amplitudes of 550 MPa and below.

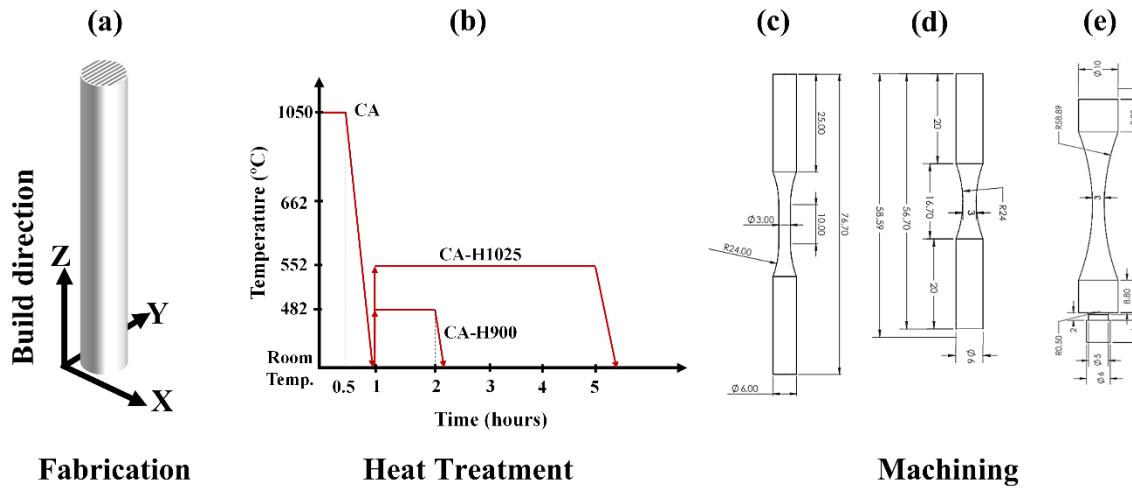


Figure 6-1. (a) The build layout used for fabricating L-PBF 17-4 PH SS specimens under Ar and N₂ shielding gas, and (b) schematic of the heat treatment procedure. The specimens' geometries are shown in (c) uniform gage, (d) hourglass for conventional fatigue testing, and (e) ultrasonic (hourglass for ultrasonic fatigue testing).

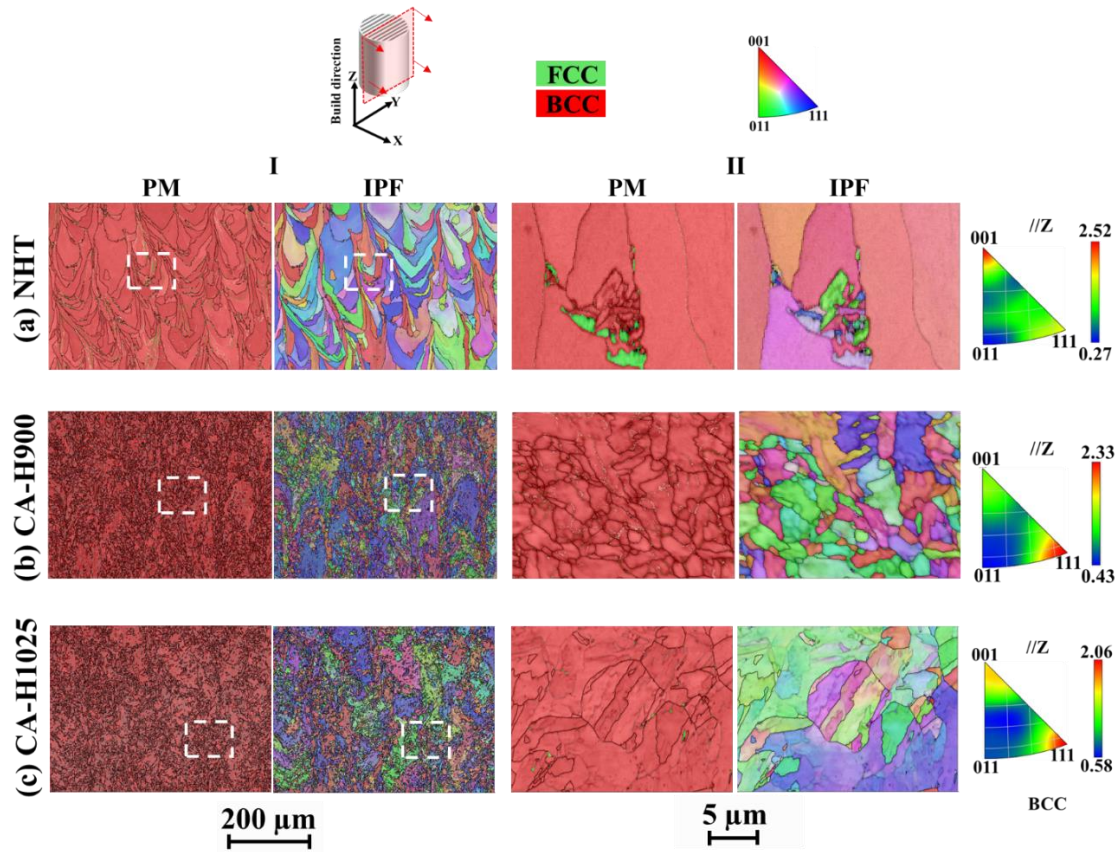


Figure 6-2. Microstructure characterization of the L-PBF 17-4 PH SS in (a) NHT, (b) CA-H900, and (c) CA-H1025 heat treatment conditions.

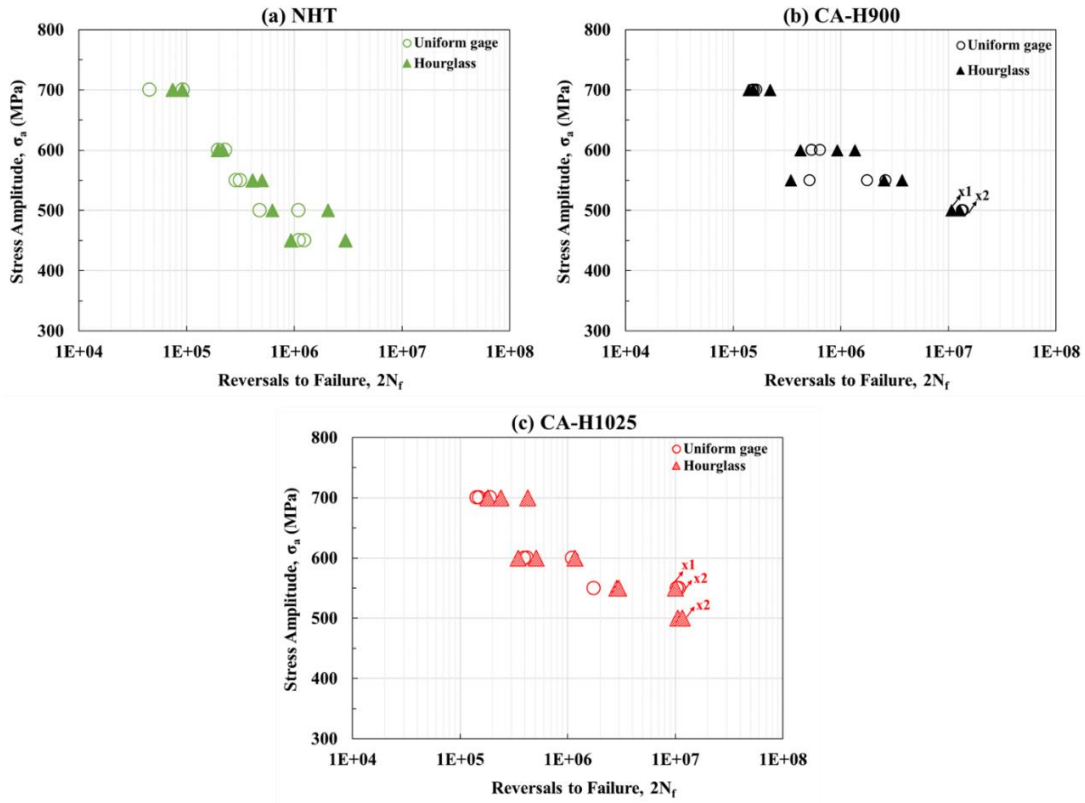


Figure 6-3. Effect of geometry on the fatigue behavior of the L-PBF 17-4 PH SS specimens in (a) NHT, (b) CA-H900, and (c) CA-H1025 heat treatment conditions, conducted using conventional fatigue test setup.

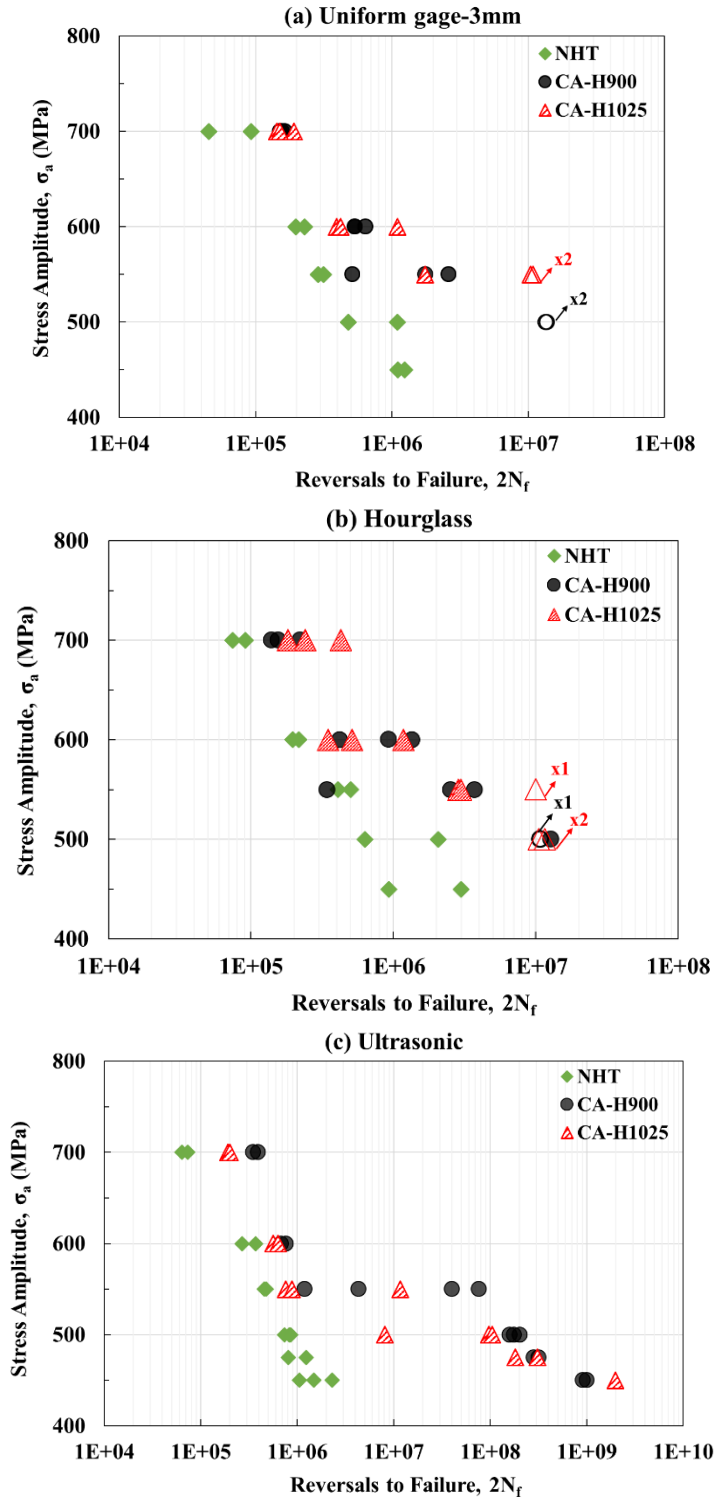


Figure 6-4. Effect of heat treatment on the fatigue behavior of L-PBF 17-4 PH SS with (a) uniform gage, (b) hourglass, and (c) ultrasonic type geometry.

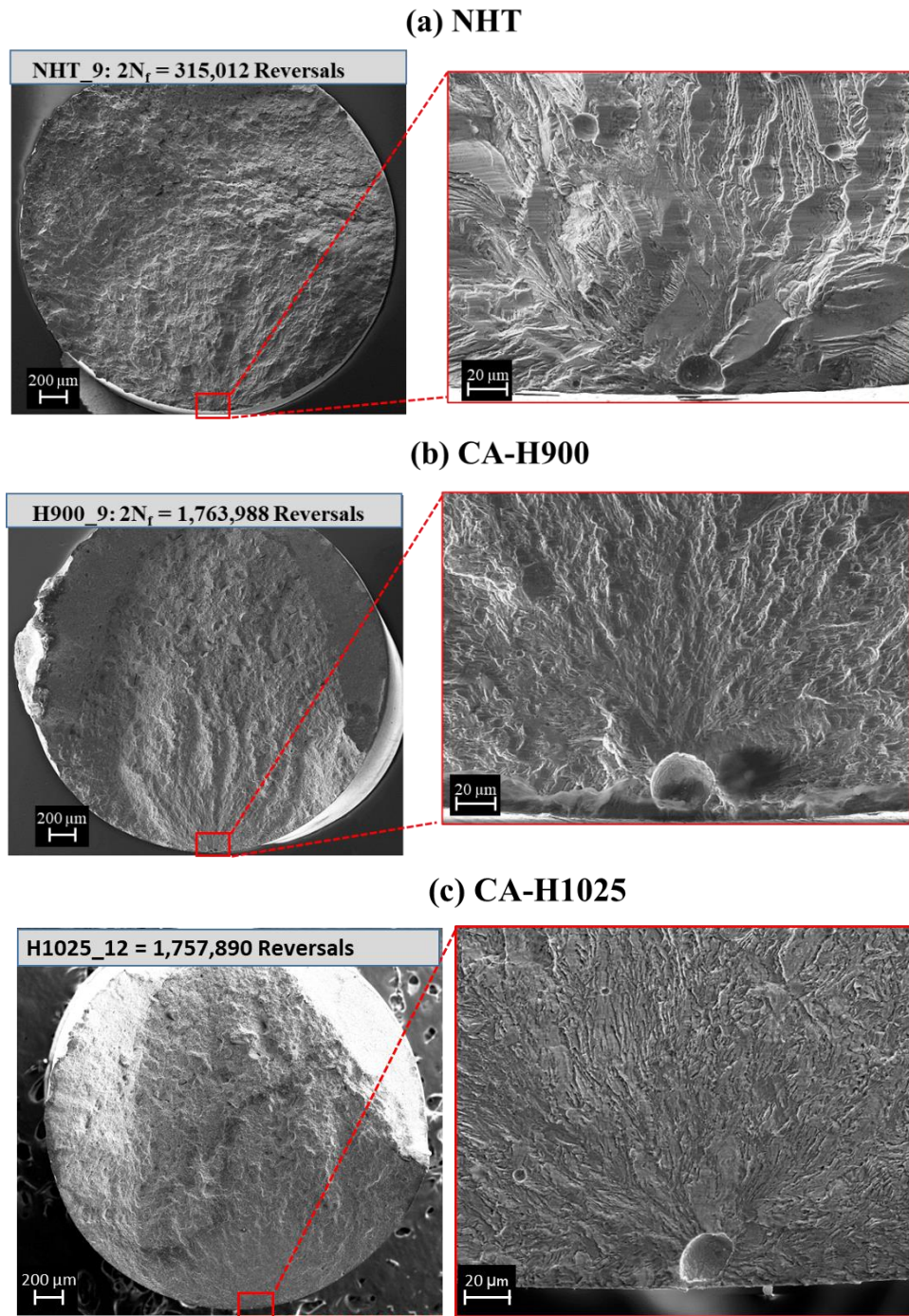


Figure 6-5. Fracture surfaces of L-PBF 17-4 PH SS specimens with uniform gage tested at 550 MPa: (a) NHT specimen with 315,012 reversals to failure, and (b) CA-H900 specimen with 1,763,988 reversals to failure, and (c) CA-H1025 specimen with 1,757,890 reversals to failure.

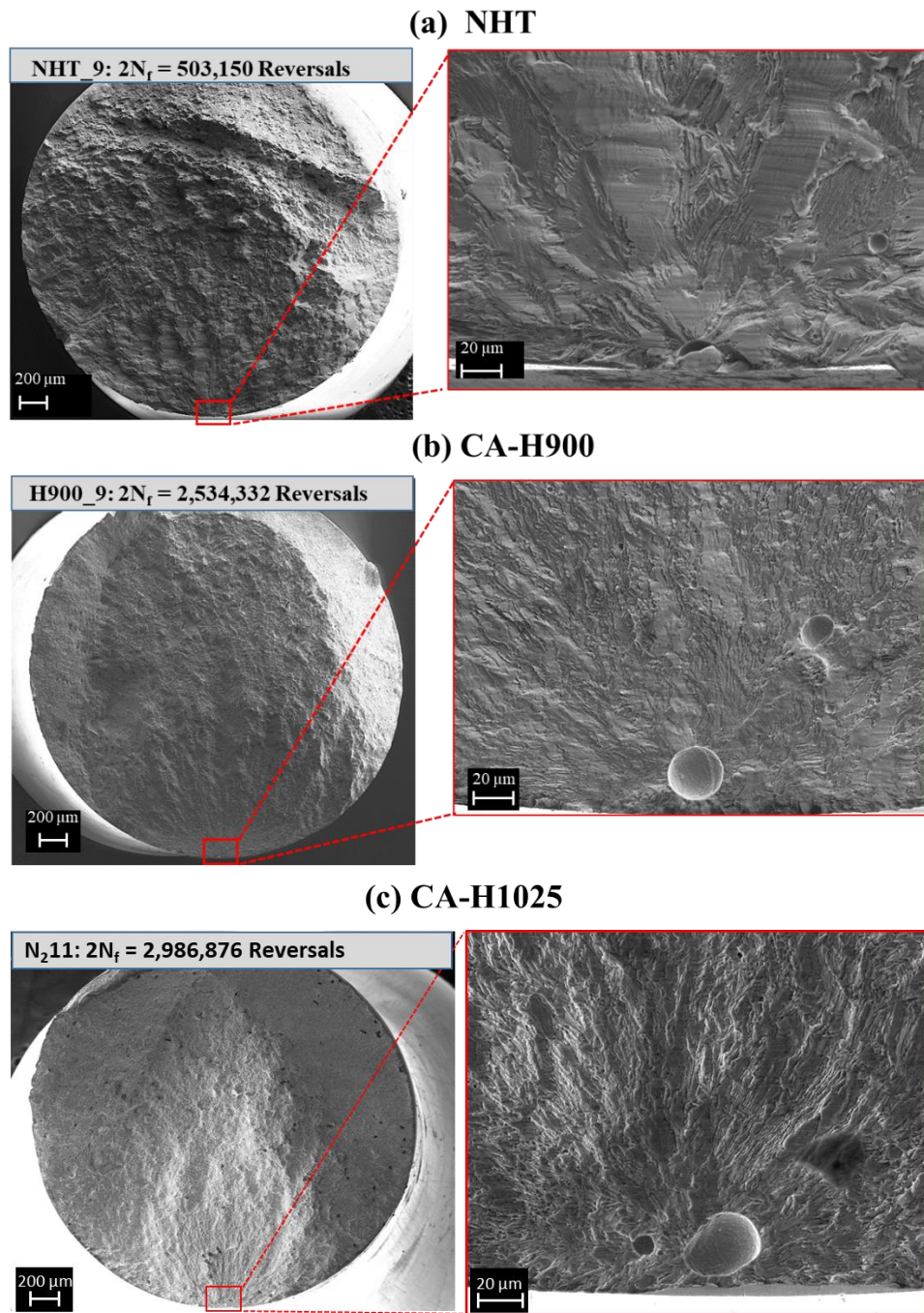


Figure 6-6. Fracture surfaces of L-PBF 17-4 PH SS specimens with hourglass gauge tested at 550 MPa: (a) NHT heat-treated specimen with 503,150 reversals to failure, and (b) CA-H900 specimen with 2,534,332 reversals to failure, and (c) CA-H1025 specimen with 2,986,876 reversals to failure.

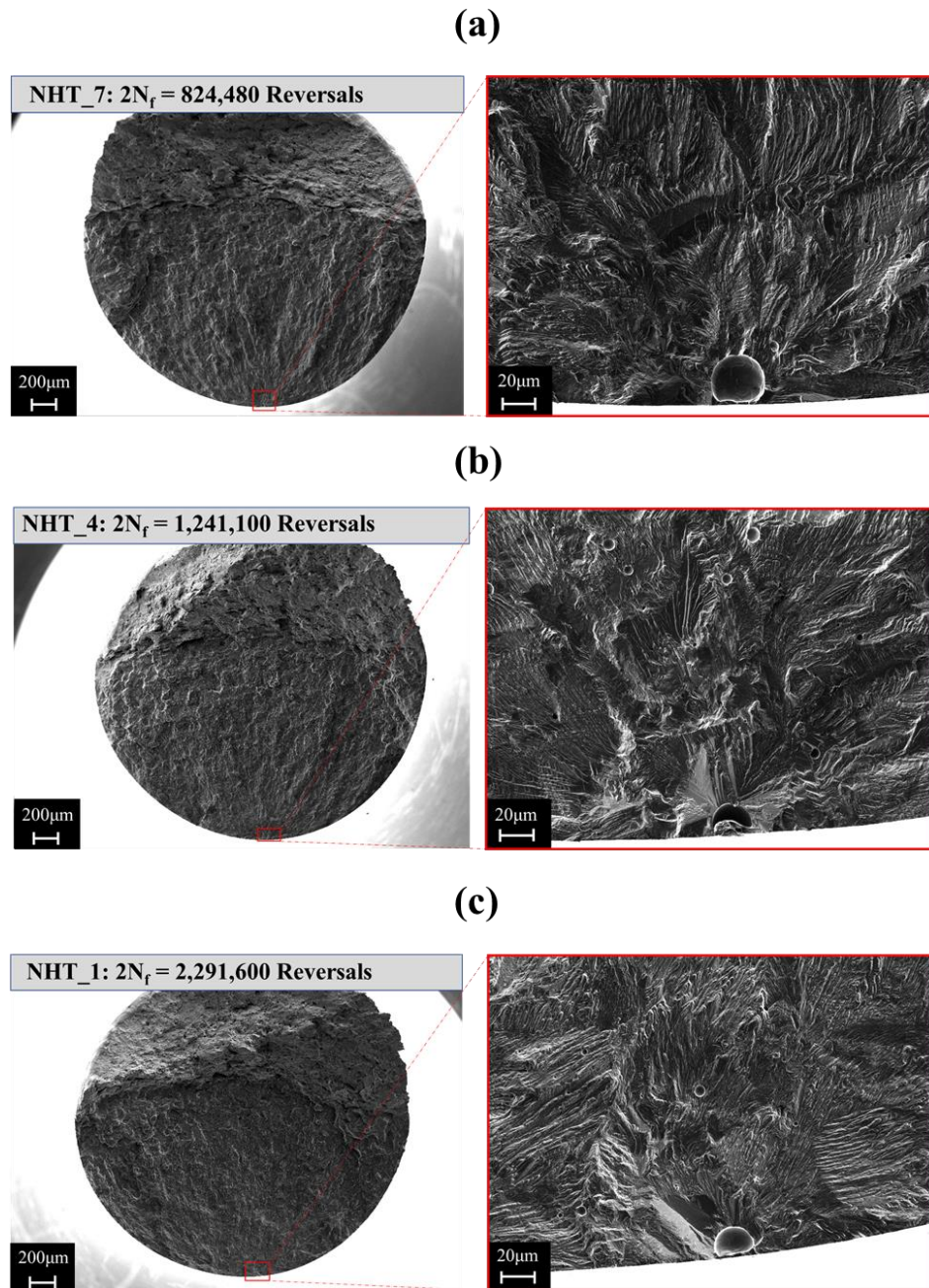


Figure 6-7. Fracture surfaces of L-PBF 17-4 PH SS ultrasonic NHT specimens with uniform gage tested at: (a) 500 MPa with 824,480 reversals to failure, (b) 475 MPa with 1,241,100 reversals to failure, (c) 450 MPa with 2,291,600 reversals to failure.

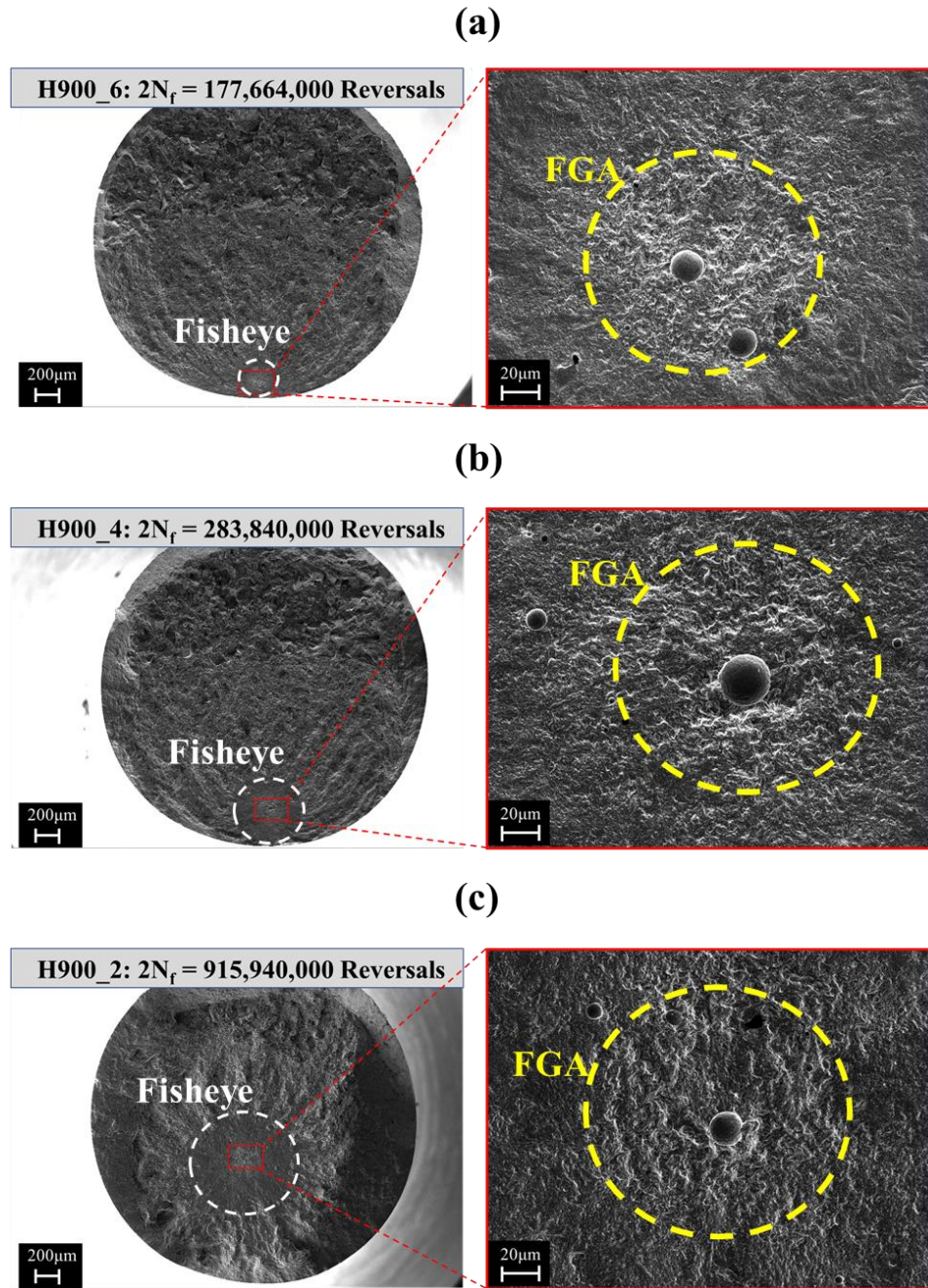


Figure 6-8. Fracture surfaces of L-PBF 17-4 PH SS ultrasonic CA-H900 specimens with uniform gage tested at: (a) 500 MPa with 177,664,000 reversals to failure, and (b) 475 MPa with 283,840,000 reversals to failure, (c) 450 MPa with 915,940,000 reversals to failure.

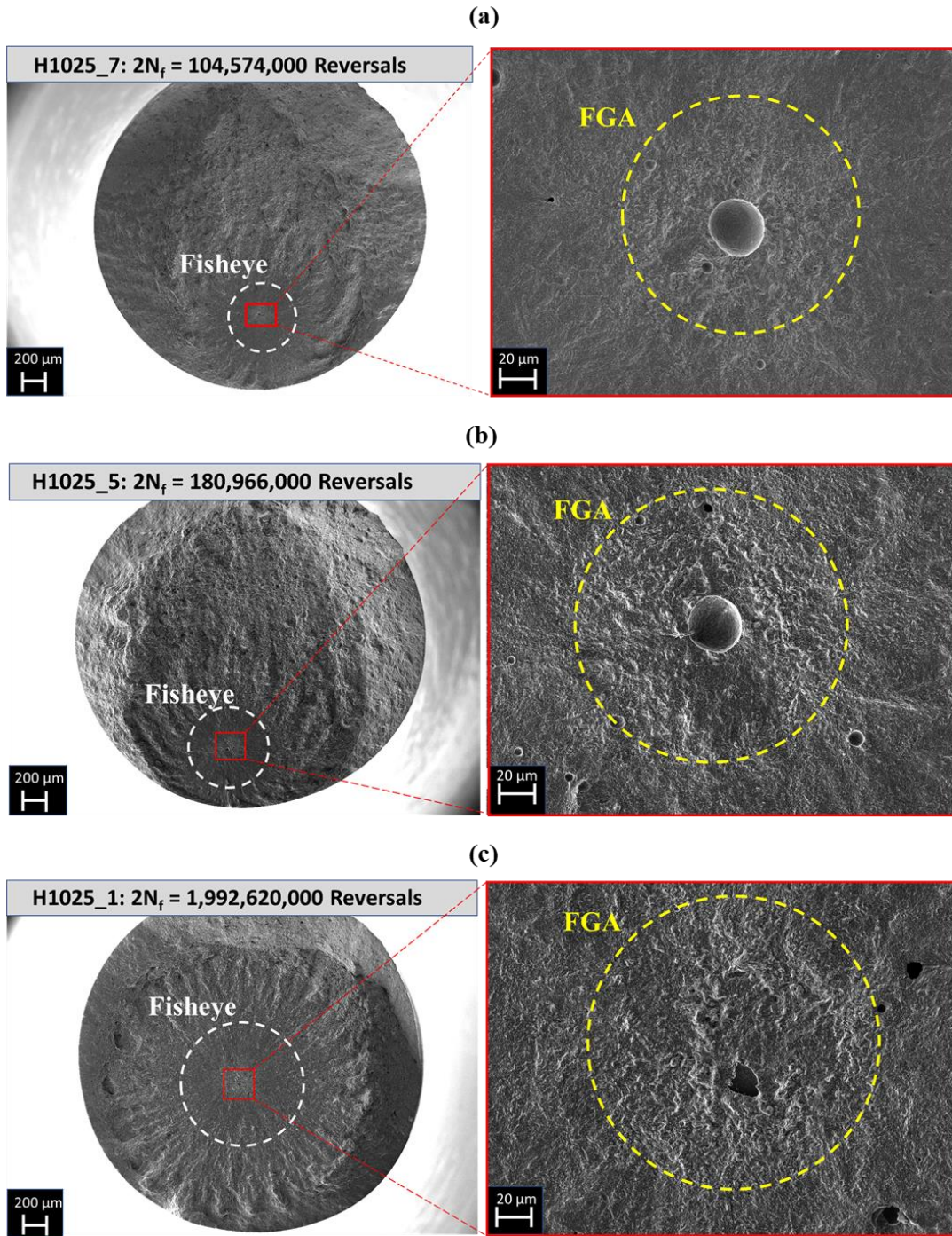


Figure 6-9. Fracture surfaces of L-PBF 17-4 PH SS ultrasonic CA-H900 specimens with uniform gage tested at: (a) 500 MPa with 177,664,000 reversals to failure, and (b) 475 MPa with 283,840,000 reversals to failure, (c) 450 MPa with 915,940,000 reversals to failure.

Table 6-1. Process parameters used for EOS M290 system to fabricate L-PBF 17-4 PH SS specimens.

| Power (W) | Scan Speed (mm/s) | Hatching Distance (mm) | Layer Thickness (mm) | Shielding Gas Type |
|------------------|--------------------------|-------------------------------|-----------------------------|---------------------------|
| 220 | 755 | 0.1 | 0.04 | Nitrogen |

Table 6-2. Fatigue data for the L-PBF 17-4 PH SS specimens with different specimen geometries in NHT condition.

| ID | Stress Amplitude, σ_a (MPa) | Uniform gage (specimen with uniform gage section tested using conventional fatigue testing) | | | Hourglass (hourglass specimen tested using conventional fatigue testing) | | | Ultrasonic (hourglass specimen tested using ultrasonic fatigue testing) | | |
|--------|------------------------------------|---|---------------------------------|---|--|---------------------------------|---|---|---------------------------------|---|
| | | Reversals to failure, $2N_f$ | \sqrt{area} (μm) | Defect Type/ Location (μm) | Reversals to failure, $2N_f$ | \sqrt{area} (μm) | Defect Type/ Location (μm) | Reversals to failure, $2N_f$ | \sqrt{area} (μm) | Defect Type/ Location (μm) |
| NHT_1 | 450 | 1,238,394 | 19 | Surface Pore | 2,999,386 | 18 | Subsurface Pore /2.40 | 2,291,600 | 18 | Surface Pore |
| NHT_2 | | 1,110,586 | 16 | Surface Pore | 931,108 | 15 | Surface Pore | 1,495,220 | 20 | Surface Pore |
| NHT_3 | | - | - | - | - | - | - | - | 1,054,220 | 18 |
| NHT_4 | 475 | - | - | - | - | - | - | 1,241,100 | 14 | Surface Pore |
| NHT_5 | | - | - | - | - | - | - | 810,700 | 11 | Surface Pore |
| NHT_6 | | - | - | - | - | - | - | 737,440 | 38 | Surface Pore |
| NHT_7 | 500 | 1,098,064 | 14 | Surface Pore | 2,070,546 | 15 | Subsurface Pore /4.24 | 854,760 | 10 | Surface Pore |
| NHT_8 | | 480,482 | 15 | Surface Pore | 630,776 | 12 | Surface Pore | 824,480 | 28 | Subsurface Pore/1.622 |
| NHT_9 | 550 | 315,012 | 20 | Surface Pore | 503,150 | 17 | Surface Pore | 477,620 | 16 | Surface Pore |
| NHT_10 | | 288,308 | 26 | Subsurface Pore/4.85 | 408,784 | N/A | N/A | 455,780 | 36 | Subsurface Pore/2.97 |
| NHT_11 | 600 | 229,920 | 27 | Subsurface Pore /6.65 | 217,370 | 18 | Surface Pore | 368,620 | 22 | Subsurface Pore/5.41 |
| NHT_12 | | 197,884 | 15 | Surface pore | 196,136 | 17 | Subsurface Pore /2.32 | 268,840 | 23 | Subsurface Pore/0.81 |
| NHT_13 | 700 | 93,046 | N/A | N/A | 91,606 | 23 | Surface Pore | 73,544 | 15 | Subsurface Pore/2.88 |
| NHT_14 | | 45,294 | N/A | N/A | 74,182 | 24 | Subsurface Pore /2.50 | 64,136 | N/A | N/A |

Surface Pore: pores on the specimen's surface, **Subsurface Pore:** pores located less than 40 μm from the specimen's surface, **Internal Pore:** pores located at 40 μm or more away from the specimen's surface.

Table 6-3. Fatigue data for the L-PBF 17-4 PH SS specimens with different geometries in CA-H900 heat treatment condition.

| ID | Stress Amplitude, σ_a (MPa) | Uniform gage (specimen with uniform gage section tested using conventional fatigue testing) | | | Hourglass (hourglass specimen tested using conventional fatigue testing) | | | Ultrasonic (hourglass specimen tested using ultrasonic fatigue testing) | | |
|---------|------------------------------------|---|--|---|--|--|---|---|--|---|
| | | Reversals to failure, $2N_f$ | $\sqrt{\text{area}}$ (μm) | Defect Type/ Location (μm) | Reversals to failure, $2N_f$ | $\sqrt{\text{area}}$ (μm) | Defect Type /Location (μm) | Reversals to failure, $2N_f$ | $\sqrt{\text{area}}$ (μm) | Defect Type/ Location (μm) |
| H900_1 | 450 | - | - | - | - | - | - | 1,004,540,000 | 20 | Internal Pore/114.06 |
| H900_2 | | | | | | | | 915,940,000 | 18 | Internal Pore/1058.2 |
| H900_3 | 475 | | | | | | | 318,940,000 | 32 | Internal Pore/63.87 |
| H900_4 | 283,840,000 | | | | | | | 28 | Internal Pore/339.2 | |
| H900_5 | 500 | 13,712,352 | N/A | Runout | 12,748,268 | N/A | Runout | 203,200,000 | 24 | Internal Pore/157.99 |
| H900_6 | | 13,437,278 | N/A | Runout | 10,747,336 | N/A | Runout | 177,664,000 | 18 | Internal Pore/134.60 |
| H900_7 | | - | - | - | - | - | - | 160,280,000 | 17 | Subsurface Pore/27.3 |
| H900_8 | 550 | 2,625,456 | 20 | Subsurface Pore /5.3 | 3,709,830 | 17 | Subsurface Pore /3.92 | 76,208,000 | 13 | Internal Pore/186.23 |
| H900_9 | | 1,763,988 | 28 | Surface Pore | 2,534,332 | 24 | Subsurface Pore /7.03 | 40,160,000 | 20 | Subsurface Pore/11.08 |
| H900_10 | | 514,518 | 13 | Surface Pore | 342,766 | 26 | Surface Pore | 4,341,800 | 13 | Surface Pore |
| H900_11 | | - | - | - | - | - | - | 1,188,760 | 19 | Surface Pore |
| H900_12 | 600 | 645,036 | 25 | Subsurface Pore /5.57 | 1,349,362 | 14 | Subsurface Pore /2.4 | 766,480 | 23 | Subsurface Pore/2.84 |
| H900_13 | | 539,380 | 14 | Surface Pore | 927,888 | 27 | Surface Pore | 679,620 | 29 | Subsurface Pore/1.216 |
| H900_14 | | 537,516 | 23 | Surface Pore | 420,652 | 19 | Surface Pore | - | - | - |
| H900_15 | 700 | 164,818 | 21 | Surface Pore | 221,046 | 20 | Surface Pore | 392,340 | 28 | Subsurface Pore/2.71 |
| H900_16 | | 156,886 | 17 | Surface Pore | 139,530 | 25 | Surface Pore | 348,580 | 25 | Subsurface Pore/0.99 |
| H900_17 | | 151,810 | 27 | Surface Pore | 155,015 | 20.38 | Subsurface Pore /3.77 | - | - | - |

Surface Pore: pores on the specimen's surface, **Subsurface Pore:** pores located less than 40 μm from the specimen's surface, **Internal Pore:** pores located at 40 μm or more away from the specimen's surface.

Table 6-4. Fatigue data for the L-PBF 17-4 PH SS specimens with different specimen geometries in CA-H1025 heat treatment condition adopted from [175].

| ID | Stress Amplitude, σ_a (MPa) | Uniform gage (specimen with uniform gage section tested using conventional fatigue testing) | | Hourglass (hourglass specimen tested using conventional fatigue testing) | | Ultrasonic (hourglass specimen tested using ultrasonic fatigue testing) | |
|----------|------------------------------------|---|--|--|--|---|--|
| | | Reversals to failure, $2N_f$ | $\sqrt{\text{area}}$ (μm) | Reversals to failure, $2N_f$ | $\sqrt{\text{area}}$ (μm) | Reversals to failure, $2N_f$ | $\sqrt{\text{area}}$ (μm) |
| H1025_1 | 475 | - | - | - | - | 1,992,620,000 | 15 |
| H1025_4 | | | | | | 308,700,000 | 20 |
| H1025_5 | | | | | | 180,966,000 | 29 |
| H1025_7 | 500 | - | - | >10,496,378 | N/A | 203,200,000 | 24 |
| H1025_8 | | | | >11,592,826 | N/A | 177,664,000 | 18 |
| H1025_9 | | | | - | - | 160,280,000 | 17 |
| H1025_10 | 550 | >10,811,080 | N/A | >10,000,000 | N/A | 11,711,200 | 15 |
| H1025_11 | | >10,407,386 | N/A | 2,986,876 | 25 | 759,240 | 25 |
| H1025_12 | | 1,757,890 | 22 | 2,851,652 | 18 | - | - |
| H1025_13 | 600 | 1,097,884 | 24 | 1,172,000 | 22 | 632,040 | 21 |
| H1025_14 | | 421,230 | 32 | 511,472 | 19 | 562,220 | 20 |
| H1025_15 | | 392,808 | 35 | 348,018 | 24 | - | - |
| H1025_16 | 700 | 190,514 | 27 | 426,756 | 22 | 200,640 | 32 |
| H1025_17 | | 150,542 | 23 | 240,604 | 19 | 191,814 | 18 |
| H1025_18 | | 143,290 | 22 | 180,958 | 12 | - | - |

**CHAPTER 7: MICROSTRUCTURE AND DEFORMATION BEHAVIOR OF
ADDITIVELY MANUFACTURED 17-4 STAINLESS STEEL: INFLUENCE OF
MANUFACTURING TECHNIQUES FROM LASER POWDER BED FUSION (L-
PBF) TO LASER POWDER DIRECTED ENERGY DEPOSITION (LP-DED)**

The following chapter has passed rigorous peer-review process and has been published in JOM in 2022.

Nezhadfar, P.D., Gradl, P.R., Shao, S. , Shamsaei, N., Microstructure and Deformation Behavior of Additively Manufactured 17–4 Stainless Steel: Laser Powder Bed Fusion vs. Laser Powder Directed Energy Deposition , JOM 2022.

7.1. Abstract

This study aims to compare the microstructure of 17-4 PH stainless steel (SS) manufactured via laser beam powder bed fusion (L-PBF) and laser powder directed energy deposition (LP-DED) in non-heat treated (NHT) and heat treated conditions. In addition, the room temperature tensile behavior of heat treated L-PBF and LP-DED 17-4 PH SS is investigated and compared with that of the wrought counterpart with the same heat treatment conditions. The results show that the L-PBF specimens have finer microstructure (ferrite + lath martensite) than the LP-DED ones (massive ferrite + Widmanstätten ferrite) in NHT condition. Electron backscatter diffraction analysis shows that the L-PBF and LP-DED specimens have twin-based substructure lath martensite after heat treatment. Despite the lower tensile strength of the LP-DED specimens than the L-PBF ones, the ductility of peak-aged LP-DED specimens were reduced due to the presence of the δ -ferrite phase having a significant plastic deformation incompatibility with the martensite.

7.2. Introduction

Additive manufacturing (AM) has transformed the manufacturing process of structural parts in various industries such as aerospace, automotive, biomedical, defense, and nuclear. The layer-by-layer and track-by-track nature of AM processes allow the manufacture of near-net-shaped parts with complex geometries, reduces the cost and lead times, and facilitates the fabrication of highly customized parts for specific applications (e.g., in the medical field) [1]. There are various types of AM techniques for metallic materials classified based on feedstock form (e.g., powder vs. wire), feeding mechanism (e.g., powder bed vs. blown powder), and energy source (e.g., laser vs. electron beam) [180].

Amongst the various AM processes, the laser powder bed fusion (L-PBF) and the laser powder directed energy deposition (LP-DED) ones are the most prominent laser-based AM processes, which have been extensively investigated in the literature [36]. The L-PBF process provides more freedom in designing near-net-shaped parts with higher geometrical resolution and precision than the LP-DED process; however, the L-PBF is typically limited to a single-powder feedstock [181]. On the other hand, the LP-DED offers better compatibility for multi-powder feedstock, functionally graded components, and the fabrication of large parts [1].

One of the specific characteristics of the laser-based AM processes is the high heating/cooling rates during fabrication resulting in a refined microstructure compared to the conventionally manufactured (CM) counterparts. Accordingly, the AM materials often have comparable static mechanical properties to, and in some cases outperform, their CM counterparts [139,182]. The mechanical performance of the AM materials is primarily

influenced by the material's structure (i.e., grain structure, texture, surface roughness, and defect structure), which is impacted by the thermal history induced during the manufacturing. The thermal history itself is governed by process parameters (i.e., powder, scan speed, etc.) and design parameters (i.e., part size and geometry, time interval, etc.). In addition to the above-mentioned influential parameters, the AM process technique (e.g., L-PBF, LP-DED, etc.) itself may also cause variations in the microstructural and mechanical properties of a material system.

The LP-DED process, due to the slower moving melt pool (typically ~10-30 mm/s [183] compared to ~1000-1700 mm/s for L-PBF [184]) created by a high powered laser (typically ~1000W), has a considerably lower cooling rate (by approximately three orders of magnitude) than L-PBF [185,186], giving the fabricated materials distinct microstructure (i.e., grain structure, crystallographic texture, precipitations, etc.) and defect content. Amato et al. [187] reported the presence of spheroidal/ellipsoidal γ'' in γ matrix of non-heat treated (NHT) L-PBF IN718, while Laves phase has been characterized in an interdendritic γ matrix of NHT LP-DED counterparts [188,189]. Xu et al. [190] have reported a lamellar $\alpha+\beta$ structure in L-PBF Ti-6Al-4V, whereas Carroll et al. [191] has shown a Widmanstätten structure along with grain boundary α phase in the coarse columnar prior β grains in LP-DED Ti-6Al-4V. It has been reported that even post thermal heat treatment may not completely diminish the differences in the microstructure of the L-PBF and LP-DED AM materials. Schneider et al. [192] reported different grain structure (i.e., size and morphology) for L-PBF and LP-DED IN718 even after applying a similar heat treatment procedure; this was attributed to the variation in their initial microstructure

(i.e., NHT condition). The L-PBF specimens showed the highest degree of homogenization and more refined grains than the LP-DED ones.

The microstructure variations of the L-PBF and LP-DED AM materials result in different mechanical responses. Babuska et al. [181] recently reported a higher tensile strength for the L-PBF CoCr specimens than the LP-DED counterparts. They have attributed this to the finer microstructure of the L-PBF specimens due to the higher cooling rate than the LP-DED ones. Donate-Buendia et al. [193] have compared the microstructure, and mechanical properties of the oxide dispersion strengthened (ODS) steels manufactured via L-PBF and LP-DED processes. Compared to LP-DED, the L-PBF process produced a finer grain structure, reduced the agglomeration of the strengthening particles (i.e., Y_2O_3), and yielded higher hardness values in the ODS steel.

The significant dependence of microstructure and mechanical properties of such known materials as IN718, Ti-6Al-4V, ODS steels, etc. on AM processes necessitates the careful evaluation of this dependence before mass adoption of AM to any other materials in key industrial sectors. The 17-4 precipitation hardening (PH) stainless steel (SS) is one of the most commonly used materials in various industries (e.g., aerospace, energy, food processing, etc.) due to its favorable chemical and mechanical properties (e.g., high corrosion resistance, high strength, and ductility, etc.) [54]. It has drawn much attention from the AM community recently due to its superior weldability [19,67]. The sensitivity of its microstructure to the cooling rate during solidification as well as the subsequent thermal exposures can potentially makes the properties of 17-4 PH SS process dependent. This study investigates and compares the microstructure and room temperature tensile behavior of 17-4 PH SS manufactured by L-PBF and LP-DED processes. The grain

structure and phase constituent of the L-PBF and LP-DED 17-4 PH SS specimens are characterized and compared in the NHT condition. In addition, the effect of various heat treatment conditions on the crystallographic texture and room temperature tensile behavior of the L-PBF and LP-DED 17-4 PH SS specimens is investigated.

7.3. Experimental Procedure

Two batches of Argon atomized 17-4 PH SS powder was used to fabricate the specimens via L-PBF and LP-DED processes, respectively. The detailed chemical compositions of the 17-4 PH SS powders used for each AM process are listed in **Table 7-1**.

An EOS M290 machine was used to fabricate the L-PBF cylindrical bars ($\phi 11$ mm). The EOS default process parameters, laser power of 220 W, scan speed of 755 mm/s, hatching distance of 0.1 mm, and layer thickness of 0.04 mm were employed, and nitrogen was used as the shielding gas. The LP-DED cylindrical bars ($\phi 15.24$ mm) were fabricated using an RPM Innovations (RPMI) 557 machine. The process parameters were as follows: power of 1070 W, layer height of 0.38 mm, travel speed of 1,016 mm/min and powder feed rate of 15.1 grams/min, and argon was used as the shielding gas.

The Thermo-Calc. software was used to generate the Fe-Cr binary phase diagram to analyze the phase transformations possible for 17-4 PH SS. The TCFE9 thermodynamic database for various Fe-based alloys and steels such as stainless steels was employed [99,194]. Besides, to incorporate the influence of all the alloy elements in generating the phase diagram, the Ni_{eq} (Nickel equivalent) and Cr_{eq} (chromium equivalent) were obtained following the Schaeffler equations [20]:

$$Ni_{eq} (wt\%) = \%Ni + 0.5(\%Mn) + 0.3(\%Cu) + 25(\%N) + 30(\%C) \quad \text{Eq.1}$$

$$Cr_{eq}(wt\%) = \%Cr + 2(\%Si) + 1.5(\%Mo) + 1.75(\%Nb) \quad \text{Eq.2}$$

The Ni_{eq} and Cr_{eq} values were further calculated for the L-PBF to be 7.6 and 16.6wt%, respectively. For the LP-DED 17-4 PH SS, the Ni_{eq} and Cr_{eq} values were 6.1 and 17.7wt%, respectively. **Figure 7-1** shows the binary phase diagram generated by Thermo-Calc. software; the Cr amount for the L-PBF and LP-DED specimens are indicated on the phase diagram to predict the phase constituents in various temperatures. According to the phase diagram, the stress relieve (SR) heat treatment was carried out at 650 °C/1 hour for L-PBF and LP-DED specimens. It has been reported in [195] that this SR procedure neither changes the microstructure nor the mechanical properties of the L-PBF and LP-DED 17-4 PH SS. All the L-PBF and LP-DED specimens underwent hot isostatic pressing (HIP) at 1163 °C/3 hours under 103 MPa pressure and were solution (Sol) treated at 1050 °C/0.5 hours (i.e., Condition A (CA)) followed by air cooling. Some specimens for each type (i.e., L-PBF and LP-DED specimens) were aged at 482 °C/1 hour (i.e., H900) known as peak-age, and some were over-aged at 621 °C/4 hours (i.e., H1150). In the following text, the heat treated specimens (i.e., SR+HIP+Sol+Age) are dubbed CA-H900 and CA-H1150. After the full heat treatment, all the specimens were machined to the final tensile testing geometry following the ASTM E8 standard [196].

The L-PBF and LP-DED specimens were cut in the gage section transversely parallel to the build direction for microstructure characterization prior to tensile testing. The microstructure was characterized in NHT and fully heat treated conditions. The samples were ground and polished using sandpapers with grits 320-4000 following by a mirror-finish polishing step using Chemo-met along with 0.2 μm colloidal silica suspension. The microstructure was further characterized on the plane parallel (XZ-plane)

to the build direction using a Zeiss Crossbeam 550 scanning electron microscope (SEM) with an electron backscatter diffraction (EBSD) detector. However, the specimens were mirror-finished using a vibratory polisher for 2 hours before conducting the EBSD analysis and electron channeling contrast imaging (ECCI).

The tensile tests were conducted on the heat treated L-PBF and LP-DED 17-4 PH SS specimens at room temperature at 0.005 mm/mm/min strain rate. The fracture surfaces were further cleaned in a bath of isopropanol and water using an ultrasonic cleaner before performing fractography using SEM.

7.4. Results and Discussion

7.4.1. NHT Microstructure

The NHT microstructure of the L-PBF and LP-DED 17-4 PH SS specimens characterized via EBSD analysis and ECCI are shown in **Figure 7-2**. It is evident that the L-PBF 17-4 PH SS specimen (**Figure 7-2(a)**) has a more refined grain structure as compared to the LP-DED 17-4 PH SS one (**Figure 7-2(b)**); the L-PBF specimen consists of fine, primarily equiaxed, ferrite grains, whereas the LP-DED one consist of very coarse columnar ferrite grains. The ECCI images with higher magnifications reveal that the microstructure of the L-PBF specimen consists of ferrite and lath martensite. In contrast, the LP-DED specimen has a ferritic microstructure consisting of the massive ferrite grains with the Widmanstätten ferrites decorating the grain boundaries.

Since the martensite-start temperature (i.e., M_s) is above room temperature for the 17-4 PH SS ($M_s=100-150$ °C) [16,64], the austenite formed during solidification transforms to the martensite upon cooling to room temperature. However, the ferritic microstructure of the NHT AM 17-4 PH SS specimens, regardless of the manufacturing

techniques, has been attributed to the “austenite by-passing” mechanism. In this mechanism, the ferrite phase formed from the liquid will not transfer to the austenite due to the high cooling rate in AM processes as compared to the conventional manufacturing techniques (e.g., casting, forging, etc.) [18].

The lath martensite in the microstructure of L-PBF 17-4 PH SS specimen (see **Figure 7-2(a)**), however, indicates that the austenite has been formed during the solidification. This may be attributed to the N₂ shielding gas used to fabricate the L-PBF specimens. It has been reported that N₂ as the shielding gas refines the grain structure and also stimulates the austenite formation during solidification [67,128,162]. Therefore, the refined ferrite grains (average grain size of ~6 μm) and the lath martensite in the microstructure are results of using N₂ as shielding gas. The coarse microstructure of the LP-DED 17-4 PH SS specimen (average grain size of ~93.1 μm) may be attributed to the lower cooling rate induced in the LP-DED process as compared to the L-PBF one. Although the cooling rate LP-DED process, is believed to be above the threshold for austenite by-passing, has been reported to have almost two to three orders of magnitude slower cooling rate than the L-PBF process [181]. In addition, the ferrite phase is more stabilized in LP-DED specimens due to the higher Cr_{eq}/Ni_{eq} value for the LP-DED 17-4 PH SS (~2.9) compared to that of the L-PBF counterpart (~2.1). The significantly different NHT microstructures of L-PBF and LP-DED 17-4 PH SS specimens not only may lead to drastically different mechanical properties, but also may be inferior in strength due to the absence of precipitates. In hope to resolve these issues, post thermal treatments are typically performed to enhance the mechanical properties of the material as well as reducing the differences in microstructure of the L-PBF and LP-DED specimens.

7.4.2. Heat Treated Microstructure

The microstructure of L-PBF and LP-DED 17-4 PH SS specimens are compared in **Figure 3** for the CA-H900 and CA-H1150 heat treatment conditions. Although there is a visible difference between the microstructures of NHT L-PBF and LP-DED 17-4 PH SS specimens (see **Figure 7-2**), post thermal treatment (i.e., SR+HIP+HT) have evidently altered the microstructures to martensite dominated one for both the L-PBF and LP-DED specimens (see **Figure 7-3**). It can be seen in **Figure 7-3(a)** and (c) that both L-PBF and LP-DED have primarily martensitic microstructure in CA-H900 heat treatment condition with a minimal fraction of retained austenite ($\sim 0.1\%$). The fraction of retained austenite is increased for both the L-PBF (**Figure 7-3(b)**) and LP-DED (**Figure 7-3(d)**) specimens undergone CA-H1150 heat treatment. This is due to the diffusion of austenite stabilizer elements (i.e., Cu, Ni, N, etc.) to the grain boundaries during the long term aging (i.e., 4 hours) at the temperature close to the austenite reversion (see **Figure 7-1**), which may have resulted in the nucleation of austenite grains [15]. However, depending on the size of the reverted austenite grains, they may/ or may not transform to martensite upon cooling. It has been well established that martensitic transformations are more difficult to occur for finer austenite grains, which may be retained after heat treatment [197].

As seen in **Figure 7-3(b)** for the CA-H1150 treated L-PBF specimen, the fraction of austenite ($\sim 4.3\%$) retained in the microstructure is higher than that of the CA-H1150 LP-DED counterpart ($\sim 0.5\%$) shown in **Figure 7-3(d)**. This can be partially ascribed to the finer initial microstructure of the L-PBF specimen than that of the LP-DED one, which results in finer reverted austenite grains that are more difficult to transform to martensite upon cooling. Moreover, using N_2 shielding gas for fabrication may increase the austenite

stabilization and hinder the martensitic transformation. It can be observed that δ -ferrite phase is retained in the microstructure of LP-DED specimens (see **Figure 7-3(c)** and (d)), regardless of the heat treatment condition, whereas the δ -ferrite phase is absent in the microstructure of the N_2 -shielded L-PBF specimens. The N_2 shielding gas has been reported to reduce the δ -ferrite phase fraction retains in the microstructure of laser-welded materials at room temperature. The N as an austenite stabilizer results in the transformation of the δ -ferrite phase to austenite during the solidification, which reduces the fraction of δ -ferrite phase retain in the microstructure at room temperature. Moreover, the L-PBF specimen has a lower Cr_{eq}/Ni_{eq} value than the LP-DED one, reducing ferrite stability during solidification.

7.4.3.Texture Analysis

The variation in thermal history induced via L-PBF and LP-DED processes influences the crystallographic texture of the AM 17-4 PH SS specimens. It has been shown that NHT L-PBF 17-4 PH SS specimen possesses a strong cube (C) along with weak γ -fiber texture components, whereas there is not a specific texture component reported for the NHT LP-DED 17-4 PH SS specimen due to its very large grain structure (see **Figure 7-2(b)**) [195]. In addition, it has been reported that performing SR heat treatment assist with the recrystallization upon further heat treatment procedures and weakens the texture [195]. To understand and compare the crystallographic texture of L-PBF and LP-DED 17-4 PH SS specimens after applying full heat treatments (i.e., SR+HIP+Sol+Age), their corresponding orientation distribution function (ODF) maps for each condition are presented in **Figure 7-4** and **Figure 7-5**. The ODF maps are analyzed in parallel to the build and loading direction (i.e., Z) suing spherical harmonics method, with keeping the

Euler angle 3 (i.e., φ_2) constant. The quantified fraction of essential texture components, i.e., Cube (C), Rotated Cube (RC), Copper (Cu), Transformed Copper (TC), Goss (G), Transformed Goss (TG), Brass (B), Transformed Brass (TB), and γ -fiber) are presented and compared for the L-PBF and LP-DED specimens in both CA-H900 and CA-H1150 conditions.

In addition to the ODF maps ($0 \leq \Phi_1, \Phi, \varphi_2 \leq 90$), the fraction of texture components for the L-PBF and LP-DED specimens undergone CA-H900 and CA-H1150 heat treatments are also provided in **Figure 7-4(c)** and **Figure 7-5(c)**, respectively. At the CA-H900 heat treatment condition, the L-PBF specimen (see **Figure 7-4(a)**) has lower texture intensity (i.e., multiple random density (mrd)), $\text{mrd}_{\text{max}}=1.85$, than the LP-DED one, $\text{mrd}_{\text{max}}=3.25$ (see **Figure 7-4(b)**). This is likely due to the finer grain structure of the L-PBF specimen and most likely with more randomly oriented grains than LP-DED one. The texture intensities for both L-PBF and LP-DED specimens are reduced as compared to their NHT conditions ($(\text{mrd}_{\text{max}})_{\text{L-PBF}}=2.03$, $(\text{mrd}_{\text{max}})_{\text{LP-DED}}=20.87$) reported in [195] and became more randomized. This is ascribed to the recrystallization occurred during HIP and further heat treatment procedures (i.e., Sol + Age). Therefore, full heat treatment could to some extent weaken texture differences between the L-PBF and LP-DED 17-4 PH SS specimens induced due to the differences in the cooling rates of the AM processes.

The main texture component for the L-PBF specimen at CA-H900 heat treatment condition is TB, whereas TC1 is the main texture component for the LP-DED specimen (see **Figure 7-4(c)**). It can be seen in **Figure 7-5(c)** that the conducting CA-H1150 heat treatment will result in a more similar trend of texture component fraction in L-PBF and LP-DED specimens as compared to the CA-H900 heat treated ones. This may be due to

the longer duration of aging close to the austenite reversion temperature and likely have resulted in partial reversion of austenite. The reverted austenite then transforms to the martensite. The transformed-type texture components represent the texture formed from the parent austenite phase (face centered cubic (fcc)) during martensitic transformation.

Ping et al. [198] have shown the formation mechanism of lath martensite with a twin substructure with $\{112\}\langle 111\rangle$ relationship. **Figure 7-6** shows the $\{112\}$ pole figures as well as the linear misorientation profiles along the arrows elongated through the selected prior austenite grain (PAG) for the L-PBF and LP-DED specimens undergone CA-H900 and CA-H1150. The poles coincidence in the $\{112\}$ maps for all the conditions are in line with the reported pole figures for martensite with Kurdjumov-Sachs (K-S) relationship with parent austenite [199]. In addition, the point-to-point misorientation profiles show the boundaries with 60° misorientation indicating the twin boundaries [75], which further proves the twin-based martensitic transformation in L-PBF and LP-DED 17-4 PH SS specimens.

7.4.4. Tensile Behavior and Fractography Analysis

The engineering stress-engineering strain curves for the L-PBF and LP-DED specimens undergone CA-H900 and CA-H1150 heat treatment conditions are presented in **Figure 7-7(a)**. The tensile properties (i.e., S_y , S_u , and %El) for the L-PBF, LP-DED, and wrought 17-4 PH SS are compared in a bar chart shown in **Figure 7-7(b)**. In general, the peak-age heat treatment (i.e., CA-H900) results in the highest tensile strength in 17-4 PH SS at the expense of the ductility, whereas the over-aging heat treatment (i.e., CA-H1150) reduces the strength and increases the ductility significantly. The high tensile strength (i.e.,

S_y , S_u) after CA-H900 condition is attributed to the formation of nano-size Cu-enriched precipitates in this heat treatment condition, while these precipitates are coarsened upon over-aging resulting in higher ductility [73].

Comparing the L-PBF and LP-DED specimens, the L-PBF specimens have higher tensile strength than those of the LP-DED counterparts regardless of the heat treatment condition. This is because of the finer microstructure obtained for the L-PBF specimens than that of the LP-DED ones (see **Figure 7-3**). The L-PBF specimen has higher, whereas the LP-DED one possesses comparable tensile strength and ductility than the wrought 17-4 PH SS. The higher tensile properties of the L-PBF 17-4 PH SS is ascribed to its finer grain structure.

Although the CA-H900 heat treated LP-DED specimen has lower tensile strength than the L-PBF counterpart and is expected to have higher ductility, its ductility is comparable to that of the L-PBF specimen with higher tensile strength. The loss of the expected ductility in CA-H900 heat treated LP-DED specimen is due to the presence of δ -ferrite in its microstructure (see **Figure 7-3(c)**). **Figure 7-8** shows the kernel average misorientation (KAM), and the Schmid factor map of the bcc slip system (i.e., $\{110\} \langle 111 \rangle$) along the loading direction (i.e., parallel to Z axis) for the LP-DED 17-4 PH SS specimens heat treated at CA-H900 (**Figure 7-8(a)** and (b)) and CA-H1150 (**Figure 7-8(c)** and (d)). The δ -ferrite phase has been indicated by arrows in KAM images and circled in the Schmid factor maps. As shown in **Figure 7-8(a)** and (b) for the CA-H900 heat treatment condition, not only the δ -ferrite phase has well-defined edges, it has a strong contrast in Schmid factor with the martensitic matrix; in other words, there is a high incompatibility

between the δ -ferrite and the matrix resulting in loss of ductility considering the material possesses high strength.

Fracture surfaces of the L-PBF and LP-DED 17-4 PH SS specimens are compared in **Figure 7-9(a)** for CA-H900, and **Figure 7-9(b)** for CA-H1150 heat treatment conditions. Both conditions result in mostly axis-symmetric fracture surfaces with the shear lips of CA-H900 condition occupying very small area fractions and those of CA-H1025 condition being large. The very well-defined cup-and-cone feature CA-H1025 fracture surfaces (**Figure 7-9(b)**) suggests that their fracture was very ductile. This is consistent with the presence of quasi-cleavage facets and cracks on the fracture surfaces of the CA-H900 heat treated specimens showing the brittle behavior, while enormous dimples formed on the fracture surfaces of the CA-H1150 heat treated specimens representing the ductile behavior.

Another main difference between the fracture surfaces of the L-PBF and LP-DED specimens is the presence of the cracks in CA-H900 condition, and dimples in CA-H1150 condition. This suggests the fracture surfaces of the former condition had radial zones which were the evidence of rapid crack propagation, while the fracture of the latter condition was governed mainly by the nucleation, growth, and coalescence of voids as well as final shearing [200]. The CA-H900 treated LP-DED specimen has larger cracks and facets than the L-PBF ones, which resulted in loss of ductility despite of having lower strength. This may be related to the presence of large δ - ferrite in the microstructure of LP-DED specimen, having high incompatibility with the matrix, which resulted in crack initiation and growth along the lath martensite boundaries. On the other hand, CA-H1150

treated LP-DED specimens have larger and deeper dimples due to the coarser microstructure, justifying its higher ductility than the L-PBF ones.

7.5. Conclusions

This study characterized and compared the non-heat treated (NHT) microstructure of 17-4 PH SS fabricated via L-PBF and LP-DED AM processes. In addition, the effect of different heat treatment procedures on the crystallographic texture and room temperature tensile deformation behavior of L-PBF and LP-DED specimens were investigated. The following conclusions are drawn based on experimental results obtained:

1. The NHT L-PBF 17-4 PH SS specimen had a more refined microstructure constituent of equiaxed ferrite grains and lath martensite, whereas the microstructure of the LP-DED counterpart was composed of coarse massive ferrite, with the Widmanstätten ferrite grains decorated the grain boundaries. The variation in the cooling/solidification rates induced by L-PBF and LP-DED processes and the differences in Cr_{eq}/Ni_{eq} value for the L-PBF and LP-DED specimens may have caused these differences in NHT microstructure.
2. The δ -ferrite phase retained in the microstructure of LP-DED 17-4 PH SS specimen at room temperature. This was ascribed to the lower cooling/solidification rate in the LP-DED process and higher Cr_{eq}/Ni_{eq} value of the LP-DED specimen compared to the L-PBF one, which stabilized ferrite in the microstructure.
3. The over-aging heat treatment procedure (i.e., CA-H1150) likely have resulted in the reversion of austenite from martensite. However, the reverted austenite was retained in the microstructure of the L-PBF specimen, while transformed to martensite in the LP-DED counterpart upon cooling. The finer microstructure in

- the L-PBF specimen resulted in finer reverted austenite, which hindered the martensitic transformation.
4. The full heat treatment cycle is required for the L-PBF and LP-DED 17-4 PH SS specimens to diminish their variation in texture. Both the L-PBF and LP-DED specimens had a twin-based martensite with K-S relationship to the parent austenite.
 5. The L-PBF 17-4 PH SS specimen outperformed LP-DED and wrought counterparts with the same heat treatment in the room temperature tensile properties. This was attributed to the finer microstructure of the L-PBF specimens.
 6. The δ -ferrite phase in the CA-H900 heat treated LP-DED specimen reduces the ductility to be comparable to that of the L-PBF counterpart even though the LP-DED specimen had lower tensile strength. The high contrast between the Schmid factor of δ -ferrite phase with the martensite matrix in $\{110\} \langle 111 \rangle$ slip system (i.e., high incompatibility with matrix), as well as the sharp edges of the δ -ferrite phase justified the reduction in ductility of the material.
 7. The quasi-cleavage facets on the fracture surfaces of the CA-H900 treated specimens represented the brittle behavior of the L-PBF and LP-DED 17-4 PH SS in CA-H900 condition, while fibrous fracture surface with dimples depicted ductile behavior of the material in CA-H1150 condition.

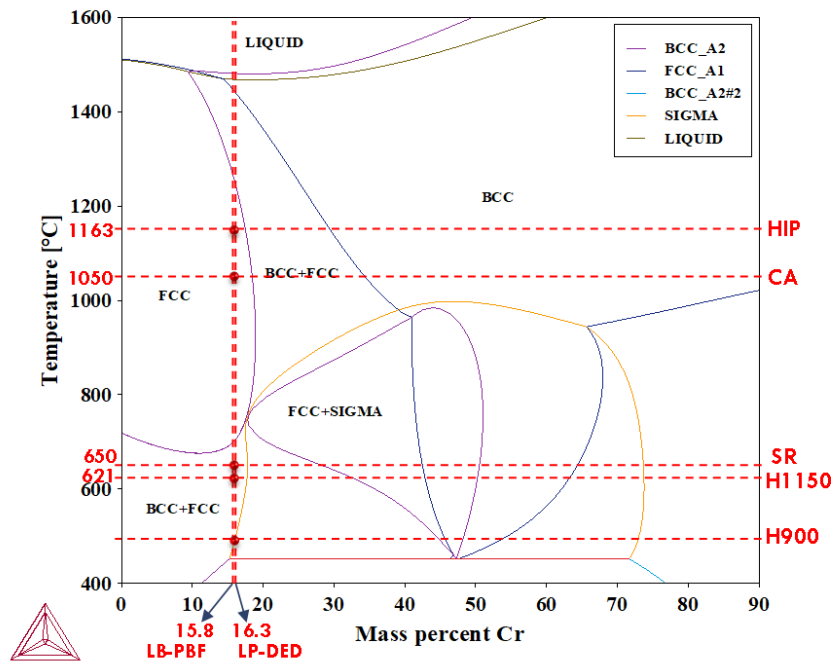


Figure 7-1. The Ni-Cr binary phase diagram samples generated by Thermo-Calc. software using TCFE9 thermodynamic database [99].

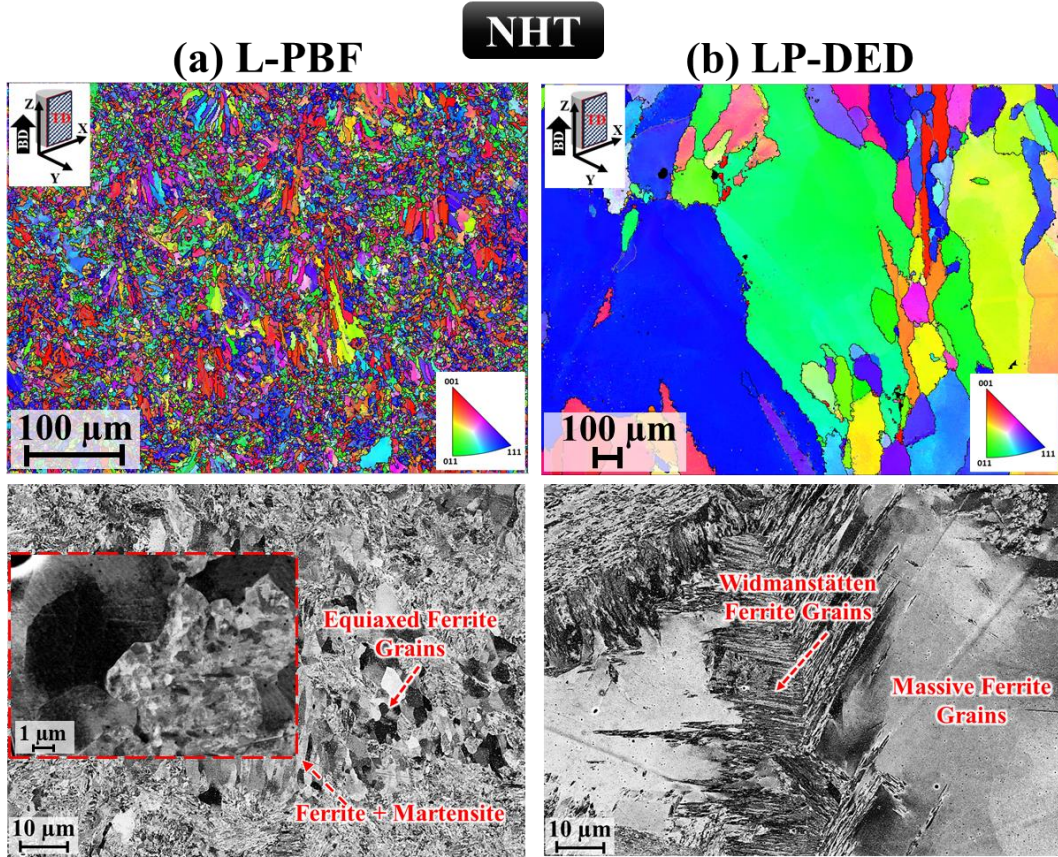


Figure 7-2. The inverse pole figure (IPF) maps along Z direction and ECCI micrographs of (a) L-PBF, and (b) LP-DED 17-4 PH SS specimens in NHT condition.

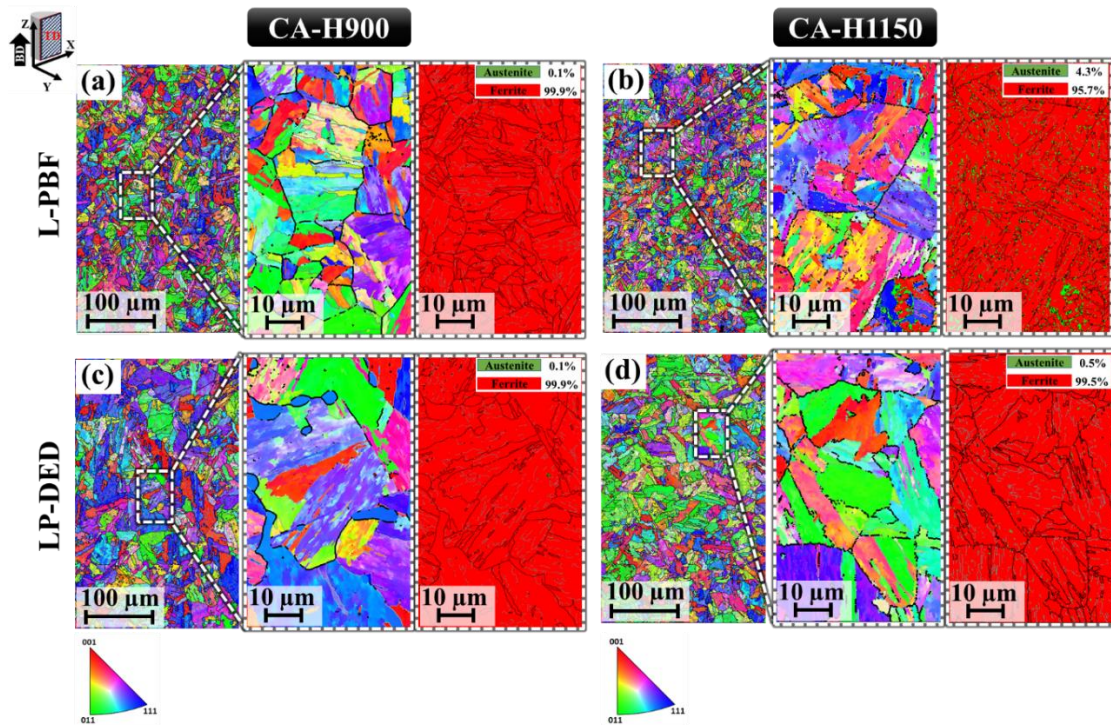


Figure 7-3. The IPF (along Z direction) and phase maps for the heat treated 17-4 PH SS specimens: (a) L-PBF and (c) LP-DED at CA-H900, and (b) L-PBF and (d) LP-DED at CA-H1150. Note that the black boundaries in magnified IPF maps (in the middle) represent the prior austenite grain (PAG) boundaries.

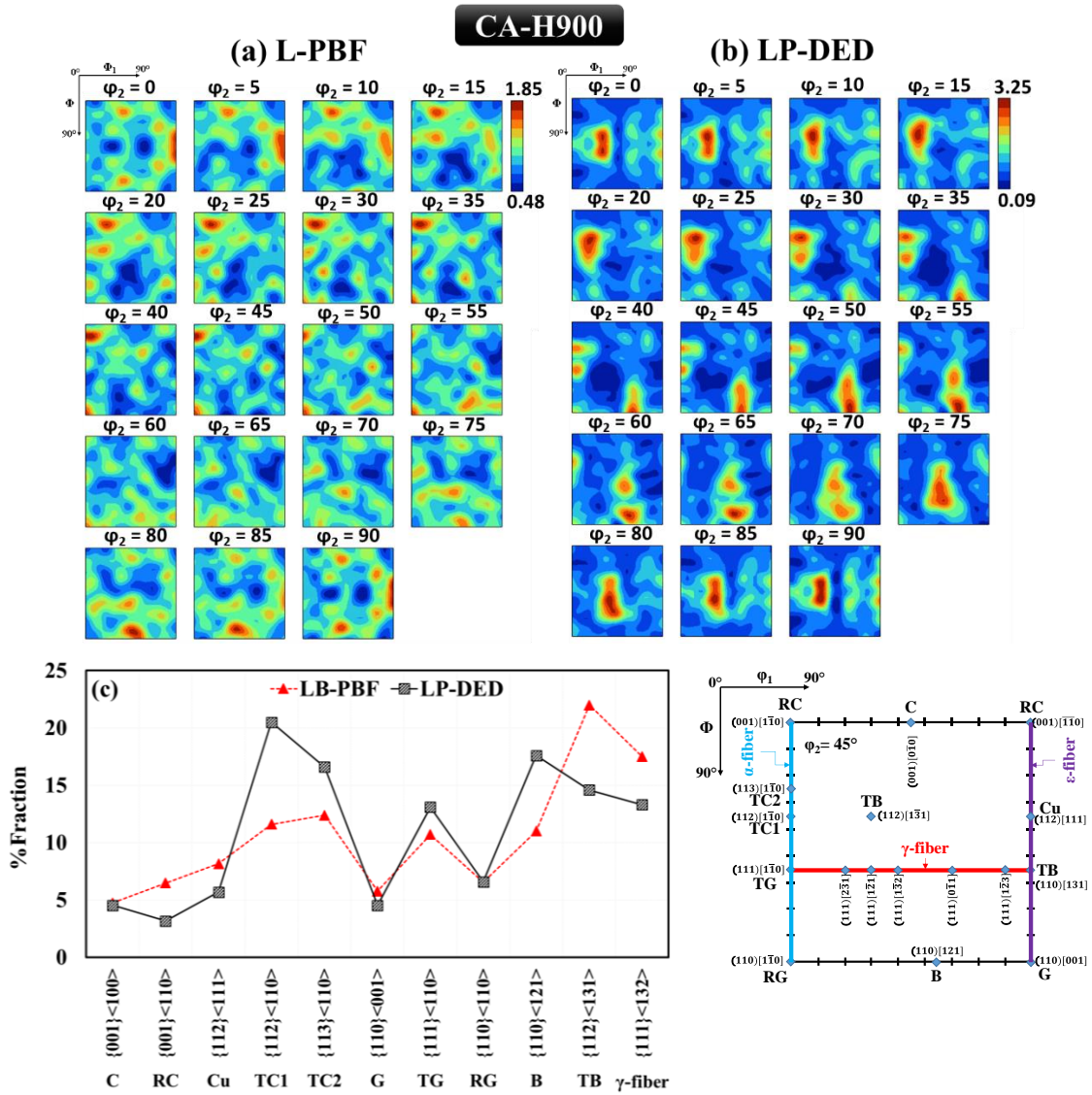


Figure 7-4. The ODF maps for the (a) L-PBF and (b) LP-DED 17-4 PH SS specimens, and (c) their quantified texture components for the CA-H900 heat treatment condition. A schematic illustration of the important texture components in bcc for $\phi_2 = 45^\circ$ is also shown.

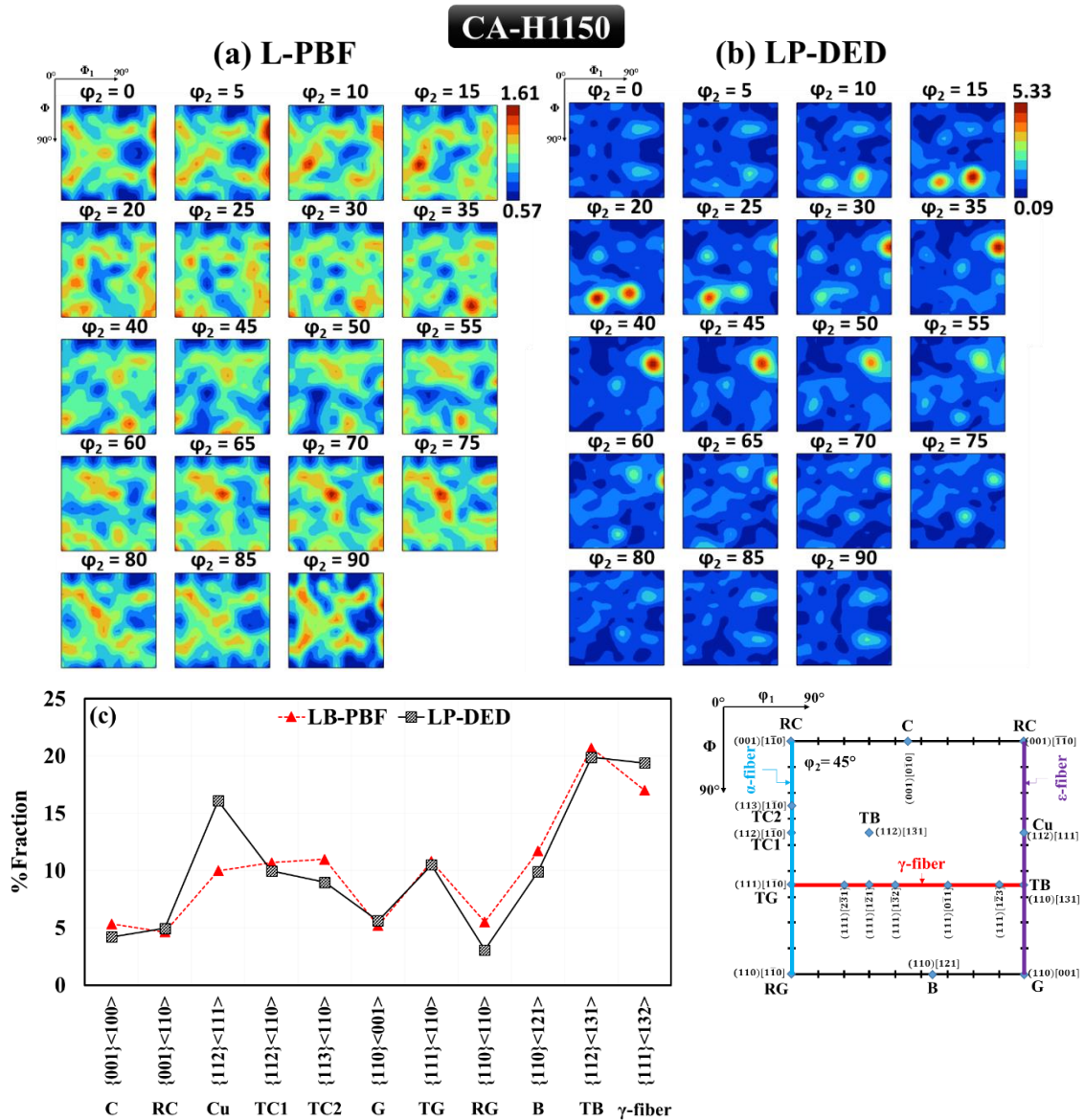


Figure 7-5. The ODF maps for the (a) L-PBF and (b) LP-DED 17-4 PH SS specimens, and (c) the quantified texture components for the CA-H1150 heat treatment condition. A schematic illustration of the important texture components in bcc for $\phi_2 = 45^\circ$ is also shown.

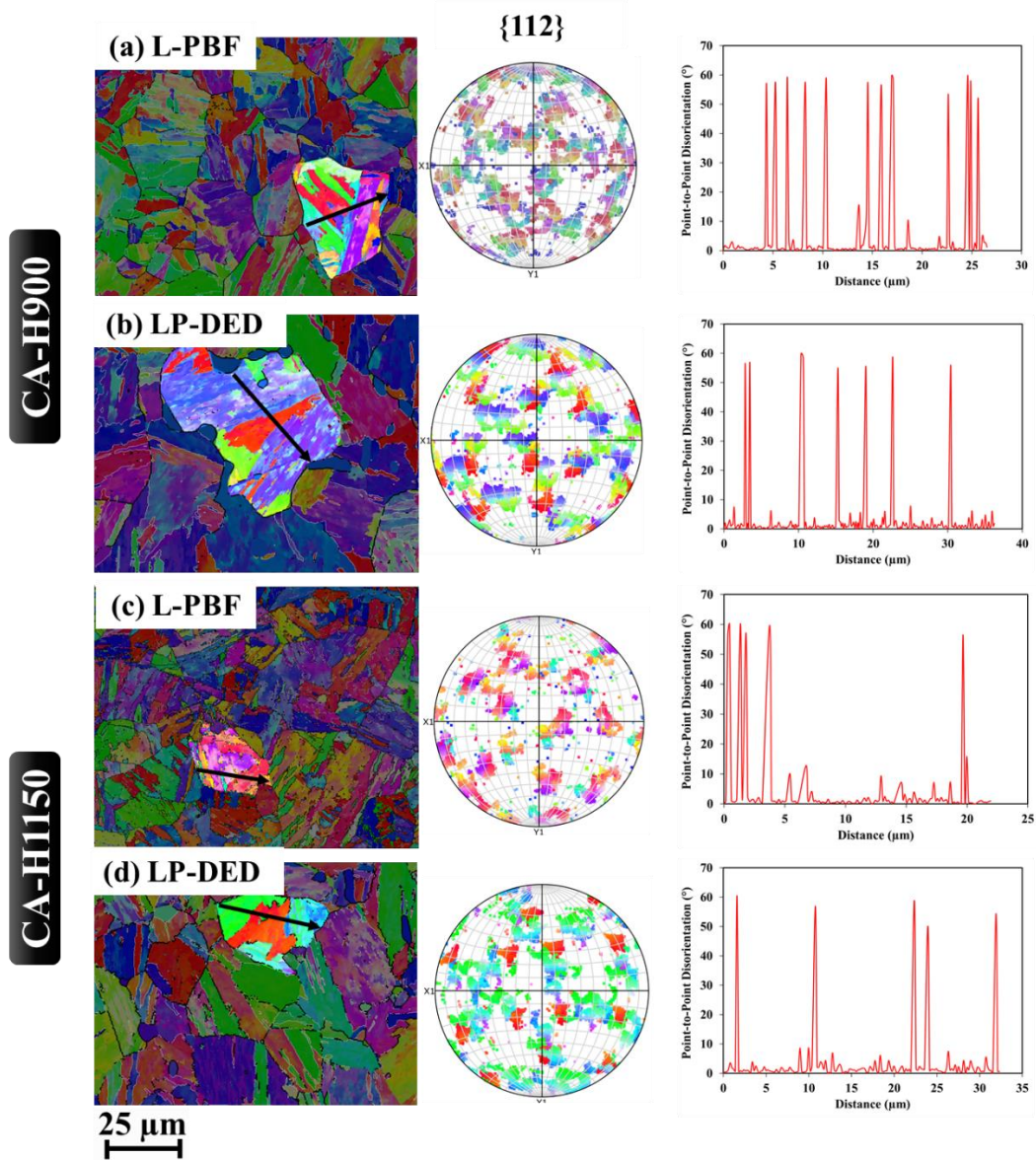


Figure 7-6. IPF maps, $\{112\}$ pole figures, and the point-to-point misorientation maps showing the twin-based substructure of the martensite in selected PAG of the L-PBF and LP-DED 17-4 PH SS specimens. CA-H900 condition: (a) L-PBF, (b) LP-DED, and CA-H1150 condition: (c) L-PBF, and (d) LP-DED.

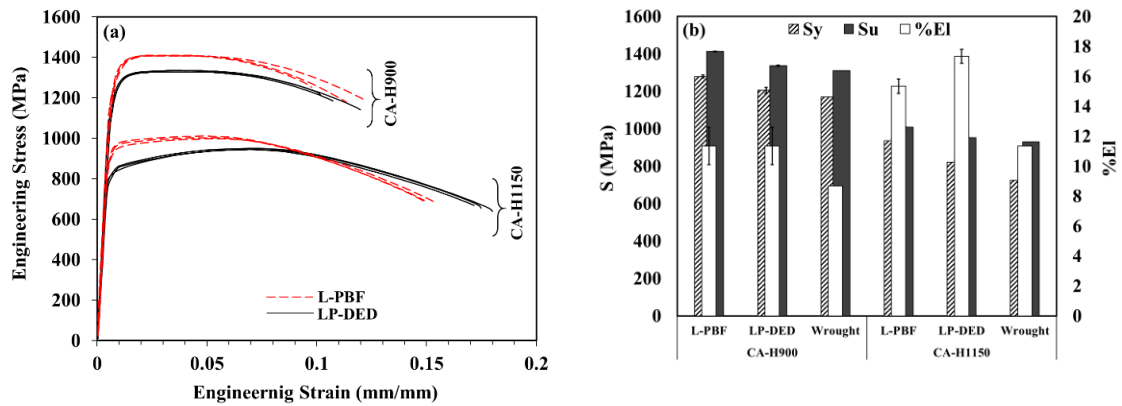


Figure 7-7. Tensile behaviors of the L-PBF and LP-DED 17-4 PH SS specimens undergone CA-H900 and CA-H1150 heat treatment conditions: (a) flow stress curves, (b) summarized tensile properties in bar chart, and (c) %elongation vs. ultimate tensile strength. The wrought data has been taken from ASTM A693 [60].

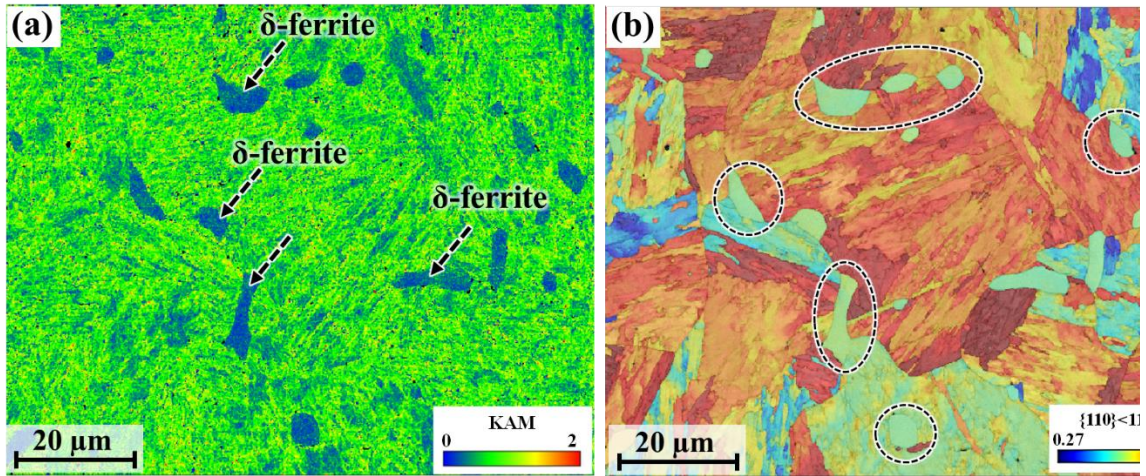


Figure 7-8. Strain analysis of the δ -ferrite phase for the LP-DED 17-4 PH SS specimen undergone CA-H900 heat treatment condition: (a) KAM, (b) Schmid factor maps. Note that loading direction parallel to Z-axis considered for generating the Schmid factor map.

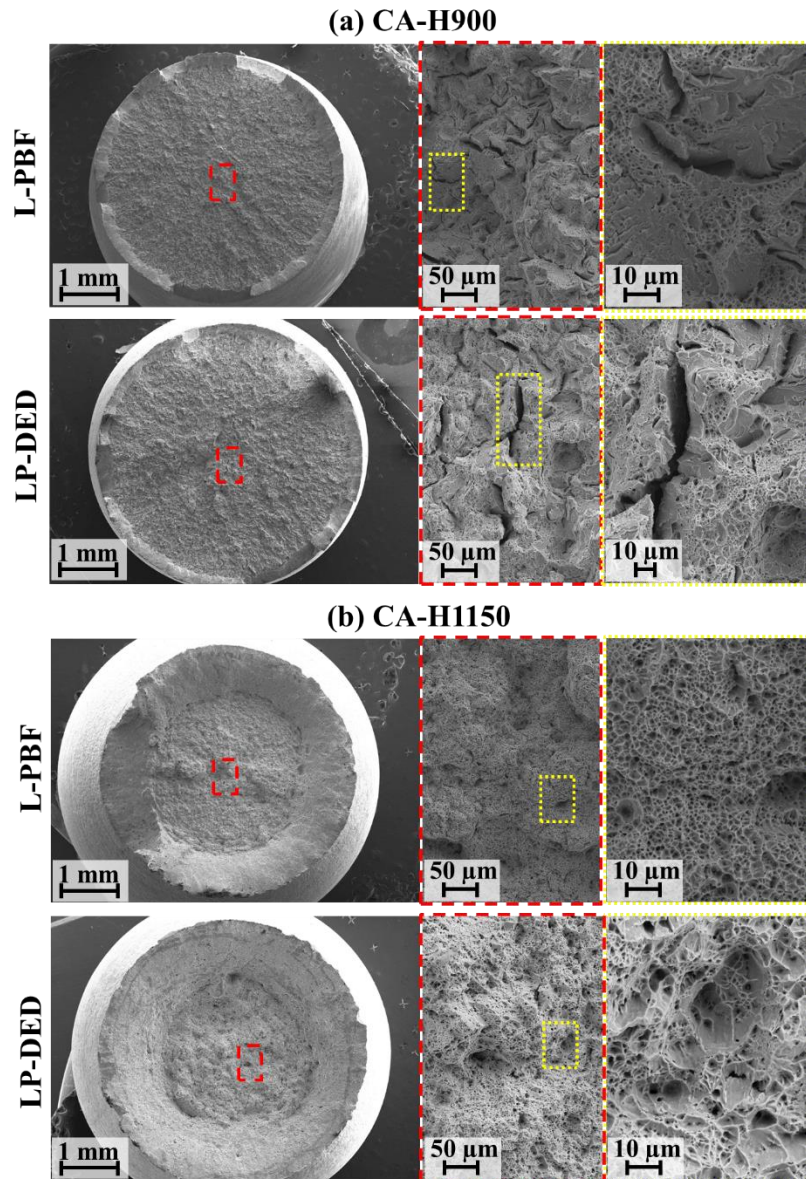


Figure 7-9. Tensile fracture surfaces of the L-PBF and LP-DED 17-4 PH SS specimens: (a) CA-H900, and (b) CA-H1150.

Table 7-1. Chemical composition for 17-4 PH SS powders used for fabrication.

| | | C | Cr | Ni | Cu | Mn | Si | Nb | Mo | N | O | P | S | Nb+T a | Fe |
|--------------------|---------|----------|-----------|-----------|-----------|-----------|-----------|-----------|-----------|----------|----------|----------|----------|-------------------|-----------|
| L- PBF | (Wt. %) | 0.01 | 15.80 | 4.60 | 3.67 | 0.51 | 0.32 | 0.32 | 0.21 | 0.02 | 0.04 | 0.035 | 0.014 | 0.27 | Bal. |
| LP- DED | (Wt. %) | 0.01 | 16.39 | 4.17 | 3.32 | 0.06 | 0.78 | 0.27 | 0.04 | 0.01 | 0.02 | 0.00 | 0.00 | 0.27 | Bal. |

**CHAPTER 8: MICROSTRUCTURE AND MECHANICAL BEHAVIOR OF
ADDITIVELY MANUFACTURED 17-4 PH STAINLESS STEEL: A
COMPARISON ACROSS L-PBF, LP-DED, AND MBJ**

The following chapter is ready to be submitted to Additive Manufacturing in 2022.

Nezhadfar, P.D., Gradl, P.R., Verquin, B., Lefebvre, F., Reynaud, C., Robert, M., Shao, S., Shamsaei, N., A comparative study on microstructure and mechanical behavior of additively manufactured 17-4 PH stainless steel: L-PBF, LP-DED, and MBJ, Additive Manufacturing.

8.1. Abstract

Different microstructures may arise when an alloy is processed by different additive manufacturing (AM) techniques due to the distinct thermal history each induces in the parts. This study focuses on 17-4 PH stainless steel (SS) fabricated via laser powder bed fusion (L-PBF), laser powder directed energy deposition (LP-DED), and metal binder jetting (MBJ) to examine the effect of AM technique and heat treatment (i.e., CA-H900 vs. CA-H1150) on the microstructure and mechanical properties (i.e., tensile and fatigue). In the non-heat treated (NHT) condition, L-PBF results in a δ -ferrite-free and finer microstructure due to using N₂ as the shielding gas and higher cooling/solidification rate. The NHT microstructures from LP-DED and MBJ are coarser and contain large, irregular-shaped δ -ferrites. Complete heat treatments (comprising hot isostatic pressing followed by homogenization and aging) can significantly diminish these differences in the microstructure. Nevertheless, the heat treated LP-DED and MBJ microstructures are slightly coarser than the L-PBF one and contain δ -ferrites, which is likely why L-PBF specimens outperforms the LP-DED and MBJ ones. Moreover, the MBJ specimens with their higher δ -ferrite content exhibited inferior tensile properties and more scattered fatigue lives compared to LP-DED ones. Between the two heat treatments considered, CA-H1150 can recondition the δ -ferrites to be smaller and more circular and thus reduce variations in mechanical properties among different processes.

8.2. Introduction

Additive manufacturing (AM), a family of layer-by-layer digital manufacturing techniques, has drawn much attention from various industrial sectors as it delivers ample opportunities for fabricating near-net-shape parts with complex internal/external geometries and reducing the production cost/leading time [201]. Among all the AM methods, laser-based techniques, e.g., laser powder bed fusion (L-PBF) and laser powder directed energy deposition (LP-DED), are perhaps the most commonly used ones [36]. Recently, metal binder jetting (MBJ), a non-laser-based solid-state AM method [202], has become a potential competitor of the L-PBF and LP-DED.

The L-PBF employs a powder bed for which a re-coater successively provides a new layer of powder with each pass, and the powder particles are melted locally in a defined pattern by a (few) high-energy laser source(s) and fused to the previously fused layers. The LP-DED does not have a powder bed and the powder is directly blown to the melt pool [1]. Although a powder bed is also involved in the MBJ, MBJ, the spread powder is selectively joined by jetting a polymeric binder, layer-by-layer, until the desired part geometry is formed. Several stages are required to further consolidate the formed parts by MBJ: curing or drying, powder removal, debinding, and sintering [2].

Significant differences exist in the fabrication procedures of the AM techniques mentioned above (i.e., L-PBF, LP-DED, and MBJ), which may make one more favorable than the others for specific applications. For instance, although L-PBF is typically limited to a single-powder feedstock within any given build, it provides more freedom in designing near-net-shaped parts with a higher geometrical resolution than the LP-DED process [181]. In contrast, LP-DED is suitable for multi-powder feedstock, functionally graded

components, and the fabrication of large parts since there is no restriction on the build box [203]. Lastly, since the shaping process via MBJ is at a low temperature (typically 80°C), there typically are no/less such issues as oxidation and residual stress, and the powder surrounding the part in the box is highly recyclable [204]. Unlike fusion-based techniques, no support structure is needed for the MBJ parts. In addition, the MBJ technique is compatible with virtually any powder material in contrast to L-PBF and LP-DED, which typically requires good weldability [205].

Each of these AM techniques induces a different thermal history to the part resulting in differences in the as-built (i.e., non-heat treated (NHT)) microstructure. For instance, Babuska et al. [181] reported L-PBF resulting in three orders of magnitude higher cooling rates than LP-DED. As a result, a finer microstructure and thus higher tensile strength were observed for L-PBF CoCr specimens than the LP-DED counterparts. Similarly, different constituent phases were reported for the IN718 when fabricated via L-PBF (spheroidal/ellipsoidal γ'' in γ matrix) vs. LP-DED (Laves phase in an interdendritic γ matrix) techniques [187–189]. A lamellar $\alpha+\beta$ structure has been reported for the L-PBF Ti-6Al-4V [190], while the LP-DED counterparts have fine lamellar Widmanstätten structure along with grain boundary α phase in the coarse columnar prior β grains [191]. It has been reported that the MBJ process results in relatively fine equiaxed grains for the 316L stainless steel (SS) compared to the columnar grain structure produced by laser-based AM techniques [204,206].

Comparing the laser-based AM techniques (i.e., L-PBF and LP-DED) with the non-laser based one (i.e., MBJ), there is a considerable variation in the thermal history a part experiences. The L-PBF and LP-DED parts experience a high cooling/solidification rate

[13,135,182] as compared to the multiple-slow-sintering-step MBJ method [3,207–209]. Interestingly, there is even a significant variation in the cooling/solidification rates of L-PBF and LP-DED methods reported; L-PBF results in three orders of magnitude higher cooling rate than LP-DED [181]. These variations in the nature of AM techniques may result in a different micro-/defect-structure, and consequently, different mechanical properties for a single material system. Therefore, heat treatments may need to be custom designed to achieve consistent mechanical properties for a material fabricated across different processes.

A vast number of studies through the literature are related to the effect of heat treatment on improving the mechanical properties of AM materials to be comparable to those of their wrought counterparts [30,210–212]. Nonetheless, the challenge is yet to be finding a post-thermal treatment that results in a comparable microstructure and mechanical performance for a single material system manufactured via different AM techniques. This assists with reducing the number of standards for each materials system with respect to the AM technique in the future. One of the AM materials that its microstructure is debated through the literature is 17-4 PH SS [16,18,26,39]. In a recent study, Nezhadfar et al. [195] compared the NHT microstructure of L-PBF 17-4 PH SS with the LP-DED counterpart. It was shown that the L-PBF 17-4 PH SS had martensite, equiaxed ferrite, and retained austenite, whereas the microstructure of the LP-DED counterpart was consisted of very coarse ferrite grains and Widmanstätten ferrite decorated the grain boundaries. However, it was shown that post-heat treatment could possibly reduce the variations in the phase constituents and the crystallographic texture of the L-PBF and LP-DED 17-4 PH SS.

Although there are several studies dedicated to the microstructure and mechanical properties of the laser-based manufactured 17-4 PH SS, there is a few that studied the microstructure of MBJ 17-4 PH SS especially after various heat treatments. It was shown that the MBJ 17-4 PH SS has a coarse martensitic structure along with δ -ferrite in the as-sintered condition, which different heat treatments are be able to refine its microstructure [171,213,214]. However, due to formation of the δ -ferrite during the sintering procedure in the MBJ process, an appropriate heat treatment is required to result in a comparable mechanical properties (tensile, and fatigue) to the laser-based AM counterparts.

Therefore, this study endeavors to evaluate and compare the microstructure and mechanical behavior of 17-4 PH SS manufactured by L-PBF, LP-DED, and MBJ methods. The grain structure and phase constituents in the NHT condition are compared. Furthermore, different heat treatments are carried out to assess the efficacy to diminish the differences in the microstructure of the 17-4 PH SS specimens fabricated via different processes. Room temperature tensile and fatigue behavior of heat treated L-PBF, LP-DED, and MBJ 17-4 PH SS specimens are compared and correlated with their microstructure. Eventually, the most effective heat treatment for alleviating the variations in the mechanical properties among the L-PBF, LP-DED, and MBJ 17-4 PH SS is suggested.

8.3. Experimental Procedures

8.3.1. Material and Fabrication Methods

In this study, 17-4 PH SS specimens were fabricated via L-PBF, LP-DED, and MBJ techniques using the pre-alloyed powders. The chemical compositions of the 17-4 PH SS powders used for each process are listed in **Table 8-1**, and the chemical compositions of the specimens after fabrication are listed in **Table 8-2**. The chemical compositions of the

powders were reported by the suppliers. For the fabricated specimens, the chemical compositions were obtained using inductive coupled plasma (ICP) and inert gas fusion (IGF) for the light elements (i.e., C, N, O).

One set of 17-4 PH SS specimens was fabricated via each different laser-based AM technique and machined to final geometry. Oversize L-PBF tensile and fatigue specimens were fabricated vertically using an EOS M290 machine in nitrogen shielding gas with the process parameters recommended by EOS. The LP-DED vertical cylindrical bars (ϕ 15.24 mm) were manufactured using RPM Innovations (RPMI) 557 machine in argon shielding gas.

One set of cylindrical bars (ϕ 12 mm) was also fabricated via the MBJ AM technique using Digital Metal Machine DM2000. The green parts underwent an air debinding cycle of soaking at 345 °C for 2 hours after powder removal. A subsequent sintering cycle was conducted using an Elnik MIM3015 T furnace in pure hydrogen at 1380 °C for 2 hours. The process parameters employed for each fabrication technique are listed in **Table 8-3**.

8.3.2. Post-Thermal Treatment

The L-PBF and LP-DED specimens were stress relieved at 650 °C for an hour. It has been shown that stress-relieving will not change the microstructure and mechanical properties of the material in fully heat treated condition [195]. For the MBJ specimens, the HIP process is generally necessary to reduce the porosities left after sintering. Therefore, to have similar heat treatment procedures for all the L-PBF, LP-DED, and MBJ specimens, an industrial HIP schedule at 1160 °C for 3 hours under 15 ksi pressure was performed on all the L-PBF, LP-DED, and MBJ specimens. According to the ASTM A693 [60] and previous heat treatment studies on the AM 17-4 PH SS, CA-H900 (peak-age), and CA-

H1150 (over-aged) heat treatment schedules were selected for obtaining the extremes in strength (i.e., CA-H900) and ductility (i.e., CA-H1150), respectively. The post-thermal treatment schedules applied to the specimens are presented schematically in **Figure 8-1**.

8.3.3. Microstructure Characterization

The specimens/bars were cut in the transverse direction (TD), parallel to the build direction (//YZ-plane) for microstructure characterization. The melt pools of the L-PBF and LP-DED specimens were characterized following the procedure proposed in Ref. [14] via etching using Braha's reagent. A Zeiss Crossbeam 550 scanning electron microscope (SEM) equipped with an Oxford electron backscatter diffraction (EBSD) detector was employed for microstructure analysis. The specimens were polished for 4 hours using a vibratory polisher with 0.02 μm colloidal silica suspension prior to conducting EBSD analysis.

8.3.4. Mechanical Properties

The fully heat treated L-PBF, LP-DED, and MBJ specimens were further machined to the tensile and fatigue geometries following ASTM E8 [196] and ASTM E606 [215] standards, respectively. The final geometries of the tensile and fatigue specimens are shown in **Figure 8-2**. Tensile and fatigue testing were carried out at room temperature. The tensile testing was conducted at 0.001 mm/mm/s strain rate, and uniaxial fully-reversed strain-controlled fatigue testing was performed at 0.005 mm/mm and 0.003 mm/mm strain amplitude levels. The frequencies for the fatigue testing were tuned based on the strain amplitude level to obtain a similar average cyclic strain rate.

8.4. Experimental Results

This section first analyzes and compares the melt pool characteristics for the L-PBF and LP-DED 17-4 PH SS specimens. It is worth noting that a melt pool is not formed in the MBJ specimens as it is a solid-state non-laser-based AM technique. The microstructures of the NHT and heat treated L-PBF, LP-DED, and MBJ specimens are then characterized and compared with each other in both NHT and heat treated conditions. The tensile and fatigue properties of heat treated L-PBF, LP-DED, and MBJ specimens are also evaluated. Moreover, the fractography results for the fatigue-tested L-PBF, LP-DED, and MBJ specimens are provided. The experimental results and immediate observations are briefly discussed in this section, while the in-depth process-structure-property relationships for the L-PBF, LP-DED, and MBJ 17-4 PH SS are formally discussed in Section 4.

8.4.1. Melt Pool Analysis: L-PBF vs. LP-DED

The melt pool analysis was carried out following the method proposed by NASA Procedure MSFC-SPEC-3717 [14] only for the L-PBF and LP-DED specimens, as there is no melt pool formation for the MBJ counterparts based on the nature of the process (i.e., solid-state non-laser-based AM technique). According to the melt pool characterization method, the melt pool depth (d_p) and melt pool overlap depth (d_o) are divided by the layer thickness (t_l); these ratios (d_p/t_l and d_o/t_l) can indicate the quality of the printing process and probability of the presence of volumetric defects, especially lack of fusion (LoF). Ratios larger than 1 suggest that the subsequently printed layer has fused to the previous layer with adequate metallurgical bonding, vice versa. Accordingly, larger ratios correspond to a lower possibility for the formation of the LoF defects.

The melt pool characteristics for the L-PBF and LP-DED 17-4 PH SS specimens are shown in **Figure 8-3(a)** and (b), respectively. As seen, the L-PBF and LP-DED specimens had ratios larger than 1 showing less possibility for LoF formation. However, the L-PBF 17-4 PH SS specimen (**Figure 8-3(a)**) possesses higher d_p/t_i , and slightly lower (almost similar) d_o/t_i than those of the LP-DED one (**Figure 8-3(b)**). The higher d_p/t_i ratio of the L-PBF 17-4 PH SS specimen may be related to the N₂ shielding gas used during the fabrication compared to the Ar shielding gas for the LP-DED 17-4 PH SS. It has been shown that N₂ shielding gas results in deeper melt pools as compared to the Ar shielding gas [162].

8.4.2. Non-heat treated (NHT) Microstructure

The microstructures of L-PBF, LP-DED, and MBJ 17-4 PH SS in NHT condition are compared in **Figure 8-4**. The inverse pole figure maps and phase maps are shown for the YZ-plane, i.e., parallel to the build direction. As seen, there is a significant variation in the grain structure and phase constituent of the NHT 17-4 PH SS specimens fabricated via different AM methods. Microstructure of the L-PBF 17-4 PH SS (**Figure 8-4(a)**) is comprised of the fine columnar and equiaxed ferrite grains (average grain size ~6 μm), a small fraction of retained austenite (~0.4% in the cross-section showed), and lath martensite, while the LP-DED counterpart (**Figure 8-4(b)**) has very coarse massive ferrite grains and the Widmanstätten ferrite on the grain boundaries (average grain size ~94 μm). The electron channeling contrast imaging (ECCI) micrographs of the lath martensite in L-PBF and Widmanstätten ferrite in LP-DED specimens have been presented in our previous study [163]. As seen in **Figure 8-4(c)**, the MBJ 17-4 PH SS may have had coarse prior austenite grains, which transformed to coarse lath martensite upon solidification, and a

small fraction of austenite has retained in the microstructure (~0.4% in the cross-section showed). In addition, string-like δ -ferrite grains remained in the MBJ specimen microstructure formed during the high-temperature sintering.

It can be seen clearly how the thermal history variation in different AM techniques influences the grain structure and phase constituent. The higher cooling rate of the L-PBF process compared to the LP-DED process (~3 times higher) results in significant grain refinement in L-PBF 17-4 PH SS specimens. In addition, using N₂ as the shielding gas in L-PBF specimens can increase the N content in the fabricated specimens; it can be seen in **Table 8-2** that the N content in the L-PBF specimen is increased by 100 ppm compared to the amount of N in the powder (see **Table 8-1**). It has been discussed in several studies that the N can diffuse to the stainless steel, promote the retained austenite in the microstructure and prohibit the formation of δ -ferrite [110,162,216]. On the other hand, due to a much slower solidification rate during the sintering of the MBJ specimens compared to the L-PBF and LP-DED, δ -ferrite grains are formed and retained in the microstructure following the solidification order of liquid \rightarrow δ -ferrite + austenite \rightarrow δ -ferrite + martensite + retained austenite [195].

8.4.3. Heat Treated Microstructure

Microstructure of the L-PBF, LP-DED, and MBJ 17-4 PH SS specimens after the full heat treatment schedules (see **Figure 8-1**), CA-H900 and CA-H1150, are presented in **Figure 8-5** and **Figure 8-6**, respectively. The IPF maps on the YZ-plane parallel to the build direction and the phase maps in higher magnification are depicted for each condition. As seen in **Figure 8-5** and **Figure 8-6**, conducting heat treatment diminishes the significant variation in the microstructure of the L-PBF, LP-DED, and MBJ 17-4 PH SS specimens

seen in **Figure 8-4**. The ferrite-based microstructure shown in the NHT condition transforms into a mostly martensitic microstructure. However, there are still differences in the phase constituent and grain structure of the L-PBF, LP-DED, and MBJ 17-4 PH SS specimens.

The L-PBF 17-4 PH SS specimen heat treated at CA-H900 condition (**Figure 8-5(a)**) has a martensitic microstructure and a small fraction of retained austenite. As seen, the heat treated L-PBF specimens inherit their fine microstructure in NHT condition; the heat treated L-PBF specimen has finer microstructure than the LP-DED and MBJ ones. The microstructures of the CA-H900 heat treated LP-DED (**Figure 8-5(b)**) and MBJ (**Figure 8-5(c)**) specimens comprise martensite and δ -ferrite. The δ -ferrite fraction in the LP-DED specimen is $\sim 4.9\%$, while a higher fraction of δ -ferrite is present in MBJ one ($\sim 12\%$).

The δ -ferrite in the LP-DED specimen is smaller and less string-like than that of the MBJ counterpart. The higher fraction of δ -ferrite in the MBJ specimen may be due to the high sintering temperature. It has been reported for the MBJ 316 SS that the fraction of δ -ferrite is increased during the sintering process [204]. It is worth noting that δ -ferrite formed during solidification in LP-DED and MBJ specimens are not eliminated even by further heat treatments; however, δ -ferrite grains are re-distributed, and the shape is changed from string-like to more globular during the prolonged aging steps (e.g., CA-H1150).

As seen in **Figure 8-6**, heat treating at CA-H1150 results in austenite reversion; the retained austenite fraction of the L-PBF, LP-DED, and MBJ specimens increased from 0.1% (see **Figure 8-5**) to $\sim 4.3\%$, $\sim 0.5\%$, and $\sim 0.9\%$, respectively. The austenite that is

reversed along the lath martensite is more stable and not transformed to martensite after cooling [217,218]. This is due to the high concentration of austenite stabilizer elements and the very small size of reversed austenite, which increases the stability of the austenite at room temperature during cooling, avoiding martensitic transformation [219].

The L-PBF 17-4 PH SS specimen (**Figure 8-6(a)**) has a higher fraction of retained austenite than the LP-DED and MBJ counterparts. This is because of using nitrogen as the shielding gas, which stabilizes austenite in the microstructure [216]. It is well established that nitrogen shielding gas promotes the stability of the austenite in stainless steels and inhibits the formation of δ -ferrite [128,216]. As was mentioned, the δ -ferrite in the LP-DED and MBJ microstructure is not eliminated; however, its shape is changed after the CA-H1150 heat treatment condition (see **Figure 8-6**); the string-like δ -ferrite may break to pieces, to a rounder shape with less sharp edges [220]. However, it seems that the morphology of the δ -ferrite in the CA-H1150 condition (**Figure 8-6(c)**) has not been changed much for the MBJ specimens compared to the CA-H900 condition (**Figure 8-5(c)**).

8.4.4. Tensile Results

Tensile properties of the L-PBF, LP-DED, and MBJ 17-4 PH SS specimens heat treated at CA-H900 and CA-H1150 conditions are presented in **Figure 8-7**, and the details are listed in **Table 8-4**. Regardless of the AM process (i.e., L-PBF, LP-DED, and MBJ), the CA-H900 heat treatment results in higher tensile strength, i.e., yield strength (YS) and ultimate tensile strength (UTS), and lower percent elongation to failure (%El) as compared to CA-H1150. This has been ascribed to the much smaller size and much higher

density of the Cu-enriched precipitates in the CA-H900 condition compared to the CA-H1150 [26].

Upon more extended aging duration at CA-H1150 heat treatment condition, the precipitates are coarsened, reducing the strength and increasing the material's ductility compared to the CA-H900 condition [96,134]. In addition, retained austenite in CA-H1150 heat treated specimens (see **Figure 8-6**) also contributes to the improvement in ductility 1) as the austenite is softer than martensite [134,221], and 2) the austenite can transform to martensite during deformation and increase the plasticity, which is referred to as the transformation induced plasticity (TRIP) phenomenon [222,223]. As seen in **Table 8-4**, regardless the AM technique, the AM 17-4 PH SS possesses comparable tensile properties to those of the wrought counterpart [60]. The similar behavior has been reported throughout the literature for various AM materials [159,224]. Nonetheless, the L-PBF specimens with the finer microstructure and absence of detrimental δ -ferrite phase outperform the wrought material.

8.4.5. Fatigue Data and Fractography

Uniaxial, fully-reversed, strain-controlled fatigue data for the L-PBF, LP-DED, and MBJ 17-4 PH SS specimens heat treated at CA-H900 and CA-H1150 are listed in **Table 8-5** and **Table 8-6**, respectively. The effect of heat treatment conditions (i.e., CA-H900 and CA-H1150) on the fatigue behavior of the L-PBF, LP-DED, and MBJ specimens tested at 0.005 mm/mm strain amplitude is presented in **Figure 8-8**. As seen, L-PBF and LP-DED 17-4 PH SS undergone CA-H900 heat treatment condition exhibit slightly superior fatigue lives to the CA-H1150 counterpart. Unlike the L-PBF and LP-DED 17-

4 PH SS specimens, the MBJ counterpart heat treated in the CA-H900 condition exhibit significantly lower fatigue lives with more scatter than the CA-H1150 ones.

Fracture surfaces of the selected L-PBF, LP-DED, and MBJ specimens in each heat treatment condition, i.e., CA-H900 and CA-H1150, are presented in **Figure 8-9**. Due to the HIP process applied to the specimens, there are no volumetric defects seen to initiate the cracks regardless of the AM process and heat treatment condition. For the L-PBF specimens, cracks initiated on the surface for both CA-H900 (**Figure 8-9(a)**) and CA-H1150 (**Figure 8-9(b)**) conditions. Considering the relatively high strain amplitude (i.e., 0.005 mm/mm), the surface crack initiation may be due to the dislocation movement to the surface and the formation of intrusions/extrusions [225]. However, there are small facets close to the surface seen on the fracture surfaces of the LP-DED specimens in both CA-H900 (**Figure 8-9(c)**) and CA-H1150 (**Figure 8-9(d)**) conditions, and large facets on the fracture surface of MBJ (**Figure 8-9(e)** and (f)) ones. These facets may correlate with the δ -ferrite grains in the microstructures of LP-DED and MBJ specimens seen in **Figure 8-5** and **Figure 8-6**.

8.5. Discussion on the Experimental Results

In this section, variations in tensile properties of the L-PBF, LP-DED, and MBJ 17-4 PH SS specimens are first discussed and correlated to the differences in their microstructure under different heat treatment conditions. The fatigue behavior and failure mechanism of the L-PBF, LP-DED, and MBJ 17-4 PH SS specimens are then compared in different heat treatment conditions. The process-structure-property relationship of AM 17-4 PH SS is investigated for different heat treatment conditions. It is also discussed whether

any heat treatment conditions can alleviate the variation in the mechanical properties of AM 17-4 PH SS fabricated via different techniques.

8.5.1. Microstructure and Tensile Behavior

As expected, variation in the thermal history among different AM processes (i.e., L-PBF, LP-DED, and MBJ) causes differences in the microstructure of the AM 17-4 PH SS after fabrication (see **Figure 8-4**). The lower the cooling rate is, the coarser grains are formed; in this case, LP-DED 17-4 PH SS specimens (**Figure 8-4(b)**) possess coarser ferrite grains than the L-PBF counterpart (**Figure 8-4(a)**) in NHT condition. Furthermore, for the MBJ specimens, for which powder sintering is the primary consolidation step, the microstructure is even coarser (**Figure 8-4(c)**) compared to LP-DED. Applying a complete heat treatment cycle, i.e., HIP + solutionizing + aging, moderately alleviates the differences in microstructure of NHT AM 17-4 PH SS to some extent (**Figure 8-5** and **Figure 8-6**). However, differences (e.g., phase constituents) in the microstructure of the L-PBF, LP-DED, and MBJ specimens still remain, which may result in variation in mechanical properties.

Tensile properties of the L-PBF, LP-DED, and MBJ 17-4 PH SS after CA-H900 and CA-H1150 heat treatment conditions are compared in **Figure 8-10(a)** and (b), respectively. As seen, L-PBF 17-4 PH SS specimens exhibit higher tensile strength (i.e., YS and UTS) and higher ductility compared to the LP-DED and MBJ counterparts at CA-H900 heat treatment condition (**Figure 8-10(a)**). This is ascribed to the finer microstructure and absence of δ -ferrite in L-PBF specimens; The average initial grain size for the L-PBF specimens is 6 μm in NHT condition, which results in nano-scale lath martensite (560 nm) after heat treatment as also has been reported in [162]. Following the Hall-Petch law, the

YS has an inverse correlation with the microstructural feature size (e.g., grain size, lath martensite size, etc.), which is in line with the results observed herein comparing the YS_{L-PBF} with YS_{LP-DED} and YS_{MBJ} .

On the other hand, the LP-DED and MBJ 17-4 PH SS have lower strength than the L-PBF one in CA-H900 condition, which is expected to result in higher ductility; however, their ductility is inferior to the L-PBF counterpart. This is attributed to the presence of δ -ferrite in the LP-DED and MBJ microstructure, as indicated in **Figure 8-5(b)**. It has been shown that the δ -ferrite grains in LP-DED 17-4 PH SS heat treated at CA-H900 possess a high contrast in Schmitt factor with the matrix [163]. The stress concentration is normally high on the sharp edges of the δ -ferrite. Therefore, due to the brittleness of the δ -ferrite [226,227], high-stress concentration, and high mismatch in Schmitt factor with the matrix [163], cracks can occur in the interface of δ -ferrite and matrix, reducing the ductility of the material. Moreover, due to the higher fraction of δ -ferrite in MBJ specimens than the LP-DED ones, the MBJ 17-4 PH SS exhibit lower ductility with a higher range of scatter.

The tensile behavior of L-PBF, LP-DED, and MBJ specimens at CA-H1150 heat treatment condition is presented in **Figure 8-10(b)**. The L-PBF 17-4 PH SS possesses higher tensile strength (i.e., YS and UTS) compared to the LP-DED and MBJ counterparts, with slightly lower ductility. The high YS of the L-PBF specimens is ascribed to its finer microstructure than the LP-DED and MBJ ones (see **Figure 8-6**). Interestingly, although the L-PBF specimens possesses higher strength than the LP-DED and MBJ specimens, its %El is only reduced by 1-2% compared to the LP-DED and MBJ specimens. This is ascribed to the considerable fraction of retained austenite (~4.3%) in the L-PBF specimen microstructure. The retained austenite has a twofold effect, first it is softer than the

martensite and can accommodate the plastic deformation by dislocation gliding. Second, retained austenite can transform to martensite during deformation and increase the plasticity and avoid reduction in strength due to the strain hardening due to the TRIP effect [16].

8.5.2. Fatigue Behavior

Fatigue lives of the L-PBF, LP-DED, and MBJ 17-4 PH SS is compared in **Figure 8-11** for CA-H900 and CA-H1150 heat treatment conditions in the LCF regime. It is well established that most portion of the fatigue life is spent in the crack growth step; therefore, the microstructure impacts the cyclic fracture toughness of the material [9]. As seen in **Figure 8-11(a)** for the CA-H900 heat treatment condition, the L-PBF 17-4 PH SS specimens outperform the LP-DED and MBJ counterparts. The higher strength and ductility of the L-PBF specimens may result in their higher cyclic fracture toughness resulting in longer fatigue lives than the LP-DED and MBJ ones. On the other hand, brittle δ -ferrite in LP-DED and MBJ specimens deteriorates their fatigue performance. Due to the strain incompatibility (i.e., the high Schmitt factor contrast between the δ -ferrite and the martensitic matrix [163], there may be a high-stress concentration on the interface of the δ -ferrite and the matrix resulting in crack formation. Furthermore, the cracks can grow on the interface of the string-like δ -ferrite grains and coalesce, thus, increasing the crack propagation rate [228]. In addition, since the δ -ferrite grains are brittle, the cracks also propagate transgranular leaving faceted features on the fracture surface of the LP-DED and MBJ specimens (see **Figure 8-9(c)** and (e), respectively).

The MBJ 17-4 PH SS heat treated at CA-H900 exhibits lower and significantly more scattered fatigue results than the LP-DED ones. The poor fatigue performance of the MBJ

17-4 PH SS may be attributed to its higher fraction of δ -ferrite (12%) compared to that of the LP-DED counterpart (4.9%). Moreover, as seen in **Figure 8-12**, some un-sintered regions are found on the fracture surfaces of some MBJ specimens, which exacerbate the material's fatigue performance. Such defects indicate that the process parameters and post-process sintering procedures may require further optimization.

The fatigue lives of L-PBF, LP-DED, and MBJ 17-4 PH SS specimens in CA-H1150 heat treatment condition are presented in **Figure 8-11(b)**. Similar to the results obtained for the CA-H900 heat treatment condition, the L-PBF 17-4 PH SS specimens exhibit better fatigue performance than the LP-DED and MBJ ones. Along with the finer microstructure in L-PBF specimens, the higher fraction of retained austenite (4.3%, as shown in **Figure 8-6(a)**) can enhance the fatigue behavior of the L-PBF 17-4 PH SS in CA-H1150 heat treatment condition. It has been reported that retained austenite enhances the LCF behavior by reducing the crack growth rate due to the TRIP effect [229,230].

The CA-H1150 heat treatment is found to alleviate the fatigue performance variation between the L-PBF, LP-DED, and MBJ specimens. As seen in **Figure 8-6(b)**, the δ -ferrite in the LP-DED specimens is more circular and less string-like than those in the CA-H900 heat treatment. The change in morphology of the δ -ferrite by applying the CA-H1150 heat treatment results in less stress concentration, thus, alleviating the detrimental effect of δ -ferrite on the fatigue behavior of the LP-DED specimens. In contrast, there is not much difference between the morphology of the δ -ferrite in the CA-H1150 and CA-H900 heat treated MBJ specimens (see **Figure 8-5(c)** and **Figure 8-6(c)**). Nonetheless, less scatter in the fatigue lives of MBJ specimens is because of the increase in ductility of the material which reduces the materials sensitivity. For the LP-DED specimens, the increase in

ductility of the material and change in the morphology of the δ -ferrite results in a slight improvement compared to the MBJ ones.

Interestingly, MBJ specimens exhibit a better fatigue performance in the CA-H1150 heat treatment condition than the CA-H900; there is less scatter in fatigue life, although the MBJ 17-4 PH SS still shows an inferior fatigue performance to the LP-DED and L-PBF counterparts. The less scatter in fatigue life of MBJ specimens is due to the higher ductility of the material in CA-H1150 heat treatment condition that alleviated the sensitivity of the material to the possible un-sintered regions as well as the δ -ferrite with sharp edges. It is worth noting that none of the CA-H1150 heat treated specimens exhibited un-sintered regions on the fracture surfaces; however, this does not mean that the un-sintered regions do not exist in the MBJ specimens.

8.6. Conclusions

This study investigated the microstructure and mechanical properties of L-PBF, LP-DED, and MBJ 17-4 PH SS. The L-PBF, LP-DED, and MBJ 17-4 PH SS microstructures were compared in NHT condition and after applying CA-H900 and CA-H1150 heat treatments. Heat treatments were carried out to understand if post-thermal treatments can alleviate the microstructure variations due to the differences in the cooling/solidification rates between the AM techniques. In addition, the tensile and fatigue behaviors of the L-PBF, LP-DED, and MBJ specimens were evaluated and compared for the CA-H900 and CA-H1150 heat treatment conditions. The following conclusions were drawn based on the obtained results:

1. The as-fabricated 17-4 PH SS's microstructure depended on the thermal history experienced during AM process. The L-PBF 17-4 PH SS had a fine ferrite + lath

- martensite + retained austenite, while the microstructure of the LP-DED counterpart consisted of coarse columnar massive ferrite + Widmanstädter ferrite, and the MBJ specimen had martensite + δ -ferrite in the microstructure in the NHT condition.
2. To some extent, heat treatment diminished the microstructural variation between the L-PBF, LP-DED, and MBJ 17-4 PH SS. The AM 17-4 PH SS's microstructure consisted of martensite and a small fraction of retained austenite after CA-H900 heat treatment. However, the amount of retained austenite increased for the CA-H1150 heat treatment condition. Regardless of the heat treatment condition, L-PBF possessed the finest microstructure, inherited from its fine microstructure in the NHT condition.
 3. The L-PBF 17-4 PH SS in CA-H900 condition had the highest YS and UTS, which was attributed to its finer microstructure. The LP-DED and MBJ specimens exhibited lower %EL than the L-PBF ones, which was ascribed to the presence of δ -ferrite in the LP-DED and MBJ induced microstructure, having a high strain incompatibility (i.e., high Schmitt factor) with the matrix.
 4. Almost Comparable tensile properties were obtained for the L-PBF, LP-DED, and MBJ specimens subjected to the CA-H1150 heat treatment. The CA-H1150 procedure decreased the strength and increased ductility of the material, which reduced the sensitivity of the LP-DED and MBJ specimens to the δ -ferrite. In addition, the CA-H1150 modified the morphology of δ -ferrite in LP-DED specimens compared to the CA-H900 condition.

5. The L-PBF 17-4 PH SS slightly outperformed the LP-DED and MBJ ones in fatigue performance regardless of the heat treatment condition. There was a significant scatter in fatigue lives of the MBJ 17-4 PH SS in CA-H900 condition, which was due to the sensitivity of the material to the string-like δ -ferrite with sharp edges and un-sintered regions. However, the scatter in fatigue life of MBJ 17-4 PH SS was decreased in the CA-H1150 heat treatment condition ascribed to the increase in ductility of the material being less sensitive to the δ -ferrite with sharp edges and un-sintered regions
6. The crack initiation occurred on the surface of the L-PBF specimens, which was attributed to the formation of intrusion/extrusion. However, the crack initiation mostly occurred from the faceted features for the LP-DED and MBJ specimens. The faceted features were attributed to the δ -ferrite in the microstructure resulting in the transgranular fracture mechanism in LP-DED and MBJ specimens.
- 7.

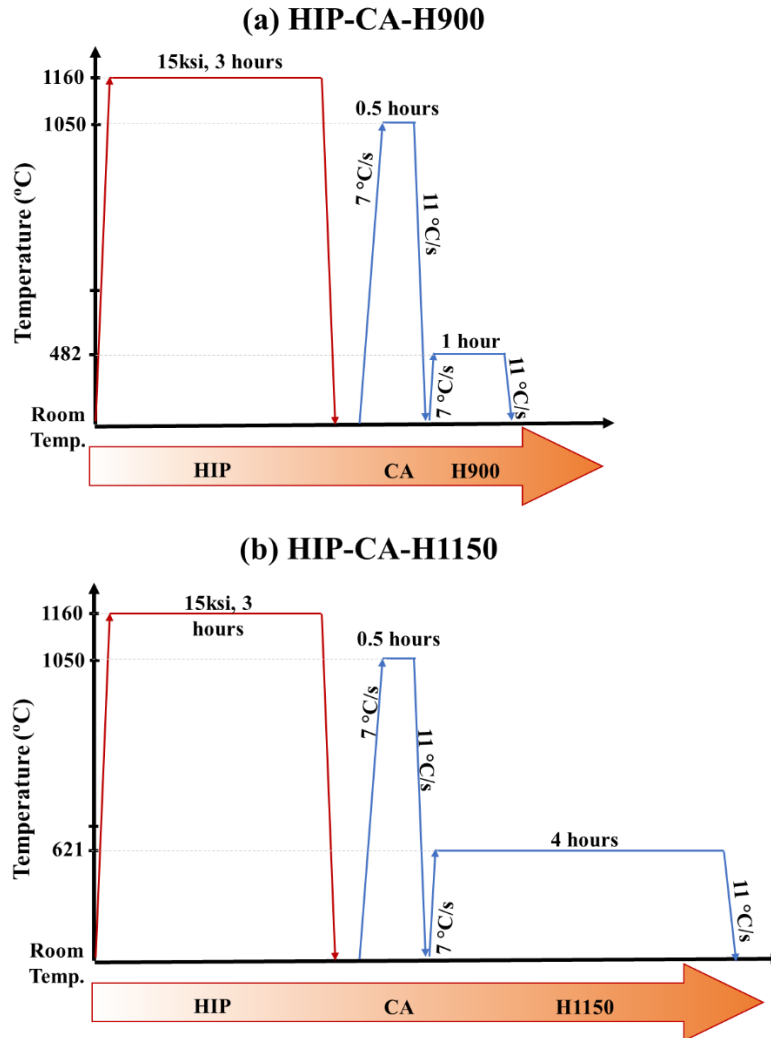


Figure 8-1. Post-thermal treatment schedules that were applied to the L-PBF, LP-DED, and MBJ 17-4 PH SS specimens: (a) HIP-CA-H900 and (b) HIP-CA-H1150.

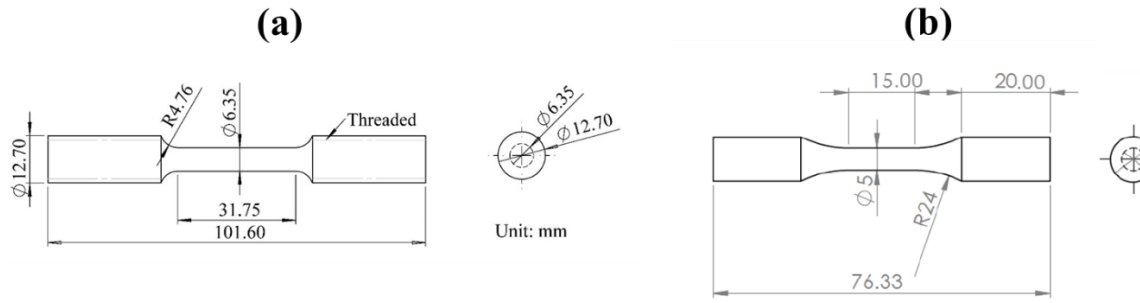


Figure 8-2. The final geometry of: (a) tensile and (b) fatigue specimens.

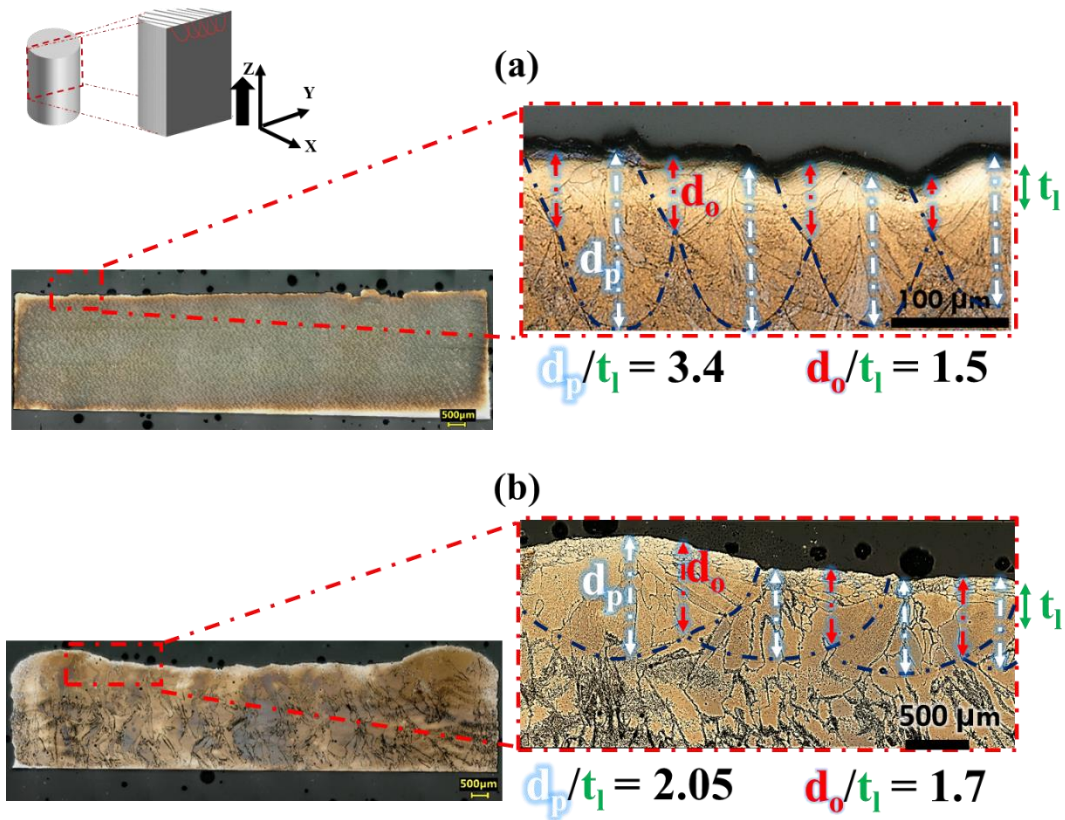


Figure 8-3. The melt pool analysis of (a) L-PBF and (b) LP-DED 17-4 PH SS specimens. Note that the d_p , d_o , and t_l are the melt pool depth, melt pool overlap depth, and layer thickness, respectively.

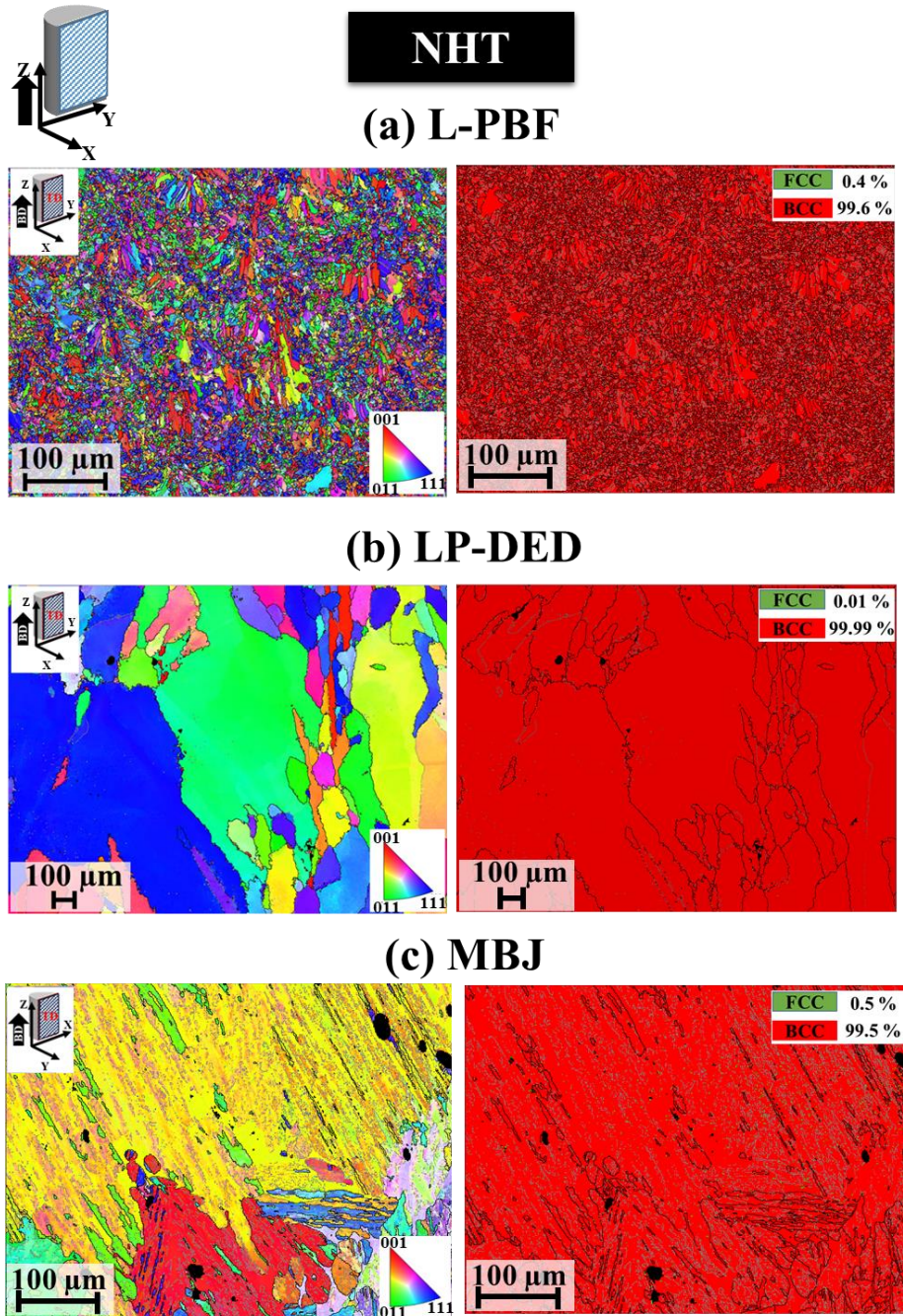


Figure 8-4. The NHT microstructure of (a) L-PBF, (b) LP-DED, and as-sintered microstructure of the (c) MBJ 17-4 PH SS. The IPF and phase maps obtained from EBSD analysis are shown.

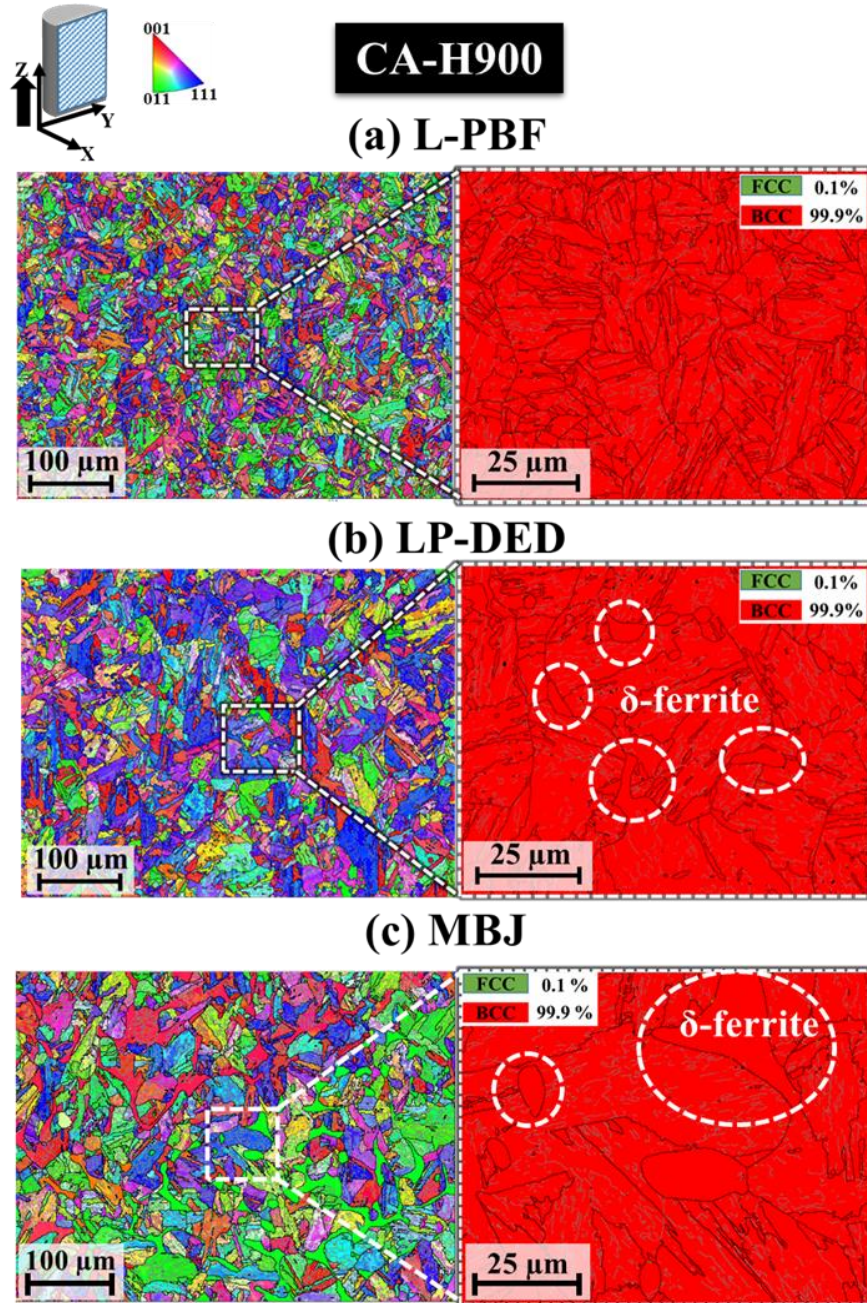


Figure 8-5. The IPF and phase maps of the heat treated 17-4 PH SS specimens at CA-H900 condition: (a) L-PBF, (b) LP-DED, and (c) MBJ.

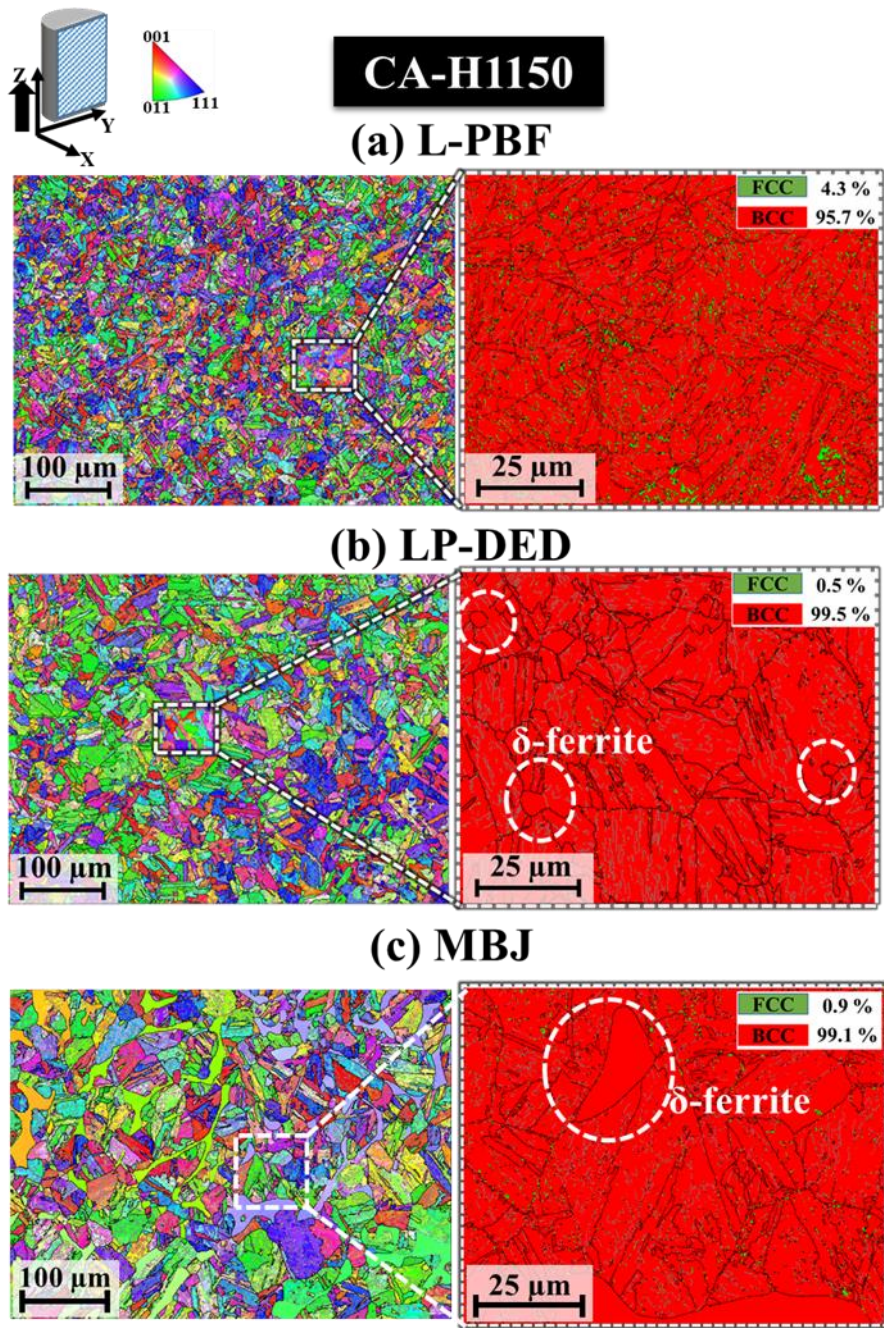


Figure 8-6. The IPF and phase maps of the 17-4 PH SS specimens, heat treated at CA-H1150 condition: (a) L-PBF, (b) LP-DED, and (c) MBJ.

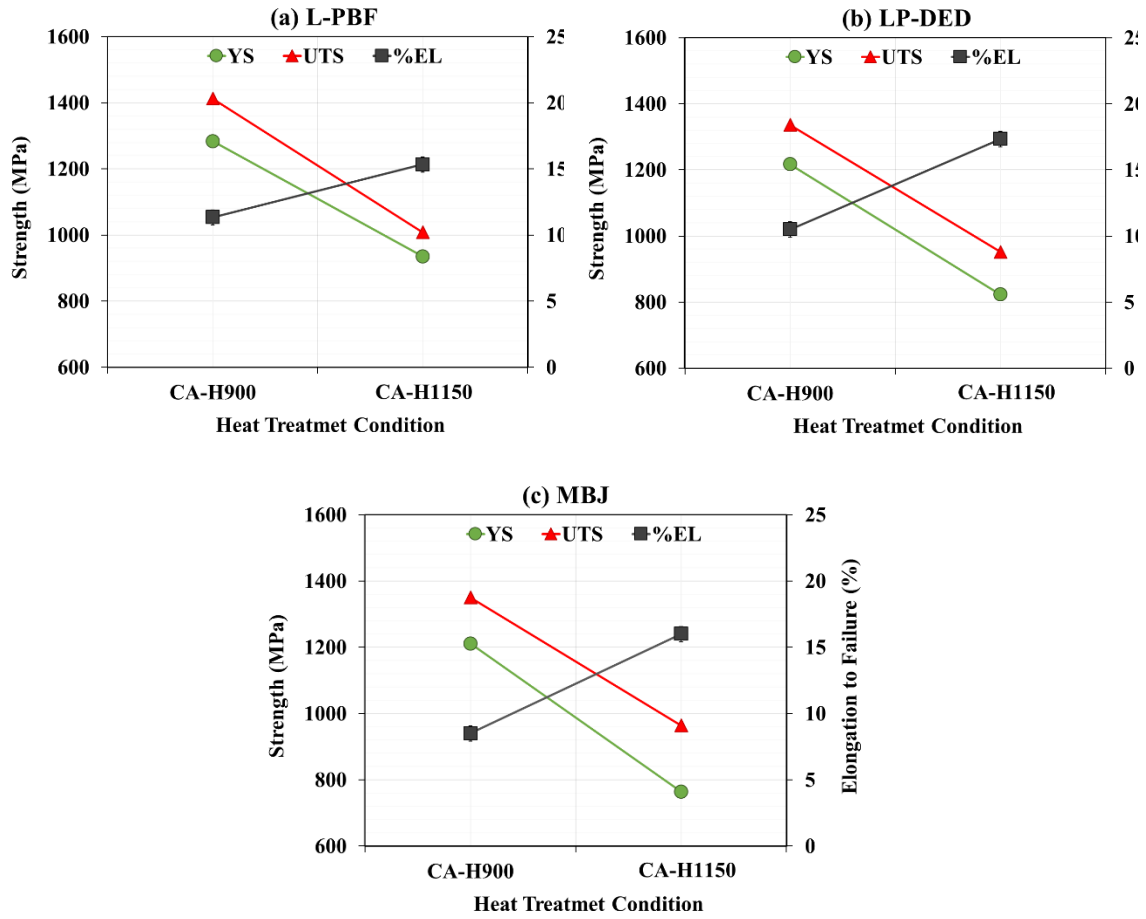


Figure 8-7. Tensile behavior of the heat treated: (a) L-PBF, (b) LP-DED, and (c) MBJ 17-4 PH SS specimens.

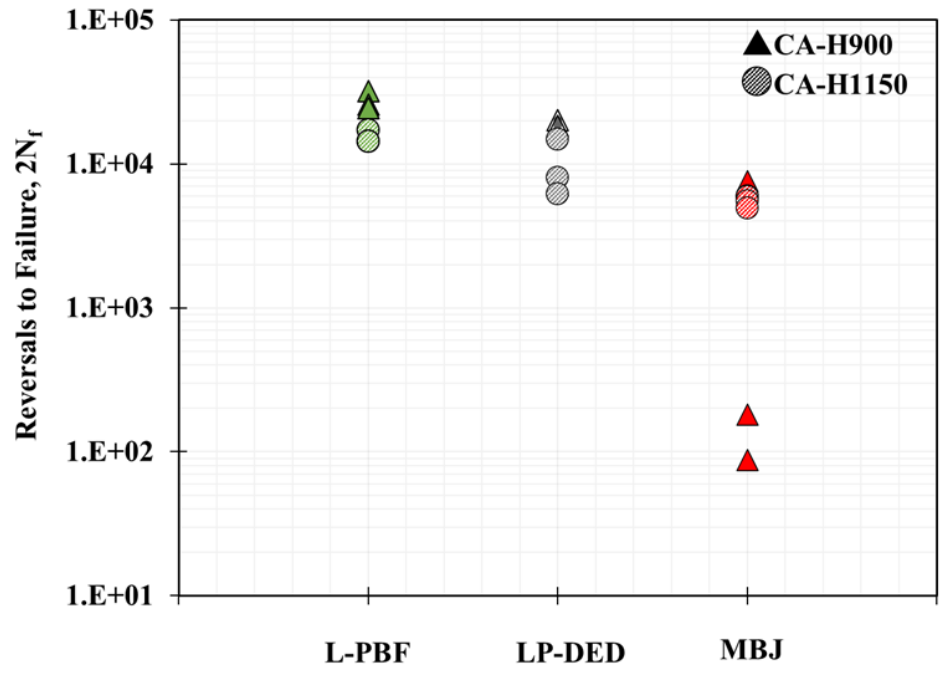


Figure 8-8. Fatigue data comparison for the AM 17-4 PH SS at CA-H900 and CA-H1150 heat treatment conditions: (a) L-PBF, (b) LP-DED, and (c) MBJ 17-4 PH SS specimens.

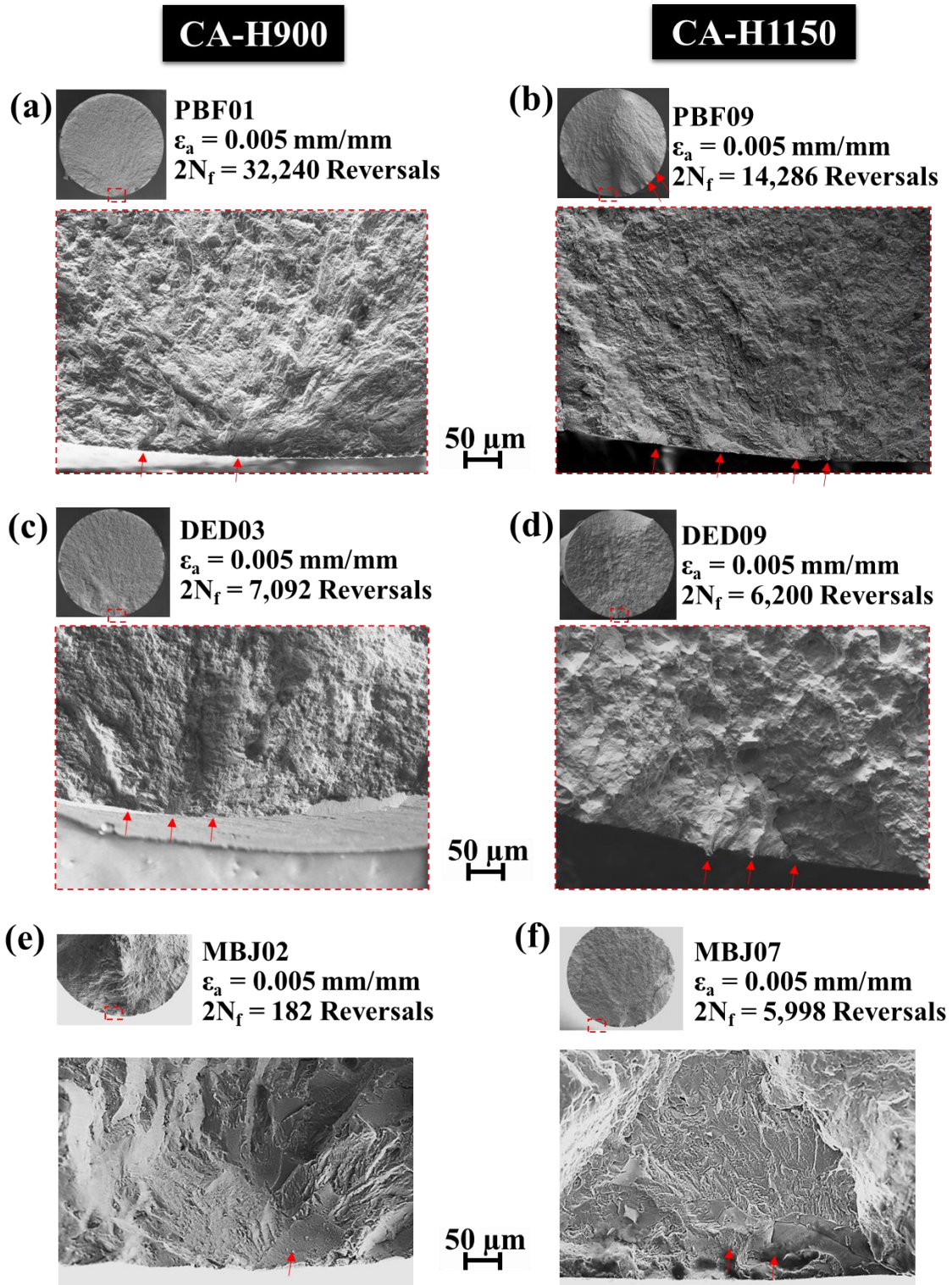


Figure 8-9. Fracture surfaces of the L-PBF, LP-DED, and MBJ 17-4 PH SS specimens in CA-H900 and CA-H1150 heat treatment conditions tested at 0.005 mm/mm strain amplitude: (a)&(b) L-PBF, (c)&(d) LP-DED, and (e)&(f) MBJ.

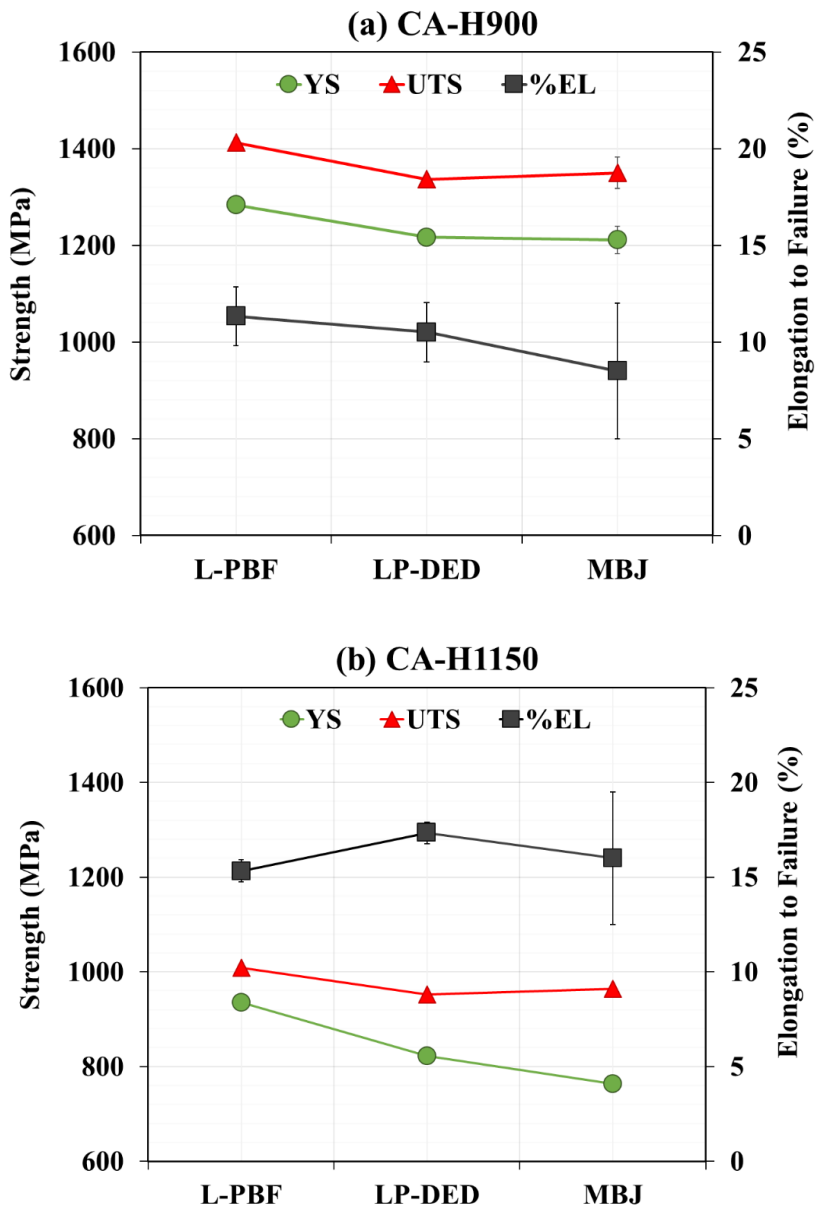


Figure 8-10. Comparison of tensile properties obtained for the L-PBF, LP-DED, and MBJ 17-4 PH SS at (a) CA-H900, and (b) CA-H1150 heat treatment conditions.

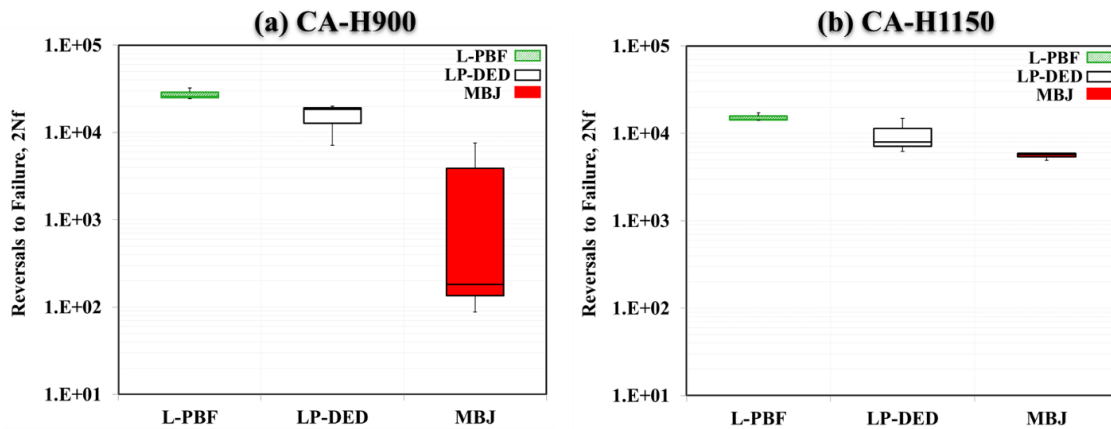


Figure 8-11. Fatigue life comparison of the L-PBF, LP-DED, and MBJ 17-4 PH SS specimens in (a) CA-H900 and (b) CA-H1150 heat treatment conditions tested at 0.005 mm/mm strain amplitude.

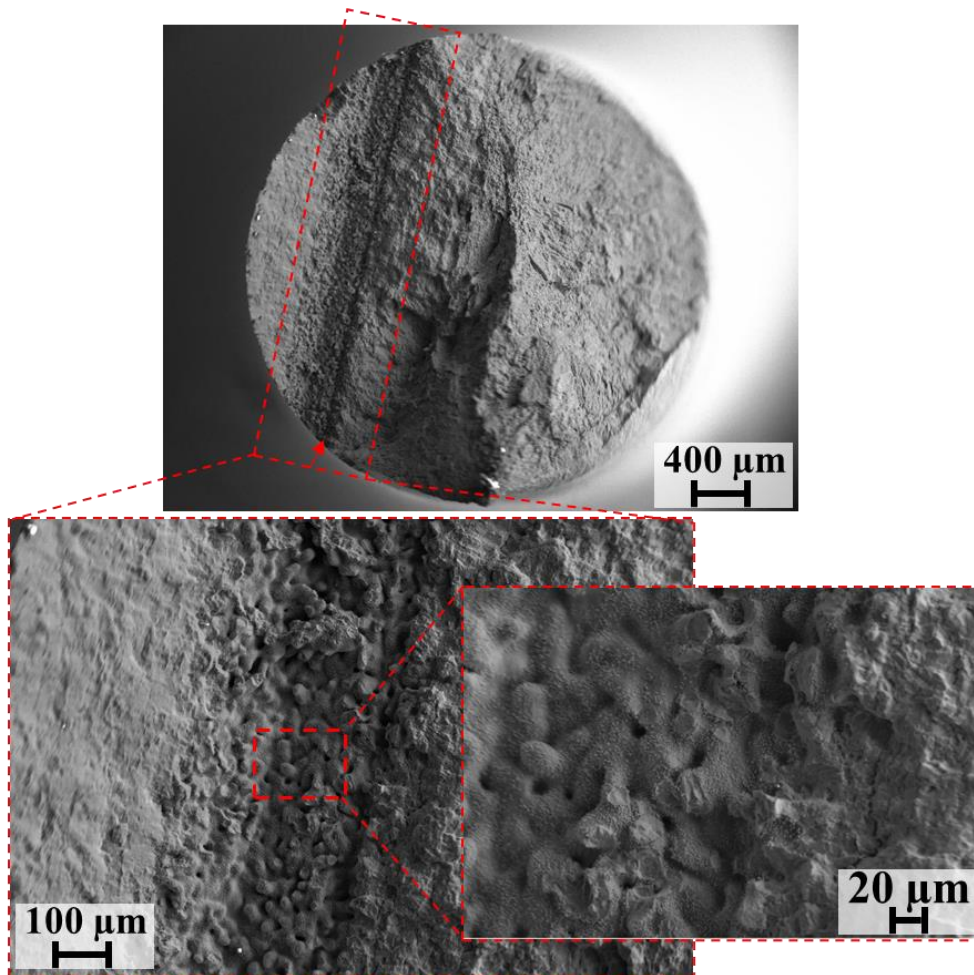


Figure 8-12. An example of the MBJ 17-4 PH SS specimen's fracture surface showing the un-sintered region.

Table 8-1. Chemical composition for 17-4 PH SS powder used for specimen fabrication via L-PBF, LP-DED, and MBJ AM techniques. The values are in wt. %.

| | C | Cr | Ni | Cu | Mn | Si | Nb | Mo | N | O | P | S | Nb+Ta | Fe |
|---------------|------|-------|------|------|------|------|------|------|------|------|-------|-------|-------|------|
| L-PBF | 0.01 | 15.80 | 4.60 | 3.67 | 0.51 | 0.32 | 0.32 | 0.21 | 0.02 | 0.04 | 0.035 | 0.014 | 0.27 | Bal. |
| LP-DED | 0.01 | 16.39 | 4.17 | 3.32 | 0.06 | 0.78 | 0.27 | 0.04 | 0.01 | 0.02 | 0.00 | 0.00 | 0.27 | Bal. |
| MBJ | 0.05 | 16.00 | 4.50 | 4.40 | 0.30 | 0.70 | 0.24 | N/A | N/A | N/A | N/A | N/A | N/A | Bal. |

Table 8-2. Chemical compositions for 17-4 PH SS specimens fabricated via L-PBF, LP-DED, and MBJ AM techniques. The values are in wt. %.

| | C | Cr | Ni | Cu | Mn | Si | Nb | Mo | N | O | P | S | Nb+Ta | Fe |
|---------------|-------|--------|-------|-------|-------|-------|-------|-------|-------|--------|--------|-------|-------|------|
| L-PBF | 0.010 | 15.570 | 4.530 | 3.570 | 0.510 | 0.360 | 0.280 | 0.210 | 0.030 | 0.050 | 0.028 | 0.015 | 0.270 | Bal. |
| LP-DED | 0.010 | 16.120 | 4.110 | 3.210 | 0.060 | 0.750 | 0.320 | 0.030 | 0.010 | 0.020 | 0.0050 | 0.005 | 0.270 | Bal. |
| MBJ | 0.020 | 16.100 | 3.560 | 3.240 | 0.420 | 0.680 | 0.330 | 0.200 | 0.008 | <0.007 | 0.010 | 0.002 | N/A | Bal. |

Table 8-3. Process parameters used for fabrication of L-PBF and LP-DED 17-4 PH SS specimens.

| L-PBF | | LP-DED | | MBJ | |
|----------------------|----------|------------------------------|-------|----------------------------------|-------|
| Laser Power (W) | 220 | Laser Power (W) | 1070 | Laser Power (W) | - |
| Layer Thickness (mm) | 0.04 | Layer Thickness (mm) | 0.38 | Layer Thickness (mm) | 0.042 |
| Scan Speed (mm/min) | 45,330 | Travel Speed (mm/min) | 1,016 | Ink Deposition (mm/min) | 200 |
| Hatch Distance (mm) | 0.01 | Powder Feed Rate (grams/min) | 15.10 | Powder Applicator Speed (mm/min) | 30 |
| Shielding Gas Type | Nitrogen | Shielding Gas Type | Argon | Shielding Gas Type | - |

Table 8-4. Tensile properties of the L-PBF, LP-DED, and MBJ 17-4 PH SS undergone CA-H900 and CA-H1150 heat treatment conditions.

| AM Process | YS (MPa) | | UTS (MPa) | | %El | |
|----------------|-----------------|---------------|--------------------|----------------|--------------|--------------|
| | CA-H900 | CA-H1150 | CA-H900 | CA-H1150 | CA-H900 | CA-H1150 |
| L-PBF | 1283.57 ± 0.35 | 934.93 ± 2.10 | 1412.00 ± 0.31 | 1008.01 ± 0.78 | 11.33 ± 1.53 | 15.33 ± 0.58 |
| LP-DED | 1216.00 ± 0.72 | 823.00 ± 0.40 | 1336.00 ± 0.53 | 951.94 ± 1.10 | 10.50 ± 1.53 | 17.33 ± 0.58 |
| MBJ | 1211.00 ± 28.00 | 764.00 ± 0.25 | 1350.00 ± 32.00 | 964.00 ± 0.25 | 8.50 ± 3.50 | 16.00 ± 3.50 |
| Wrought | 1170 | 725 | 1310 | 930 | 10 | 16 |

Table 8-5. Fully reversed fatigue test results for heat treated AM 17-4 PH SS specimens at CA-H900 condition.

| | ID | ϵ_a (mm/mm) | $\frac{\Delta\epsilon_e}{2}$ (mm/mm) | $\frac{\Delta\epsilon_p}{2}$ (mm/mm) | σ_a (MPa) | σ_m (MPa) | $2N_f$ (Reversals) |
|--------|-----------|-------------------------|---|---|---------------------|---------------------|-----------------------|
| | PB01 | 0.0050 | 0.0050 | 0.0000 | 993 | 2 | 32,240 |
| L-PBF | PB02 | 0.0050 | 0.0050 | 0.0000 | 975 | -5 | 25,898 |
| | PB03 | 0.0050 | 0.0050 | 0.0000 | 978 | -38 | 24,410 |
| | DED01 | 0.0050 | 0.0049 | 0.0001 | 1022 | -77 | 20,102 |
| LP-DED | DED02 | 0.0050 | 0.0049 | 0.0001 | 950 | 49 | 18,360 |
| | DED03 | 0.0050 | 0.0049 | 0.0001 | 1039 | -91 | 7,092 |
| | MBJ01 | 0.0050 | 0.0049 | 0.0001 | 965 | 15 | 7,596 |
| MBJ | MBJ02 | 0.0050 | 0.0050 | 0.0000 | 989 | -1 | 182 |
| | MBJ03 | 0.0050 | 0.0050 | 0.0000 | 983 | -12 | 88 |

Table 8-6. Fully-reversed fatigue test results for heat treated AM 17-4 PH SS specimens at CA-H1150 condition.

| | ID | ϵ_a (mm/mm) | $\frac{\Delta\epsilon_e}{2}$ (mm/mm) | $\frac{\Delta\epsilon_p}{2}$ (mm/mm) | σ_a (MPa) | σ_m (MPa) | $2N_f$ (Reversals) |
|--------|-----------|-------------------------|---|---|---------------------|---------------------|-----------------------|
| | PBF07 | 0.0050 | 0.0046 | 0.0004 | 872 | -44 | 17,122 |
| L-PBF | PBF08 | 0.0050 | 0.0045 | 0.0005 | 874 | -32 | 14,388 |
| | PBF09 | 0.0050 | 0.0045 | 0.0005 | 883 | -31 | 14,286 |
| | DED07 | 0.0050 | 0.005 | 0.0042 | 813 | -25 | 14,800 |
| LP-DED | DED08 | 0.0050 | 0.005 | 0.0042 | 820 | -29 | 8,000 |
| | DED09 | 0.0050 | 0.005 | 0.0042 | 824 | -23 | 6,200 |
| | MBJ07 | 0.0050 | 0.0040 | 0.0010 | 799 | -14 | 5,998 |
| MBJ | MBJ08 | 0.0050 | 0.0039 | 0.0011 | 782 | -15 | 5,904 |
| | MBJ09 | 0.0050 | 0.0040 | 0.0010 | 795 | -11 | 5,528 |
| | MBJ10 | 0.0050 | 0.0040 | 0.0010 | 785 | -11 | 4,922 |

CHAPTER 9: SUMMARY AND POTENTIAL FUTURE WORK

9.1. Summary and General Discussion

The objectives and hypotheses defined in the introduction chapter are responded to by the findings of this study in this chapter. The overall objective of this study is to establish the process-structure-property relationships of the AM 17-4 PH SS, focusing on the effect of the process (i.e., AM process, process parameters) and post-thermal processes (heat treatment, hot isostatic pressing (HIP)) on the micro-/defect-structure and mechanical properties of this material. The main conclusions are drawn based on the experimental results and discussion presented for every one of the hypotheses in the following sections. Finally, the potential ideas for future works are listed and briefly justified.

***Objective 1:** Effect of heat treatment on the microstructure, tensile, and fatigue behavior of the L-PBF 17-4 PH SS in as-built and machined surface conditions.*

This objective aimed to investigate the effects of various standard heat treatments known for the wrought 17-4 PH SS on the microstructure and mechanical properties (i.e., tensile and fatigue) of the AM counterpart. The grain structure and phase constituent of the L-PBF 17-4 PH SS in non-heat treated (NHT) condition was characterized and compared with those of the heat treatment conditions. Tensile behavior of the L-PBF 17-4 PH SS heat treated in various conditions was obtained and correlated to the microstructure differences. Effects of different heat treatment conditions on the fatigue performance of the material in as-built and machined surface conditions were studied; the effect of defects (i.e., surface roughness, porosity) and microstructure on crack initiation and propagation were discovered. Finally, the best heat treatment procedure was proposed based on the microstructure homogeneity, tensile, and fatigue results for the L-PBF 17-4 PH SS.

Hypothesis 1a: the most common heat treatment procedure for the wrought 17-4 PH SS may not be appropriate for the AM counterparts to obtain the required property and performance. This is mainly due to the presence of process-induced defects, which makes the material vulnerable to failure upon conducting inappropriate heat treatment procedures.

Conclusion 1a:

In CHAPTER 2, various standard heat treatment conditions for the wrought 17-4 PH SS were applied to the L-PBF counterpart to evaluate their impact on both the microstructure and the mechanical properties of the L-PBF 17-4 PH SS specimens. The strength of the material was found to be enhanced regardless of the heat treatment procedure. This was due to the precipitation hardening behavior of the material. However, it was shown that conducting CA prior to aging increases the strength of the material more than heat treatment conditions without the CA step. This was attributed to the microstructure homogenization and phase transformation from ferrite to austenite, and to martensite by performing the CA step, which improved the precipitation hardenability of the material.

As expected, the CA-H900 heat treatment condition, the well-known heat treatment procedure for the 17-4 PH SS, caused scatter in fatigue results in the high cycle fatigue regime. This was ascribed to the material's high strength, which made it more sensitive to process-induced defects, i.e., surface roughness and pores, in specimens with as-built surface and machined surface conditions, respectively. Based on the microstructure, tensile and fatigue results, the CA-H1025 heat treatment procedure was proposed as the most proper standard heat treatment for the L-PBF 17-4 PH SS. This heat treatment condition resulted in homogenized microstructure, high strength (less than CA-H900 and more than

other heat treatment conditions), acceptable ductility (more than CA-H900 condition), and lack of scattering in fatigue results.

Hypothesis 1b: knowing that the surface roughness initiates the fatigue cracks, the microstructure obtained by different heat treatment procedures may be influential in retarding the crack initiation and enhancing the fatigue performance.

Conclusion 1b:

It was shown in CHAPTER 2 that fatigue cracks initiated from the surface notches in specimens with as-built surface conditions as well as from pores in machined surface conditions regardless of the heat treatment condition. However, heat treatment could affect the fatigue lives due to the change in the material's microstructure and toughness, influencing the material's crack initiation and propagation resistance. The influence of performing CA prior to aging was shown by comparing the fatigue and fracture behavior of the CA-H1025 heat treatment condition with the H1025 one. Although a similar fracture area was observed for both heat treatment conditions in the HCF regime, multiple crack initiations were seen in the CA-H1025 heat treated specimen with as-built surface condition compared to the H1025 one. The multiple crack initiation sites in the CA-H1025 heat-treated specimen were attributed to its lower fatigue crack growth rate, which allowed the multiple cracks to initiate during cycling loading. The lower crack growth rate in the CA-H1025 condition was due to the coarse precipitates and finer microstructure compared to the H1025 condition.

Objective 2: *Effect of heat treatment and build orientation on the fatigue crack growth (FCG) behavior of the L-PBF 17-4 PH SS*

The second objective aimed to investigate the effect of direct aging versus solutionizing followed by aging on the microstructure and FCG behavior of the L-PBF 17-4 PH SS. In addition, the effect of notch orientation with respect to the build direction on the crack growth behavior was evaluated and correlated to the microstructure obtained by each heat treatment condition.

Hypothesis 2a: there may be a build orientation dependency in FCG behavior of the L-PBF 17-4 PH SS due to the columnar grain structure.

Conclusion 2a:

Effect of heat treatment on the microstructure and the FCG behavior of L-PBF 17-4 PH SS with different notch orientations (see **Figure 3-1**) were studied in CHAPTER 3. It was shown that direct aging at H1025 (i.e., 552 °C for 4 hours followed by air cooling) did not change the coarse columnar grain morphology and eliminate the melt pool boundaries (see **Figure 3-4(a)**). In addition, a network of δ -ferrite grains was observed on the columnar grain boundaries. For the specimens with the notch parallel to the build direction—in other words, the notch parallel to the columnar grains—cracks were formed on the notch after heat treatment (**Figure 3-5(a)**). This was attributed to the segregation of elements to the grain boundaries and the presence of δ -ferrite on grain boundaries, which weakened the grain boundaries' strength. Therefore, premature crack formation occurred with the notch parallel to the columnar grain boundaries.

On the other hand, for the specimens with the notch perpendicular to the build direction (i.e., perpendicular to the columnar grains), the crack propagated in mode I and deviated to mode II (i.e., parallel to the build direction) as it continued to grow. This behavior indicates the crack's tendency to propagate along the columnar grain boundaries. The EBSD results showed that the crack grew along the least resistance path provided by δ -ferrite/martensite interfaces in grain boundaries.

Hypothesis 2b: direct aging heat treatment may not reduce the fatigue anisotropy, while solution annealing heat treatment may diminish the anisotropy in FCG behavior.

Conclusion 2b:

It was observed that conducting CA-H900 not only refined the microstructure and eliminated the melt pool boundaries but also broke the network chain of δ -ferrite on the grain boundaries and re-distributed them in the microstructure. The FCG test results showed a notch orientation independence for the CA-H900 heat treated specimens; the vertical specimens (i.e., notch parallel to the build direction) exhibit similar FCG behavior to the perpendicular counterparts (i.e., notch perpendicular to the build direction). This was ascribed to the fine lath martensite microstructure (**Figure 3-4(b)**) as opposed to the columnar grains in H1025 heat treated specimens, as well as the absence of the detrimental δ -ferrite network on the grain boundaries. It was shown that L-PBF and wrought 17-4 PH SS specimens have a similar FCG behavior in the Paris regime regardless of the notch orientation.

Objective 3: *To investigate the effect of process manipulation on the micro-/defect-structure and mechanical properties of the L-PBF 17-4 PH SS.*

The third objective aimed to study the effects of shielding gas type on the micro-/defect-structure of the L-PBF 17-4 PH SS. To this end, all the recommended process parameters were kept constant, and only the shielding gas was changed from Ar to N₂. The melt pool size, geometry, grain structure, defects size, and population were characterized and compared for the N₂-shielded and Ar-shielded specimens. The microstructure after heat treatment was also compared and correlated to the initial state of microstructure in each case. The mechanical properties, i.e., tensile, fatigue, and FCG behavior of the heat treated N₂-shielded and Ar-shielded specimens, were evaluated and associated with the differences in their micro-/defect-structure. Finally, the shielding gas type, geometry, and heat treatment effect was investigated up to the VHCF regime.

Hypothesis 3a: the thermo-physical properties of the shielding gas type used in the fabrication environment may cause variation in the thermal history the part experiences during fabrication. This may influence the level of defects in the AM part.

Conclusion 3a:

In CHAPTER 4 the effect of process parameter maneuvering by altering the shielding gas type was shown on the micro-/defect-structure of the L-PBF 17-4 PH SS. The N₂ was used instead of the Ar as the shielding gas for fabrication, keeping all the other process parameters constant (laser power, scan speed, gas flow rate, etc.). It was shown that N₂-shielded specimens result in deeper melt pools compared to the Ar-shielded ones (see **Figure 4-4**). This was attributed to the higher conductivity of N₂ (almost 40% higher) than the Ar, leading to more heat absorption by the material from the plume formed on top of the melt pool. In addition, due to the deeper melt pools, more previously fused layers were re-melting by depositing a new layer, which reduced the thermal gradient and,

consequently, cooling/solidification rate. This allowed the gas entrapped pores to escape from the melt pool; therefore, the N₂-shielded specimens had fewer and smaller defect compared to the Ar-shielded counterparts as shown in **Figure 4-5**.

Hypothesis 3b: the solubility of the shielding gas in the material may result in changes in the microstructure, consequently, the material's mechanical properties.

Conclusion 3b:

A columnar grain structure was observed for both the N₂-shielded and Ar-shielded ones **Figure 4-2**; however, N₂-shielded specimens had equiaxed, fine grains in some regions (**Figure 4-2(a)**). These refined equiaxed grains were mostly seen close to the gas entrapped pores around the melt pool. This was attributed to the diffusion of the N to the material according to the considerable solubility of the N in the high-Cr stainless steels. The grain refinement was ascribed to the possible chromium nitride precipitation pinning the grain boundaries and hindering the grain growth. Moreover, heterogeneous grain nucleation may have occurred on precipitates that formed fine grains. In addition, diffusion of the N to the material stabilized the austenite, and a fraction of retained austenite was characterized in the microstructure of N₂-shielded specimens. The N₂-shielded L-PBF 17-4 PH SS was found to have a higher strength and ductility than the Ar-shielded counterparts (see **Figure 4-6** and **Table 4-4**). Higher strength of the N₂-shielded L-PBF 17-4 PH SS was ascribed to its finer grain structure, and higher ductility was attributed to the absence of the δ -ferrite and presence of retained austenite in the microstructure. It was observed that applying CA-H1025 heat treatment (proposed in CHAPTER 2) changed the microstructure of the L-PBF 17-4 PH SS to a martensitic microstructure and eliminated the melt pool boundaries as well as columnar grains. However, the N₂-shielded specimens were found to

have smaller lath martensite (average of ~560 nm) compared to the Ar-shielded ones (average of ~1400 nm). This was due to the finer grain structure of the N₂-shielded specimens prior to heat treatment in NHT condition. The N₂-shielded specimens outperformed the Ar-shielded counterparts moderately in LCF and considerably in the HCF regime. The latter was due to the fewer and smaller pores and the former was ascribed to the higher ductility of the N₂-shielded specimens than the Ar-shielded ones. It was shown in CHAPTER 5 that N₂-shielded specimens also outperform Ar-shielded specimens in the VHCF regime tested via ultrasonic fatigue testing. The effect of geometry (hourglass vs. uniform gage section) on fatigue behavior of the L-PBF 17-4 PH SS was also investigated in CHAPTER 5. Results showed that the L-PBF 17-4 PH SS fatigue behavior is independent of geometry. Using N₂ as shield gas resulted in a moderately lower FCG rate for L-PBF 17-4 PH SS in a wide range of ΔK levels, which was related to the microstructure refinement (thinner lath martensite). In addition, Ar-shielded specimens have lower cyclic fracture toughness due to both the larger size and the higher number of pores in the specimens.

Hypothesis 3c: in the case of using a shielding gas type that reduces the defect density in the material, the most common heat treatment (i.e., CA-H900 condition) may still be applicable.

Conclusion 3c:

Fatigue behavior of the N₂-shielded L-PBF 17-4 PH SS was evaluated in different heat treatment conditions –NHT, CA-H900, and CA-H1025– with different geometries and fatigue testing schemes, conventional and ultrasonic, in CHAPTER 6. It was shown that the NHT specimens exhibit slightly inferior fatigue lives in LCF and significantly

lower fatigue lives in HCF and VHCF compared to the CA-H900 and CA-H1025 specimens. Interestingly, using N₂ shielding gas for fabricating the L-PBF 17-4 PH SS reduced the defect size and population, resulted comparable fatigue behavior for the CA-H900 and CA-H1025 heat treated specimens; however, CA-H900 heat treated L-PBF 17-4 PH SS is more sensitive to defects under cyclic loading than CA-H1025 heat treated counterparts. This is ascribed to the high strength and lack of ductility in CA-H900 heat treated condition. In addition, due to the high sensitivity of the CA-H900 heat treated specimens to the defects, a geometry dependency was observed for the CA-H900 condition.

Objective 4: Effect of AM technique on the structure-property-relationships of AM 17-4 PH SS and the influence of the heat treatment on diminishing the microstructure and mechanical properties variation

In the last objective, the goal was to understand the influence of the AM technique on the microstructure (i.e., grain structure, phase constituent, crystallographic texture) and mechanical properties (i.e., tensile, fatigue) of the AM 17-4 PH SS. In addition, the purpose is to find the best heat treatment scheme to diminish the variations in the microstructure of AM 17-4 PH SS induced by different AM techniques. The specimens were fabricated via L-PBF, LP-DED, and MBJ techniques, and their microstructural variations were characterized for the NHT condition. Two different heat treatments were applied to the specimens after the HIP process. The tensile and fatigue behavior of the L-PBF, LP-DED, and MBJ 17-4 PH SS were evaluated and discussed concerning the microstructural variations. Finally, the best heat treatment process to alleviate the effect of AM technique on varying the mechanical performance of AM 17-4 PH SS was suggested.

Hypothesis 4a: AM techniques with different procedure characteristics may result in different microstructural features due to variation in thermal histories.

Conclusion 4a:

In CHAPTER 7 and CHAPTER 8, variations in the microstructure of AM 17-4 PH SS fabricated via different AM techniques, L-PBF, LP-DED, and MBJ, were investigated. It was observed that for a single material system, i.e., 17-4 PH SS, significant microstructure variation (i.e., grain size, morphology, and phase constituent) existed governed by the AM technique. This was attributed to the nature of AM techniques' procedure. The L-PBF and LP-DED, laser-based AM techniques, caused a very high cooling/solidification rate during fabrication, whereas the MBJ, a non-laser-based AM technique, induced a much lower cooling rate. Interestingly, the L-PBF technique also had a higher cooling rate (almost three times) than the LP-DED technique. Accordingly, it was observed that L-PBF 17-4 PH SS had fine columnar and equiaxed ferrite grains along with martensite and a fraction of retained austenite. The LP-DED 17-4 PH SS had very coarse columnar massive ferrite grains, and the Widmanstätten ferrite decorated the grain boundaries. The MBJ microstructure consisted of lath martensite and string-like δ -ferrite.

Hypothesis 4b: applying proper heat treatments may diminish the microstructure differences and reduce the mechanical properties variation for the L-PBF, LP-DED, and MBJ 17-4 PH SS.

Conclusion 4b:

It was observed that applying a full heat treatment, i.e., HIP + Sol. + Age, is required to unify the microstructure of the AM 17-4 PH SS fabricated via different techniques.

Although heat treatment diminishes the differences in the microstructure of L-PBF, LP-DED, and MBJ 17-4 PH SS, there were still differences in the microstructure that existed. This was ascribed to the dominant role of the initial microstructure. In CHAPTER 7, it was shown that HIP+CA-H1150 heat treatment resulted in an almost comparable crystallographic texture for the L-PBF and LP-DED 17-4 PH SS as compared to HIP+CA-H900 heat treatment condition. In CHAPTER 8, the HIP+CA-H900 heat treatment resulted in more variations in the mechanical properties (i.e., tensile and fatigue) of the L-PBF, LP-DED, and MBJ 17-4 PH SS. This was because this heat treatment could not alleviate the microstructural differences sufficiently. However, the HIP+CA-H1150 heat treatment condition resulted in less variation in the tensile and fatigue results, which attributed to a more resembled microstructure for the L-PBF, LP-DED, and MBJ 17-4 PH SS. In general, the L-PBF 17-4 PH SS outperformed the LP-DED and MBJ counterparts in mechanical properties (i.e., tensile and fatigue), which was attributed to the finer microstructure as well as the absence of detrimental δ -ferrite grains.

9.2. Potential Future Studies

The results obtained from the current study indicated the importance of investigating the process-structure-property relationships for a single material system (i.e., 17-4 PH SS herein) fabricated via different AM techniques. As observed and discussed, post-process treatment (e.g., surface and heat treatment) is essential in improving AM 17-4 PH SS's mechanical properties. This study has thoroughly investigated the effect of standard heat treatments suggested for the wrought 17-4 PH SS on the microstructure, tensile, and fatigue properties of the AM counterpart. It is shown that the most common heat treatment for the wrought 17-4 PH SS is not necessarily appropriate for the AM counterpart, also depending

on the AM technique. However, this study suggested a heat treatment for the AM 17-4 PH SS regardless of the AM technique to obtain similar mechanical properties to some extent. Nonetheless, comparison studies must be conducted on the effect of these standard heat treatments on different physical, tribological, and corrosion properties of the AM 17-4 PH SS. Some potential proposed studies can be defined for master's or Ph.D. level dissertations for future prospective students following the concept of the present dissertation:

- A) Understanding the synergistic effect of heat treatment, build orientation, and AM technique on the corrosion/ corrosion-fatigue performance of AM 17-4 PH SS.
- B) Investigating the effect of heat treatment on the fretting fatigue performance of AM 17-4 PH SS.
- C) Optimizing the process parameters for the MBJ 17-4 PH SS to enhance the mechanical properties comparable to the L-PBF counterparts.
- D) Effect of heat treatment on AM 17-4 PH SS thermos-physical properties.

The present author has conducted preliminary research regarding one of the above-mentioned potential topics. The wear behavior of the L-PBF 17-4 PH SS has been investigated for the most common heat treatment recommended for wrought material (i.e., CA-H900) in [172]. This study can be an excellent initiative for potential future study (B) above.

CHAPTER 10: REFERENCES

- [1] N. Shamsaei, A. Yadollahi, L. Bian, S.M. Thompson, An overview of Direct Laser Deposition for additive manufacturing; Part II: Mechanical behavior, process parameter optimization and control, *Addit. Manuf.* 8 (2015) 12–35.
- [2] A. Mostafaei, A.M. Elliott, J.E. Barnes, F. Li, W. Tan, C.L. Cramer, P. Nandwana, M. Chmielus, Binder jet 3D printing – Process parameters, materials, properties, and challenges, *Prog. Mater. Sci.* (2020) 100707.
- [3] B. Verquin, S. Hoguein, C. Reynaud, C. Quentin, *Metal additive manufacturing - The essentials*, 2019.
- [4] S.R. Daniewicz, N. Shamsaei, An introduction to the fatigue and fracture behavior of additive manufactured parts, *Int. J. Fatigue.* 94 (2017) 167.
- [5] A. Yadollahi, N. Shamsaei, S.M. Thompson, A. Elwany, L. Bian, Effects of building orientation and heat treatment on fatigue behavior of selective laser melted 17-4 PH stainless steel, *Int. J. Fatigue.* 94 (2017) 218–235.
- [6] T. DebRoy, H.L. Wei, J.S. Zuback, T. Mukherjee, J.W. Elmer, J.O. Milewski, A.M. Beese, A. Wilson-Heid, A. De, W. Zhang, Additive manufacturing of metallic components – Process, structure and properties, *Prog. Mater. Sci.* 92 (2018) 112–224.
- [7] Y. Kok, X.P. Tan, P. Wang, M.L.S. Nai, N.H. Loh, E. Liu, S.B. Tor, Anisotropy and heterogeneity of microstructure and mechanical properties in metal additive manufacturing: A critical review, *Mater. Des.* 139 (2018) 565–586.

- [8] Y.J. Liu, Z. Liu, Y. Jiang, G.W. Wang, Y. Yang, L.C. Zhang, Gradient in microstructure and mechanical property of selective laser melted AlSi10Mg, *J. Alloys Compd.* 735 (2018) 1414–1421.
- [9] R.I. Stephens, A. Fatemi, R.R. Stephens, H.O. Fuchs, *Metal fatigue in engineering*, John Wiley & Sons, 2000.
- [10] A.J. Sterling, B. Torries, N. Shamsaei, S.M. Thompson, D.W. Seely, Fatigue behavior and failure mechanisms of direct laser deposited Ti–6Al–4V, *Mater. Sci. Eng. A.* 655 (2016) 100–112.
- [11] A. Fatemi, R. Molaei, J. Simsiriwong, N. Sanaei, J. Pegues, B. Torries, N. Phan, N. Shamsaei, Fatigue behaviour of additive manufactured materials: An overview of some recent experimental studies on Ti-6Al-4V considering various processing and loading direction effects, *Fatigue Fract. Eng. Mater. Struct.* 42 (2019) 991–1009.
- [12] A. Yadollahi, N. Shamsaei, Additive manufacturing of fatigue resistant materials: Challenges and opportunities, *Int. J. Fatigue.* 98 (2017) 14–31.
- [13] R. Shrestha, N. Shamsaei, M. Seifi, N. Phan, An investigation into specimen property to part performance relationships for laser beam powder bed fusion additive manufacturing, *Addit. Manuf.* 29 (2019).
- [14] NASA, MSFC-SPEC-3717 - Specification for Control and Qualification of Laser Powder Bed Fusion Metallurgical Processes, (2017) 58.
- [15] P.D. Nezhadfar, R. Shrestha, N. Phan, N. Shamsaei, Fatigue behavior of additively manufactured 17-4 PH stainless steel: Synergistic effects of surface roughness and

- heat treatment, *Int. J. Fatigue*. 124 (2019) 188.
- [16] L. Facchini, N. Vicente, I. Lonardelli, E. Magalini, P. Robotti, A. Molinari, Metastable Austenite in 17-4 precipitation-hardening stainless steel produced by selective laser melting, *Adv. Eng. Mater.* 12 (2010) 184–188.
- [17] G. V. Kurdjumov, A.G. Khachaturyan, Phenomena of carbon atom redistribution in martensite, *Metall. Trans.* 3 (1972) 1069–1076.
- [18] M. Alnajjar, F. Christien, K. Wolski, C. Bosch, Evidence of austenite by-passing in a stainless steel obtained from laser melting additive manufacturing, *Addit. Manuf.* 25 (2019) 187–195.
- [19] S. Cheruvathur, E.A. Lass, C.E. Campbell, Additive manufacturing of 17-4 PH stainless steel: Post-processing heat treatment to achieve uniform reproducible microstructure, *JOM*. 68 (2015) 930–942.
- [20] P.D. Nezhadfar, E. Burford, K. Anderson-Wedge, B. Zhang, S. Shao, S.R. Daniewicz, N. Shamsaei, Fatigue crack growth behavior of additively manufactured 17-4 PH stainless steel: Effects of build orientation and microstructure, *Int. J. Fatigue*. 123 (2019) 168–179.
- [21] A. Poudel, A. Soltani-Tehrani, S. Shao, N. Shamsaei, Effect of powder characteristics on tensile properties of additively manufactured 17-4 PH stainless steel, 2021 *Int. Solid Free. Fabr. Symp.* (2021). <https://repositories.lib.utexas.edu/handle/2152/90691> (accessed July 11, 2022).
- [22] S. Vunnam, A. Saboo, C. Sudbrack, T.L. Starr, Effect of powder chemical

composition on the as-built microstructure of 17-4 PH stainless steel processed by selective laser melting, *Addit. Manuf.* (2019) 100876.

- [23] P.D. Nezhadfar, A. Soltani-Tehrani, A. Sterling, N. Tsolas, N. Shamsaei, The effects of powder recycling on the mechanical properties of additively manufactured 17-4 PH stainless steel, in: *Proc. 29th Annu. Int. Solid Free. Fabr. Symp. – An Addit. Manuf. Conf.*, 2018: pp. 1292–1300.
- [24] A. Soltani-Tehrani, J. Pegues, N. Shamsaei, Fatigue behavior of additively manufactured 17-4 PH stainless steel: the effects of part location and powder re-use, *Addit. Manuf.* 33 (2020).
- [25] S. Pasebani, M. Ghayoor, S. Badwe, H. Irrinki, S. V Atre, Effects of atomizing media and post processing on mechanical properties of 17-4 PH stainless steel manufactured via selective laser melting, *Addit. Manuf.* 22 (2018) 127–137.
- [26] L.E. Murr, E. Martinez, J. Hernandez, S. Collins, K.N. Amato, S.M. Gaytan, P.W. Shindo, Microstructures and properties of 17-4 PH stainless steel fabricated by Selective Laser melting, *J. Mater. Res. Technol.* 1 (2012) 167–177.
- [27] H. Gu, H. Gong, D. Pal, K. Rafi, T. Starr, B. Stucker, Influences of energy density on porosity and microstructure of selective laser melted 17-4PH stainless steel, in: *Solid Free. Fabr. 2013 Proc. 23rd Annu. Int. Solid Free. Fabr. Symp. – An Addit. Manuf. Conf. Austing, TX, 2013*, 2013.
- [28] D. Palanisamy, P. Senthil, Optimization on Turning Parameters of 15-5PH Stainless Steel Using Taguchi Based Grey Approach and Topsis, *Arch. Mech. Eng.* 63 (2016) 397–412. <https://www.infona.pl/resource/bwmeta1.element.baztech-2ee89703->

1b06-47b3-9a82-79b07486e853 (accessed August 17, 2020).

- [29] R. Shrestha, P.D. Nezhadfar, M. Masoomi, J. Simsiriwong, N. Pham, N. Shamsaei, Effects of Design Parameters on Thermal History and Mechanical Behavior of Additively Manufactured 17-4 PH Stainless Steel, in: Proc. 29th Annu. Int. Solid Free. Fabr. Symp. – An Addit. Manuf. Conf., 2018.
- [30] K. Li, J. Zhan, T. Yang, A.C. To, S. Tan, Q. Tang, H. Cao, L.E. Murr, Homogenization timing effect on microstructure and precipitation strengthening of 17-4PH stainless steel fabricated by laser powder bed fusion, *Addit. Manuf.* 52 (2022) 102672.
- [31] Q. Shi, F. Qin, K. Li, X. Liu, G. Zhou, Effect of hot isostatic pressing on the microstructure and mechanical properties of 17-4PH stainless steel parts fabricated by selective laser melting, *Mater. Sci. Eng. A.* 810 (2021) 141035.
- [32] S. Sarkar, C.S. Kumar, A.K. Nath, Effect of different heat treatments on mechanical properties of laser sintered additive manufactured parts, *J. Manuf. Sci. Eng. Trans. ASME.* 139 (2017).
- [33] D. Herzog, V. Seyda, E. Wycisk, C. Emmelmann, Additive manufacturing of metals, *Acta Mater.* 117 (2016) 371–392.
- [34] W.E. Frazier, Metal Additive Manufacturing: A Review, *J. Mater. Eng. Perform.* 23 (2014) 1917–1928.
- [35] K. V Wong, A. Hernandez, A Review of Additive Manufacturing, *ISRN Mech. Eng.* 2012 (2012) 1–10.

- [36] T.D. Ngo, A. Kashani, G. Imbalzano, K.T.Q. Nguyen, D. Hui, Additive manufacturing (3D printing): A review of materials, methods, applications and challenges, *Compos. Part B Eng.* 143 (2018) 172–196.
- [37] D. Greitemeier, C. Dalle Donne, F. Syassen, J. Eufinger, T. Melz, Effect of surface roughness on fatigue performance of additive manufactured Ti–6Al–4V, *Mater. Sci. Technol.* 32 (2016) 629–634.
- [38] B. Torries, A. Imandoust, S. Beretta, S. Shao, N. Shamsaei, Overview on Microstructure- and Defect-Sensitive Fatigue Modeling of Additively Manufactured Materials, *Jom.* 70 (2018) 1853–1862.
- [39] A. Yadollahi, N. Shamsaei, S.M. Thompson, A. Elwany, L. Bian, Effects of building orientation and heat treatment on fatigue behavior of selective laser melted 17-4 PH stainless steel, *Int. J. Fatigue.* 94 (2017) 218–235.
- [40] J.J. Lewandowski, M. Seifi, Metal Additive Manufacturing: A Review of Mechanical Properties, *Annu. Rev. Mater. Res.* 46 (2016) 151–186.
- [41] L. Bian, S.M. Thompson, N. Shamsaei, Mechanical properties and microstructural features of direct laser-deposited Ti-6Al-4V, *Jom.* 67 (2015) 629–638.
- [42] T.M. Mower, M.J. Long, Mechanical behavior of additive manufactured, powder-bed laser-fused materials, *Mater. Sci. Eng. A.* 651 (2016) 198–213.
- [43] A.S. Johnson, S. Shao, N. Shamsaei, S.M. Thompson, L. Bian, Microstructure, Fatigue Behavior, and Failure Mechanisms of Direct Laser-Deposited Inconel 718, *Jom.* 69 (2016) 597–603. <http://link.springer.com/10.1007/s11837-016-2225-2>

(accessed May 31, 2019).

- [44] S. Sarkar, C. Siva Kumar, A. Kumar Nath, Effect of mean stresses on mode of failures and fatigue life of selective laser melted stainless steel, *Mater. Sci. Eng. A.* 700 (2017) 92–106.
- [45] A.B. Spierings, T.L. Starr, K. Wegener, Fatigue performance of additive manufactured metallic parts, *Rapid Prototyp. J.* 19 (2013) 88–94.
- [46] H.K. Rafi, T.L. Starr, B.E. Stucker, A comparison of the tensile, fatigue, and fracture behavior of Ti-6Al-4V and 15-5 PH stainless steel parts made by selective laser melting, *Int. J. Adv. Manuf. Technol.* 69 (2013) 1299–1309. <https://link.springer.com/article/10.1007/s00170-013-5106-7> (accessed August 17, 2020).
- [47] F. Cabanettes, A. Joubert, G. Chardon, V. Dumas, J. Rech, C. Grosjean, Z. Dimkovski, Topography of as built surfaces generated in metal additive manufacturing: A multi scale analysis from form to roughness, *Precis. Eng.* 52 (2018) 249–265.
- [48] J. Pegues, M. Roach, R.S. Williamson, N. Shamsaei, Surface roughness effects on the fatigue strength of additively manufactured Ti-6Al-4V, *Int. J. Fatigue.* 116 (2018) 543–552.
- [49] G. Jacob, C. Brown, A. Donmez, S. Watson, J. Slotwinski, Effects of powder recycling on stainless steel powder and built material properties in metal powder bed fusion processes, *Adv. Manuf. Ser. (NIST AMS)-100-6.* (2017).

- [50] M. Averyanova, P. Bertrand, B. Verquin, Studying the influence of initial powder characteristics on the properties of final parts manufactured by the selective laser melting technology, *Virtual Phys. Prototyp.* 6 (2011) 215–223.
- [51] P.E. Carrion, A. Soltani-Tehrani, N. Phan, N. Shamsaei, Powder Recycling Effects on the Tensile and Fatigue Behavior of Additively Manufactured Ti-6Al-4V Parts, *Jom.* (2018).
- [52] A. Yadollahi, N. Shamsaei, S.M. Thompson, D.W. Seely, Effects of process time interval and heat treatment on the mechanical and microstructural properties of direct laser deposited 316L stainless steel, *Mater. Sci. Eng. A.* 644 (2015) 171–183.
- [53] B. Torries, N. Shamsaei, Fatigue Behavior and Modeling of Additively Manufactured Ti-6Al-4V Including Interlayer Time Interval Effects, *Jom.* 69 (2017) 2698–2705.
- [54] M.R. Stoudt, R.E. Ricker, E.A. Lass, L.E. Levine, Influence of postbuild microstructure on the electrochemical behavior of additively manufactured 17-4 PH stainless steel, *JOM.* 69 (2017) 506–515.
<https://www.ncbi.nlm.nih.gov/pubmed/28757787>.
- [55] B. Van Hooreweder, Y. Apers, K. Lietaert, J.P. Kruth, Improving the fatigue performance of porous metallic biomaterials produced by Selective Laser Melting, *Acta Biomater.* 47 (2017) 193–202.
<https://www.ncbi.nlm.nih.gov/pubmed/27717912>.
- [56] P. Edwards, M. Ramulu, Fatigue performance evaluation of selective laser melted Ti-6Al-4V, *Mater. Sci. Eng. A.* 598 (2014) 327–337.

- [57] S. Leuders, M. Thöne, A. Riemer, T. Niendorf, T. Tröster, H.A. Richard, H.J. Maier, On the mechanical behaviour of titanium alloy TiAl6V4 manufactured by selective laser melting: Fatigue resistance and crack growth performance, *Int. J. Fatigue*. 48 (2013) 300–307.
- [58] K.H. Bin Zhang Shuai Shao, Nima Shamsaei, Scott M. Thompson, Effect of Heat Treatment and Hot Isostatic Pressing on the Morphology and Size of Pores in Additive Manufactured Ti-6Al-4V Parts, *Proc. 28th Annu. Int. Solid Free. Fabr. Symp. – An Addit. Manuf. Conf.* (2018) 7.
- [59] C. Schade, *Processing, Microstructures and Properties of a Dual Phase Precipitation-Hardening PM Stainless Steel*, 2010.
- [60] ASTM A693-16, Standard specification for precipitation-hardening stainless and heat-resisting steel plate, sheet, and strip, 2016.
- [61] A. Bayode, S. Pityana, E.T. Akinlabi, M.B. Shongwe, Effect of scanning speed on laser deposited 17-4PH stainless steel, in: *Mech. Intell. Manuf. Technol. (ICMIMT), Int. Conf., IEEE*, 2017: pp. 1–5.
- [62] Y. Sun, R.J. Hebert, M. Aindow, Effect of heat treatments on microstructural evolution of additively manufactured and wrought 17-4PH stainless steel, *Mater. Des.* 156 (2018) 429–440.
- [63] P.D. Nezhadfar, M. Masoomi, S.M. Thompson, N. Phan, N. Shamsaei, Mechanical properties of 17-4 PH stainless steel additively manufactured under Ar and N₂ shielding gas, in: *Proc. 29th Annu. Int. Solid Free. Fabr. Symp. – An Addit. Manuf. Conf., Austing, TX*, 2018: pp. 1301–1310.

- [64] T. LeBrun, T. Nakamoto, K. Horikawa, H. Kobayashi, Effect of retained austenite on subsequent thermal processing and resultant mechanical properties of selective laser melted 17–4 PH stainless steel, *Mater. Des.* 81 (2015) 44–53.
- [65] ASTM E606/E606M, Standard Test Method for Strain-Controlled Fatigue Testing, ASTM Stand. (2012).
- [66] ASTM E3-11, Standard guide for preparation of metallographic specimens, (2017).
- [67] W. Liu, J. Ma, M.M. Atabaki, R. Pillai, B. Kumar, U. Vasudevan, H. Sreshta, R. Kovacevic, Hybrid Laser-arc Welding of 17-4 PH Martensitic Stainless Steel, *Lasers Manuf. Mater. Process.* 2 (2015) 74–90.
- [68] H. Mirzadeh, A. Najafizadeh, Aging kinetics of 17-4 PH stainless steel, *Mater. Chem. Phys.* 116 (2009) 119–124.
- [69] ASTM, Standard Practice for X-Ray Determination of Retained Austenite in Steel with Near Random Crystallographic Orientation, ASTM Int. (2013).
- [70] E.O.S. GmbH, EOS StainlessSteel 17-4PH, (n.d.).
- [71] T.L. Starr, K. Rafi, B. Stucker, C.M. Scherzer, Controlling phase composition in selective laser melted stainless steels, *Power (W)*. 195 (2012) 195.
- [72] R. Colaço, R. Vilar, Stabilisation of retained austenite in laser surface melted tool steels, *Mater. Sci. Eng. A.* 385 (2004) 123–127.
- [73] G.E. Dieter, D.J. Bacon, *Mechanical metallurgy*, McGraw-hill New York, 1986.
- [74] P.D. Nezhadfar, A. Zarei-Hanzaki, S.S. Sohn, H.R. Abedi, Characterization of twin-like structure in a ferrite-based lightweight steel, *Met. Mater. Int.* 22 (2016).

- [75] P.D. Nezhadfar, A. Zarei-Hanzaki, S.S. Sohn, H.R. Abedi, The microstructure evolution and room temperature deformation behavior of ferrite-based lightweight steel, *Mater. Sci. Eng. A.* 665 (2016) 10–16.
- [76] A. Weidner, A. Müller, H. Biermann, Portevin Le Chatelier Effect in a Metastable Austenitic CrMnNi Steel, *Mater. Today Proc.* 2 (2015) S623–S626.
- [77] B.A.B. A. H. Cottrell, Dislocation Theory of Yielding and Strain Ageing of Iron, *Proc. Phys. Soc. A* 69 (1948).
- [78] J. Kim, S.-J. Lee, B.C. De Cooman, Effect of Al on the stacking fault energy of Fe–18Mn–0.6C twinning-induced plasticity, *Scr. Mater.* 65 (2011) 363–366.
- [79] H. Halim, D. Wilkinson, M. Niewczas, The Portevin–Le Chatelier (PLC) effect and shear band formation in an AA5754 alloy, *Acta Mater.* 55 (2007) 4151–4160.
- [80] H.J. Rack, D. Kalish, The strength, fracture toughness, and low cycle fatigue behavior of 17-4 PH stainless steel, *Metall. Mater. Trans. B.* 5 (1974) 1595–1605.
- [81] K.-C. Hsu, C.-K. Lin, High-temperature fatigue crack growth behavior of 17-4 PH stainless steels, *Metall. Mater. Trans. A.* 35 (2004) 3018–3024.
- [82] P.D. Nezhadfar, E. Burford, K. Anderson-Wedge, B. Zhang, S. Shao, S.R. Daniewicz, N. Shamsaei, Fatigue crack growth behavior of additively manufactured 17-4 PH stainless steel: Effects of build orientation and microstructure, *Int. J. Fatigue.* 123 (2019) 168–179.
- [83] J.L.J. Richard C. Rice John Bakuckas, and Steven Thompson, *Metallic Materials Properties Development and Standardization (MMPDS)*, (2003).

- [84] C.Y. Yap, C.K. Chua, Z.L. Dong, Z.H. Liu, D.Q. Zhang, L.E. Loh, S.L. Sing, Review of selective laser melting: Materials and applications, *Appl. Phys. Rev.* 2 (2015) 41101.
- [85] M. Seifi, M. Gorelik, J. Waller, N. Hrabe, N. Shamsaei, S. Daniewicz, J.J. Lewandowski, Progress towards metal additive manufacturing standardization to support qualification and certification, *Jom.* 69 (2017) 439–455.
- [86] M. Seifi, A. Salem, D. Satko, J. Shaffer, J.J. Lewandowski, Defect distribution and microstructure heterogeneity effects on fracture resistance and fatigue behavior of EBM Ti–6Al–4V, *Int. J. Fatigue.* 94 (2017) 263–287.
- [87] K. V Yang, P. Rometsch, T. Jarvis, J. Rao, S. Cao, C. Davies, X. Wu, Porosity formation mechanisms and fatigue response in Al-Si-Mg alloys made by selective laser melting, *Mater. Sci. Eng. A.* 712 (2018) 166–174.
- [88] S. Romano, A. Brückner-Foit, A. Brandão, J. Gumpinger, T. Ghidini, S. Beretta, Fatigue properties of AlSi10Mg obtained by additive manufacturing: Defect-based modelling and prediction of fatigue strength, *Eng. Fract. Mech.* 187 (2018) 165–189.
- [89] A. Fatemi, R. Molaei, S. Sharifimehr, N. Shamsaei, N. Phan, Torsional fatigue behavior of wrought and additive manufactured Ti-6Al-4V by powder bed fusion including surface finish effect, *Int. J. Fatigue.* 99 (2017) 187–201.
- [90] A. Yadollahi, N. Shamsaei, S.M. Thompson, A. Elwany, L. Bian, M. Mahmoudi, Fatigue behavior of selective laser melted 17-4 PH stainless steel, in: *Proc. 26th Int. Solid Free. Fabr. Symp. Austin, TX, 2015.*

- [91] R. Shrestha, N. Simsiriwong, N. Shamsaei, N. Thompson, L. Bian, Effect of Build Orientation on the Fatigue Behavior of Stainless Steel 316L via a Laser-Based Power Bed Fusion Process, *Solid Free. Fabr. Proc.* (2016) 605–616.
- [92] A. Riemer, S. Leuders, M. Thöne, H.A. Richard, T. Tröster, T. Niendorf, On the fatigue crack growth behavior in 316L stainless steel manufactured by selective laser melting, *Eng. Fract. Mech.* 120 (2014) 15–25.
- [93] X. Ran, D. Liu, J. Li, H. Wang, X. Cheng, J. Zhang, H. Tang, X. Liu, Effects of microstructures on the fatigue crack growth behavior of laser additive manufactured ultrahigh-strength AerMet100 steel, *Mater. Sci. Eng. A.* 721 (2018) 251–262.
- [94] C.F. Arisoy, G. Başman, M.K. Şeşen, Failure of a 17-4 PH stainless steel sailboat propeller shaft, *Eng. Fail. Anal.* 10 (2003) 711–717.
- [95] J. Srinath, S.K. Manwatkar, S.V.S.N. Murty, P.R. Narayanan, S.C. Sharma, K.M. George, Metallurgical Analysis of a Failed 17-4 PH Stainless Steel Pyro Bolt Used in Launch Vehicle Separation Systems, *Mater. Perform. Charact.* 4 (2015) MPC20140063.
- [96] P.D. Nezhadfar, R. Shrestha, N. Phan, N. Shamsaei, Fatigue behavior of additively manufactured 17-4 PH stainless steel: Synergistic effects of surface roughness and heat treatment, *Int. J. Fatigue.* 124 (2019).
- [97] M. Mahmoudi, A. Elwany, A. Yadollahi, S.M. Thompson, L. Bian, N. Shamsaei, Mechanical properties and microstructural characterization of selective laser melted 17-4 PH stainless steel, *Rapid Prototyp. J.* 23 (2017) 280–294.

- [98] ASTM E647, Standard test method for measurement of fatigue crack growth rates, (2016).
- [99] TCFE9 Thermo-Calc Software, TCFE9: TCS Steel and Fe-alloys Database, (2017) 1–38. www.thermocalc.com.
- [100] A.L. Schaeffler, Selection of austenitic electrodes for welding dissimilar metals, *Weld J.* 26 (1947) 601–620.
- [101] C.N. Hsiao, C.S. Chiou, J.R. Yang, C.S.C. C.N. Hsiao J.R. Yang, Aging reactions in a 17-4 PH stainless steel, *Mater. Chem. Phys.* 74 (2002) 134–142.
- [102] J. Tian, W. Wang, W. Yan, Z. Jiang, Y. Shan, K. Yang, Cracking due to Cu and Ni segregation in a 17-4 PH stainless steel piston rod, *Eng. Fail. Anal.* 65 (2016) 57–64.
- [103] Z. Feng, The lattice parameter of gamma iron and iron-chromium alloys, (2015).
- [104] R.W. Hertzberg, *Deformation and fracture mechanics of engineering materials*, (1989).
- [105] B. Van Hooreweder, D. Moens, R. Boonen, J.-P.J. Kruth, P. Sas, Analysis of Fracture Toughness and Crack Propagation of Ti6Al4V Produced by Selective Laser Melting, *Adv. Eng. Mater.* 14 (2012) 92–97.
- [106] A. Ladewig, G. Schlick, M. Fisser, V. Schulze, U. Glatzel, Influence of the shielding gas flow on the removal of process by-products in the selective laser melting process, *Addit. Manuf.* 10 (2016) 1–9.
- [107] L.E. Murr, E. Martinez, K.N. Amato, S.M. Gaytan, J. Hernandez, D.A. Ramirez,

- P.W. Shindo, F. Medina, R.B. Wicker, Fabrication of metal and alloy components by additive manufacturing: Examples of 3D materials Science, *J. Mater. Res. Technol.* 1 (2012) 42–54.
- [108] M.B. Mathisen, H.L. Larsen, Solidification refinement and general phase transformation control through application of insitu gas jet impingement in metal additive manufacturing, 2019.
- [109] P. Kah, J. Martikainen, Influence of shielding gases in the welding of metals, *Int. J. Adv. Manuf. Technol.* 64 (2013) 1411–1421.
- [110] M. Keskitalo, K. Mäntyjärvi, J. Sundqvist, J. Powell, A.F.H. Kaplan, Laser welding of duplex stainless steel with nitrogen as shielding gas, *J. Mater. Process. Technol.* 216 (2015) 381–384.
- [111] M. Keskitalo, J. Sundqvist, K. Mäntyjärvi, J. Powell, A.F.H. Kaplan, The influence of shielding gas and heat input on the mechanical properties of laser welds in ferritic stainless steel, *Phys. Procedia.* 78 (2015) 222–229.
- [112] N. Seto, S. Katayama, A. Matsunawa, High-speed simultaneous observation of plasma and keyhole behavior during high power CO₂ laser welding: Effect of shielding gas on porosity formation, *J. Laser Appl.* 12 (2000) 245–250.
- [113] J. Sun, P. Nie, K. Feng, Z. Li, B. Guo, E. Jiang, The elimination of pores in laser welds of AISI 304 plate using different shielding gases, *J. Mater. Process. Technol.* 248 (2017) 56–63.
- [114] A.M. Meyer, M.D. Toit, Interstitial diffusion of carbon and nitrogen into heat-

affected zones of 11-12% chromium steel welds, *Weld. JOURNAL-NEW YORK-*.
80 (2001) 275-s.

[115] P. Bajaj, A. Hariharan, A. Kini, P. Kürnsteiner, D. Raabe, E.A. Jäggle, Steels in additive manufacturing: A review of their microstructure and properties, *Mater. Sci. Eng. A.* (2019) 138633.

[116] M. Song, R. Zhou, J. Gu, Z. Wang, S. Ni, Y. Liu, Nitrogen induced heterogeneous structures overcome strength-ductility trade-off in an additively manufactured high-entropy alloy, *Appl. Mater. Today.* 18 (2020) 100498.

[117] S. Katayama, Y. Kawahito, M. Mizutani, Elucidation of laser welding phenomena and factors affecting weld penetration and welding defects, *Phys. Procedia.* 5 (2010) 9–17.

[118] J. Ahn, E. He, L. Chen, J. Dear, C. Davies, The effect of Ar and He shielding gas on fibre laser weld shape and microstructure in AA 2024-T3, *J. Manuf. Process.* 29 (2017) 62–73.

[119] J.W. Elmer, J. Vaja, H.D. Carlton, R. Pong, The effect of Ar and N₂ shielding gas on laser weld porosity in steel, stainless steels, and nickel, *Weld J.* 94 (2015) 313s-325s.

[120] R. Akhter, M. Davis, J. Dowden, P. Kapadia, M. Ley, W.M. Steen, A method for calculating the fused zone profile of laser keyhole welds, *J. Phys. D. Appl. Phys.* 22 (1989) 23–28.

[121] P. Behjati, A. Kermanpur, A. Najafizadeh, H. Samaei Baghbadorani, L.P.

- Karjalainen, J.G. Jung, Y.K. Lee, Effect of nitrogen content on grain refinement and mechanical properties of a reversion-treated Ni-Free 18Cr-12Mn austenitic stainless steel, *Metall. Mater. Trans. A.* 45 (2014) 6317–6328.
- [122] A. Di Schino, M. Barteri, J.M. Kenny, Effects of grain size on the properties of a low nickel austenitic stainless steel, *J. Mater. Sci.* 38 (2003) 4725–4733.
- [123] Y. Kawahito, M. Mizutani, S. Katayama, High quality welding of stainless steel with 10 kW high power fibre laser, *Sci. Technol. Weld. Join.* 14 (2009) 288–294.
- [124] R.O. Ritchie, A.W. Thompson, On macroscopic and microscopic analyses for crack initiation and crack growth toughness in ductile alloys, *Metall. Trans. A.* (1985).
- [125] S. Hertzman, M. Jarl, A Thermodynamic Analysis of the Fe-Cr-N System, n.d.
- [126] P. Sathiya, M.Y.A. Jaleel, Influence of shielding gas mixtures on bead profile and microstructural characteristics of super austenitic stainless steel weldments by laser welding, *Int. J. Adv. Manuf. Technol.* 54 (2011) 525–535.
- [127] A.M. Galloway, N.A. McPherson, T.N. Baker, An evaluation of weld metal nitrogen retention and properties in 316LN austenitic stainless steel, *Proc. Inst. Mech. Eng. Part L J. Mater. Des. Appl.* 225 (2011) 61–69.
- [128] R.K. Okagawa, R.D. Dixon, D.L. Olson, The Influence of Nitrogen from Welding on Stainless Steel Weld Metal Microstructures Soluble nitrogen is found to exert a major influence-particularly on the quantity and distribution of weld metal delta ferrite, *Weld. Res. Suppl.* (1983) 204s-209s.
- [129] S. Tammam-Williams, H. Zhao, F. Léonard, F. Derguti, I. Todd, P.B. Prangnell, XCT

analysis of the influence of melt strategies on defect population in Ti–6Al–4V components manufactured by Selective Electron Beam Melting, *Mater. Charact.* 102 (2015) 47–61.

[130] P.D. Nezhadfar, A. Soltani-Tehrani, N. Shamsaei, Effect of preheating build platform on microstructure and mechanical properties of additively manufactured 316L stainless steel, in: *Proc. 30th Annu. Int. Solid Free. Fabr. Symp. – An Addit. Manuf. Conf.*, 2019.

[131] E. Pereloma, D. Edmonds V, Phase transformations in steels 2: diffusionless transformations, high strength steels, modelling and advanced analytical techniques, Woodhead Publishing, 2012.

[132] M. Moallemi, A. Zarei-Hanzaki, S.-J. Kim, C. Hong, P.D. Nezhadfar, Deformation behavior of a high-plasticity nano/ultrafine-grained N-bearing duplex stainless steel: Twin/twin-like induced plasticity effect, *Mater. Sci. Eng. A.* 700 (2017).

[133] R. Manojkumar, S. Mahadevan, C.K. Mukhopadhyay, B.P.C. Rao, Aging behavior of 17-4 PH stainless steel studied using XRDLPA for separating the influence of precipitation and dislocations on microstrain, *J. Mater. Res.* 32 (2017) 4263–4271.

[134] G.E. Dieter, *Mechanical Metallurgy*, 3rd ed., McGraw-Hill, Boston, MA, MA, 1986.

[135] F. Khodabakhshi, M.H. Farshidianfar, A.P. Gerlich, M. Nosko, V. Trembošová, A. Khajepour, Effects of laser additive manufacturing on microstructure and crystallographic texture of austenitic and martensitic stainless steels, *Addit. Manuf.* 31 (2020) 100915.

- [136] S. Morito, H. Saito, O. T., T. Furuhashi, T. Maki, Effect of austenite grain size on the morphology and crystallography of lath martensite in low carbon steels, *ISIJ Int.* 45 (2005) 91–94.
- [137] S. Tammis-Williams, P.J. Withers, I. Todd, P.B. Prangnell, The influence of porosity on fatigue crack initiation in additively manufactured titanium components, *Sci. Rep.* 7 (2017).
- [138] S. Romano, A. Abel, J. Gumpinger, A.D. Brandão, S. Beretta, Quality control of AlSi10Mg produced by SLM: Metallography versus CT scans for critical defect size assessment, *Addit. Manuf.* 28 (2019) 394–405.
- [139] R. Molaie, A. Fatemi, N. Sanaei, J. Pegues, N. Shamsaei, S. Shao, P. Li, D.H. Warner, N. Phan, Fatigue of additive manufactured Ti-6Al-4V, Part II: The relationship between microstructure, material cyclic properties, and component performance, *Int. J. Fatigue.* 132 (2020) 1.
- [140] M. Tang, P.C. Pistorius, Oxides, porosity and fatigue performance of AlSi10Mg parts produced by selective laser melting, *Int. J. Fatigue.* 94 (2017) 192–201.
- [141] J.W. Pegues, S. Shao, N. Shamsaei, N. Sanaei, A. Fatemi, D.H. Warner, P. Li, N. Phan, Fatigue of additive manufactured Ti-6Al-4V, Part I: The effects of powder feedstock, manufacturing, and post-process conditions on the resulting microstructure and defects, *Int. J. Fatigue.* 132 (2020) 105358.
- [142] S. Romano, P.D. Nezhadfar, N. Shamsaei, M. Seifi, S. Beretta, High cycle fatigue behavior and life prediction for additively manufactured 17-4 PH stainless steel: Effect of sub-surface porosity and surface roughness, *Theor. Appl. Fract. Mech.* 106

(2020) 102477.

- [143] P. Li, D.H. Warner, J.W. Pegues, M.D. Roach, N. Shamsaei, N. Phan, Investigation of the mechanisms by which hot isostatic pressing improves the fatigue performance of powder bed fused Ti-6Al-4V, *Int. J. Fatigue*. 120 (2019) 342–352.
- [144] Z. Xu, W. Wen, T. Zhai, Effects of pore position in depth on stress/strain concentration and fatigue crack initiation, in: *Metall. Mater. Trans. A Phys. Metall. Mater. Sci.*, 2012: pp. 2763–2770.
- [145] S. Beretta, S. Romano, A comparison of fatigue strength sensitivity to defects for materials manufactured by AM or traditional processes, *Int. J. Fatigue*. 94 (2017) 178–191.
- [146] D. Kumar, S. Idapalapati, W. Wang, S. Narasimalu, Effect of surface mechanical treatments on the microstructure-property-performance of engineering alloys, *Materials (Basel)*. 12 (2019).
- [147] D. Wilson, F.P.E. Dunne, A mechanistic modelling methodology for microstructure-sensitive fatigue crack growth, *J. Mech. Phys. Solids*. 124 (2019) 827–848.
- [148] A. Mostafaei, C. Zhao, Y. He, S. Reza Ghiaasiaan, B. Shi, S. Shao, N. Shamsaei, Z. Wu, N. Kouraytem, T. Sun, J. Pauza, J. V. Gordon, B. Webler, N.D. Parab, M. Asherloo, Q. Guo, L. Chen, A.D. Rollett, Defects and anomalies in powder bed fusion metal additive manufacturing, *Curr. Opin. Solid State Mater. Sci.* 26 (2022) 100974.

- [149] America Makes, AMSC, Standardization Roadmap for Additive Manufacturing - Version 2.0, Am. Makes ANSI Addit. Manuf. Stand. Collab. 2 (2018) 1–203.
- [150] H. Gruber, P. Karimi, E. Hryha, L. Nyborg, Effect of Powder Recycling on the Fracture Behavior of Electron Beam Melted Alloy 718, Powder Metall. Prog. 18 (2018) 40–48.
- [151] C.L. Druzgalski, A. Ashby, G. Guss, W.E. King, T.T. Roehling, M.J. Matthews, Process optimization of complex geometries using feed forward control for laser powder bed fusion additive manufacturing, Addit. Manuf. 34 (2020) 101169.
- [152] M. Teimouri, M. Asgari, Mechanical performance of additively manufactured uniform and graded porous structures based on topology-optimized unit cells, <https://doi.org/10.1177/0954406220947119>. 235 (2020) 1593–1618. <https://journals.sagepub.com/doi/full/10.1177/0954406220947119> (accessed January 31, 2022).
- [153] S. Lee, Z. Ahmadi, J. Pegues, M. Mahjouri-Samani, N. Shamsaei, Laser Surface Treatment for Improving Fatigue Performance of Additive Manufactured Ti-6Al-4V Parts, Opt. Laser Technol. (2020) Under Review.
- [154] C. Liang, Y. Hu, N. Liu, X. Zou, H. Wang, X. Zhang, Y. Fu, J. Hu, Laser polishing of Ti6Al4V fabricated by selective laser melting, Metals (Basel). 10 (2020) 1–13.
- [155] W.J. Oh, Y. Son, S.Y. Cho, S.W. Yang, G.Y. Shin, D.S. Shim, Solution annealing and precipitation hardening effect on the mechanical properties of 630 stainless steel fabricated via laser melting deposition, Mater. Sci. Eng. A. 794 (2020) 139999.

- [156] P.D. Nezhadfar, S. Thompson, A. Saharan, N. Phan, N. Shamsaei, Structural integrity of additively manufactured aluminum alloys: Effects of build orientation on microstructure, porosity, and fatigue behavior, *Addit. Manuf.* 47 (2021) 102292.
- [157] M. Avateffazeli, M. Haghshenas, Ultrasonic fatigue of laser beam powder bed fused metals: A state-of-the-art review, *Eng. Fail. Anal.* 134 (2022) 106015. <https://linkinghub.elsevier.com/retrieve/pii/S1350630721008761> (accessed January 7, 2022).
- [158] S. Shao, M.M. Khonsari, J. Wang, N. Shamsaei, N. Li, Frequency dependent deformation reversibility during cyclic loading, *Mater. Res. Lett.* 6 (2018) 390–397. <https://www.tandfonline.com/doi/abs/10.1080/21663831.2018.1469172> (accessed June 16, 2022).
- [159] M. Muhammad, P. Frye, J. Simsiriwong, S. Shao, N. Shamsaei, An investigation into the effects of cyclic strain rate on the high cycle and very high cycle fatigue behaviors of wrought and additively manufactured Inconel 718, *Int. J. Fatigue.* 144 (2021) 106038.
- [160] U. Krupp, A. Giertler, K. Koschella, Microscopic Damage Evolution During Very High Cycle Fatigue (VHCF) of Tempered Martensitic Steel, *Procedia Eng.* 160 (2016) 231–238.
- [161] C. Bathias, P.C. (Paul C. Paris, *Gigacycle fatigue in mechanical practice*, (2005) 304.
- [162] P.D. Nezhadfar, K. Anderson-Wedge, S.R. Daniewicz, N. Phan, S. Shao, N. Shamsaei, Improved high cycle fatigue performance of additively manufactured 17-

4 PH stainless steel via in-process refining micro-/defect-structure, *Addit. Manuf.* 36 (2020) 101604.

[163] P.D. Nezhadfar, P.R. Gradl, S. Shao, N. Shamsaei, Microstructure and Deformation Behavior of Additively Manufactured 17–4 Stainless Steel: Laser Powder Bed Fusion vs. Laser Powder Directed Energy Deposition, *JOM.* (2021) 1–13. <https://link.springer.com/article/10.1007/s11837-021-05032-y> (accessed February 13, 2022).

[164] P.D. Nezhadfar, P.R. Gradl, S. Shao, N. Shamsaei, Microstructure and Deformation Behavior of Additively Manufactured 17–4 Stainless Steel: Laser Powder Bed Fusion vs. Laser Powder Directed Energy Deposition, *JOM.* (2021) 1–13.

[165] L. Pun, G.C. Soares, M. Isakov, M. Hokka, Effects of strain rate on strain-induced martensite nucleation and growth in 301LN metastable austenitic steel, *Mater. Sci. Eng. A.* 831 (2022) 142218.

[166] C. Du, R. Petrov, M.G.D. Geers, J.P.M. Hoefnagels, Lath martensite plasticity enabled by apparent sliding of substructure boundaries, *Mater. Des.* 172 (2019) 107646.

[167] U. Krupp, A. Giertler, K. Koschella, Microscopic Damage Evolution During Very High Cycle Fatigue (VHCF) of Tempered Martensitic Steel, *Procedia Eng.* 160 (2016) 231–238.

[168] M. Muhammad, P.D. Nezhadfar, S. Thompson, A. Saharan, N. Phan, N. Shamsaei, A comparative investigation on the microstructure and mechanical properties of additively manufactured aluminum alloys, *Int. J. Fatigue.* 146 (2021) 106165.

- [169] G. Krauss, *Steels: Heat treatment and processing principles*, 1990.
- [170] J.R. Lee, M.S. Lee, H. Chae, S.Y. Lee, T. Na, W.S. Kim, T.S. Jun, Effects of building direction and heat treatment on the local mechanical properties of direct metal laser sintered 15-5 PH stainless steel, *Mater. Charact.* 167 (2020) 110468.
- [171] Z. Zhao, H. Wang, P. Huo, P. Bai, W. Du, X. Li, J. Li, W. Zhang, Effect of Solution Temperature on the Microstructure and Properties of 17-4PH High-Strength Steel Samples Formed by Selective Laser Melting, *Met.* 2022, Vol. 12, Page 425. 12 (2022) 425. <https://www.mdpi.com/2075-4701/12/3/425/htm> (accessed March 10, 2022).
- [172] S. KC, P.D. Nezhadfar, C. Phillips, M.S. Kennedy, N. Shamsaei, R.L. Jackson, Tribological behavior of 17-4 PH stainless steel fabricated by traditional manufacturing and laser-based additive manufacturing methods, *Wear.* 440-441 (2019) 203100.
- [173] P.D. Nezhadfar, R. Shrestha, N. Phan, N. Shamsaei, Fatigue data for laser beam powder bed fused 17-4 PH stainless steel specimens in different heat treatment and surface roughness conditions, *Data Br.* 25 (2019) 104215.
- [174] J. Pegues, M. Roach, R. Scott Williamson, N. Shamsaei, Volume effects on the fatigue behavior of additively manufactured Ti-6Al4V parts, *Solid Free. Fabr. 2018 Proc. 29th Annu. Int. Solid Free. Fabr. Symp. - An Addit. Manuf. Conf. SFF 2018.* (2020) 1373-1381. <https://repositories.lib.utexas.edu/handle/2152/90213> (accessed June 25, 2022).
- [175] P.D. Nezhadfar, J. Welsh, J. Simsiriwongc, S. Shuai, N. Shamsaeia, Very High

Cycle Fatigue Behavior of Additively Manufactured 17-4 PH Stainless Steel: Effect of Shielding Gas Type, Under Rev. (n.d.).

- [176] M.S. Moyle, N. Haghdadi, X.Z. Liao, S.P. Ringer, S. Primig, On the microstructure and texture evolution in 17-4 PH stainless steel during laser powder bed fusion: Towards textural design, *J. Mater. Sci. Technol.* 117 (2022) 183–195.
- [177] Y. De Li, L.L. Zhang, Y.H. Fei, X.Y. Liu, M.X. Li, On the formation mechanisms of fine granular area (FGA) on the fracture surface for high strength steels in the VHCF regime, *Int. J. Fatigue.* 82 (2016) 402–410.
- [178] Y. Hong, C. Sun, The nature and the mechanism of crack initiation and early growth for very-high-cycle fatigue of metallic materials – An overview, *Theor. Appl. Fract. Mech.* 92 (2017) 331–350.
- [179] W. Li, H. Deng, Z. Sun, Z. Zhang, L. Lu, T. Sakai, Subsurface inclusion-induced crack nucleation and growth behaviors of high strength steels under very high cycle fatigue: Characterization and microstructure-based modeling, *Mater. Sci. Eng. A. Complete* (2015) 10–20.
<https://www.infona.pl//resource/bwmetal.element.elsevier-1e31078f-7eb2-3db0-ad90-f101be0f52e7> (accessed July 11, 2022).
- [180] D.D. Gu, W. Meiners, K. Wissenbach, R. Poprawe, Laser additive manufacturing of metallic components: materials, processes and mechanisms, *Int. Mater. Rev.* 57 (2013) 133–164.
- [181] T.F. Babuska, B.A. Krick, D.F. Susan, A.B. Kustas, Comparison of powder bed fusion and directed energy deposition for tailoring mechanical properties of

traditionally brittle alloys, *Manuf. Lett.* 28 (2021) 30–34.

[182] A. Jinoop, C. Paul, K. Bindra, Laser-assisted directed energy deposition of nickel super alloys: A review, *Proc. Inst. Mech. Eng. Part L J. Mater. Des. Appl.* 233 (2019) 2376.

[183] J. Simpson, J. Haley, C. Cramer, O. Shafer, A. Elliott, B. Peter, L. Love, R. Dehoff, Considerations for Application of Additive Manufacturing to Nuclear Reactor Core Components, ORNL/TM-2019-1190, Oak Ridge Natl. Lab. 1190 (2019) 1. www.osti.gov (accessed September 26, 2021).

[184] Q. Guo, C. Zhao, M. Qu, L. Xiong, L.I. Escano, S.M.H. Hojjatzadeh, N.D. Parab, K. Fezzaa, W. Everhart, T. Sun, L. Chen, In-situ characterization and quantification of melt pool variation under constant input energy density in laser powder bed fusion additive manufacturing process, *Addit. Manuf.* 28 (2019) 600–609.

[185] A. Saboori, A. Aversa, G. Marchese, S. Biamino, M. Lombardi, P. Fino, Microstructure and Mechanical Properties of AISI 316L Produced by Directed Energy Deposition-Based Additive Manufacturing: A Review, *Appl. Sci.* 2020, Vol. 10, Page 3310. 10 (2020) 3310. <https://www.mdpi.com/2076-3417/10/9/3310/html> (accessed September 6, 2021).

[186] M. Ma, Z. Wang, X. Zeng, A comparison on metallurgical behaviors of 316L stainless steel by selective laser melting and laser cladding deposition, *Mater. Sci. Eng. A.* 685 (2017) 265–273.

[187] K.N. Amato, S.M. Gaytan, L.E. Murr, E. Martinez, P.W. Shindo, J. Hernandez, S. Collins, F. Medina, Microstructures and mechanical behavior of Inconel 718

- fabricated by selective laser melting, *Acta Mater.* 60 (2012) 2229–2239.
- [188] F. Liu, X. Lin, H. Leng, J. Cao, Q. Liu, C. Huang, W. Huang, Microstructural changes in a laser solid forming Inconel 718 superalloy thin wall in the deposition direction, *Opt. Laser Technol.* 45 (2013) 330–335.
- [189] L.L. Parimi, G. Ravi, D. Clark, M.M. Attallah, Microstructural and texture development in direct laser fabricated IN718, *Mater. Charact.* 89 (2014) 102–111.
- [190] W. Xu, M. Brandt, S. Sun, J. Elambasseril, Q. Liu, K. Latham, K. Xia, M. Qian, Additive manufacturing of strong and ductile Ti–6Al–4V by selective laser melting via in situ martensite decomposition, *Acta Mater.* 85 (2015) 74–84.
- [191] B.E. Carroll, T.A. Palmer, A.M. Beese, Anisotropic tensile behavior of Ti-6Al-4V components fabricated with directed energy deposition additive manufacturing, *Acta Mater.* 87 (2015) 309–320.
- [192] J. Schneider, Comparison of Microstructural Response to Heat Treatment of Inconel 718 Prepared by Three Different Metal Additive Manufacturing Processes, *JOM.* 72 (2020) 1085–1091. <https://link.springer.com/article/10.1007/s11837-020-04021-x> (accessed September 6, 2021).
- [193] C. Doñate-Buendia, R. Streubel, P. Kürsteiner, M.B. Wilms, F. Stern, J. Tenkamp, E. Bruder, S. Barcikowski, B. Gault, K. Durst, J.H. Schleifenbaum, F. Walther, B. Gökce, Effect of nanoparticle addition on the microstructure and microhardness of oxide dispersion strengthened steels produced by laser powder bed fusion and directed energy deposition, *Procedia CIRP.* 94 (2020) 41–45.

- [194] S. Cao, Determination of the Fe-Cr-Ni and Fe-Cr-Mo Phase Diagrams at Intermediate Temperatures using a Novel Dual-Anneal Diffusion-Multiple Approach, The Ohio State University, 2013.
- [195] P.D. Nezhadfar, P. Gradl, S. Shuai, N. Shamsaei, A Comparative Study on the Microstructure and Texture Evolution of L-PBF and LP-DED 17-4 PH Stainless Steel during Heat Treatment, in: Proc. 32nd Annu. Int. Solid Free. Fabr. Symp. – An Addit. Manuf. Conf., 2021.
- [196] ASTM Standard E8/E8M-13a, Standard test methods for tension testing of metallic materials, 2006. www.astm.org, (accessed June 19, 2020).
- [197] C. Celada-Casero, J. Sietsma, M.J. Santofimia, The role of the austenite grain size in the martensitic transformation in low carbon steels, *Mater. Des.* 167 (2019) 107625.
- [198] D.H. Ping, S.Q. Guo, M. Imura, X. Liu, T. Ohmura, M. Ohnuma, X. Lu, T. Abe, & H. Onodera, Lath formation mechanisms and twinning as lath martensite substructures in an ultra low-carbon iron alloy, 8 (2018) 14264. www.nature.com/scientificreports/ (accessed September 20, 2021).
- [199] C. Cayron, One-step theory of fcc-bcc martensitic transformation, *Acta Crystallogr. Sect. A Found. Crystallogr.* 69 (2012) 498–509. <https://arxiv.org/abs/1211.0495v1> (accessed September 26, 2021).
- [200] M.E. Stevenson, P.D. Umberger, S.F. Uchneat, Fracture Appearance and Mechanisms of Deformation and Fracture, ASM International, 2021.

- [201] M. LaMonica, Additive Manufacturing-Innovations, Advances, and Applications, 2013.
- [202] ISO/ASTM 52900:2015(E), Standard Terminology for Additive Manufacturing – General Principles – Terminology, (n.d.).
- [203] B. Blakey-Milner, P. Gradl, G. Snedden, M. Brooks, J. Pitot, E. Lopez, M. Leary, F. Berto, A. du Plessis, Metal additive manufacturing in aerospace: A review, Mater. Des. 209 (2021) 110008.
- [204] S. Mirzababaei, S. Pasebani, A review on binder jet additive manufacturing of 316L stainless steel, J. Manuf. Mater. Process. 3 (2019) 82. www.mdpi.com/journal/jmmp (accessed May 25, 2021).
- [205] C.-H. Hung, W.-T. Chen, M.H. Sehhat, M.C. Leu, The effect of laser welding modes on mechanical properties and microstructure of 304L stainless steel parts fabricated by laser-foil-printing additive manufacturing, Int. J. Adv. Manuf. Technol. 2020 1123. 112 (2020) 867–877. <https://link.springer.com/article/10.1007/s00170-020-06402-7> (accessed August 26, 2021).
- [206] A. Röttger, J. Boes, W. Theisen, M. Thiele, C. Esen, A. Edelmann, R. Hellmann, Microstructure and mechanical properties of 316L austenitic stainless steel processed by different SLM devices, Int. J. Adv. Manuf. Technol. 108 (2020) 769–783.
- [207] P. Nandwana, A.M. Elliott, D. Siddel, A. Merriman, W.H. Peter, S.S. Babu, Powder bed binder jet 3D printing of Inconel 718: Densification, microstructural evolution and challenges☆, Curr. Opin. Solid State Mater. Sci. 21 (2017) 207–218.

- [208] M. Turker, D. Godlinski, F. Petzoldt, Effect of production parameters on the properties of IN 718 superalloy by three-dimensional printing, *Mater. Charact.* 59 (2008) 1728–1735.
- [209] A. Mostafaei, Y. Behnamian, Y.L. Krimer, E.L. Stevens, J.L. Luo, M. Chmielus, Effect of solutionizing and aging on the microstructure and mechanical properties of powder bed binder jet printed nickel-based superalloy 625, *Mater. Des.* 111 (2016) 482–491.
- [210] L.M.S. Santos, L.P. Borrego, J.A.M. Ferreira, J. de Jesus, J.D. Costa, C. Capela, Effect of heat treatment on the fatigue crack growth behaviour in additive manufactured AISI 18Ni300 steel, *Theor. Appl. Fract. Mech.* 102 (2019) 10–15. <https://www.sciencedirect.com/science/article/pii/S0167844218305251> (accessed April 12, 2019).
- [211] A. Kumar, Y. Bai, A. Eklund, C.B. Williams, Effects of Hot Isostatic Pressing on Copper Parts Fabricated via Binder Jetting, *Procedia Manuf.* 10 (2017) 935–944.
- [212] W. Li, S. Li, J. Liu, A. Zhang, Y. Zhou, Q. Wei, C. Yan, Y. Shi, Effect of heat treatment on AlSi10Mg alloy fabricated by selective laser melting: Microstructure evolution, mechanical properties and fracture mechanism, *Mater. Sci. Eng. A.* 663 (2016) 116–125.
- [213] P.D. Nezhadfar, B. Verquin, L.P. Lefebvre, C. Reynaud, M. Robert, N. Shamsaei, Effect of Heat Treatment on the Tensile Behavior of 17-4 PH Stainless Steel Additively Manufactured by Metal Binder Jetting, in: *Solid Free. Fabr. 2019 Proc. 30th Annu. Int. Solid Free. Fabr. Symp. - An Addit. Manuf. Conf. SFF 2019*, 2019:

pp. 2271–2281.

- [214] D. Huber, P. Stich, A. Fischer, Heat Treatment of 17–4 PH Stainless Steel Produced by Binder Jet Additive Manufacturing (BJAM) from N₂-Atomized Powder, *Prog. Addit. Manuf.* 7 (2022) 187–199. <https://link.springer.com/article/10.1007/s40964-021-00224-z> (accessed July 12, 2022).
- [215] ASTM E606/E606M–12, Standard test method for strain-controlled fatigue testing, ASTM Int. (2012).
- [216] G. Yang, F. Deng, S. Zhou, B. Wu, L. Qin, J. Zheng, Influence of shielding gas nitrogen content on the microstructure and mechanical properties of Cu-reinforced maraging steel fabricated by wire arc additive manufacturing, *Mater. Sci. Eng. A.* 832 (2022) 142463.
- [217] K.T.S. Takaki, Y. Tokunaga, Reversion Austenite mechanism from Deformation Induced Martensite in Metastable Austenitic Stainless Steels to, 1991.
- [218] L. Morsdorf, O. Jeannin, D. Barbier, M. Mitsuhashi, D. Raabe, C.C. Tasan, Multiple mechanisms of lath martensite plasticity, *Acta Mater.* 121 (2016) 202–214.
- [219] H. Song, S.S. Sohn, J.H. Kwak, B.J. Lee, S. Lee, Effect of Austenite Stability on Microstructural Evolution and Tensile Properties in Intercritically Annealed Medium-Mn Lightweight Steels, *Metall. Mater. Trans. A Phys. Metall. Mater. Sci.* 47 (2016) 2674–2685.
- [220] W. Do Yoo, J.H. Lee, K.T. Youn, Y.M. Rhyim, Study on the Microstructure and Mechanical Properties of 17-4 PH Stainless Steel Depending on Heat Treatment and

Aging Time, Solid State Phenom. 118 (2006) 15–20.
<https://www.scientific.net/SSP.118.15> (accessed June 27, 2022).

- [221] D.A. Porter, K.E. Easterling, Phase transformations in metals and alloys (revised reprint), CRC press, 2009.
- [222] S. Saberipour, A. Zarei-Hanzaki, H.R. Abedi, M. Moallemi, Interplay of austenite and ferrite deformation mechanisms to enhance the strength and ductility of a duplex low-density steel, *J. Mater. Res. Technol.* 18 (2022) 755–768.
- [223] P. Bajaj, A. Hariharan, A. Kini, P. Kürnsteiner, D. Raabe, E.A. Jäggle, Steels in additive manufacturing: A review of their microstructure and properties, *Mater. Sci. Eng. A.* 772 (2020) 138633.
- [224] N. Guennouni, A. Barroux, C. Grosjean, D. Maisonnette, E. Nivet, E. Andrieu, D. Poquillon, L. Laffont, C. Blanc, Comparative study of the microstructure between a laser beam melted 17-4PH stainless steel and its conventional counterpart, *Mater. Sci. Eng. A.* 823 (2021) 141718.
- [225] H.K. Rafi, T.L. Starr, B.E. Stucker, A comparison of the tensile, fatigue, and fracture behavior of Ti–6Al–4V and 15-5 PH stainless steel parts made by selective laser melting, *Int. J. Adv. Manuf. Technol.* 69 (2013) 1299–1309.
- [226] F. Kellogg, E. Vasilev, A. Kudzal, J. Taggart-Scarff, J. Marsico, M. Knezevic, B. McWilliams, Physical simulations of heat-affected zone microstructures to compare weldability characteristics of additively manufactured and wrought 17-4 stainless steel, *Mater. Charact.* 185 (2022) 111714.

- [227] F.C. Hull, Sponsored by the Welding Research Council Delta Ferrite and Martensite Formation in Stainless Steels From studies of 70 chill-cast stainless steel alloy types, nickel-and chromium-equivalents of 13 elements are evaluated for use in a revised Schaeffler diagram, n.d.
- [228] E.K. Tschegg, H.O.K. Kirchner, K.H. Schwalbe, Cracks at interfaces of different cohesion, *Acta Metall. Mater.* 41 (1993) 2783–2790.
- [229] P.I. Christodoulou, A.T. Kermanidis, G.N. Haidemenopoulos, D. Krizan, K. Polychronopoulou, Effect of retained austenite stability on cyclic deformation behavior of low-alloy transformation-induced plasticity steels, *Fatigue Fract. Eng. Mater. Struct.* (2019).
- [230] P. Christodoulou, EFFECT OF RETAINED AUSTENITE TRANSFORMATION ON THE FATIGUE EFFECT OF RETAINED AUSTENITE TRANSFORMATION ON THE FATIGUE BEHAVIOUR OF ALUMINUM CONTAINING TRIP STEELS by A thesis submitted to the Department of Mechanical Engineering University of Thessaly, University of Thessaly, 2018.